Improved Active Interrogation Methods for Nuclear Nonproliferation and Homeland Security Applications

by

Cameron Alan Miller

A dissertation submitted in partial fulfillment
of the requirements for the degree of
Doctor of Philosophy
(Nuclear Engineering and Radiological Sciences)
in the University of Michigan
2020

Doctoral Committee:

Professor Sara A. Pozzi, Chair
Dr. Shaun D. Clarke
Dr. Cameron G.R. Geddes, Lawrence Berkeley National Laboratory
Professor David D. Wentzloff
Dr. Namdoo Moon, Department of Homeland Security, CWMD

Cameron Alan Miller

cmillera@umich.edu

ORCID iD: 0000-0003-1310-0310

DEDICATION

To my family, on both peninsulas.

Acknowledgments

I would like to thank my advisor Professor Sara Pozzi for the opportunity to pursue a PhD degree in the incredible nuclear engineering community at the University of Michigan. I will always appreciate the mentorship provided by Professor Pozzi and Dr. Shaun Clarke in the Detection for Nuclear Nonproliferation Group. I would also like to thank my doctoral committee for the guidance and inspiration through my graduate school career.

I could not have reached this point without my family, and especially my parents, whose support has always encouraged me to continue my academic supports. I would like to thank my fiancé Ashley, who has supported and encouraged me throughout my entire PhD student career, and continues to do so as we embark on many new journeys. Many thanks as well to Wendell, the infinite source of cheer and energy.

This journey has been much more fulfilling because of my many collaborators and mentors along the way, especially the DNNG students, past and present.

This research was made possible in part by the US Department of Homeland Security Academic Research Initiative under Grant No. 2016-DN-077-ARI106, and the Consortium for Verification Technology under Department of Energy National Nuclear Security Administration award No. DE-NA0002534.

TABLE OF CONTENTS

Chapter

LIST OF FIGURES

FIGURE

LIST OF TABLES

TABLE

LIST OF APPENDICES

APPENDIX

LIST OF ABBREVIATIONS

ABG active background

ADC analog-to-digital converter

ALARA as low as is reasonably achievable

BPE borated polyethylene

BWR boiling water reactor

CDCIS Compton Dry-Cask Imaging Scanner

CFD constant fraction discriminator

CoK continuity of knowledge

CoMPASS CAEN Multi-PArameter Spectroscopy Software

DDAA differential die-away analysis

DU depleted uranium

FOM figure of merit

FWHM full width at half maximum

HEU highly enriched uranium

IAEA International Atomic Energy Agency

LET linear energy transfer

LEU low enriched uranium

linac linear accelerator

LPA laser-driven plasma accelerator

LWR light-water reactor

MPS quasi-monoenergetic photon source

NPT Treaty on the Non-Proliferation of Nuclear Weapons

PMT photomultiplier tube

PSD pulse shape discrimination

PUR pile up rejection

PWR pressurized water reactor

SNM special nuclear material

SNR signal to noise ratio

TNA thermal neutron analysis

ABSTRACT

Highly enriched uranium is arguably the most difficult material to detect in the realm of nuclear security and safeguards, but is of great concern for its possible role in developing nuclear weapons. Uranium-235 emits very few neutrons, and the low energy photons it emits are easily shielded, making passive detection of highly enriched uranium very difficult. Actively interrogating the material with neutron or photon sources can provide a much more prominent detection signal. These sources of radiation can be used to either induce detectable emissions in the material, or radiograph the material to distinguish it from possible shielding. Active interrogation presents detection challenges in signal quality and operational feasibility, especially because currently-available sources mostly emit photons that can be easily shielded and are below photonuclear energy thresholds. My research will focus on addressing these challenges by demonstrating advantages of photon interrogation based on recent enabling technologies, both from the perspective of the interrogating source and the detection system.

Inverse Compton scattering quasi-monoenergetic photon sources using a laser-driven plasma accelerator are a developing technology that has strong potential to advance photon interrogation methods. These sources use the laser wakefield phenomenon to accelerate electrons to very high energy. Photons from a secondary laser beam interact with these electrons through inverse Compton scattering, producing a photon source highly focused in energy and space. The energy of these photons can be tuned to penetrate shielding and induce photonuclear reactions. The work presented here is based on quasi-monoenergetic photon sources at the University of Nebraska Lincoln and the Lawrence Berkeley National Laboratory. Through Monte Carlo simulations, I have demonstrated the capability to image heavily shielded nuclear material, validated by experiment. These studies showed increased accuracy for hidden nuclear material detection over traditional bremsstrahlung sources.

A 9-MeV linac has been installed at UM, which outputs a high intensity of photons capable of inducing photonuclear reactions. This high photon intensity makes neutron detection and identification challenging, but we are developing methods to detect prompt neutrons in-pulse with organic scintillators. These methods incorporate high throughput data acquisition, active background reduction, and collaboratively developed neural-network based pulse discrimination and recovery. Initial experiments interrogating lead and tungsten surrogates for highly enriched uranium have identified elevated neutron counts for the cases with target present over active background.

Compared to a quasi-monoenergetic photon source, the bremsstrahlung source produces many low-energy photons that only contribute to surrounding dose rates. To demonstrate this dosimetric advantage, and verify shielding for the operation of various accelerators, a method for measuring dose rates was required. An organic scintillator based strategy was developed to provide a replicable and dual-particle dose rate detection method. This method has been used to simultaneously measure neutron and gamma dose rates from isotopic sources; these results show reasonable agreement with traditional instruments. Future experiments will demonstrate the method with active interrogation sources.

The results of my research will enable the use of organic scintillators and novel photon sources for use in an active interrogation scenario to prevent the spread of nuclear material.

CHAPTER 1

Introduction

1.1 Motivation

Fission was discovered in December 1938 by the chemists Otto Hahn and Fritz Strassman, with some skepticism. Their experiment was designed to create new heavy elements by bombarding uranium with neutrons produced by a mixture of radium and beryllium, but they observed a much lighter element: barium. Hahn wrote to their colleague, physicist Lise Meitner: “Perhaps you can suggest some fantastic explanation. We ourselves realize that [uranium] can’t really burst into Ba” [1]. Meitner and her nephew Otto Robert Frisch indeed developed a fantastic theory, describing an atom cleaved in two through nuclear fission. Their theory was soon experimentally confirmed.

The fissioning of uranium releases an extraordinary amount of energy, and neutrons are released as well, enabling chain reactions of fissioning uranium nuclei. The discovery of this process therefore gave rise to reliable, efficient, and clean electricity production with nuclear energy, but it also led to the advent of nuclear weapons. The destructive power of a nuclear weapon is so great, that they have only been used twice in warfare, at the end of World War II; however, during the tensions of the Cold War Era, tens of thousands of weapons were produced on both sides of the conflict.

This rapid increase in destructive nuclear capabilities made clear the urgent need for limitations. The Treaty on the Non-Proliferation of Nuclear Weapons (NPT) [2] was opened for signature on the first of July, 1968, and entered into force in 1970, then renewed in perpetuity in 1995. The NPT seeks to prevent the spread of nuclear weapons, without inhibiting peaceful uses of nuclear technology. Complete nuclear disarmament is also a goal of the treaty. The signing countries (all but five currently) agree that countries not possessing nuclear weapons prior to 1967 would never seek to obtain or develop them. Countries possessing nuclear weapons at the time (United States, Russia, United Kingdom, France, and China) agree not to transfer to other states any nuclear weapons, related technology, or knowledge, but to cooperate in the development of peaceful nuclear technology, and to strive towards complete disarmament. Four states have never been adherent to the NPT: India, Pakistan, Israel, and South Sudan. India and Pakistan have made their possession of nuclear weapons known, and it is generally assumed that Israel possesses nuclear weapons. South Sudan has not yet signed since its inception in 2011. North Korea was a one-time signatory of the treaty, but withdrew in 2003 and publicly announced possession of nuclear weapons in 2005. Several other non-weapons states, as well as non-state actors, have been suspected of attempting to develop nuclear weapons.

The primary barrier to the development of nuclear weapons is acquiring the required nuclear material. This material is referred to as special nuclear material (SNM), and is defined in 10 CFR part 74.4 [3] as “plutonium, uranium-233, uranium enriched in the isotope ^{233}U or in the isotope ^{235}U”. Uranium enriched to more than 20% ^{235}U (highly enriched uranium (HEU)) is additionally considered to be SNM of strategic significance. It is much easier to steal or smuggle the required material than a fully assembled nuclear weapon. Millions of kilograms of both HEU and plutonium exist worldwide, and the theft and proliferation of this material is concerning for nuclear weapons development by non-NPT-state and non-state actors. The major source of concern for the theft of SNM is material stored in former Soviet Union countries. The general state of security at facilities in these countries, decades of inadequate accounting, and amount of material stored (estimated to be 600 metric tons) leaves this material at risk to be stolen by terrorists [4]. In addition former Soviet Union facilities, sources of concern for theft of SNM include: Pakistan, research reactors, established nuclear weapons programs, marine propulsion systems, and civilian plutonium or HEU [4]. Given the availability of material, and extreme consequences of a nuclear weapon in terrorist hands, the security community requires technology to prevent the spread of SNM.

The global commerce system is a likely avenue for the distribution of nuclear material, and the clandestine spread of nuclear material into the United States is of great concern. Passive scanning is the most prevalent method used for detecting this material, and while passive detection may serve to detect radiological threats that emit high levels of radiation, some nuclear-weapons-usable materials (especially HEU) emits low amounts of radiation. HEU very rarely spontaneously fissions, and only emits low energy gamma rays that can easily be shielded. In order to more reliably detect these materials, active interrogation uses an external radiation source to induce more prominent and detectable emissions than natural radiation. This interrogation is especially useful for detecting HEU, which is more available than other types of SNM and emits little radiation passively.

1.2 Overview of Current State of Active Interrogation

Sources of interrogating radiation can be grouped into one of two categories: naturally-radioactive, or artificially-driven sources. While radioactive material is readily available, the output is not easily tailored to specific applications, and it is always "on" or emitting radiation, possibly contributing radiation dose to anyone nearby. Naturally-radioactive sources of radiation can also be stolen themselves, and fashioned into radiological dispersion device (RDD) or "dirty bomb", which distributes radioactive material with conventional explosives. Artificial sources of radiation, driven by electrically- or laser-driven particles, are therefore an appealing alternative to natural sources of radiation. These accelerators can be tuned to specific requirements of applications, and do not contain high levels of radioactive materials.

Wilhelm Röntgen was the first to artificially create X-rays with a early accelerator in 1895. He was performing experiments with sealed cathode-ray tube, when he noticed a nearby barium platinocyanide screen fluorescing. It was later understood that the cathode rays were actually electrons accelerated by the current in the tube, and these electrons curved and slowed down through the bremsstrahlung process in the sealing material, releasing energy in the form of X-rays. Accelerator technology advanced in the 20^{th} century with the development of the linear accelerator by Wideroe in 1928, the cyclotron by Lawrence in 1931. These accelerators enabled kinetic energies in excess of 10 MeV. Further advancements saw protons and electrons accelerated to 300 MeV by 1950 [5]. Nuclear and high-energy physics have traditionally driven the development of this technology, but many other fields have found use for accelerators including medicine and nuclear security.

According to 6 U.S. Code section 982 [6], 100 percent of cargo containers originating outside of the United States must be screened (meaning at a minimum, to be radiographed) before passing through a domestic seaport. This goal has not yet been met due to the cost and technical challenges involved. The current status of cargo screening is outlined by the U.S. Congressional Budget Office in [7]: all 12 million incoming cargo containers per year are passively scanned, but only 5% of these are screened with X-ray or gamma-ray systems.

The challenges preventing the widespread deployment of active interrogation screening methods are many. While radiography of cargo containers is more immediately feasible, a true active interrogation method of inducing SNM signatures presents many difficulties. While demonstration systems have been developed, no full systems have been deployed for commercial operations.

1.3 Dissertation Contribution

In this dissertation, I demonstrate advanced active interrogation capabilities enabled by emerging technologies in the field. A variety of interrogating source and detector combinations have been investigated to support the deployment of active interrogation systems for the detection of nuclear weapons. Chapter 2 contains general discussions of these sources, detectors, and signal acquisition methods.

The results of two neutron interrogation experimental campaigns are discussed in Chapter 3. Both experiments involved interrogation of nuclear material with advanced neutron sources. The first campaign used conventional radiation detectors to not only detect SNM, but also other forms of contraband. Organic scintillator detectors were used in the second experiment to characterize SNM using methods that, to my knowledge, have not previously been explored.

Interrogation of material with a high-energy source of bremsstrahlung X-rays is discussed in Chapter 4, including the effort to install a linear accelerator at the University of Michigan. Photon-induced neutrons were detected with an organic scintillator, demonstrating promise for a novel photofission detection system.

The advantages of a laser-driven plasma accelerator Thomson scattering quasi-monoenergetic photon source for nonproliferation applications are studied in Chapter 5. Through a collaboration with the University of Nebraska, a radiography proof-of-concept for this new technology is presented. My simulation results agree with the results of experiments performed by Nebraska researchers. The simulation study of such a source is then expanded to support further laboratory ventures, and advanced nonproliferation applications.

Chapter 6 presents a novel method for detecting radiation dose contributions from both neutrons and photons using an organic-scintillator. Because the radiation emitted by an interrogating source is always of concern for personal protection, it is important that a reliable dosimetry method is in place. The presented method is an attempt to improve upon the current dose detection techniques.

In Chapter 7, I draw conclusions from the work presented in this dissertation and present suggested paths for future research.

CHAPTER 2

Interrogating Sources and Detection

2.1 Interrogation Sources

The discussion in this work will focus on the most commonly used interrogating particles, photons and neutrons. Because both of these particles have neutral charge, they can penetrate through shielding and into a sample at moderate energies (MeV), while also possessing the ability to induce fissions in SNM [8]. This section will give an overview of the common ways to produce neutrons and photons in the MeV range required for active interrogation.

2.1.1 Isotopic Sources

Certain radioisotopes emit photons alone, and some emit neutrons and photons. Gamma-ray sources are usually isotopes that undergo beta decay. These isotopes decay into excited states of a daughter nucleus, which then emits energy in the form of a gamma ray as it de-excites. Common isotopes used as gamma-ray sources include ^{22}Na, ^{57}Co, ^{60}Co, and ^{137}Cs [9]. The gamma rays emitted by these sources are too low to induce photonuclear reactions in SNM, where the reaction thresholds are at least 5.3 MeV [10]. Example photonuclear cross sections for ^{235}U are shown in Fig. 2.1 [11]. Isotopic photon sources can be useful for radiography, and are discussed in this work in the context of detector calibration.

Neutrons produced by isotopic sources can be emitted through spontaneous fission or an (α,n) reaction. Californium-252 is a commonly used spontaneous fission source, due to its convenient

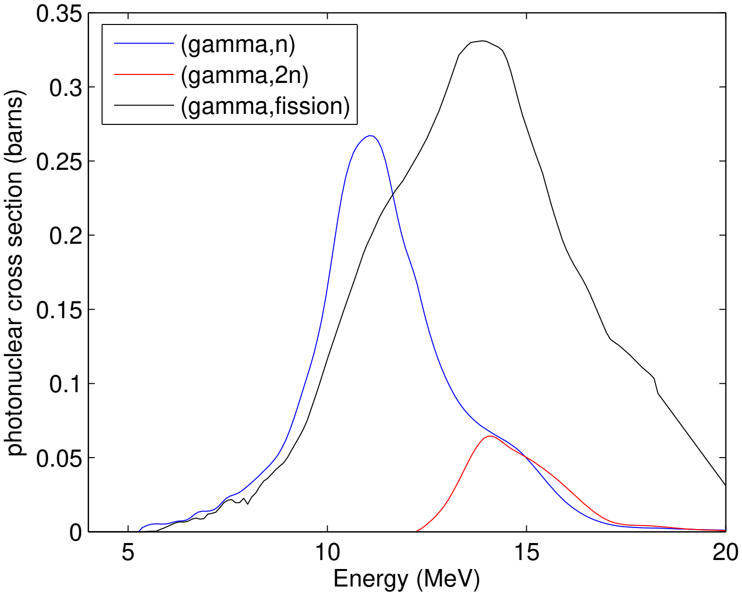

Figure 2.1: ^{235}U photonuclear cross sections: (γ,n), (γ,2n), and (γ,fission) [11].

half-life of 2.65 years and high neutron output of 2.30×10^6 n/s per microgram [9]. The neutrons emitted by this source through spontaneous fission have energy along a Watt spectrum peaked near 1 MeV, with an average of about 2 MeV. Most isotopic neutron sources based on the (α,n) reaction use beryllium as the target nuclide for this reaction [9]. The neutron spectrum from the emitted by alpha-Be source spectra regardless of alpha contributor isotope, because the the neutron energy is dependent on the excitation state of the resulting ^{12}C nucleus. These excited states result in neutron emissions in somewhat defined peaks, as shown in 2.2 from [12]. The alpha contributor used in this work is ^{239}Pu. A ^{239}Pu-Be source emits about 10^7 neutrons per second with a Curie of ^{239}Pu, which has a long enough half-life (24,000 years) to have an effectively constant source rate for laboratory purposes [12]. Because most of the neutron energy peaks are of higher energy than the average energy from a spontaneous fission spectrum, (α,n) sources are a good laboratory option for harder-energy spectrum neutrons.

Isotopic sources with photonuclear reactions as the source of neutrons are also available. These sources are based on a gamma-emitter surrounded by a beryllium- or deuterium-containing medium [9]. However, the required gamma-flux is extremely high, necessitating short lived iso-

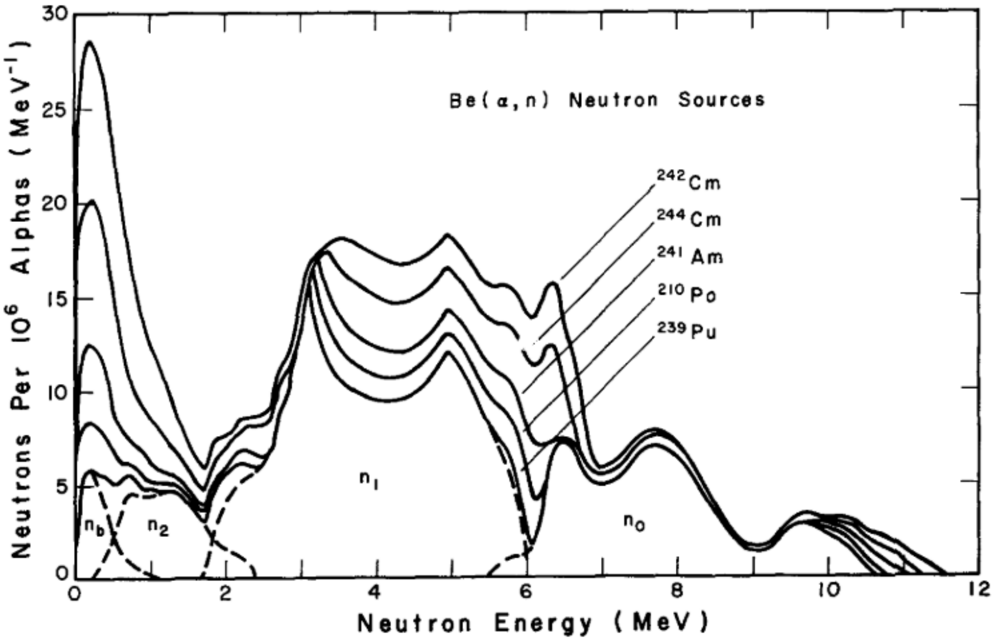

Figure 2.2: (α,n) source spectra [12].

topes, and the resulting neutron energy is generally less than 1 MeV. Therefore, these sources are not utilized in this work.

In this work a ^{252}Cf source is used as a source of neutrons due to its practicality in the lab and the fact that the emitted energy spectrum is a fission Watt spectrum. This energy spectrum allows the source to act as a suitable proxy for the expected fission neutron spectrum, which is a positive indicator of SNM. A ^{239}Pu-Be source is also used as an alternative neutron spectrum for testing at higher neutron energy. Fewer neutrons per photon are emitted as well, so particle discrimination is more accurate. The use of a ^{239}Pu-Be source use for particle discrimination optimization is discussed further in Section 2.3.3.

2.1.2 Accelerator-Based Neutron Sources

Accelerated charged particles, commonly deuterons, can be used to induce neutron generating reactions in deuterium or tritium targets. Neutron sources based on these reactions are referred to as ”neutron generators”. Neutron generators generally accelerate the deuterons to relatively low energy for optimal reaction rates (about 100 to 200 keV), and therefore they do not contribute

Figure 2.3: Starfire nGen™-400 neutron generator [15].

significant additional energy to the outgoing neutrons. In this configuration the resulting neutrons have energy of about 2.45 MeV from the D-D reaction, and 14.1 MeV from the D-T reaction. The neutron flux can be varied by controlling the current of deuterons, but tritium targets produce about 100 times more neutrons than a deuterium target for the same deuteron current. This increase in D-T neutron output is because the D-T cross section is about a factor of 100 greater in the approximately 100 keV deuteron energy range [13]. Additional energy can be added to the outgoing neutron with increased deuteron acceleration, but the cross sections drop of after about 100 keV for D-T, and 2 MeV for D-D [14]. These neutron generators can produce a high flux of neutrons with a relatively small accelerator, with an example shown in 2.3 from [15].

Other accelerator based sources employ other light ion reactions including ^{9}Be(d,n), ^{7}Li(p,n), and ^{3}H(p,n). The ^{7}Li(p,n) reaction can be used to produce 60 keV neutrons, although the process is more complex than standard neutron generators [16].

2.1.3 Bremsstrahlung Photon Sources

The most common method for high-energy photon production is to use an electron accelerator to produce high-energy photons through the bremsstrahlung reaction [8]. The accelerated electrons are directed at a high-Z conversion target, where the electron energy is converted to bremsstrahlung photons. These photons are emitted in all directions, but are biased in the direction of the acceler-

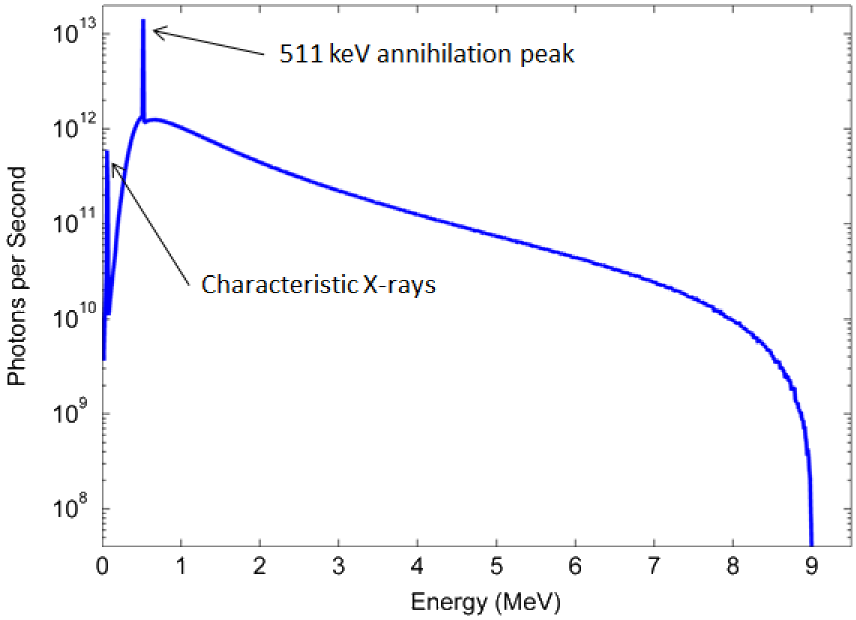

Figure 2.4: Simulated bremsstrahlung photon spectrum resulting from 9 MeV accelerated electrons incident on a copper-backed tungsten conversion target.

ated electrons. The energy spectrum of these photons is continuous with a maximum energy equal to the energy of the incident electrons, but the emission of lower energy photons is much more likely. An example 9-MeV maximum bremsstrahlung photon spectrum is shown in 2.4. While a small proportion of the photon spectrum is in the energy range near 9 MeV, most photons are emitted with much lower energy. The average photon energy of the spectrum in 2.4 is about 1.5 MeV. This spectrum also shows low energy contribution from the 511 keV annihilation peak and characteristic tungsten X-rays, with energies of about 59 and 67 keV.

The electron energy for a bremsstrahlung source used in active interrogation is chosen so that the resulting photons have sufficient energy to induce photonuclear reactions. Therefore, the minimum energy is 6 MeV, although 9-10 MeV is more practical and common because electron energy for screening of cargoes is limited by federal regulation (21 CFR 179.21) to 10 MeV [8].

Bremsstrahlung photon sources can be operated in either pulsed (10s-100s Hz) mode [17] or quasi-continuous (100s MHz) mode [18]. These sources are generally operated in the range of 10 μA current, which produce about 6×10^{13} photons per second. When pulsed the typical pulse width of a bremsstrahlung source is on the order of microseconds.

2.1.4 Nuclear Reaction Photon Sources

Certain nuclear reactions induced by accelerating charged particles into a target can be employed to produce high-energy, monoenergetic photons [19, 20, 21, 22, 23]. One reaction that has been employed in active interrogation research is ^{11}B(d,nγ)^{12}C. This reaction produces isotropic, monoenergetic photons at either 4.4 or 15.1 MeV, which have been used for dual-energy radiography and for inducing fission reactions [23]. Research is continuing into the development of such sources for photon production, and their relevance for active-interrogation nonproliferation applications.

2.1.5 Thomson Scattering Quasi-Monoenergetic Photon Sources

Photon sources based on Thomson scattering (i.e., inverse-Compton scattering) produce photons with narrow energy and angular spread [24, 25, 26, 27]. An quasi-monoenergetic photon source (MPS) accelerates electrons either by conventional accelerator means [28] or with a compact laser-driven plasma accelerator (LPA) [25, 29, 30]. This work focuses on photons produced with LPA electrons, which are accelerated to 100s of MeV through laser wakefield acceleration [31] by a driving laser. This acceleration is accomplished by passing a laser pulse through a gas jet, ionizing the gas and creating a plasma. The electrons are moved out of the center of this plasma channel much faster than the heavier protons, creating an electric field ”wake”. This electric field (on the order of GeV/cm) then accelerates electrons to very high energies over short distances. Photons from a separate scattering laser are then scattered off of these high-energy electrons through Thomson scattering. This scattering is precisely performed when the accelerated electrons are at their peak energy, before decelerating on the other side of the wake.

Compared to bremsstrahlung source photons, these resulting photons have a very narrow energy and angular spread, both dependent on the properties of the electron beam.

A simulated 8 MeV MPS spectrum based on current capabilities is shown in 2.5, compared to an 8-MeV endpoint bremsstrahlung photon spectrum. An important note on this comparison is that the emitted photons here are tallied in all directions. In practice, all MPS photons could be

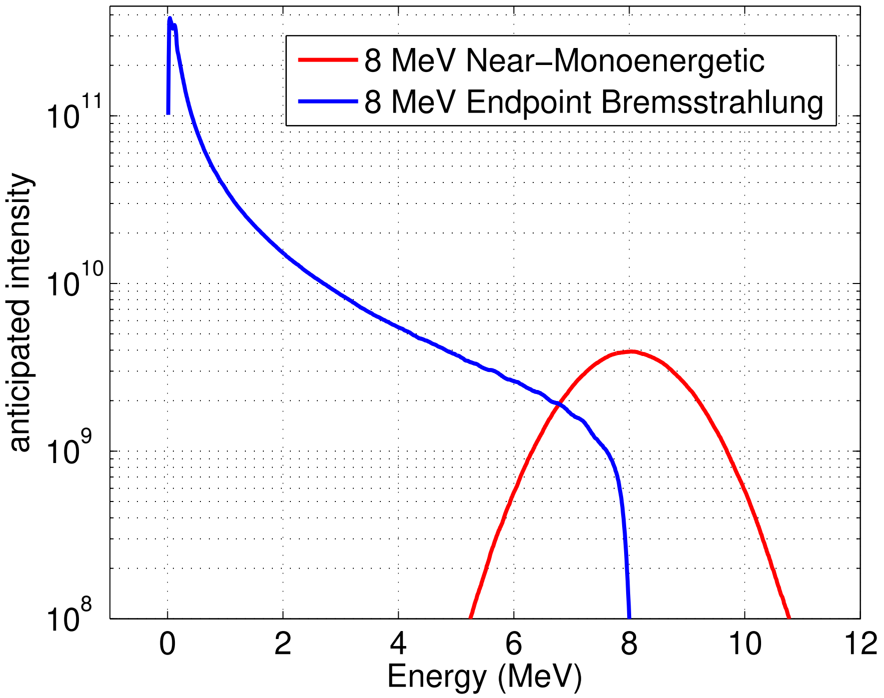

Figure 2.5: Energy spectra for an 8-MeV tuned MPS source, and an 8-MeV endpoint bremsstrahlung linac, emitted photons accounted for in all directions.

directed onto a target, while fewer than 1/10,000 photons from the bremsstrahlung source would be directed at the same target, due to the required collimation of the beam.

The energy and angular properties of MPS beams are attractive for active-interrogation nonproliferation applications, because the photon energy can be tuned to an energy that is optimal for radiography or photoneutron production. The narrow angular spread allows for a high rate of photon-delivery to the interrogation target. Research is ongoing to make these sources much more compact (to be truck-deployable), and increase the photon flux delivered.

2.2 Detectors

Two particles emitted by sources of radioactivity or interrogated material are of interest for detection in this work: neutrons and photons. Neutrons are classified into three general energy ranges: slow neutrons with energy less than 0.5 eV, fast neutrons with energy greater than about

100 keV, and epithermal neutrons in between. The detection methods for fast and thermal energy range neutrons are very different; slow neutron detection is discussed in section 2.2.1, while fast neutron detection is covered in section 2.2.2. The detection of photons is discussed in the context of scintillators in section 2.2.2.

2.2.1 Capture-based Neutron Detectors

The most efficient means of detecting slow neutrons is to employ a reaction with a high neutron cross section in this energy range. The resulting heavy charged particles can be subsequently detected [9]. An exothermic reaction is chosen so that the resulting reaction products posses the energy of the full Q-value of the reaction. Therefore, any slow neutron interaction will result in a deposited energy equal to the known Q-value of the reaction, assuming full energy deposition by the reaction products. Any other events can be discriminated away as unwanted interactions, such as from gamma rays.

In this work, the capture-based neutron detectors are filled with ^{3}He gas, and use the ^{3}He(n,p)^{3}H reaction. This reaction has a Q-value of 764 keV and the thermal cross section (at neutron energy = 0.025 ev) is 5330 barns [9]. The trend in this cross section is inversely proportional to neutron energy as shown in Fig. 2.6 from [32].

Helium-3 detectors are ideal for detection of thermal neutrons in high-photon fields, because any photon interactions will release much less energy than neutron captures due to the low-density, gaseous nature of the medium. Detectors based on this reaction are effectively blind to photons, but intense photon fields may result in enough photon interactions to register a pulse in the neutron range.

Detectors based on the ^{3}He reaction can also be used to indirectly detect fast neutrons. The fast neutrons must be moderated to energies where the cross section of the reaction is larger for the highest detection efficiency. The ^{3}He is sensitive to fast neutrons with much lower probability (Fig. 2.6) but, as shown in Fig. 2.7, with sufficient direct fast neutron flux the energy of the neutron can affect the measured spectrum through elastic scattering. In practice, this effect must be taken

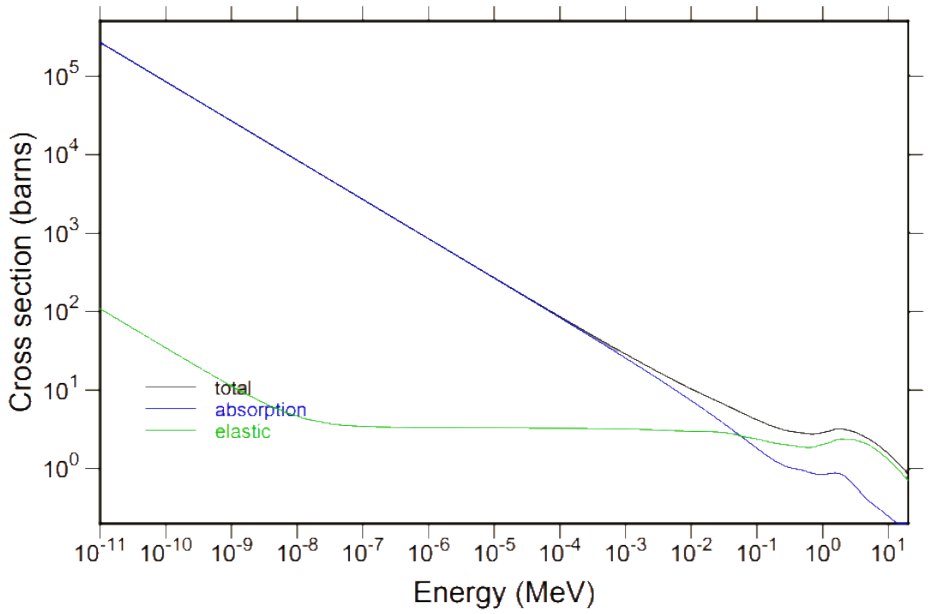

Figure 2.6: ^{3}He neutron cross sections [32].

into account.

^{3}He detectors are able to efficiently detect neutrons, and are generally blind to photons. However, the pulses can be very long, and large amounts of moderating material is required, reducing their mobility. Another disadvantage is that ^{3}He gas is sourced from the decay of tritium used in the construction of nuclear weapons, and is therefore somewhat expensive and difficult to obtain.

2.2.2 Scintillation Detectors

Radiation can induce fluorescent light in materials known as scintillators [9, 33]. A scintillation material is chosen so that it can efficiently and quickly convert radiation energy depositions linearly to scintillation light. The light can be transported through the material with minimal losses, and can be collected by a photomultiplier tube (PMT) [9]. Information about the incident radiation can be derived from this light pulse. Scintillators are generally classified as organic or inorganic. Organic scintillators generally have a low average atomic number which leads to high neutron detection efficiency, and inorganic scintillators have higher average atomic numbers for greater

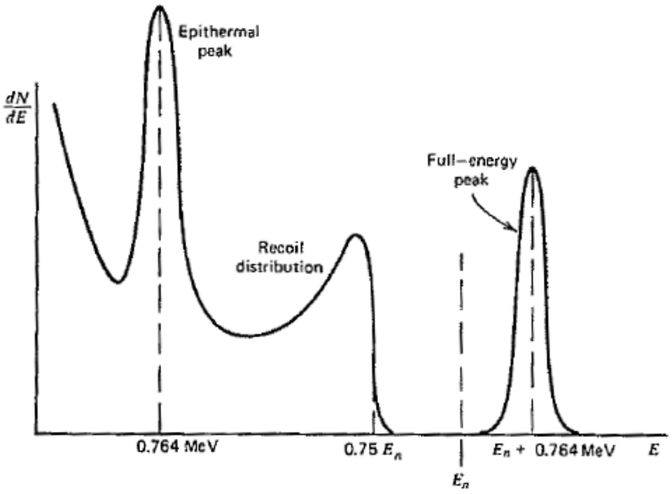

Figure 2.7: Idealized energy spectrum of charged particles expected from fast neutrons incident on a ^{3}He detector [9].

photon detection efficiency.

2.2.2.1 Inorganic Scintillators

In addition to their high photon-sensitivity, the density and high atomic number of inorganic scintillators lead to full-energy depositions by photons, enabling accurate gamma-ray spectroscopy [9]. These detectors also have excellent light output and linearity, but can have relatively slow light pulses.

Electrons in the inorganic scintillator crystal are usually bound at lattice sites in the valence band, but when excited by radiation can be elevated in energy to the conduction band of the crystal. This elevation to the conduction band leaves a hole in the valence band, and when a conduction band electron then returns to the valence band, energy is released in the form of a photon; however, this photon is often not in the visible range, and is inefficiently collected by the PMT. Impurity molecules, known as activators, can be added to the crystal to combat this inefficiency [9]. At the sites where these activators are present, electrons can descend from the conduction band to the valence band across a reduced gap, emitting a lower energy photon in the visible range. The band gap allowed by these activator molecules determines the scintillation emission spectrum, and leads to greater spectral coupling to the PMT.

The alkali halide crystal sodium iodide, with thallium activator impurities added during growth, is a very popular inorganic scintillator. NaI(Tl) offers excellent light output, can be used to perform gamma-ray spectroscopy, and is relatively cheap to produce in large sizes. For these reasons, I use NaI(Tl) detectors in this work for gamma detection and spectroscopy purposes.

2.2.2.2 Organic Scintillators

While organic scintillators have a lower atomic number than inorganic scintillators, and therefore cannot easily perform gamma-ray spectroscopy, they are sensitive to fast neutrons due to their hydrogen content [9]. Organic scintillators also generally yield less light, but offer very fast light response. This fast response can be useful for applications that are sensitive to the timing of pulses. Another useful property of some organic scintillators is the potential for pulse shape discrimination (PSD). Due to their sensitivity to neutrons, and ability to discriminate between neutrons and photons, the bulk of the detection studies in this work will focus on organic scintillators.

In organic scintillators, neutrons deposit energy on hydrogen nuclei (protons) or carbon nuclei, and photons deposit their energy on atomic electrons. The recoil products then excite scintillator molecules along their tracks. The particle depositions are observed by detecting scintillation light in the material as these excited molecules de-excite [9]. The light is then measured as a voltage pulse, and can then be converted to energy deposited by the particle. The relationship between photon energy and light production is unity by definition in scintillators; however, it is nonlinear for neutrons energy deposition. This nonlinearity is due to the fact that the resulting recoil proton or carbon nucleus from a neutron scatter excites molecules in a higher density than photons, especially at low energies. This higher density excitation leads to a higher chance of quenching, or when excited molecules recombine without releasing visible light. This difference in the energy deposition to light output relationship is illustrated in Fig. 2.8.

The semi-empirical function based on the model proposed by Birks [33] is used for the conversion from measured light output to neutron energy deposited in a stilbene detector [34]. It is

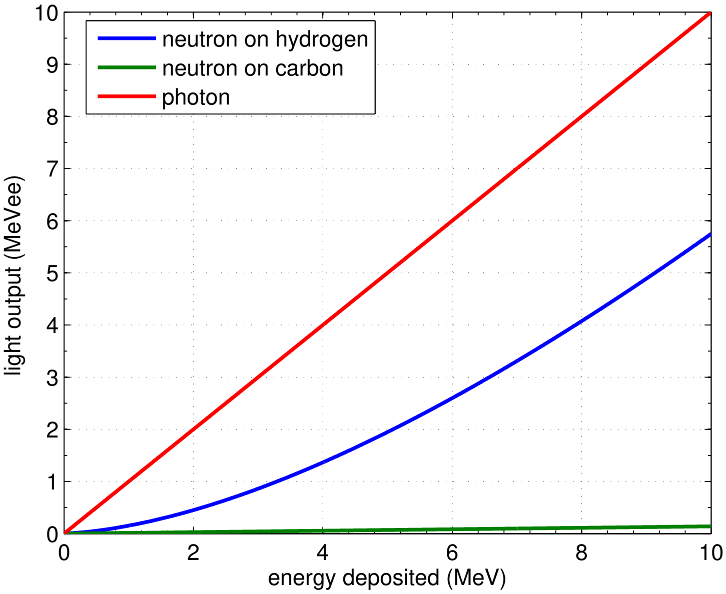

Figure 2.8: Neutron and photon energy deposition to light output conversions based on Birks formulation for 2 in. diameter by 2 in. length stilbene detector [34].

important to note that this relationship applies only to neutron depositions on hydrogen. As shown in Fig. 2.8, the light produced by neutron scatters on carbon nuclei is negligible compared to light resulting from neutron scatters on hydrogen nuclei. The maximum energy transferred to a carbon nucleus by a neutron elastic scattering is much lower than to a lighter hydrogen nucleus, and the molecules excited by the carbon nucleus are highly likely to undergo quenching. Therefore, I assume that all neutron interactions registered by the detector are the result of neutrons scattering on a hydrogen nucleus. Furthermore, the inversion of the Birks neutron energy deposition to light output model relies on the assumption that each detected neutron pulse is the result of a single scatter by a neutron on a hydrogen nucleus. This assumption is not always true, because the neutron can scatter multiple times in the detector, on either hydrogen or carbon. However, I have shown that this assumption is accurate by simulating multiple scatters with MCNPX-PoliMi [35], which is treated as the ”exact response” in Fig. 2.9, and the same information was approximated as single pulses for the ”approximate response”. This comparison showed that for a fission spectrum, the approximated response is within 3% of the true response, assuring the utility of the single-scatter assumption.

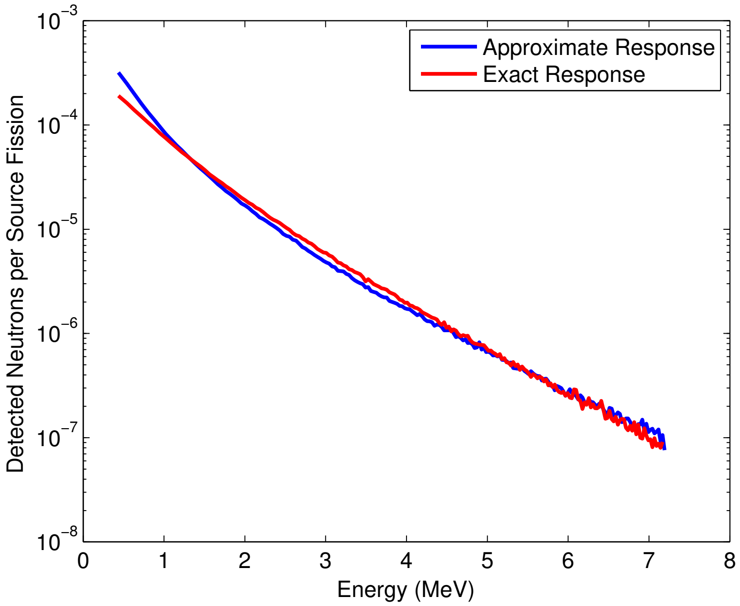

Figure 2.9: Approximated single scatter on hydrogen response for 5.08 cm diameter by 5.08 cm stilbene crystal compared to exact response from simulated ^{252}Cf spontaneous fission neutrons.

In addition to the ability to accurately extract energy deposition from organic scintillators, a key property of interest is pulse shape discrimination capability. When a neutron or alpha particle deposits energy onto a recoil proton or nucleus, that proton has a high rate of energy loss, *dE/dx*, compared to a recoil electron resulting from an electron interaction. This large *dE/dx* leads to a high concentration of excited triplet states in the scintillator, and when these excited molecules combine the result is a ground state and singlet state molecule. The singlet state molecule then decays, leading to delayed fluorescence. This elevated rate of delayed fluorescence from neutron interactions results in a greater fraction of light emitted in the slow component (beginning approximately 20 ns after the start of the pulse in fast scintillators) of the scintillation pulse [9]. Example representative pulses are shown in Fig. 2.10 [36], demonstrating that particles with recoil products with higher *dE/dx* result in pulses with higher light intensity in the slow component of the pulse. The difference in slow component light can be used to discriminate particles, as discussed further in Section 2.3.3.

The organic scintillator of choice for this study is stilbene ($C_{14}H_{12}$), because it exhibits the excellent capability to discriminate between neutrons and photons, especially at low energies [37,

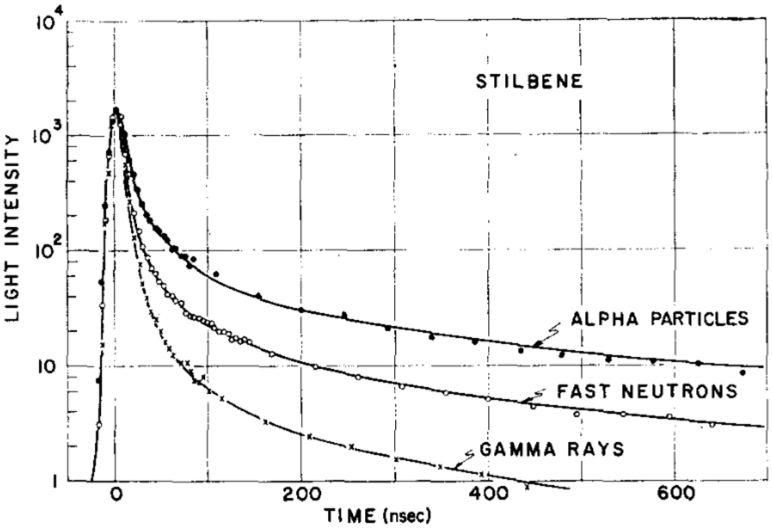

Figure 2.10: Representative pulses in a stilbene scintillator, scaled at the peak to arbitrary light intensity [36].

38]. With modern solution-growth techniques result in further advantages in PSD and light output, and stilbene crystals up to 5.08 cm in diameter can be produced efficiently [39]. The light output models have also been studied fairly well, allowing for accurate conversion from light output to deposited neutron energy [34].

2.3 Digital Pulse Processing

In this work the analog voltage pulses from a detector operating in pulse mode are read out with CAEN x730 waveform digitizers [40]. These digitizers are flash analog-to-digital converter (ADC) -based waveform digitizers, with a 14-bit amplitude resolution and a 500 MHz sampling rate. These digitizers can be interfaced with an acquisition computer with 2 tools built around the DPP-PSD [41] firmware: a custom data acquisition software package, DAFCA [42], or a CAEN-developed acquisition interface, CAEN Multi-PArameter Spectroscopy Software (CoMPASS) [43].

With these data acquisition software packages, pulses can be acquired digitally in either ”full waveform” mode, where every digitized sample is recorded, or ”list” mode where only key information (timestamp, pulse integral, channel number, etc.) is passed to the digitizer. Acquiring in list mode acquisition is useful when many detectors are used in one experiment, or a high count rate is expected with any number of detectors. Often the limiting factor for the count rate that can be observed in an experiment is the data-throughput rate, or how quickly the digitizer can pass data to the acquisition computer. List mode can reduce the amount of data passed to the computer per pulse by a factor of 10-100 depending on the pulse length of the detector. Therefore, acquiring in this mode allows for count rates of 10-100x larger to be observed without data handling issues.

2.3.1 Energy Determination

As discussed in Section 2.2.2, the energy deposited in a scintillating detector by a particle is directly related to the light output, measured as a voltage pulse. A monoenergetic photon source (generally ^{137}Cs) is used to calibrate the light output spectrum of the detector to an energy deposition range. Because capture-based detectors offer limited energy information, they will not be discussed here.

While similar in operation, organic and inorganic scintillators must be calibrated slightly differently. The relatively high atomic number of inorganic scintillators allows for full-energy deposition by photons, while the low-Z composition of organic scintillators does not. In the MeV-range of the particles of interest for this work, Compton scattering is the dominant interaction by photons in an organic scintillator [9]. Therefore, the Compton edge, or maximum energy deposited by a photon through Compton scattering on an atomic electron, is the most prominent measured feature to use for detector calibration.

Figure 2.11 shows two spectra used for calibration. Figure 2.11(a) is a ^{137}Cs spectrum measured with a NaI(Tl) detector, exhibiting the full deposition peak of the 662 keV energy gamma ray. Peaks from multiple full-energy depositions can be seen at 1.324 and 1.986 MeV. By definition, the light output of the gamma-ray full-energy deposition is 662 keVee. A calibration factor can be applied to this spectrum directly relating either the pulse peak voltage value or the full integral value of the pulse at this peak to 662 keVee. In this work, detectors are generally calibrated using

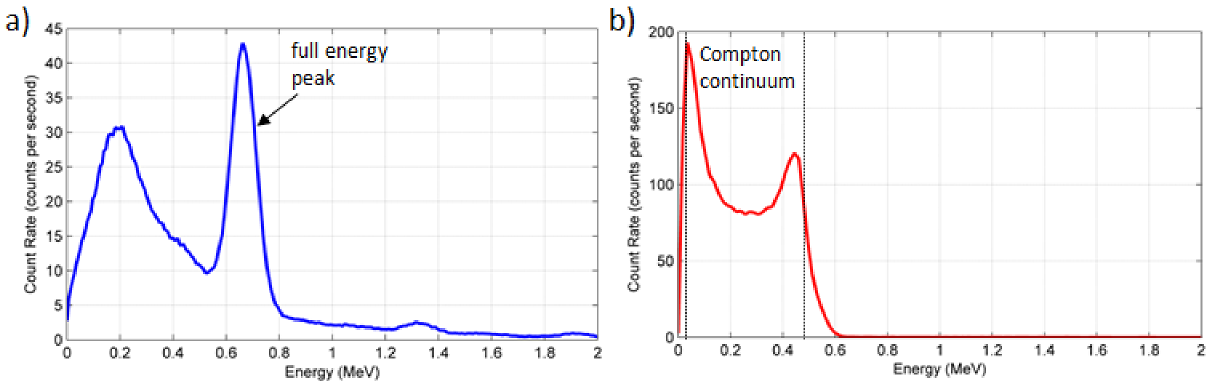

Figure 2.11: ^{137}Cs gamma-ray spectra measured with a NaI(Tl) detector (a) and a stilbene detector (b).

the pulse integral value, and indeed for list-mode operation, where only timestamp and integral information is recorded, this is the only option. The scaling to the ^{137}Cs gamma-ray light output allows all measurements taken with this detector configuration to be scaled to light output, and then to energy since the relationship is one-to-one.

Figure 2.11(b) shows the ^{137}Cs spectrum measured with a stilbene detector, where only the Compton continuum is observed. In theory, the Compton continuum should be a step function with an edge at the maximum energy that a 662 keV photon can deposit in a Compton backscatter: 478 keV. However, in practice, the energy resolution and contribution from multiple scatters in the detector cloud the edge into a Gaussian slope. Using the method in [44] it was determined that calibrating the point at 80% of the Compton edge peak to 478 keV yields an accurate voltage to light output calibration.

For photon interactions, the light output value can then be converted directly to energy, but for neutron interactions, a light output to energy function must be applied as discussed in Section 2.2.2.2 because the light output of a neutron interaction is a nonlinear energy-dependent function.

2.3.2 Timing Determination

The global time of the sample that first crosses a set voltage trigger threshold is treated as the timestamp of a pulse. In DAFCA, the recorded time is the ”coarse” timestamp, and is reported in units of the sampling time, 2 ns. This sampling rate limits the time resolution of a pulse to 2 ns, but the option is available to improve time resolution by enabling a zero-crossing constant fraction discriminator (CFD) module to account for the slope of the pulse rise time [41]. With this option enabled, the inter-sample time is reported as the ”fine” time stamp. CoMPASS handles timing in much the same way, although one timestamp is reported in units of ps, whether or not zero-crossing CFD is enabled [43].

2.3.3 Pulse Shape Discrimination

As discussed in section 2.2.2.2, certain organic scintillators, including stilbene, possess properties enabling PSD between neutrons and photons. The increased slow component light fraction due to neutron interactions can be quantified by comparing the ”tail integral” and ”total integral” of a pulse[45]. This technique is referred to as charge integration PSD, and the integration regions are illustrated in Fig. 2.14.

When operating in list mode, these integrals cannot be computed because full waveform sample information is not reported. To perform PSD when acquiring in list mode, I tuned the recorded ”gates” shown in Fig. 2.12 to optimize PSD, and enable efficient PSD for high count-rate measurements.

The calculated or reported integrals can be compared in a variety of ways, including directly to each other, or as a ratio against pulse height or the total pulse integral. These properties can be used to develop a discrimination line to classify pulses as a neutron or photon. An example of a tail integral vs. total integral plot is shown in Fig. 2.15, with the discrimination line shown as a function of total integral.

The discrimination line is chosen by using an algorithm to slice the integral points into discrete regions, and to fit Gaussian functions to the separate neutron and photon components of those sliced regions[46]. The minimum point between the fitted Gaussian functions is then considered to be the optimal discrimination point for that region. By fitting a function to the optimal points extracted from each ”point” a discrimination line is formed. This type of algorithm offers an

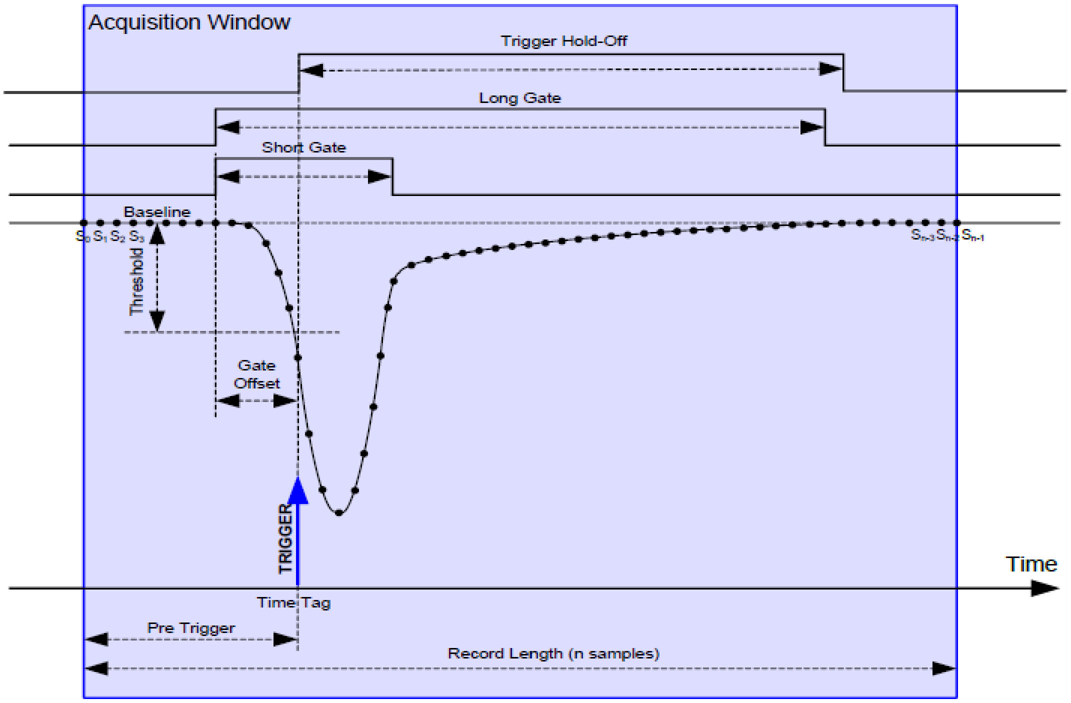

Figure 2.12: DPP-PSD tunable settings: the short gate, long gate, and gate offset can be tuned to optimize PSD [41].

accurate, replicable way of determining the optimal discrimination line for a given detector and experimental configuration.

Drawbacks to charge integration PSD include difficulty discriminating low energy pulses and the fact that pile-up pulses may contribute to elevated neutron counts. Improving low energy discrimination may be done by adjusting the gain settings of the detector, or by preventing the detection of low-energy photons with external high-Z shielding. Piled-up pulses contribute to elevated neutron counts because any additional that arrives in the tail integral region of the pulse contributes to the magnitude of the tail integral, increasing the chance of false classification as a neutron in any charge integration algorithm. Techniques for reducing this effect depend on whether pulses are acquired in full-waveform or list mode, and are discussed below.

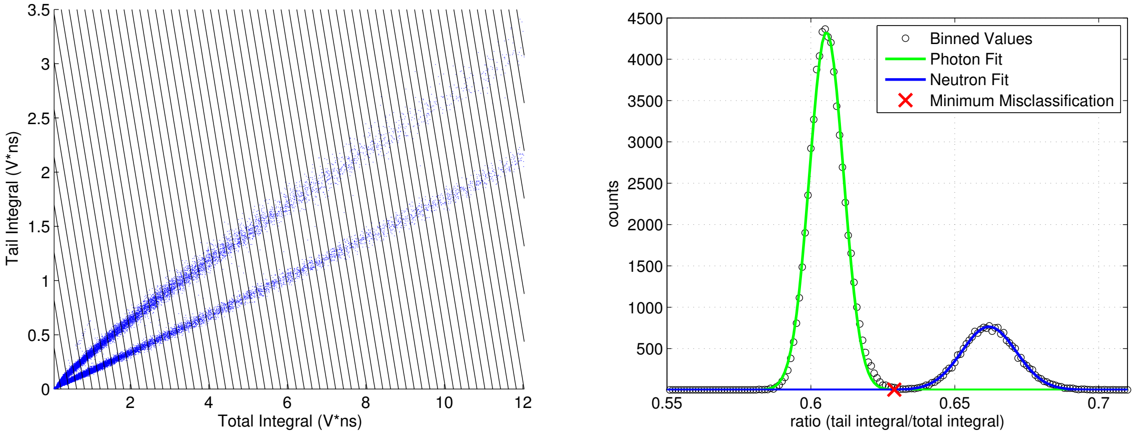

(a) (b)

Figure 2.13: Results of Gaussian fitting algorithm used for charge integration PSD discrimination line determination: sliced regions (a) and representative Gaussian fits of the neutron and photon regions for one sliced region (b) [46].

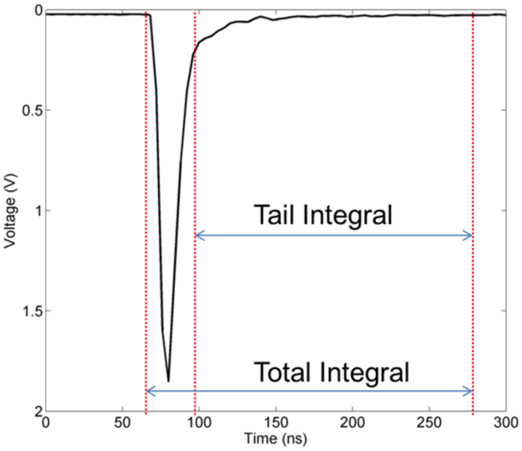

Figure 2.14: Illustration of a representative voltage pulse in stilbene, with tail and total integration regions.

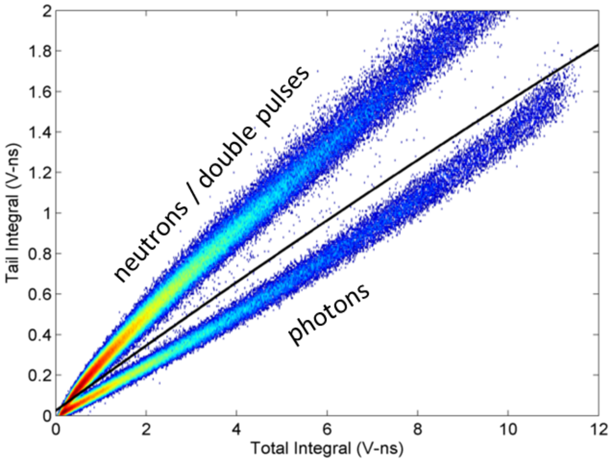

Figure 2.15: Tail integral vs. total integral plot for lead shielded (α,n) source (plutonium-beryllium) pulses measured with stilbene.

2.3.3.1 Full Waveform Acquisition Pile-up Pulse Rejection

In full-waveform acquisition mode, all information from the digitized pulse is available to determine if a second pulse has arrived within the acquisition window. To determine if a second pulse has piled up on the tail of the pulse, a rise in the samples is searched for, with a magnitude a fraction of the main pulse's height. A fractional rise of 6% of the pulse magnitude is used in this work [38]. From the example in 2.14, the pulse magnitude is about 1.8 V. By applying the 6% fractional pileup cleaning method, any rise in the tail of this pulse with a magnitude greater than 0.11 V would qualify the pulse as a pile-up pulse, and it would be discarded.

2.3.3.2 List Mode Acquisition Pile-up Pulse Rejection

Because list mode does not pass the full pulse information for analysis, the waveform cannot be searched for fractional increases in magnitude. Pile-up pulse rejection is therefore performed within the digitizer itself, with an on-board CAEN pile up rejection (PUR) algorithm.

The on-board algorithm rejects pulses if the waveform decreases and then increases again by a PUR-gap, shown in Fig. 2.16, set by the user between 0 and 4096 bits. This method is effective for rejecting pulses when acquiring in list mode, but because this rejection is performed on-board, there is no way to analyze these rejected pulses or directly measure the rejection rate.

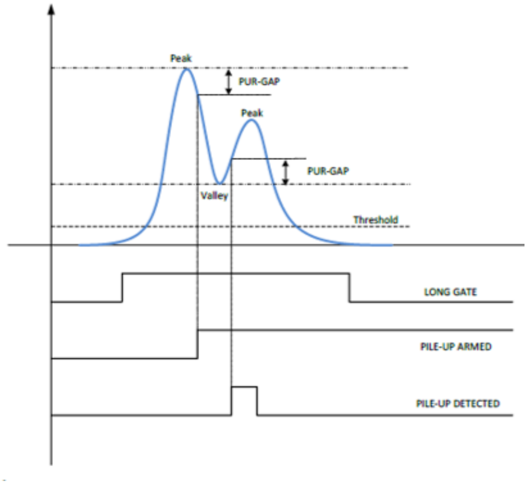

Figure 2.16: CAEN DPP-PSD firmware pulse parameters used for PUR algorithm to reject pile-up pulses [41].

CHAPTER 3

Contraband Detection, Identification, and Characterization with Neutron Generators

Neutron interrogation is an attractive technique for nonproliferation and contraband detection applications because neutrons are highly penetrating through high-Z materials, and can induce easily detectable signatures [8]. Neutron-induced fission and radiative capture reactions are used in this work to detect, identify, and characterize a variety of materials. Because neutron generators emit both neutrons and photons, techniques are used to exploit the unique properties of the radiation emitted by these reactions of interest.

Two experimental campaigns were carried out to investigate the capabilities of neutron generators for active interrogation, and are discussed in the following two sections. The first was performed as part of a neutron generator technology demonstration for contraband detection using well-established radiation detectors. The second experiment was at Niowave, Inc. in Lansing, Michigan. A neutron generator was used to drive a subcritical assembly, with organic scintillators deployed to detect the resulting signatures.

3.1 Contraband Detection and Identification with Traditional Detectors

The goal of this experimental campaign was to demonstrate contraband detection using advanced neutron generators and both ^{3}He and NaI(Tl) detectors. The contraband of interest consisted of SNM as well as simulants of drugs and explosive compounds. Both D-D and and D-T neutron generators were used as intense sources of neutrons. The D-D produced a neutron flux on the order of 10^8 neutrons per second, while the D-T source output was about a factor of 100 greater. The focus of these experiments was on demonstrating the efficacy of the sources, so the detectors used were those traditionally used by the interested communities. Photons were used to identify drug and explosive compounds, and neutrons were used to identify SNM. Large, 15.24 cm diameter × 15.24 cm NaI(Tl) detectors were used for photon detection, and a fast-neutron-shielded bank of 23 ^{3}He tubes was used for neutron detection.

3.1.1 Detection Method Overview

The neutron detection technique used for SNM detection was differential die-away analysis (DDAA) [47, 48]. DDAA is an active interrogation technique that uses a pulsed neutron source to interrogate an item of interest. When SNM is subjected to a neutron pulse, fissions will occur. Fissions are induced either by the fast neutrons directly, or by neutrons thermalized in the item itself or the surroundings. Resultant fission neutrons are then reflected and either continue fission chains, leak out of the system, or are detected. Therefore, the field of neutrons will "die-away" as fewer fissions are induced after the neutron generator pulse turns off. If SNM is not present, this decay of the neutron field is much faster because there is no chain of induced fissions [49].

The neutron detection rate is proportional to the neutron population in the environment. By measuring the neutron detection rate as a function of time after the pulse, the population die-away rate is measured. In this work, the ^{3}He neutron detector is blinded to thermal neutrons by thermal neutron absorbing materials, so that in theory, only prompt fission neutrons are detected after the

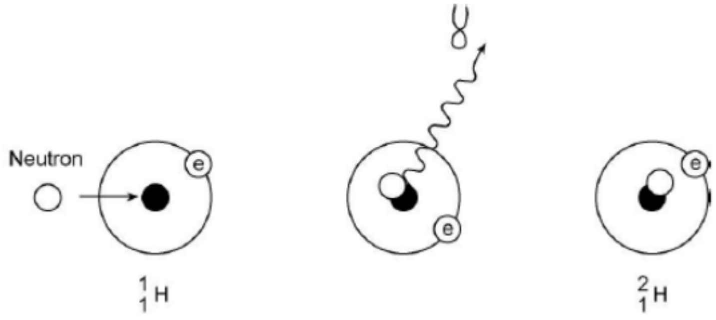

Figure 3.1: Radiative capture reaction for hydrogen atom [52].

neutron generator pulse. In practice, even without fissionable material present, reflected neutrons with enough energy and thermal neutrons leaking through the shield still create a detected signal. This signal decays quickly and is low in magnitude, so the longer die-away from interrogated SNM is still apparent.

The neutron-induced photon detection technique used in this work for drug and explosive-compound detection was "single-sided" thermal neutron analysis (TNA) [50, 51]. TNA is based on the radiative capture reaction, shown in Fig. 3.1 from [52]. In radiative capture, a nucleus captures a thermal neutron, and radiates a characteristic gamma ray. This photon is then detected, and elevated counts in the characteristic energy range can be used as a positive signal of isotopic presence. Because fast-neutron generators are the neutron sources for this work, moderation is required to induce radiative capture with appreciable efficiency. The source neutrons are moderated in hydrogenous material placed around the generator, the surroundings, or in the interrogated material itself. "Single-sided" refers to the fact that the neutron generator, moderating material, and detectors were all placed on the same side of the target.

3.1.2 Detectors and Data Acquisition

For these experiments, two 15.24 cm diameter × 15.24 cm NaI(Tl) detectors and one bank of 23 ^{3}He tubes were used. The 23 ^{3}He tubes were ganged into eleven readout BNC signal cables. Each NaI(Tl) detector output was read out through one signal cable, and the accelerator pulse time was also read out through a BNC signal cable. Each accelerator output a 5 V square pulse, and was triggered on the rising edge, to use this trigger timestamp as the beginning of the accelerator pulse. All 14 readout channels were digitized with a 16-channel CAEN V1730, and acquired using the DAFCA readout software, discussed in Section 2.3.

Moderating material (polyethylene) was stacked around the neutron generators in every direction except for the direct path to the interrogated target. The polyethylene directed as many additional neutrons as possible towards the target, increasing the reaction rate of induced fission or capture reactions. Some of the reflected neutrons were thermalized, which increases their chance of inducing capture reactions. The direct fast neutrons can also induce fast-fission reactions, and can be thermalized in the target to be better captured.

Both the NaI(Tl) and ^{3}He detectors were shielded with borated rubber, and the NaI(Tl) was additionally shielded with powdered lithium carbonate, all to reduce the effects of thermal neutrons on the detectors directly. For DDAA analysis, thermal neutrons can arrive at any time through the decay profile, and can cloud the detected time-profile resulting from fission neutrons. TNA is also affected by thermal neutrons; while NaI(Tl) detectors are not generally sensitive to neutrons directly, both sodium and iodine can be activated to short-lived radioactive isotopes. Natural ^{127}I can be activated to ^{128}I, which decays with a 25 minute half life and emits gamma rays in the 100s of keV range [53]. Natural ^{23}Na is most likely activated to ^{24}Na, which decays with a 15 hour half life, emitting photons at 1.37 or 2.75 MeV [53]. Activation photon emissions can then be detected by the NaI(Tl) detector, and make observation of the characteristic capture gamma rays more difficult for TNA.

Python 3.7 scripts were developed to run DAFCA and process the acquired data in real-time. The real-time TNA Python script (shown in Appendix A) was used to acquire and process TNA NaI(Tl) data for contraband and drug detection. The NaI(Tl) detectors were calibrated to energy by the full 2 μs length of the pulse, for a range of about 400 keV - 14 MeV. The detected energy information was parsed into a 35-keV binned histogram every two seconds, and summed with all previously detected data in the measurement. When a contraband item was in place, this spectrum was plotted against previously measured data acquired when no target was in place. The “no target” data were plotted at the same rate as the live data to the difference in acquired energy spectra due to target presence. Time-stamp information from each detected photon was also recorded, so that time gates could be applied to the data with reference to the neutron generator pulse. Time-tagging enabled vetoing of photons emitted either during the neutron pulse or after radiative capture photons were expected. Only accepting detections between the end of the generator pulse and 1.5 ms after the generator pulse trigger was found to isolate radiative capture photons well. The resulting interrogated-item energy spectrum exhibits higher counts in the region of the characteristic capture gamma ray energies for isotopes of interest.

The neutron-detection Python 3.7 script for SNM detection (shown in Appendix B) uses ^{3}He pulse timing as the main signal information. As discussed in Section 2.2.1 the ^{3}He pulse size is generally not related to the incident neutron energy prior to thermalization. Because DDAA is based on timing alone, the energy is not useful here. Every ^{3}He pulse timestamp is referenced back to the neutron generator pulse by subtracting away the preceding generator pulse timestamp. Then a 20-μs binned DDAA profile with respect to the neutron generator pulse time is computed. The timing profile is computed and displayed every two seconds, and summed to all previously processed data from the measurement. As with the TNA script, a previously acquired "no target" DDAA profile is plotted at the same rate as an SNM interrogation measurement. The SNM interrogation measurement exhibits a longer neutron die-away time, and greater neutron count rates at all times after the generator pulse.

3.1.3 Detection Results

Fig. 3.2 shows a TNA photon energy spectrum collected during D-D neutron interrogation of a drug simulant. The signature for this particular simulant is the presence of chlorine. The characteristic capture gamma-ray energies [54] are labelled on the figure with dashed lines. The red dashed line shows a characteristc hydrogen capture gamma-ray energy, which is also detected due to hydrogen presence in the concrete surroundings of the experiment, the moderating material, and the drug simulant material itself. Certain characteristic gamma ray energies show distinct

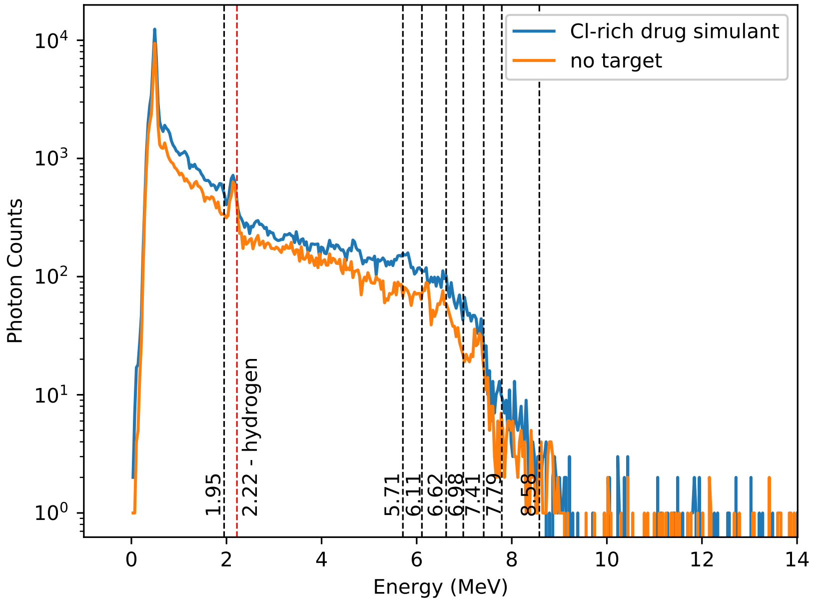

Figure 3.2: Measured TNA photon energy spectrum for chlorine rich drug simulant vs. no target, interrogated with D-D generator for five minutes. Radiative capture peaks shown by dashed lines.

increases in signal over the no-target case, including 1.95, 5.71, and 6.98 MeV. Towards the higher end of the energy range, there are fewer counts and degraded energy resolution, so differences in the spectra are not as clear. Fig. 3.2 also exhibits an increased count rate over the full energy range from the sample presence. This increased count rate is due to partial energy depositions by gamma rays across the full energy range.

Fig. 3.3 shows a TNA photon energy spectrum collected during D-T interrogation of an explosive simulant. In this case, nitrogen is the positive signal for explosives presence. Nitrogen exhibits many radiative capture lines, and the most identifiable energy is 10.83 MeV [55]. This gamma ray is prominent because photons in this high-energy range are quite rare. One exception is the 10.6 MeV line from ^{30}Si [56], which is a low-abundance isotope of silicon but should be treated as a possible contaminant for nitrogen content detection. The resolution of NaI(Tl) detectors at such high energy is poor. There are also effects from pair production in this energy range, where the 10.83 MeV radiative capture gamma ray creates an electron-positron pair. The positron then annihilates in the medium, releasing two 511 keV photons [9]. Based on conversations with and research performed by C. Meert and D. Goodman at the Univiersity of Michigan, it is not uncommon for some of these photons to escape the detector. Each time an escape occurs, the energy deposition by a 10.83 MeV is further reduced by 511 keV. Gamma detection peaks from capture reactions on iron are dominant in the detected spectrum below about 9.5 MeV. For these reasons, a nitrogen capture-gamma region was defined from 9.5 to 11 MeV. Because the efficiency of NaI(Tl) is also low at high energies, we needed to produce as many capture reactions as possible. The D-T neutron generator was used for interrogation of this simulant, because it produces a higher flux of neutrons than the D-D generator. In the tested configuration, the D-D generator was unable to produce a nitrogen signature in a reasonable time. While thermalization of the 14.1 MeV neutrons requires more time and moderating material than the 2.45 MeV D-D neutrons, the increased flux output by the D-T generator more than compensated for this effect. The greater number of neutrons induce more capture reactions than a D-D generator could, increasing the probability of detecting a nitrogen capture-reaction gamma ray. Fig. 3.3 shows elevated counts in this region: 357 counts with the simulant present and 184 without, for a net total of 173 ± 23 photon counts. The elevated counts in the region indicate that nitrogen is present in the explosive compound simulant, although certainty could be improved with higher count rates and by suppressing effects of capture reactions in the iron surroundings.

Figures 3.4 and 3.5 show DDAA neutron decay time profiles for SNM detection for both D-D and D-T interrogated targets. The D-D generator was pulsed at 200 Hz, for a 5 ms period, and the D-T generator was pulsed at 100 Hz for a 10 ms period. Both generators were operated with a 5% duty factor, or percentage "on" time, for a D-D pulse length of 250 μs and a D-T pulse length of 500 μs. Both cases show similar slower decay of neutron counts with SNM presence, and elevated counts in the region after the source neutron pulse.

The slope of the die-away profiles for both the SNM and no target cases after approximately 1.5 ms for Fig. 3.4 and 3 ms for Fig. 3.5 indicate inadequate scattered neutron shielding. Especially in the no-target cases where no fission is occurring, the slope should be zero, with any counts due to natural background. The slope is due to neutrons scattering around the laboratory

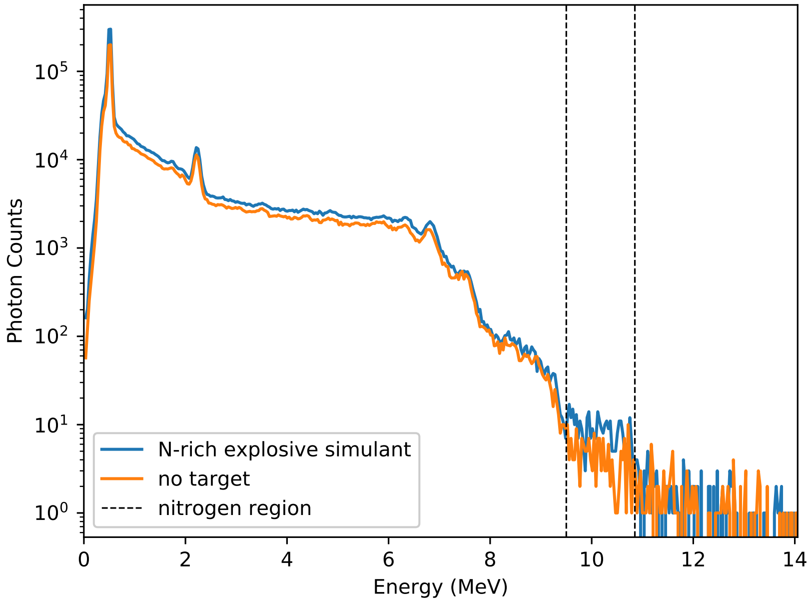

Figure 3.3: Measured TNA photon energy spectrum for nitrogen rich explosive simulant vs. no target, interrogated with D-T generator for 30 minutes. Nitrogen region bounded by black dashed lines.

space and returning to the ^{3}He module where they are detected. Performing these experiments with little surrounding material would decrease this effect, but may be impractical for personal protection reasons. Increased thermal neutron shielding in the direction of the interrogation sample and increased full-spectrum neutron shielding in all other directions could more practically reduce this effect, and better isolate the true fission die-away profile.

3.1.4 Conclusions

These experiments have demonstrated that contraband interrogated by both D-D and D-T generators can be detected with traditional NaI(Tl) and ^{3}He detectors. The detection of SNM using DDAA is quite clear, as induced fission reactions greatly slow the neutron decay from the generator pulse in the environment. However, these experiments were performed with bare SNM and the presence of shielded materials is a greater challenge under investigation [57].

The detection of drug or explosive compound contraband with TNA is a difficult problem due

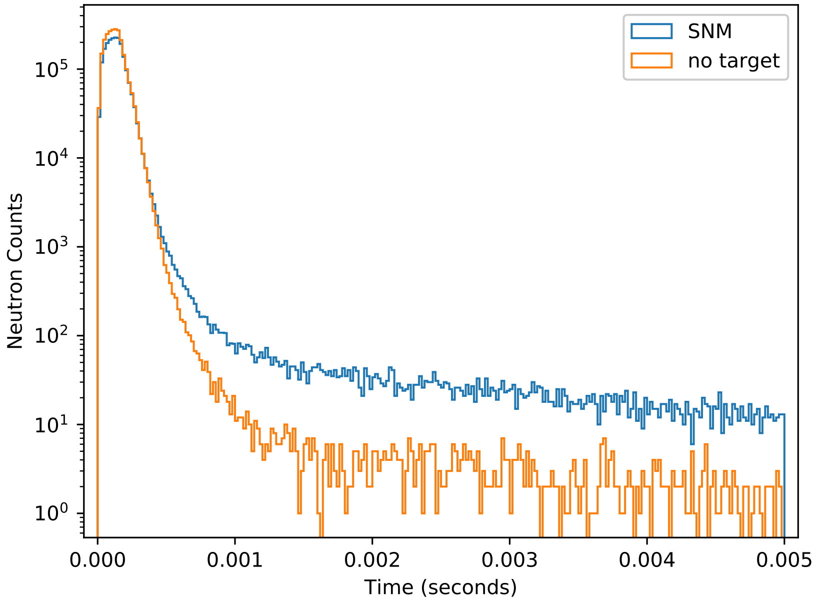

Figure 3.4: DDAA profile for SNM sample vs. no target, interrogated with D-D generator for five minutes.

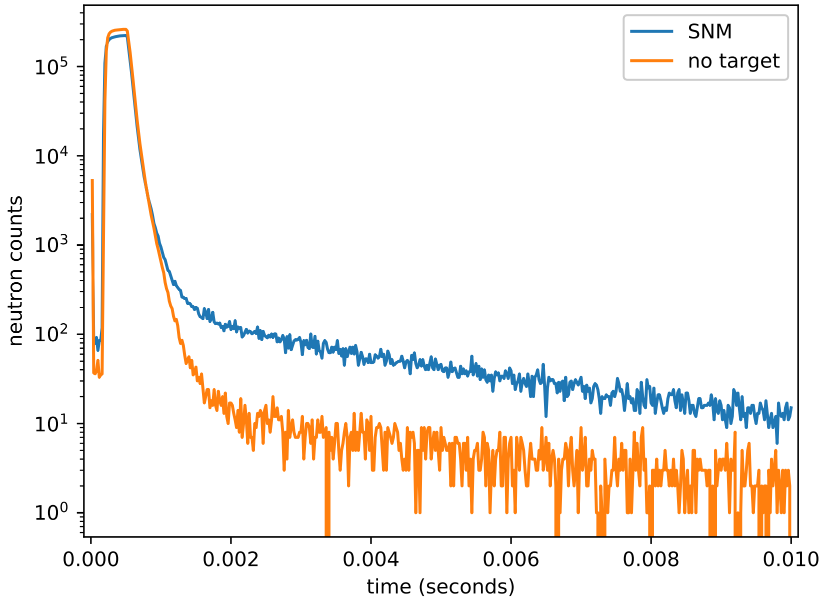

Figure 3.5: DDAA profile for SNM sample vs. no target, interrogated with D-T generator for five minutes.

to the magnitude of the ”background” signal when no target is present. Many isotopes in common materials produce photons when bombarded with neutrons: hydrogen and carbon in concrete, iron and carbon in steel, etc. All of these photons make detection of radiative capture gamma rays from identifying isotopes in contraband difficult, especially when the contraband is shielded or in small quantities. Positive identification of contraband materials would also require the detection of multiple signature isotopes in the material, and the proportions of each, to discriminate against normal commercial materials. Deployment of this detection would require an array of efficient, high-resolution detectors with advanced spectroscopy techniques.

3.2 Subcritical Assembly Characterization with Organic Scintillators

Detection of a variety of contraband materials under irradiation by neutron generators was demonstrated in Section 3.1 with traditional detectors. SNM was identified with DDAA, but in this section, I demonstrate more detailed characterization of SNM with an organic scintillator. The goal of this experiment was to characterize a subcritical (neutron population decreases for each fission generation) nuclear fuel assembly irradiated by a pulsed neutron generator through DDAA. The die-away profiles of both neutrons and photons were used to estimate the reactivity of the assembly.

Accurate determination of the reactivity of a neutron pulsed assembly using analysis similar to DDAA has been shown in [58] with thermal neutron detectors. The shape of the neutron population decay can be used to inform the reactivity of the assembly. The analysis presented in [58] is based primarily on the detection of delayed neutrons because of the time scale of thermal neutron detectors. A thermal neutron counter requires time for moderation to thermalize the prompt neutrons, and this thermalization time can cloud the die-away profile [59]. The prompt neutron die-away time profile from interrogated fissile material was previously measured with fast neutron detectors [49] to detect fissile material. Fissile material can be further characterized with the Rossi-alpha method [60]. This method uses the frequency of time differences between particle detection events to determine how correlated in time the emissions of a source are. A higher frequency of short time difference detections implies a correlated emitting source. Passive Rossi-alpha methods for determining characteristics of fissile material have been demonstrated using fast neutron detectors [61] and thermal neutron detectors [62].

This section demonstrates the use of a fast neutron counting organic scintillator to estimate the reactivity of a subcritical assembly from the measured DDAA profile. This method is related to Rossi-alpha techniques for the estimation of k_{eff}, and additional information from photon detection was examined. The use of a fast neutron detector in this experiment allowed for measurement of prompt neutrons, which arrive very quickly after the end of the interrogation pulse, and are much more numerous than delayed neutrons. This increase in statistics is beneficial for obtaining a more accurate estimate of reactivity for low-flux subcritical assemblies. The pulsed nature if this active interrogation experiment allows for correlation of neutron detection times to this fixed pulse time, instead of self-correlation of neutron detection events, as in the Rossi-alpha method. The DDAA profile calculated by the relationship between neutron detection times and neutron generator pulse time enables characterization of the assembly reactivity.

The reactivity of the assembly is informed by the calculation of k_{eff}, which is determined from the exponential fit of the DDAA profile described by

$$c(e^{\alpha t}), \tag{3.1}$$

where c is a scaling factor, α describes the exponential change of the neutron population, and t is the time from the end of the neutron generator pulse. The background chance plateau has been subtracted in this analysis by subtracting the mean of counts after 2.5 ms in the die-away profile. The α from this fit is then used to calculate the reactivity, ρ, of the assembly with

$$\alpha = \frac{\rho - \beta}{\Lambda}, \tag{3.2}$$

adapted from [63, 64]. In Eq. 3.2, β is the effective delayed neutron fraction, and Λ is the mean generation time. These parameters are geometry specific, and are calculated for the specific assembly in simulation. The value of k_{eff} is then calculated with

$$\rho = \frac{k_{\text{eff}} - 1}{k_{\text{eff}}}. \tag{3.3}$$

The calculation of the point kinetics parameters β and λ assume that the assembly is in a critical state. The comparison to simulated k_{eff}, the calculation of which does not depend on this assumption, will demonstrate that these calculations hold for subcritical systems in the context of this experiment.

The subcritical fuel assembly tested was loaded with 35 low enriched uranium (LEU) fuel rods (6.4 wt.% ^{235}U) in the form of uranium dioxide, and 23 natural uranium rods in metal form. The total masses are 1.645 kg of LEU (105 g of ^{235}U) and 4.486 kg of natural uranium. The assembly is housed in a 56 cm diameter × 88 cm aluminum barrel, filled 71 cm high with water.

The assembly was interrogated with a pulsed Starfire nGen-300 D-D neutron generator [65]. The 100-kV generator was pulsed at 100 Hz, with a 2% duty cycle. The design peak neutron output is 5×10^7 neutrons per second, for an average neutron output of 10^6 neutrons per second. The generator was used to interrogate the assembly for 90 minutes.

The detection setup consisted of four 5.08 cm diameter × 5.08 cm stilbene crystals and two 7.62 cm diameter × 7.62 cm Eljen-309 liquid scintillator cells, all coupled to PMTs. Negative bias voltage was applied with a CAEN high voltage power supply. The signals from these detectors were read out with an 8-channel CAEN 5730 digitizer, using the CAEN CoMPASS acquisition software, discussed in Section 2.3.

The generator was inserted into the barrel so that the neutrons were emitted 8.73 cm horizontally from the center of the assembly, and was vertically centered about the fuel rods. The detectors were arranged around the same horizontal plane, about 45 degrees clockwise from the neutron generator port. The experimental setup is shown in Fig. 3.6. The stilbene crystals and PMTs are encased in black plastic in the upper layer and left side of the bottom layer, and the Eljen-309

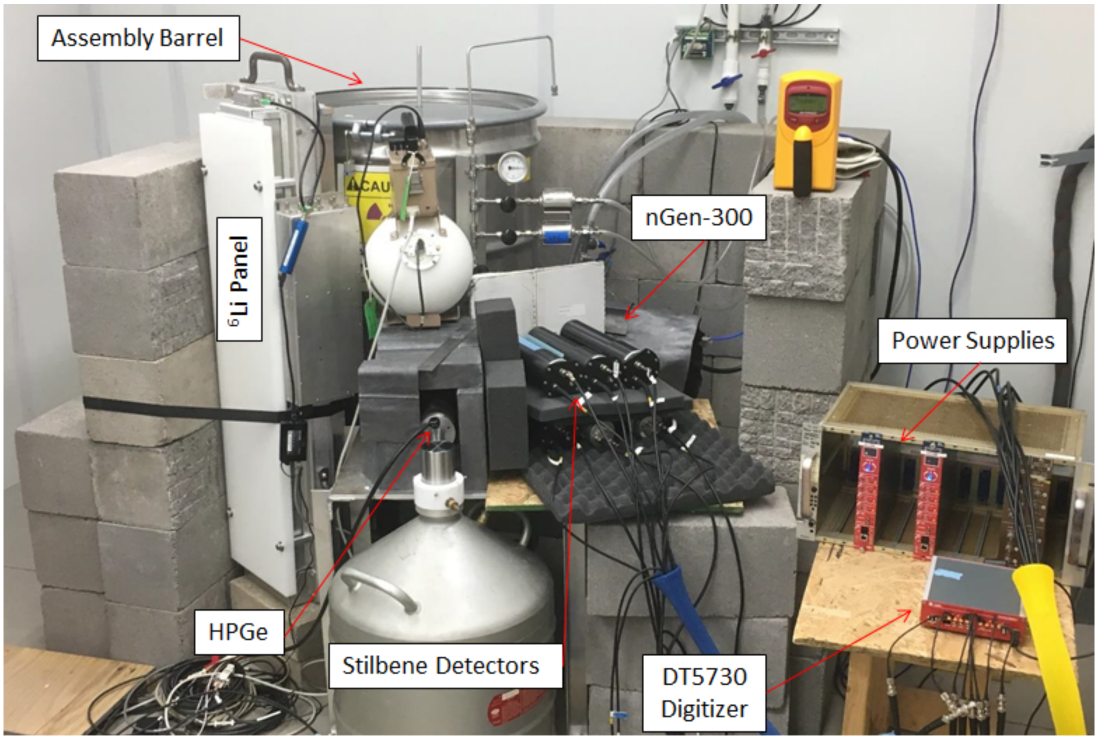

Figure 3.6: Organic scintillator detection setup for Niowave subcritical assembly interrogated by a pulsed neutron generator.

detectors are housed in aluminum in the center and right of the bottom layer. A RemCounter, high purity germanium detector, and ^{6}Li neutron detection panel were also arranged around the assembly. The setup was shielded by concrete blocks on three sides for personal protection shielding. The organic scintillators were shielded by 1.27 cm of lead to reduce the contribution of photons from fission products and the neutron generator.

Simulations of the assembly were performed with MCNPX-PoliMi [35] and MCNP 6.1 with KCODE calculations [66]. The model of this assembly was developed by F. Odeh at Niowave, and I added additional organic scintillator cells and event-by-event detection with PoliMi. A cross section of the model is shown in Fig. 3.7. The neutron generator pulsing is replicated in the simulation, and both neutrons and photons detection events are collected in the stilbene crystal with an MCNPX-PoliMi detector cell.

The PSD discriminating function was determined by fitting a power function to the measured data shown in Fig. 3.8. PSD is performed by comparing the ratio of the slow decay integral to

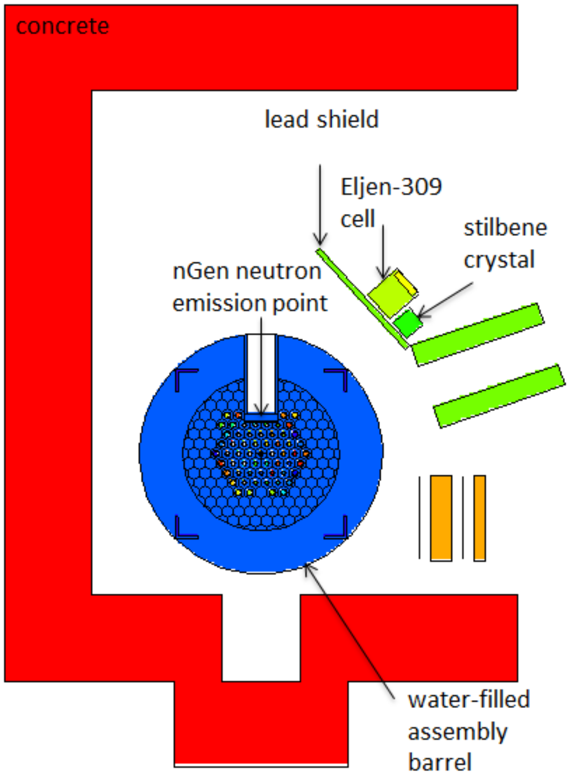

Figure 3.7: MCNP model cross section of the assembly barrel and surroundings.

the full integral of each pulse. Both of these integrals end 47 samples after the maximum pulse amplitude index, the total integral begins five samples before this point, and the tail integral begins 10 samples after. These values were determined by using SlicePSD [46] to slice the data and optimize pulse shape discrimination by maximizing figure of merit (FOM) per slice. FOM is defined as

$$FOM = \frac{d}{FWHM_g + FWHM_n}, \tag{3.4}$$

where FWHM$_g$ is the full width at half maximum (FWHM) of the photon fit of the slice (example in Fig. 2.13), FWHM$_n$ is the FWHM of the neutron fit, and d is the distance between the peaks of the fits.

The power function fit to these data as a discrimination line was defined as

$$\frac{I_{\text{tail}}}{I_{\text{total}}} = -0.1709 \times {I_{\text{total}}}^{0.114} + 0.361, \tag{3.5}$$

where I_{tail} and I_{total} are the tail and total integrals of each pulse, respectively.

With the ability to discriminate neutrons and photons, the die-away profiles were processed for each particle type. The die-away profile was calculated from the detected particles using the same method as in Section 3.1. Because MCNP calculates events based on independent source particles, the die-away profile from simulation was developed by constructing a histrogram of the recorded times of neutron detection events in the detector cell, scaled by the generator neutron output. Because a detector that is sensitive to both neutrons and photons was used in this experiment, the die-away profiles can be calculated for each. The comparison of these simulated and measured die-away profiles is shown in Fig. 3.9.

Figure 3.9 shows that the measured and simulated neutron die-away profiles agree very well. This agreement demonstrates that the system is modelled well, and the generator neutron output used to scale simulations is accurate. A discrepancy in count rate is seen while the neutron generator pulse is on (less than 200 μs). This discrepancy is due to the idealized, uniform emission of

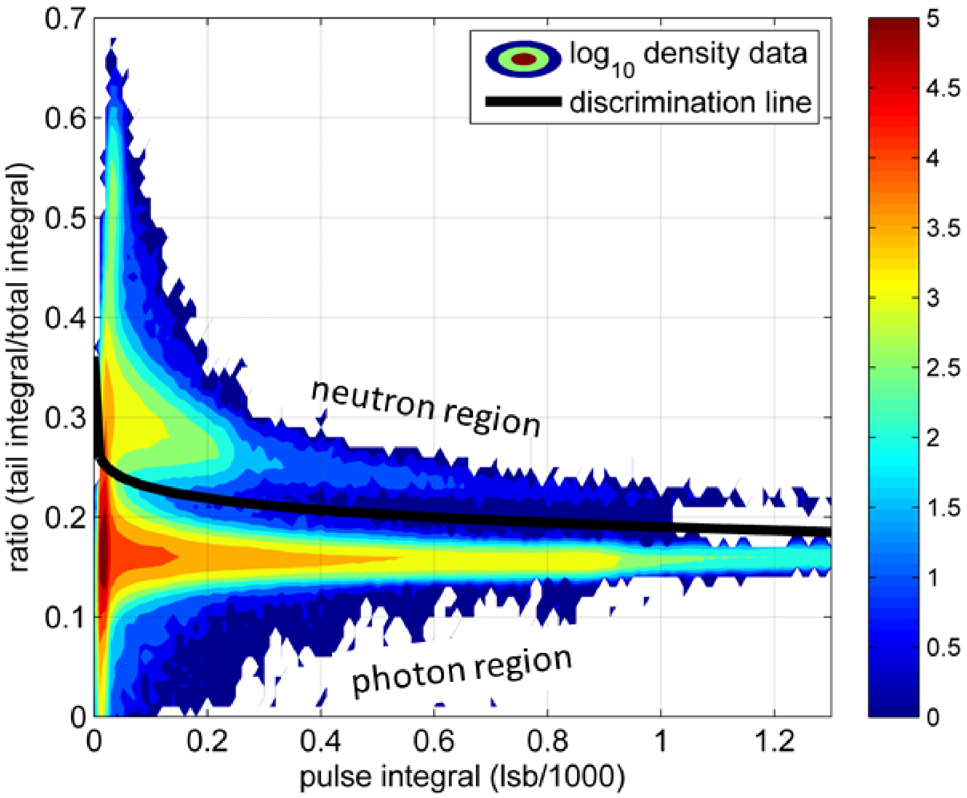

Figure 3.8: Pulse data measured from interrogated assembly barrel filled with water. The discriminating line is a power function fit to the integral ratio vs. total integral of the pulse.

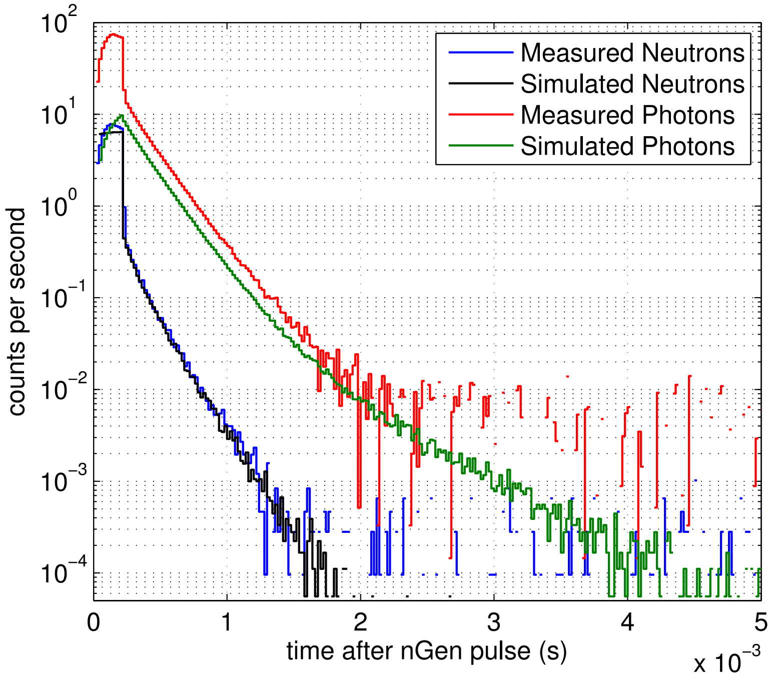

Figure 3.9: Experimental and simulated die-away profiles for neutron and photons emitted by the assembly with neutron generator interrogation.

neutrons during the generator pulse in the simulation, while the actual generator has a non-uniform plasma density and therefore non-uniform neutron emission during the pulse. The photon count rate is greater both during the accelerator pulse and in the die-away region after the pulse. The pulse-on discrepancy is likely due to the absence of generator emitted X-rays in the simulation, but this discrepancy does not affect further analysis of the data. The count rate increase in the die-away region is most likely due to the omission of fuel-decay photons in the simulation. Because this increase is a uniform shift of the count rate, it likewise does not affect further analysis.

Fig. 3.9 also shows that there are two components to the die-away profile. The second component is especially prominent in the simulated photon die-away profile, dominating after about 1.8 ms. It is important to isolate the primary neutron exponential decay fit described in Eq. 3.2. It was suspected that the secondary component was due to the effects of the concrete shielding and floor around the assembly barrel. This time-profile component was either because neutrons were reflected back into the system by the concrete to cause more fissions, or neutrons were thermalized and captured in the concrete over 100s of μs, producing radiative capture gamma rays.

This hypothesis was tested by simulating the system with the concrete in the model, and with it removed. These simulated die-away profiles are shown in Fig 3.10. While the concrete seems to have little effect on the neutron population decay time, the photon decay time comparison shows that the second component is eliminated with removal of the concrete. This elimination confirms that the concrete contributes to the second component of the decay, which was found to be significant after 700 μs from the start of the nGen pulse. It is also likely that capture reactions in the concrete are the major contributor, because the neutron decay time was not significantly affected.

The contribution of capture photons was further confirmed by tallying the simulated incident photons on the face of the stilbene detector in the model. Many distinct capture lines are observed in Fig. 3.11, but these peaks are more dominant over the Watt fission spectrum after 700 μs. This simulated tally confirms that radiative capture photons are the major contributor to the secondary decay component, and the primary fission-related decay is limited to less than 700 μs from the start of the generator pulse.

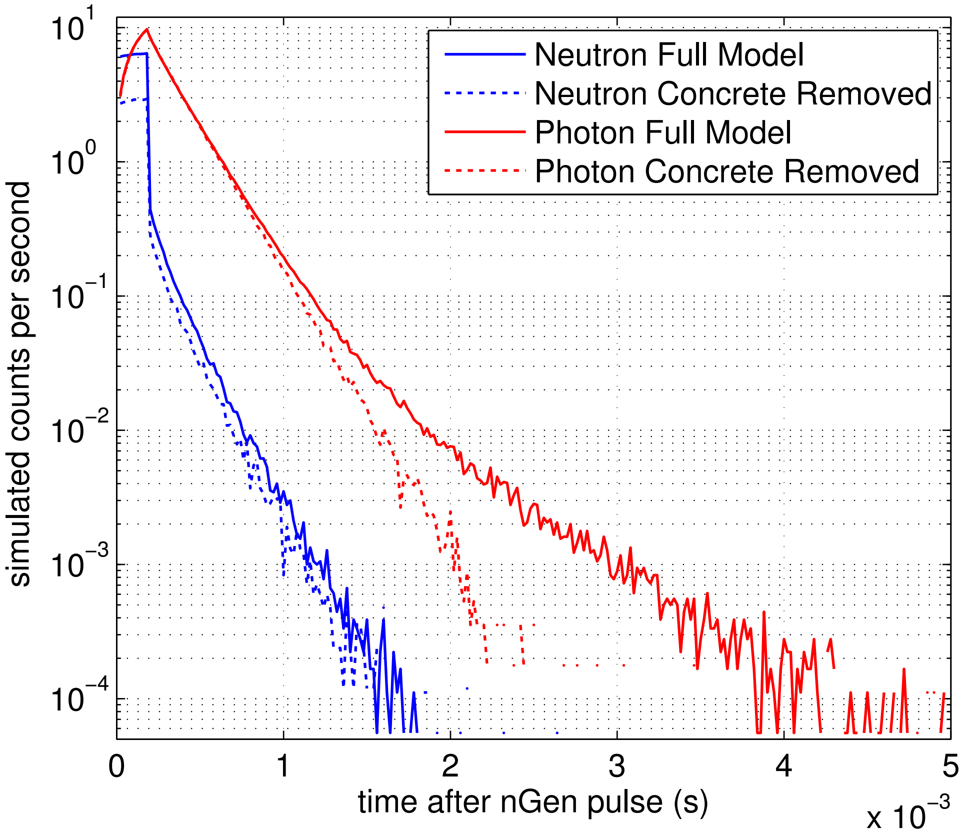

Figure 3.10: Simulated neutron and photon die-away profiles with and without concrete surroundings in the model.

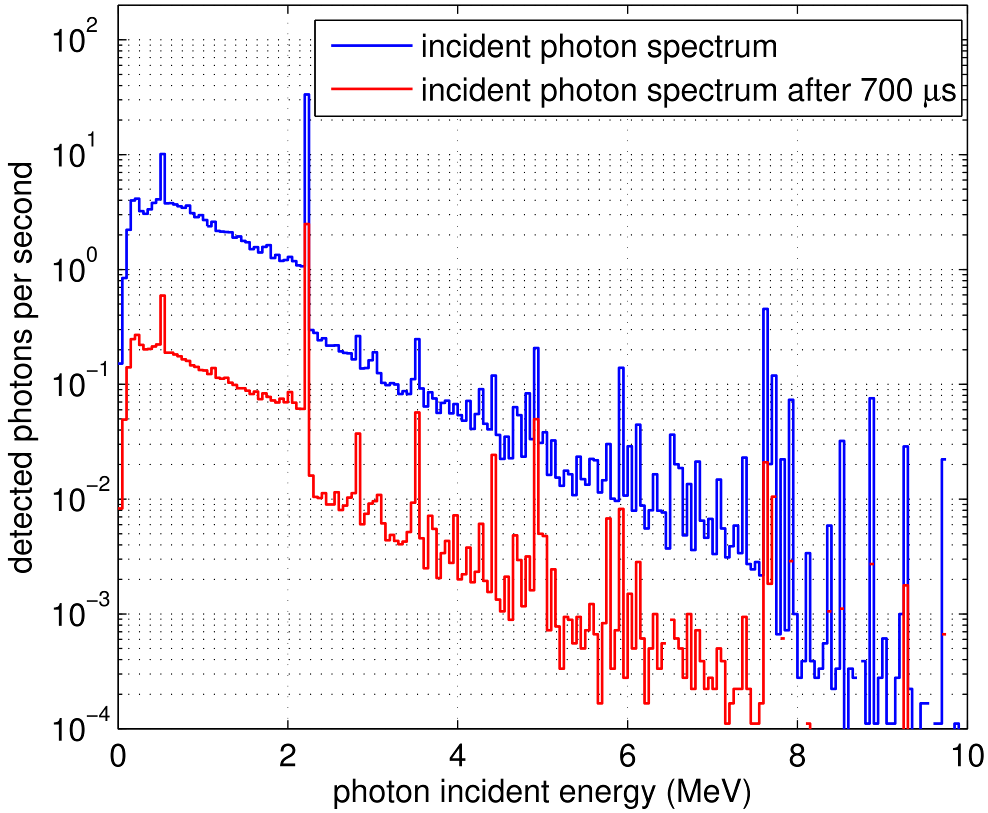

Figure 3.11: Comparison of incident photon spectrum for all times after nGen pulse, and 700 μs after pulse.

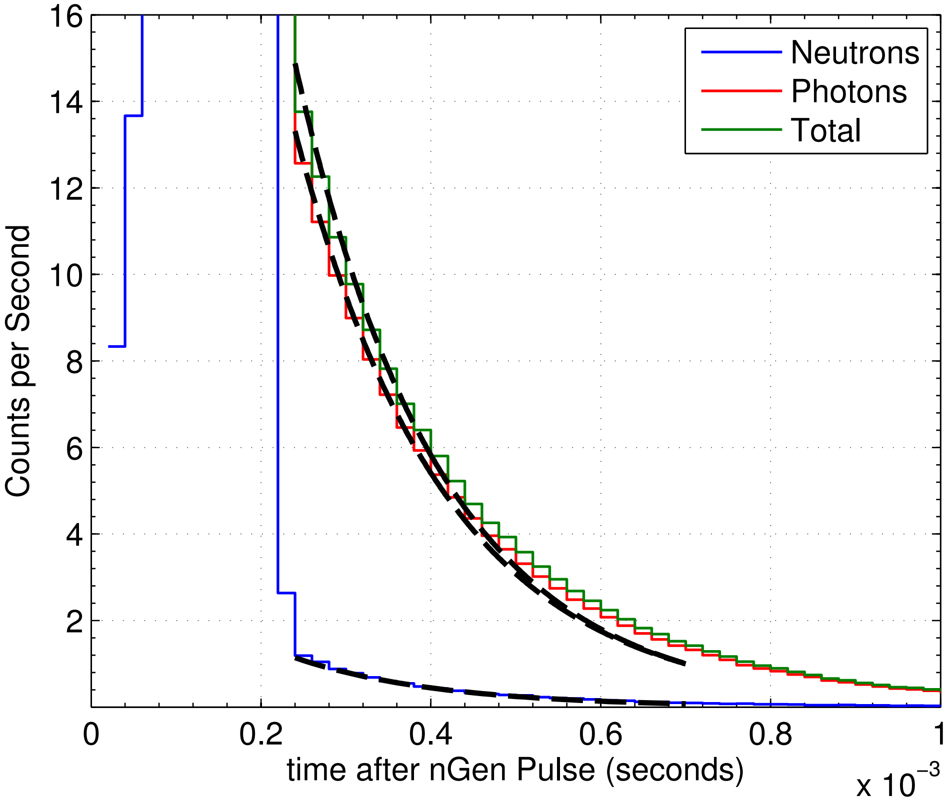

Figure 3.12: Exponential functions fitted to the measured die-away profiles. This figure shows only the fitting region of the die-away profiles.

An exponential function in the form of Eq. 3.1 can be fit to the die-away profiles with the bounds provided by the simulated concrete removal study with the MATLAB curve fitting toolbox [67]. The fits were calculated for the total detected die-away and for the discriminated neutron and photon die-away profiles. These fits are shown in Fig. 3.12 with the parameters listed in Table 3.1.

The calculation of k_{eff} from the measured data is performed with Eqs. 3.2 and 3.3. The β and Λ values are calculated with the MCNP6.1 KCODE point kinetics parameters option, and were determined to be 0.00768 ± 0.00115 and 189.05 ± 3.45 μs respectively. The simulated k_{eff} was also calculated using 200 cycles with 10,000 source neutrons per cycle.

Table 3.1 shows that the k_{eff} calculated from the measured neutron die-away profile agrees within uncertainty with the MCNP6 simulated value. This agreement demonstrates the promising capability to use organic scintillators to inform reactivity measurements of neutron-pulsed subcrit-

Table 3.1: Calculated k_{eff} with exponential fitting parameters, compared to MCNP6.1 KCODE result.

	c	α	k_{eff}
total die-away	45.36 ± 1.65	-5141 ± 109	0.509 ± 0.002
neutron die-away	2.07 ± 0.26	-7274 ± 412	0.422 ± 0.016
photon die-away	43.64 ± 1.50	-5095 ± 102	0.509 ± 0.002
MCNP6.1	-	-	0.4179 ± 0.0005

ical assemblies. The die-away profiles without performing PSD and from photons alone are not as accurate, likely due to other sources of photons from the neutron generator and the decay of the nuclear fuel. However, the photon count rate is much higher, and the non-PSD die-away profile could offer a quick check of reactivity.

3.3 Conclusions

Pulsed neutron generators were used in the experiments described in this chapter to identify a drug simulant, an explosive compound simulant, and SNM. Further properties of nuclear fuel containing ^{235}U were characterized by pulsing a subcritical reactor with a D-D neutron generator.

Drug and explosive contraband simulants were identified through the use of TNA. The neutron generators produced a large flux of fast neutrons, and these were moderated to thermal energies in the surroundings, the target material, and additional hydrogenous moderating material. Specific isotopic contents were identified by observing characteristic neutron capture photon energy peaks with a NaI(Tl) detector. Complete identification of contraband materials would require an array of efficient, high-resolution detectors with advanced spectroscopy techniques to determine the proportion of each isotope present.

SNM was identified with the DDAA technique. Pulsed neutrons induced fissions in the material, which resulted in a longer, elevated die-away profile than with no SNM present. Helium-3 detectors were used to capture this time dependent neutron profile. While SNM was identified quickly in this demonstration, shielding from cargo materials would make detection more difficult.

The DDAA technique was also used to characterize the reactivity of a subcritical assembly driven by a pulsed neutron generator. The die-away profile was measured with a PSD-capable organic scintillator (stilbene), and was used to calculate the k_{eff} of the system. These calculations utilized point kinetics parameters from simulation. The k_{eff} calculated with the time-decay of the neutron population was very accurate when compared to Monte Carlo simulation. PSD is necessary for high accuracy, but non-PSD capable detectors could be used for a quick check of reactivity properties based on the detected photon population.

Neutrons are a powerful tool for interrogating material of interest, because they can penetrate many forms of shielding, and induce unique reactions. However, some reactions yield weak signals that could then be shielded, and neutron signals may be masked by the interrogating particles themselves. Photons can be used as an alternative interrogating source, or in conjunction with neutrons for more robust interrogation.

CHAPTER 4

Bremsstrahlung-Induced Photoneutron Detection with Organic Scintillators

High-energy photons can be used to interrogate cargo and induce photofission reactions SNM. Electron accelerators are widely available for the production of large amounts of high-energy bremsstrahlung photons; however, currently-deployed systems can be very expensive and difficult to widely deploy [18].

This chapter outlines work to develop an alternative photon-based active interrogation system, that employs a commercially available medical linear accelerator (linac) [17] and stilbene organic scintillator detectors, which are relatively cheap to manufacture and widely available [68]. The use of a widely available linac greatly reduces capital, operational, and maintenance costs opposed to Rhodotrons currently employed in active interrogation systems [18]. Additionally, organic scintillators operate on a time scale that enables the detection of prompt fission neutrons within the pulse of the linac. The ability to detect prompt neutrons increases the available measurable signal over the detection of only delayed fission neutrons, as is typically done. The detection of photofission neutrons, identified through timing correlation or detected energy, is a telling sign of the presence of SNM. This chapter presents research performed to shield and install the linac at the University of Michigan and preliminary experiments with interrogated material detection with organic scintillators, sourced from [69] and [70]. The reduced cost and technical advances of this interrogation system increases the potential for deployability in shipping ports, and increases the probability of detecting shielded highly enriched uranium.

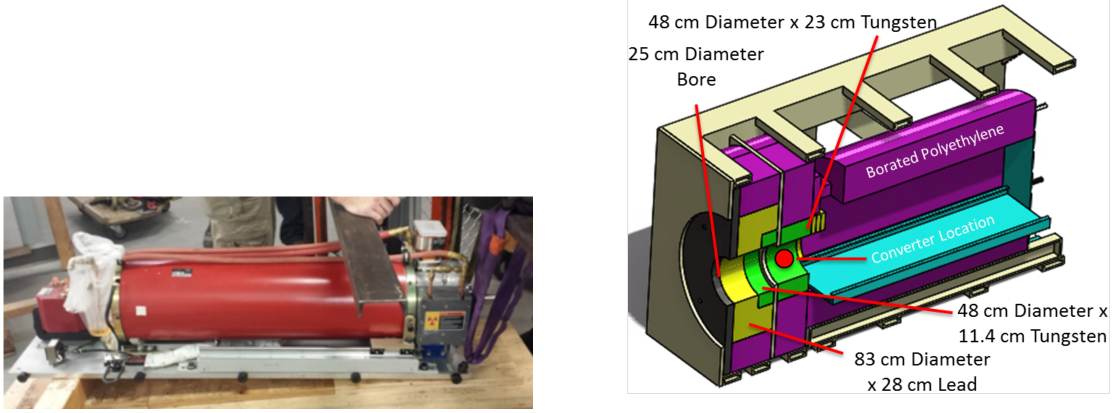

(a) (b)

Figure 4.1: Varian M9 accelerator main component (a) and shielding enclosure (b). The main accelerator component is housed behind the circular aluminum plate on the back end of the shielding enclosure.

4.1 Shielding and Installation

A Varian 9-MV [17], 1-kW linac was delivered to the University of Michigan in July 2017 to enable this investigation into the feasibility of using organic scintillators for active interrogation signature detection. The accelerator was generously loaned to the University by the U.S. Department of Homeland Security, Countering Weapons of Mass Destruction Office, through a Cooperative Research and Development Agreement. The linac was previously used at Rapiscan Systems, and is housed in a shielding enclosure tailored to homeland security applications. The main accelerating structure and the shielding enclosure are shown in Fig. 4.1. The linac can operate between 10 and 100 μA, which corresponds to pulse rates of 25-250 Hz. The width of the electron pulses is 4 μs. SNM proxies will be interrogated by 9 MeV endpoint bremsstrahlung photons to induce photonuclear reactions. The challenge in this investigation is to discriminate these neutrons from the large photon flux scattered by the target, and the photons directly from the accelerator. Shielding of the accelerator will limit the extraneous dose to operators and detectors, while allowing for optimal flux on the target.

The linac is housed in the basement floor of the Nuclear Engineering Laboratory at the University of Michigan, which formerly housed the Ford Nuclear Reactor [71]. While the reactor building walls provide significant shielding to the public from the accelerator, there are certain spatial constraints that provide challenges for shielding in the laboratory. The beamline is directed towards a separate laboratory space, and must be fully attenuated to keep dose rates below occupational limits. A door to this separate laboratory is also in the down-beam direction, and must be shielded. The overall goal of this shielding study is to fully cover a 30 cm×30 cm square target of material with the full, unfiltered flux of the beam, while keeping dose rates below safety limits. It is also ideal to limit the amount of shielding in the target area to reduce the probability of non-signal particles being created near or scattering into the detectors.

Dose rates were simulated with MCNPX 2.7.0 [72] and MCNPX-PoliMi [35]. These simulations supported the safety certification process and pre-installation experiment planning. Once the accelerator was installed, dose rates were evaluated with standard dose rate survey meters to complete safety certification with University of Michigan Radiation Safety Services and the State of Michigan.

The model for the accelerator laboratory was designed in MCNP using measurements of the space and construction documents. The shielding enclosure for the accelerator was modeled using exterior measurements and Rapiscan-provided interior diagrams. The largest unknown aspect of the accelerator model was the dimensions of the conversion target itself, as it is a proprietary Varian design.

The known design value for this accelerator is that the dose rate at 1 m from the target is 2700 Rad/min. It is also known from correspondence with Varex Imaging Corporation that the cylindrical conversion target is tungsten with a copper layer on the downstream side. The target dimensions were estimated to be 23 mm of tungsten backed with 15 mm of copper. This tested target dimension results in a simulated dose rate 16% greater than the specified value. With uncertainties in dose rate measurement techniques, I assumed that this design offers a conservative estimate to the true target dimensions.

Fig. 4.2 shows that the photon flux is forward directed without any additional shielding, reducing the need for transverse shielding of the conversion target. Fig. 2.4 shows the simulated 9 MeV

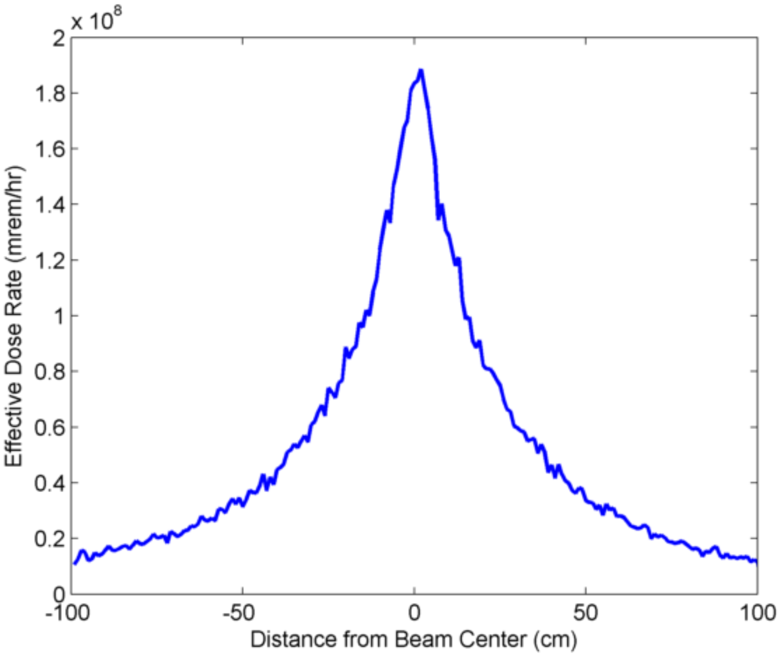

Figure 4.2: Simulated photon dose rate beam profile 1 m from bare electron conversion target.

endpoint bremsstrahlung photon spectrum resulting from 9 MV electrons imparted on a heavy metal target. Along with the inherent forward directedness of the source the custom shielding enclosure cuts the beam to a 16.7° half-angle cone.

The accelerator in its shielding enclosure shown in Fig. 4.3 is placed in a shielded room within the laboratory. The placement of the linac is shown in Fig. 4.4. The cone of the beam will be further reduced by secondary collimators in the linac vault. With this arrangement fully modeled in MCNP, operational parameters can be optimized against dose rate.

To obtain accurate simulation results while minimizing the necessary computation time, multiple approaches were taken depending on the goal of the simulation. These goals can be split into two main categories: detector response to an irradiated target and dose rate assessment.

4.1.1 Detection Simulations

Detector response simulations require acquisition of a simulated energy spectrum, so a detailed estimator is required. Simulated photons from the accelerator are incident on a target material, and a detector is facing the interrogation target. This detector is 50 cm away from the target perpen-

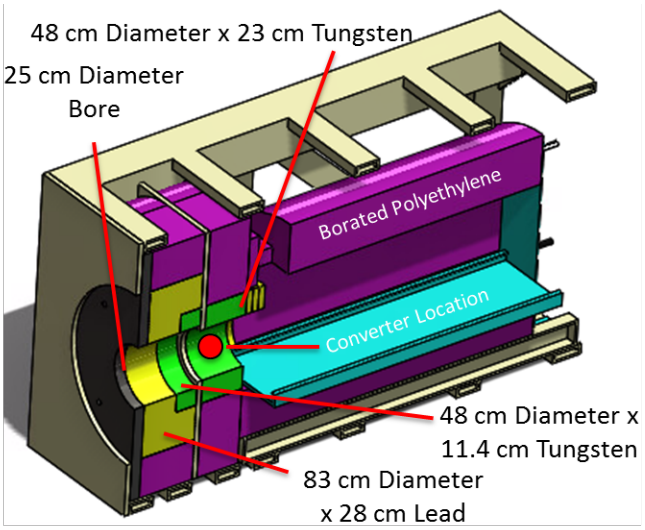

Figure 4.3: Shielding enclosure for linear accelerator (modeled by Rapiscan Systems).

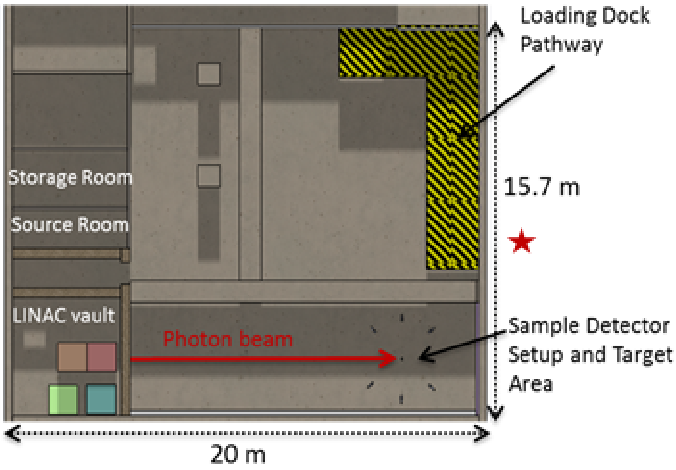

Figure 4.4: Laboratory setup with linac location and beamline orientation.

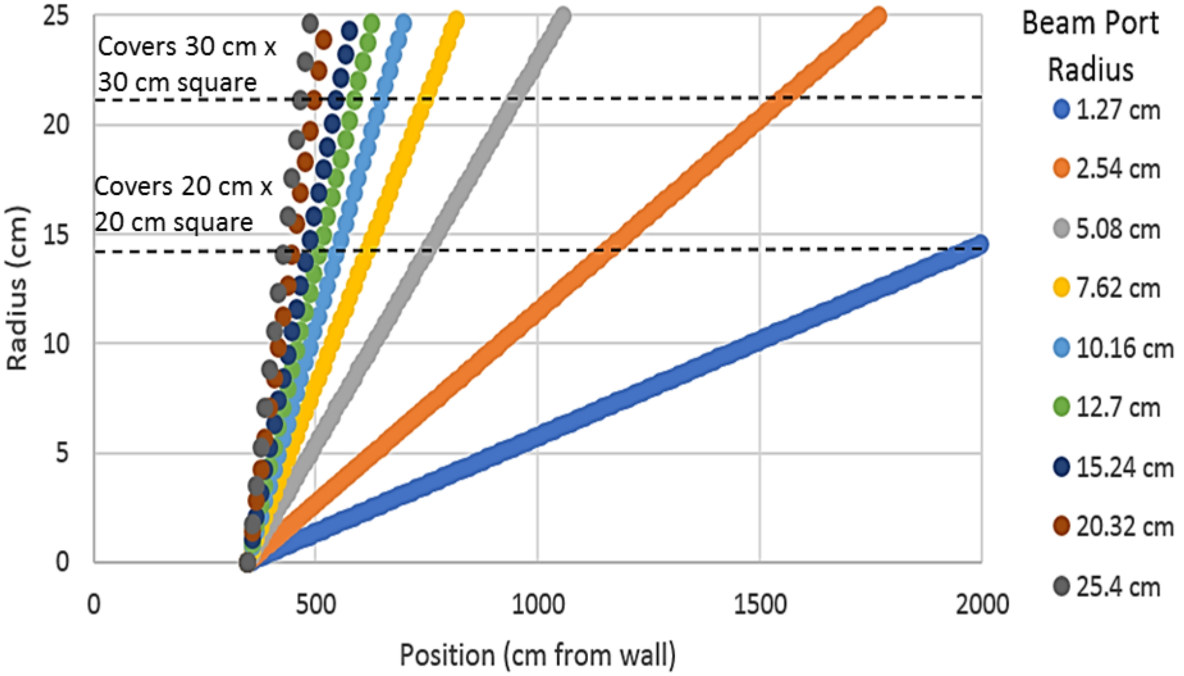

Figure 4.5: Square target coverage with different size beam ports in linac vault.

dicular to the beam direction. Because the signature produced by the source photons interacting in the target is of interest here, effects from other particles scattered around the laboratory can be ignored. The flux due to these particles is many orders of magnitude below the flux resulting from the main beam. The target will be placed 12 m from the source, so the photons are assumed to be a parallel beam. These assumptions allow for simplifying the model to a parallel beam of photons over the face of the target, with nothing in the model but detector and target. The results can be scaled appropriately based on the known geometry and source parameters.

The goal of this project is to develop methods for using organic scintillators in an active interrogation system. The design of the shielding for the laboratory must therefore allow for adequate flux on the target to produce the relevant signatures.

Fig. 4.5 shows that the beam is capable of fully covering a 30 cm square target 12 m from the photon source if the bore is at least 5 cm in diameter.

To observe the trend of the target size effect, cube targets of increasing size were simulated. These targets were tested with 4 possible target materials: lead, tungsten, heavy water (D_2O) and

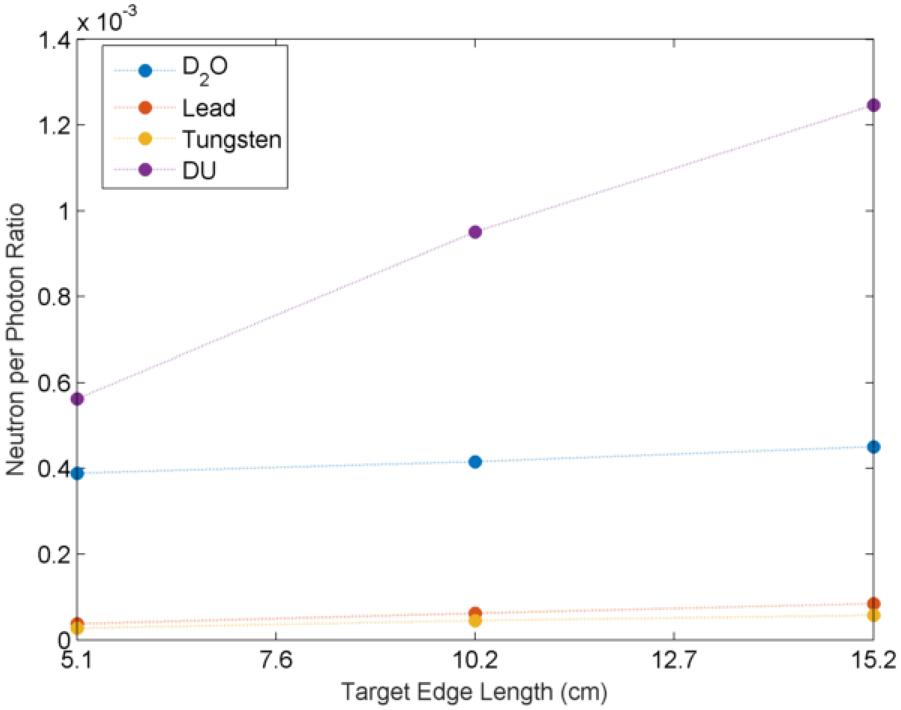

Figure 4.6: Signal-to-noise ratio of particles leaving target for different size targets of possible SNM surrogate materials. Statistical uncertainty smaller than markers.

depleted uranium (DU). Because induced neutron emission is a strong signal of special nuclear material, detection of neutrons is treated as a valuable signal for detecting SNM. The best surrogate material for SNM will produce the highest ratio of neutrons per photon. Neutrons are produced through photofission or (γ,n) reactions, and photons are scattered from the beam incident on the target, or are resultant from pair-production interactions in the target.

While DU and D_2O have the highest ratio of neutrons to photons as shown in Fig. 4.6, these ratios are fairly low, demonstrating the challenge of detecting neutrons in a large photon flux. With the accelerator installation, detection methods will be developed to overcome this challenge.

4.1.2 Dose Mapping

To simulate dose rates, a dose-converted [73] flux mesh tally is used in MCNPX. Full spatial and source profile integrity is required. Because dose rates must be shown for the entire lab space, the entire lab geometry was simulated.

The source has a spatial dependence as well (shown in 4.2), and any simplifications would lead to inaccuracies in the dose rates. Therefore, the source was modeled directly from the electron beam to preserve spatial integrity and maximize statistical sampling. The complication with this modeling is that charged particle transport is very slow in MCNP, because many samples are performed to account for the particle's energy loss through coulombic interactions.

A large simulated detector volume can be used to generate statistically sound results in a reasonable computation time. In this case, a mesh tally was defined using 50 cm cube voxels. The voxel size was chosen based on the size of a human, and the fact that minute spatial variations in the dose rate map are not expected to affect the overall results in such a large space. Therefore, the calculated dose rate can be averaged over these relatively large voxels.

While a large beam would be ideal for maximum target coverage, dose rates must be considered. The location of the star in Fig. 4.4 is where there is a loading dock door, which the beamline is directed towards. Although the laboratory on the other side of the door is not a public space, this is the limiting location for dose rate, and should be kept under 5 mrem/hr [74] while the beam is on.

A 20.3 cm thick lead beamstop was designed to reduce the dose contribution of the direct beam into adjacent this laboratory below this limit as well. The 61 cm thick concrete wall of the laboratory space additionally reduces this intensity of the beam.

With the original shielding arrangement shown in Fig. 4.7 (a), the dose rate was simulated at the limiting position with different size beam bores. For initial certification, the accelerator will be tested at its lowest available current, 10 μA. The dose rate with these parameters is estimated to be 4.5 mrem/hr for the 2.5 cm bore and 18.6 mrem/hr for the 5 cm bore. In Section 4.1.1, it was decided that at least a 5 cm bore is desired for target coverage, so additional shielding was required to meet the dose rate goal of 5 mrem/hr.

Fig. 4.7 (b) shows the additional lead collimator, which is a 74 cm square, 41 cm inches thick. This size collimator covers the full profile of the beam at that location. The dose rates simulated with this secondary collimator in the model are shown in Fig. 4.8.

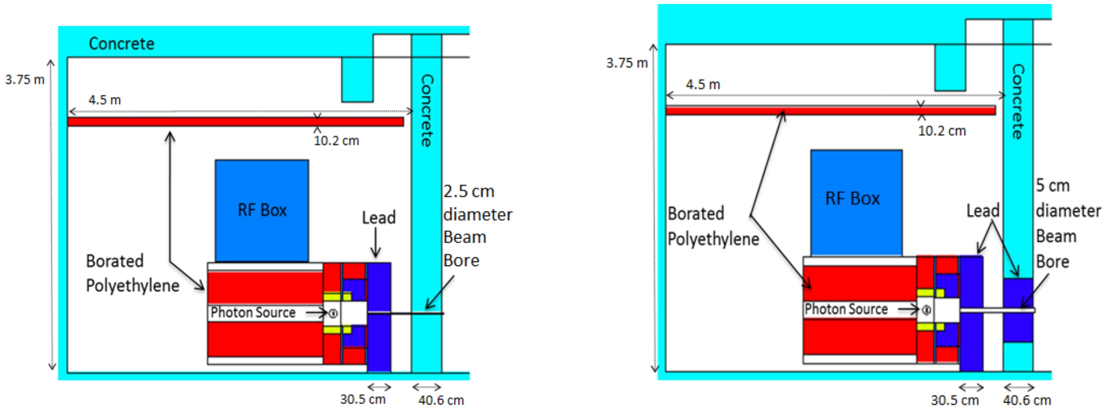

(a) (b)

Figure 4.7: Elevation view of shielding for linac enclosure, with base shielding shown (a), and an additional secondary lead collimator (b). The beam bore through the down-beam wall collimates the beam to the desired size.

The full photon dose rate map is shown in Fig. 4.8 (a), and the dose rate at the limiting location is below the target dose rate at 4.2 mrem/hr. Figuree 4.8 (b) also shows that neutron dose is not a concern outside of the linac vault itself.

The simulated shielding design provided the basis for implementation and conditional operational licensing, but based on practicality and budgetary concerns, as well as initial dose rate survey measurements, slight alterations were made. For this design the linac current was also increased to 20 μA as this was found to be the lowest practical operating current. The primary collimator between the linac enclosure and the secondary collimator was eliminated, greatly reducing the mass and cost of lead required. Simulations showed that this approach did not lead to a significant increase in dose rates in the room. However, due to some inaccurate assumptions of ceiling thickness this led to elevated photon dose rates to public areas in the upwards direction when measured with a survey ion chamber. This issue was solved by installing a 30.5 cm thick lead shield above the beam between the linac enclosure and the vault wall. The model of the installed shielding design is shown in Fig. 4.9 with photographs of individual components shown in Fig. 4.10. The MCNP input deck for this shielding arrangement in the laboratory is listed in Appendix C.

The simulated dose rates for this shielding configuration are shown in Fig. 4.11. The simulated

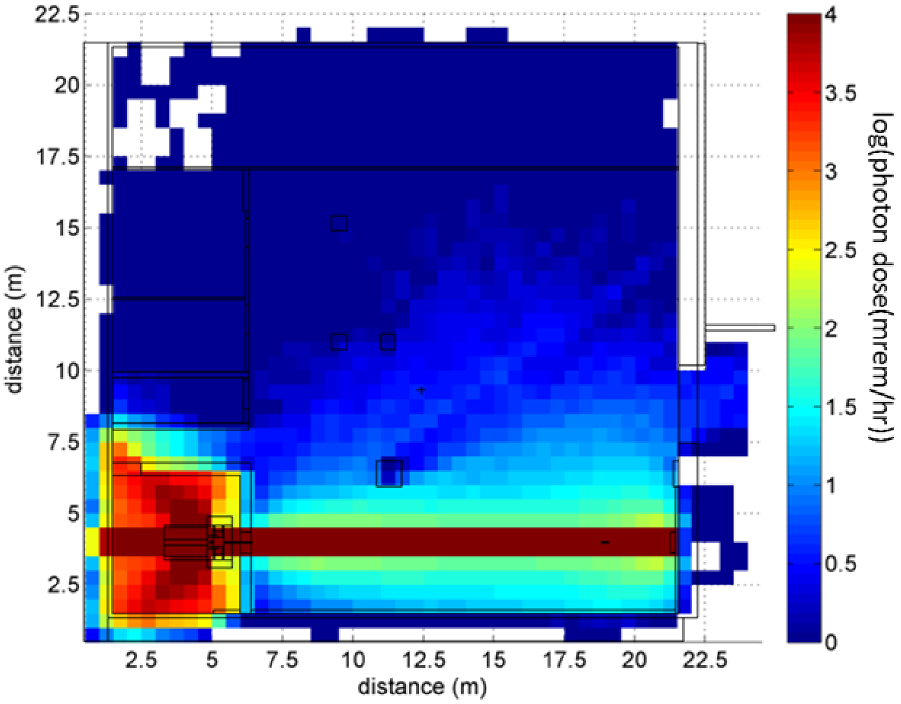

(a)

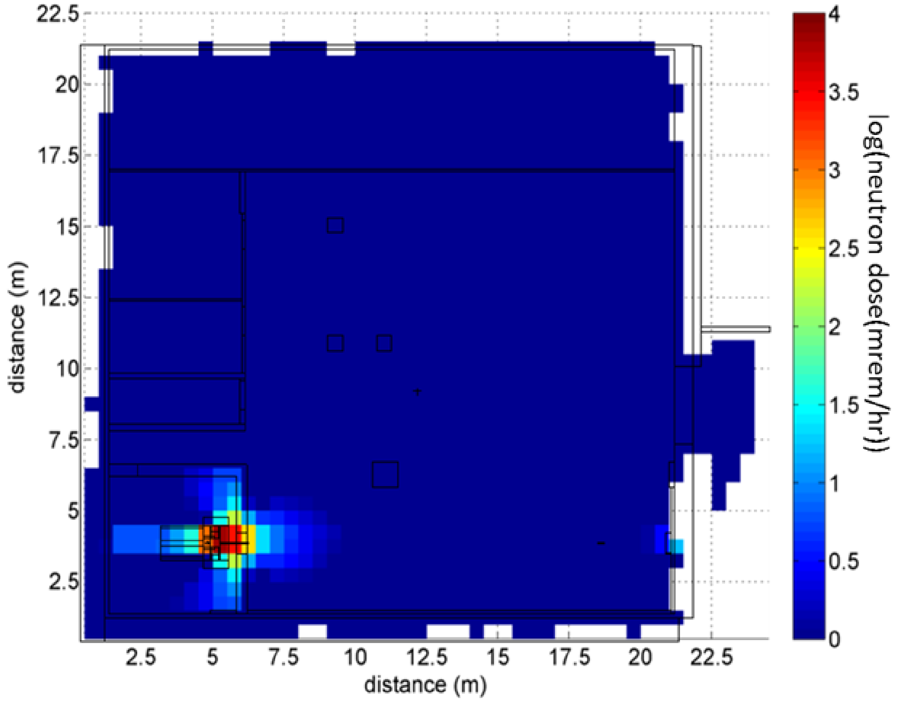

(b)

Figure 4.8: Preliminary simulated dose rate maps of accelerator laboratory space: photon (a) and neutron (b).

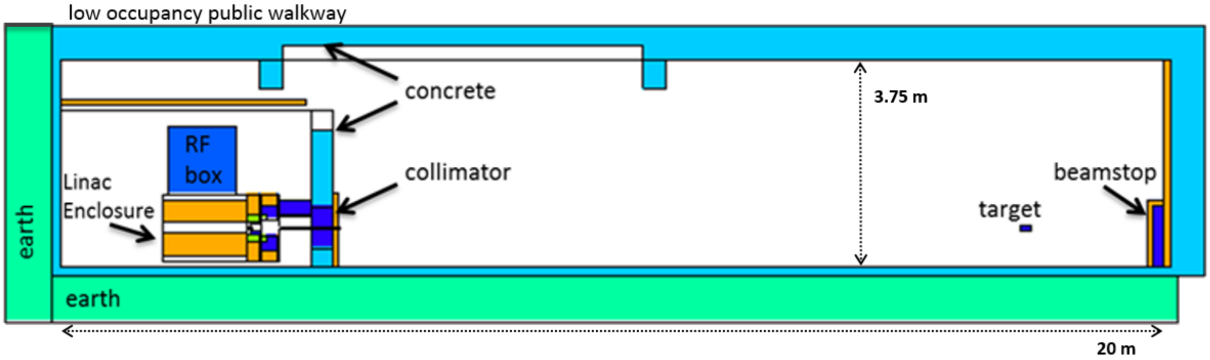

Figure 4.9: Elevation view of model of installed shielding for linac facility.

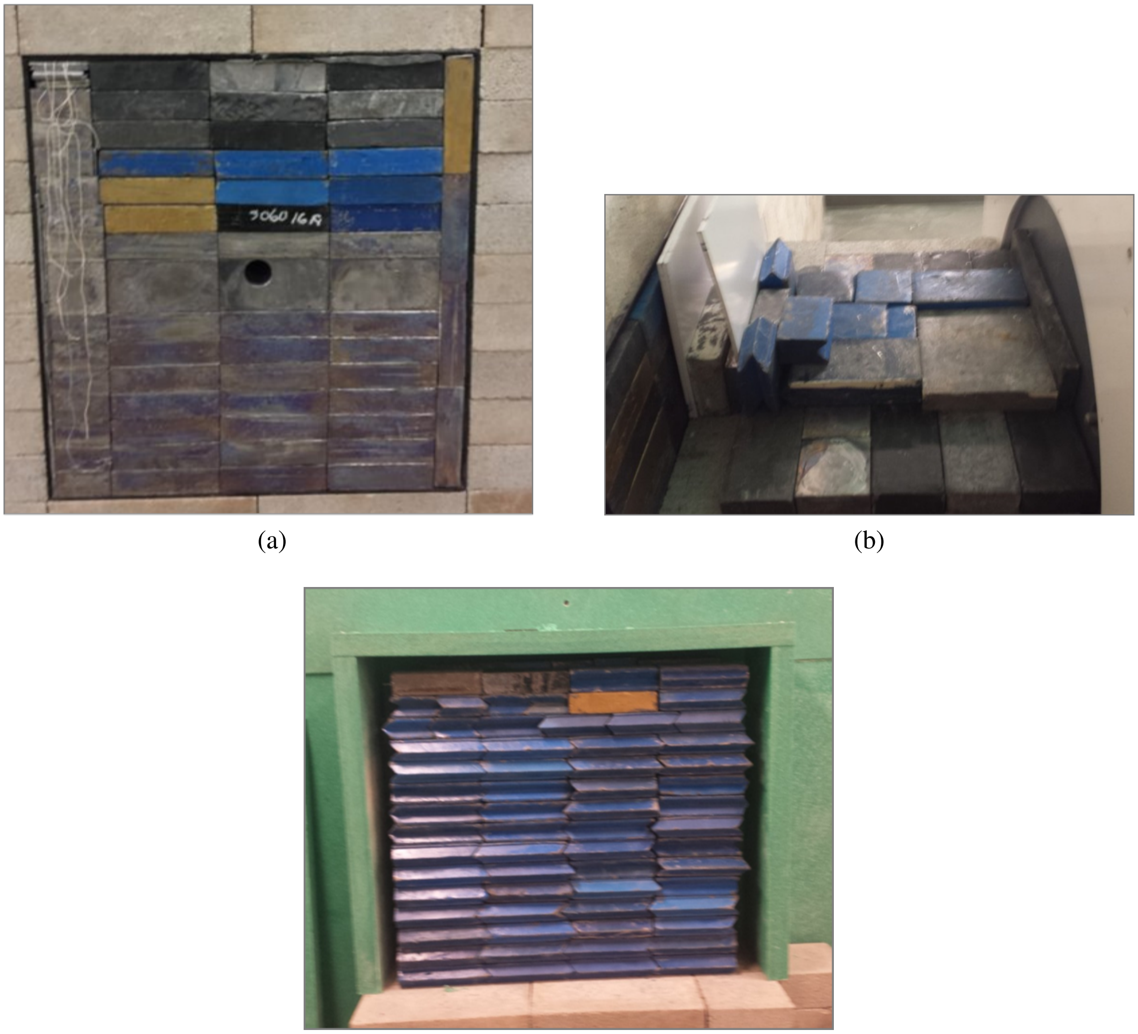

(a) (b)

(c)

Figure 4.10: Shielding components installed for linac laboratory: collimator (a), lead shielding above beam in vault (b), and beamstop (c).

dose rate to the public walkway above the linac is 1.4 mrem/hr. With all of the simulated rates below mandated limits, final survey measurements were performed. The results of the survey are shown in Fig. 4.12, and the measured dose rates on the public walkway above the linac were 1.4 mrem/hr and background for photon and neutron respectively.

There are discrepancies between the simulated and measured dose rates, with a large underestimation of neutron dose rate. However, photon dose rate is dominant, and the photon dose rate predictions are much closer to the measured rates. The 5.8 mrem/hr measured dose rate to the right of Fig. 4.12 is slightly higher than the limit of 5 mrem/hr in that area, but during operation that area is made inaccessible. These survey results satisfied State of Michigan requirements for operation of the linac, and it was certified for research use in June 2018.

The shielding design developed with MCNP simulations provided a plan to suppress dose rates below targeted limits. The concrete linac vault is sufficient to shield the photoneutrons produced in the shielding enclosure. While additional photon shielding is required to meet the dose rate goals, it was incorporated into the linac vault area, leaving the beamline open for experiments. This shielding configuration allows for full-flux coverage of a 30 cm square target. Complete target coverage maximizes photoneutron production in a large target, enabling practical experimental design for the testing of organic scintillators.

While the limited space and orientation of the laboratory provided challenges for developing a shielding design, it was possible to develop a practical shielding plan. For the detector response simulations, constraining the problem allowed for accurate characterization of detected spectra with practical computation time to assure maximum particle flux on the interrogation target. Full charged-particle simulation with large detector voxels allowed for accurate simulation of the entire lab space, and survey measurements confirmed the viability of the shielding design.

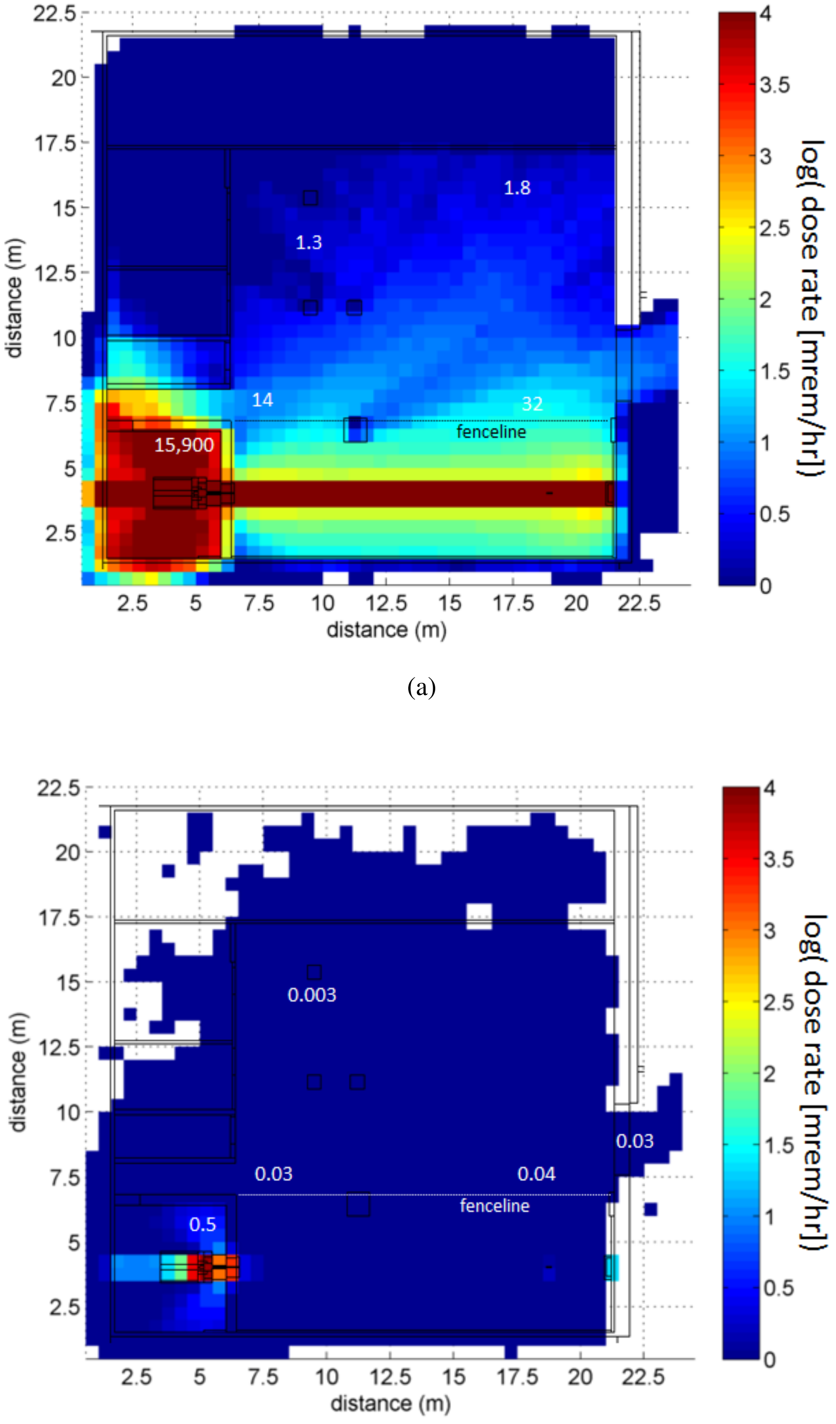

(a)

(b)

Figure 4.11: Simulated dose rate maps for shielding installed in linac laboratory: photon (a) and neutron (b). The labeled fenceline is an interlocked security fence, and dose rates are labeled around the laboratory in mrem/hr.

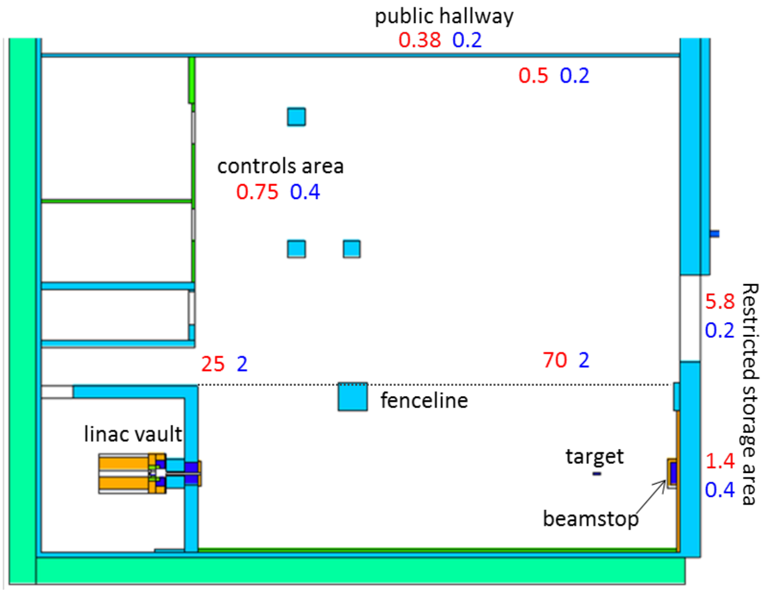

Figure 4.12: Dose rate survey results with Victoreen 451 ion chamber measured photon dose rates shown in red and Eberline ASP-1 remball measured neutron dose rates shown in blue, all in mrem/hr.

4.2 Neutron Active Background Minimization Study with ^{3}He Detectors

Neutrons from the active background (ABG), or neutrons that result from interactions anywhere but in the interrogation target, must be minimized to increase the probability of detecting neutrons resulting from interactions in the target. Source photons and photons either emitted or scattered from the interrogation target must be shielded from the detector as well to increase the accuracy of particle identification through PSD. However, photon ABG suppression is achieved in conjunction with the personal protection shielding discussed in section 4.1, so this section will focus on neutron flux mitigation.

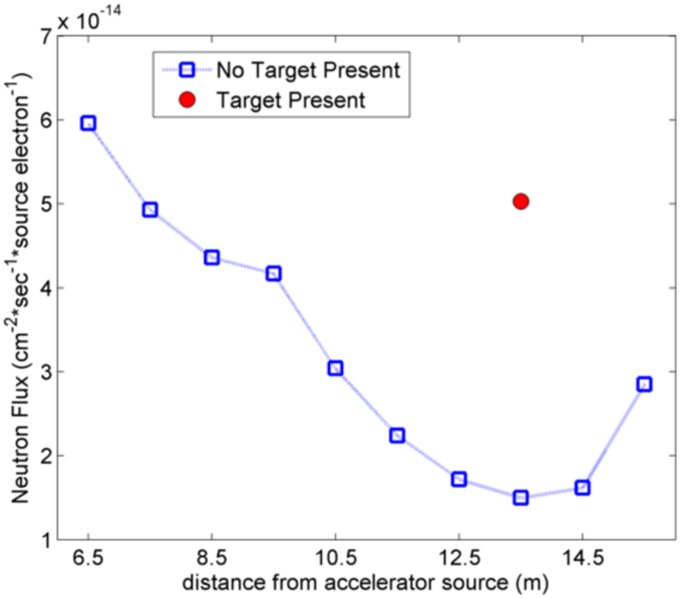

Figure 4.13: Simulated neutron flux along linac beamline, with 10.16 cm of BPE surrounding collimator and beamstop.

The main sources of non-interrogation target produced neutrons are the beam collimator and beamstop, which bookend the beamline experimental area. These components are built of lead, which is a well-known source of neutrons from Pb(γ,n) reactions. The neutron flux was simulated at 1 m increments along the length of the beamline area, 50 cm from the beam center. It was determined that with a 10.2 cm thick coating of borated polyethylene (BPE) around the beamstop and on the collimator, the active background neutrons would account for 29% of the the neutron flux emitted by a 1000 cm^3 lead target placed 13.5 m from the photon source, as shown in Fig. 4.13.

With the BPE shielding in place for mitigation of ABG neutrons measurements were performed to confirm the location of the minimum neutron contribution. These measurements were done with a 23-tube fast-neutron sensitive ^{3}He module read out through eleven channels with a CAEN V1730 digitizer [75]. Neutron count rate was measured at the same locations along the length of the beamline as the simulated cases. This detector was chosen due to its insensitivity to photons and reliable neutron detection, discussed in Section 2.2.1. The ^{3}He panel is coated with cadmium to capture incoming thermal neutrons below 0.5 eV and ^{10}B to capture many thermal

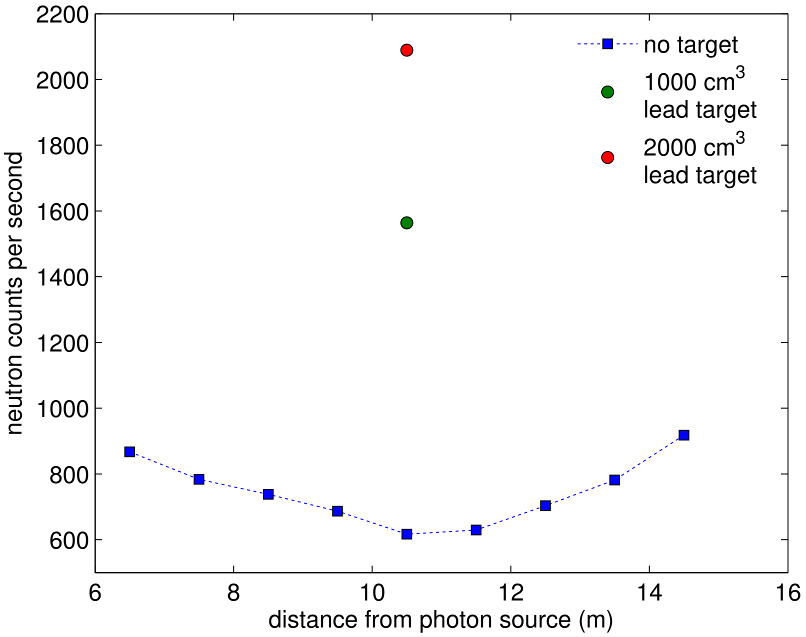

Figure 4.14: Helium-3 module measurements along beamline. Blue points show active background neutrons, with neutrons contributed by interrogated lead targets in red and green. Statistical error bars are smaller than markers.

and epithermal neutrons. Lead targets of 1000 and 2000 cm^3 were placed in the beam at the minimal active background neutron location. Because the thermal neutron shielded ^{3}He detector is primarily sensitive to fast neutrons, these experiments can inform the expected increase in neutron count rate due to target presence measured with stilbene, which is only sensitive to neutrons above approximately 0.5 MeV.

The minimum active background neutron contribution is shown in Fig. 4.14 at 10.5 m from the photon source at the linac conversion target. At this point, active background contribution is limited to 39% and 29% of the overall signal detected from the interrogated 1000 cm^3 and 2000 cm^3 lead targets, respectively. The difference in location points to discrepancies in the distribution of the modeled neutron flux, but the magnitude of the background contribution is identical to the simulated prediction. For the following organic scintillator experiments 10.5 m from the photon source is used as the optimal location for minimum ABG contribution to the signal.

4.3 Organic Scintillator Experiments

Prompt neutrons induced by the installed linac can be detected by employing the PSD capability and fast time-scale operations of organic scintillators. Prompt neutron detection yields a stronger signal than delayed neutron signatures from SNM because only 0.5% of emitted neutrons are delayed.

The challenges of this detection environment include isolating the nuclear material fast neutron emissions from interrogating photons and active background signals, as discussed in Section 4.2, and detecting a large flux of particles on a short time scale. These ABG photons are either scattered into the detector by the interrogation target or surrounding material, or originate from the accelerator itself. Traditional charge-integration PSD [45] performance in this detection environment has been investigated, in conjunction with the development of a new neural-network based approach for PSD along with pulse recovery [76].

4.3.1 Preliminary Experiments

Preliminary tests were performed with an Eljen-309 7.62 cm diameter × 7.62 cm liquid organic scintillator [77] read out with a CAEN V1730 digitizer, with the PMT operated at a bias voltage of -1000 V. For preliminary testing this detector behaved reasonably similarly to a stilbene detector, and because there are many in the group's possession, it was more disposable than a stilbene detector if something went wrong. The detector was placed at the minimum ABG point along the beamline, 50 cm from the center of the beam, with 5.08 cm of lead shielding towards the beam of photons and towards the accelerator itself. Pulses were recorded with an 8 μs window. The pulse of photons emitted by the linac is on during the first 4 μs of the window.

The pulses recorded during this testing are shown in Fig. 4.15. The pulses exhibited extreme pile-up, and photon pulses are observed in the digitized traces for the full 4 μs that the linac pulse is on. This pile-up implied that the photon flux on the detector is much too large for individual pulses to be resolved. In addition to occluding individual pulse information, this extreme pile-up leading

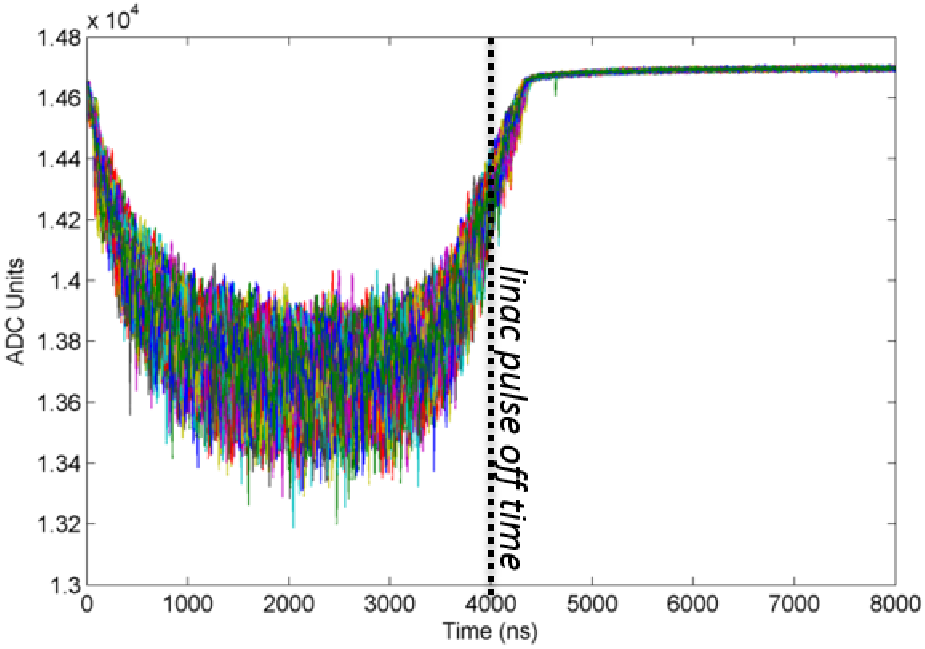

Figure 4.15: Pulses recorded with Eljen-309 organic scintillator in preliminary linac testing.

to PMT saturation makes PSD impossible. Additional pulses arriving in the tail integral of the first pulse can artificially increase the tail-to-total ratio of the pulse, possibly falsely interpreting it as a neutron pulse [38]. Steps to reduce the flux must be taken to enable accurate pulse discrimination and information collection.

4.3.2 Shielded Experiments

Experiments were performed in an environment of reduced flux by placing a detector in a full five-sided lead cave, 10.16 cm thick. The distance from the detector to the beam was also increased to 1.7 m. The experimental setup is shown in Fig. 4.16.

For these initial PSD performance experiments a 5.08 cm diameter × 5.08 cm stilbene organic scintillator was used, for the reasons discussed in section 2.2.2.2. The fact that stilbene produced very fast pulses increases the probability of acquiring single pulses in the high-flux environment created by the linac. For demonstration, the stilbene detector was used to record detected pulses during the full 4 μs linac pulse, shown in Fig. 4.17a. With this detector shielding and configuration

Figure 4.16: Stilbene detector housed in 10.16 cm lead cave, 1.7 m from tungsten target placed in beam center.

individual detected pulses can be resolved, as shown in Fig. 4.17b. However, the actual pulse window used for these experiments was much shorter at 144 ns to increase the probability to detect single particle pulses.

The SNM surrogate interrogation targets chosen for this experiment were a 2000 cm^3 lead target and a 500 cm^3 tungsten target. These targets were chosen for their photonuclear cross sections. Both materials have effective photonuclear thresholds near 8 MeV, with lead cross sections peaking at about 600 mb and tungsten at about 400 mb, both near 13 MeV [78]. These materials act as a practical experimental surrogate for SNM.

To preemptively eliminate pile-up pulses, any pulse with a signal increase greater than 6% of the original pulse height was classified as a double pulse and discarded. Pulses that exceeded the dynamic range maximum were also discarded; PSD was then performed on the cleaned pulses.

Fig. 4.18 demonstrates the large number of instances pile-up pulses, which are generally observed as pulses exhibiting a ratio outside of the expected neutron and photon “clouds,” or ranges of tail-to-total integrals. Pile-up pulse cleaning eliminates some of the pulses above the discrimination line, but many remain. Some pulses recorded here have also been misclassified as neutrons when they are truly small pile-up pulses. Conversely, pulses classified as pile-up pulses and dis-

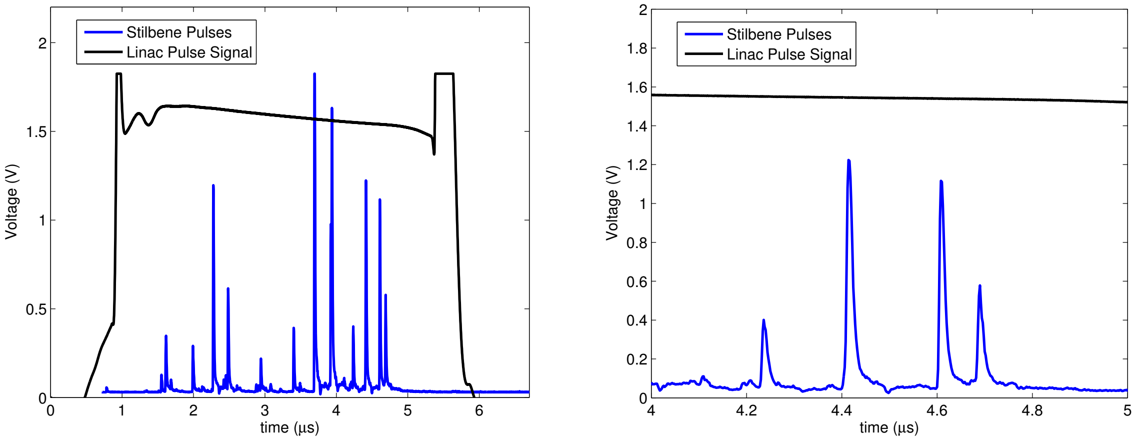

(a) (b)

Figure 4.17: Sample pulse structure with stilbene pulse train and trace of linac magnetron current (a) and the same pulse train and magnetron current trace zoomed in between 4 and 5 μs (b).

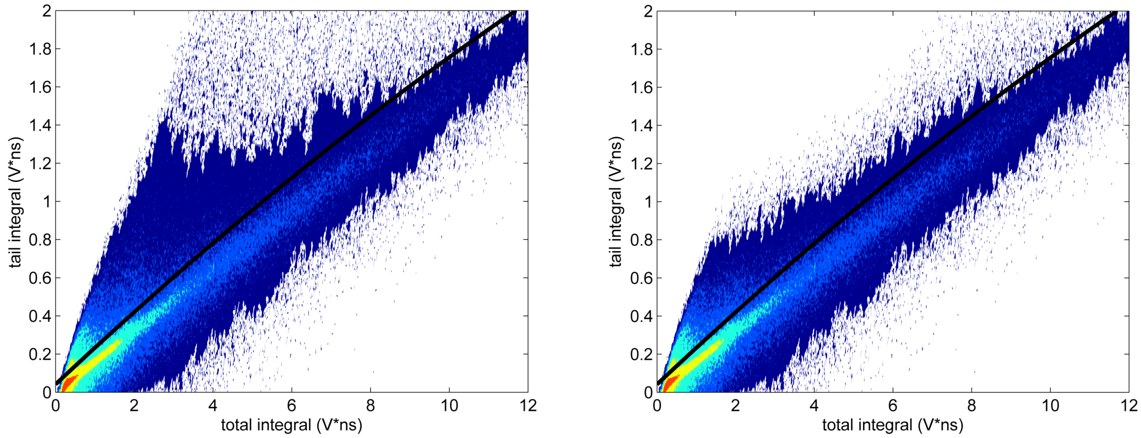

(a) (b)

Figure 4.18: 2000 cm^3 lead target interrogation PSD tail-total integral plots measured with 5.08 cm diameter × 5.08 cm diameter stilbene detector before (a) and after (b) fractional pulse height pile-up pulse cleaning. The discrimination line is shown in black, and is defined as: tail integral = -0.00227×(total integral)^2 + 0.19399×(total integral) + 0.041738.

Table 4.1: Interrogated target stilbene measured results.

Target	Photon/Neutron Ratio	Fraction of Pulses Cleaned Away	Neutrons per Second
2000 cm^3 Pb	2.12	0.578	78.4 ± 0.2
500 cm^3 W	2.13	0.575	78.9 ± 0.2
No target	2.32	0.565	75.4 ± 0.2

carded may truly be neutrons. Pulses have also been cleaned out when the signal either clips, or does not return to baseline which is likely due to a partial double pulse.

The measured results of these experiments are shown in Table 4.1. The discarded pulse fraction remains very large for all experiments, demonstrating the need for pulse recovery techniques. With the targets in the beamline a modest increase in neutron count rate is observed. This increase over the active background is much lower than the increase from a target present expected from the previously discussed ^{3}He experiments. With the same lead target, an increase in neutron count rate by a factor of approximately 3.4 is expected based on the ^{3}He data. Additionally, some difference in neutron production is expected between the lead and tungsten targets. Lead has higher photonuclear cross sections, but tungsten is denser. With the greater volume of lead, greater neutron production is expected than tungsten. The fact that the expected trends are not observed in the data in Table 4.1 is likely due to imperfect pulse collection and processing, and the high piled-up pulse fraction. While not yet providing expected neutron count rates, these stilbene measurements demonstrate the potential merits of this active interrogation signature detection method, which will be improved in the future with a neural network based PSD and pulse recovery approach.

Using PSD-capable organic scintillators to detect neutrons in a high-energy, high-flux photon environment offers a cost-effective means to detect shielded special nuclear material. However, there are many challenges that must be overcome before this method can be implemented. This work has demonstrated that laboratory conditions can be tailored to allow for experiments to demonstrate this technology with SNM-surrogate interrogation targets. These experiments have shown that these targets contribute a modest increase in detected neutrons over the active background, with aggressive double pulse cleaning. The magnitude of the increase compared to the measured increase with a ^{3}He module demonstrates the need for advanced PSD and pulse processing methods. An in-development neural network based pulse processing algorithm will allow for more efficient PSD and recovery of information from both pulses in a pile-up pulse event, which are currently both discarded.

4.4 Conclusions

We acquired a commercially available 9-MV Varian linac at the University of Michigan to enable an investigation into the use of organic scintillators with a cost-effective, widely-available, reliable, and easily operated linac photon source for secondary screening of cargo containers for hidden SNM. This cost reduction is of interest to the security community because cost of deployment is a major obstacle to screening 100% of cargo containers that enter the United States.

The design and construction of the shielding for this linac satisfied requirements for conditional operation certification. By then facilitating the installation and dose rate surveying for the accelerator, the requirements were met for research operation of the accelerator in the laboratory.

Simulations enabled predictions about detector respose through MCNP, both to the interrogated target and the active background created by the laboratory. These simulations proved useful in shielding design refinements to mitigate active background due to photoneutrons produced in the collimator and beamstop. The accuracy of these simulations was verified for neutron ABG mitigation with ^{3}He module measurements, and experimental plans were adjusted accordingly. Organic scintillator PSD performance was then evaluated in a linac interrogation environment with stilbene detection experiments, and to my knowledge demonstrate prompt photoneutron detection during a linac pulse with an organic scintillator for the first time. The confidence of photoneutron detection versus pile-up pulse detection is low however, and future work will serve to increase discrimination capabilities.

This work is the proof-of-concept for a full system implementation of a commercially available linac and organic scintillators for detection of hidden SNM in secondary cargo screening. With continued research and the on-board implementation of a neural-network algorithm for PSD and pile-up pulse recovery this system will offer an appealing, cost-effective alternative to currently-proposed cargo screening active interrogation systems.

CHAPTER 5

Improved Active Interrogation for Nonproliferation using Quasi-Monoenergetic Photon Sources

Photon active interrogation is a well-established area of active interrogation research, and offers many solutions to the shortcomings of passive detection of hidden SNM. While bremsstrahlung photon sources are reliable and readily available, other sources of photons currently in development may offer greatly improved interrogation performance. These include sources based on nuclear reactions (Section 2.1.4) and sources producing high-energy photons with Thomson scattering (Section 2.1.5). Both of these sources are quasi-monoenergetic, producing photons with low energy spread, in contrast to the broad-band bremsstrahlung sources discussed in Section 2.1.3 and Chapter 4. The discussion in this chapter is drawn in-part from [79, 80] and [24] and focuses on studies of Thomson scattering sources hereinafter referred to as MPSs, which, in addition to low energy spread, offer the additional advantages of tunable energy, narrow angular spread, and short photon pulse duration.

MPSs inherently improve on many of the source properties of broad-band bremsstrahlung sources that lead to problems for nonproliferation applications [8, 81, 82, 83]. Benefits for applications include increased specificity and reduced dose for radiography of highly attenuating materials such as shielded SNM and active interrogation to induce photonuclear reactions. The MPS sources studied in this chapter use electrons accelerated by LPAs, which is essential for nonproliferation as MPSs using traditional electron accelerators are much too large to be deployable. This chapter presents a simulated radiography proof-of-concept study validated by experiment, an investigation into shielding considerations for a Thomson-scattering photon source, and a simulated study into a specific nonproliferaton application of such a source: dry storage cask contents verification.

5.1 Radiography Proof-of-Concept

Traditional bremsstrahlung sources of photons can be used to radiograph cargo containers; however, to more effectively discriminate between high-Z materials dual- or multi-energy radiography can be employed [84, 85]. An MPS source can enable true dual-energy radiography because the photon output can be tuned to specific energies, and can even be ”interlaced” where the photons alternate between two set energies on every pulse. This section demonstrates the low-dose, high-contrast radiography capabilities of an MPS source with a shielded uranium target, and further demonstrates source advantages for radiography through simulation.

5.1.1 Simulated Image Contrast Validation

The experimental design for this radiography proof-of-concept is a uranium disc shielded on both faces by steel plates. Two arrangements were tested: a 6 mm thick uranium disk shielded by 6 mm thick steel plates, and an 8 mm thick uranium disk shielded by 40 mm steel plates. The MPS photon beam was used to radiograph the shielded uranium with a voxelated CsI detector as shown in Fig. 5.1. These experiments were performed in the Extreme Light Laboratory at the University of Nebraska-Lincoln by Chen, et. al. [79] with the electron accelerator and photon source driven by the Diocles laser system [86]. The peak power of the laser was 150 TW, and produced electrons peaked at 500 MeV. The resulting photon beam from Thomson scattering was emitted in an approximately 7 mrad (milliradian) cone, with a calculated peak energy of 6.5 MeV and a 45% FWHM energy spread [79].

The quality of the radiograph image is defined in terms of relative contrast C (Eq. 5.1) where I is the average background intensity near the object of interest and ΔI is the change in intensity

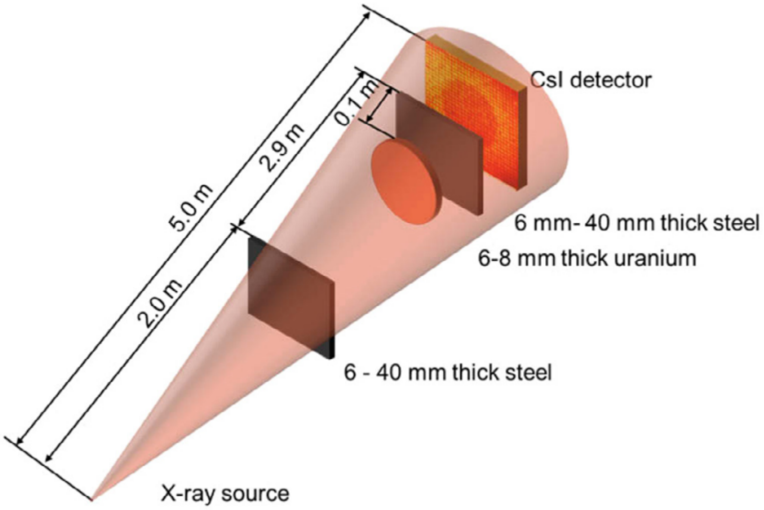

Figure 5.1: Idealized experimental setup used for shielded uranium radiography experiment. In the experiment discussed in this section the spot size of the beam was smaller that the size of the uranium disc [79].

caused by the object of interest [79]. The signal to noise ratio (SNR) is defined by Eq. 5.2 where σ_{I} is the standard deviation of the background intensity [79].

$$C = \frac{\Delta I}{I} \tag{5.1}$$

$$SNR = \frac{\Delta I}{\sigma_{\mathrm{I}}} \tag{5.2}$$

The results of the radiography experiments are shown in Fig. 5.2. The average measured intensity in an area covering 9 voxels, illustrated as black boxes on the images, was used to calculate the relative contrast. These 9-voxel averages were performed in different locations in the two cases because these images were taken with a single beam shot, aligned to the edge of the disc. This alignment is apparent because only one edge of the disc in each case is exposed.

The relative contrasts for the shielded 6 mm and 8 mm thick uranium discs are 0.39 and 0.41 respectively. The SNRs of these cases are 3 and 2 respectively. These experiments were performed with a single shot, so multiple shots would increase these SNR values and therefore the accuracy

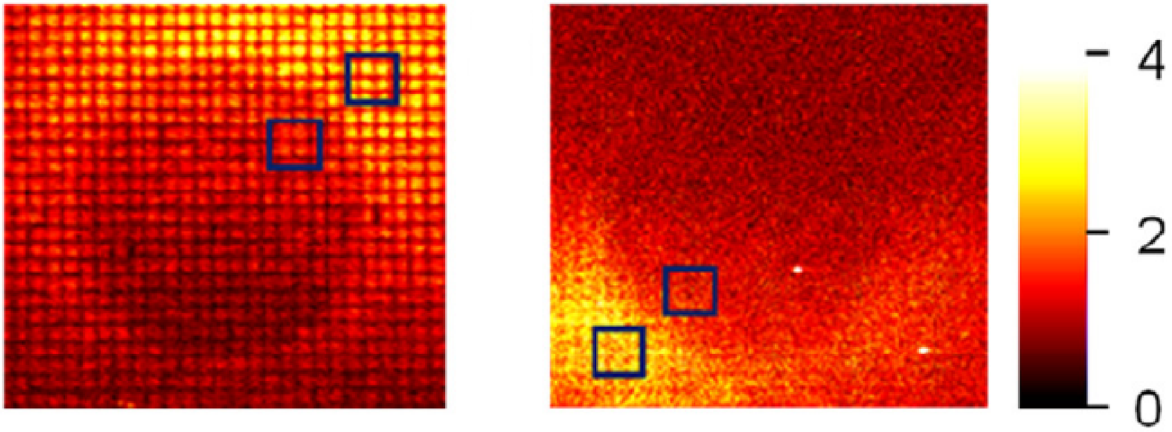

Figure 5.2: Experimental radiography image of the 6 mm steel shielded 6 mm uranium disc (left) and of the 40 mm steel shielded 8 mm uranium disc (right) [79].

of the relative contrast.

Simulated radiography images of the same shielded uranium cases were then produced with MCNPX [72], shown in Fig. 5.3. The intensity of the image was simulated with a type 1 energy deposition mesh tally voxelated in the same geometric space as the CsI detector model. The 6-mm uranium disc case resulted in a relative contrast of 0.40, and the 8-mm disc yielded a relative contrast of 0.42. The uncertainties on these values are negligible due to strong statistical certainty from the simulation of 6×10^9 source photons. The relative contrast values agree well with experimental values, and the change due to increased uranium and shielding thickness is consistent with experiment. This agreement confirms the accuracy of these simulations, and enables MCNPX simulations to be used in further studies of MPS radiography capabilities.

5.1.2 Radiography Parameter Study

Although MPS photon beams have relatively low energy spread (about 40% FWHM in current iterations) compared to bremsstrahlung, it is important to know how this spread effects radiography image quality. The impact of energy spread on image quality informs the direction of source development for future research efforts. To test the effect of energy spread, radiography test cases were simulated with different beam energy spreads and mean energies, and compared to the calculated

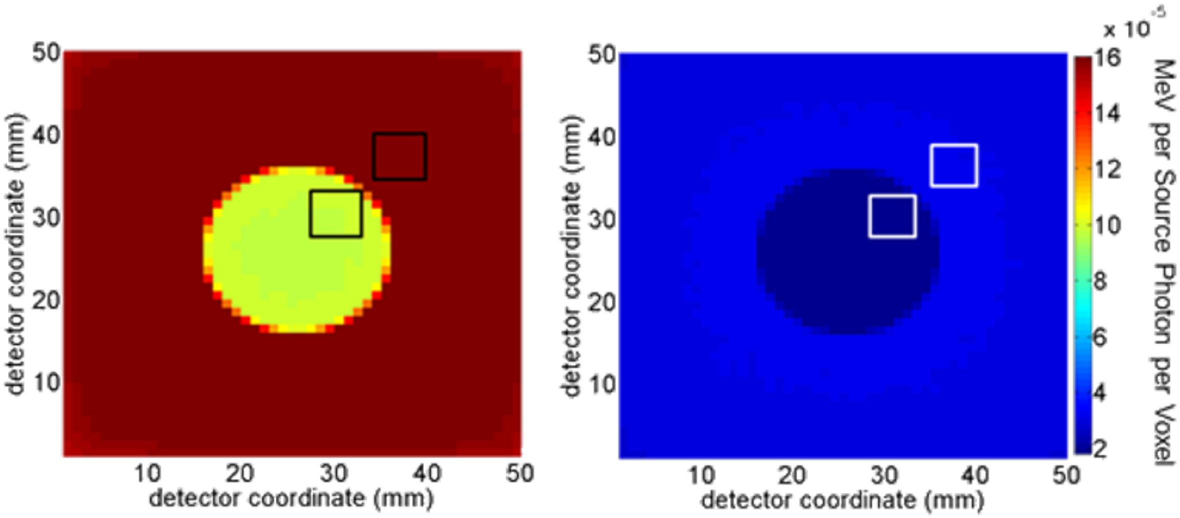

Figure 5.3: MCNPX simulated radiography of shielded 6 mm (left) and 8 mm (right) uranium discs [79].

relative contrast.

The model for these tests is shown in Fig.5.4. The 107 cm × 107 cm × 101 cm wood pallet has a cavity with a 5 × 5 × 5 cm HEU cube in the center. A 6-mm glass vacuum window between the source and the pallet is accounted for. A $CdWO_4$ detector is modeled with 1.5-cm thickness. $CdWO_4$ is a common detector for cargo container radiography, and it is voxellated in the simulation to produce a radiographic image. The simulation space is filled with air to account for air-scatter effects. The simulated source of photons had energy of either 6 or 9 MeV, with both energies simulated with either 10% or 40% FWHM energy spread.

The 2-D midplane cross sections of the radiographs is shown in Fig. 5.5. By comparing the radiographs with each beam energy, it was observed that energy spread had little effect. The image cross sections are nearly the same for 10% or 40% FWHM. The photon beams with the larger FWHM showed a transmission ratio of about 1% greater. This small 1% effect showed that the current capabilities Thomson photon source energy spread are sufficient for providing the advantages of monoenergetic photon radiography over broadband radiography.

This simulation can also inform the photon flux required for radiography. The required photon source flux for scanning a cargo container depends on many parameters they may change from

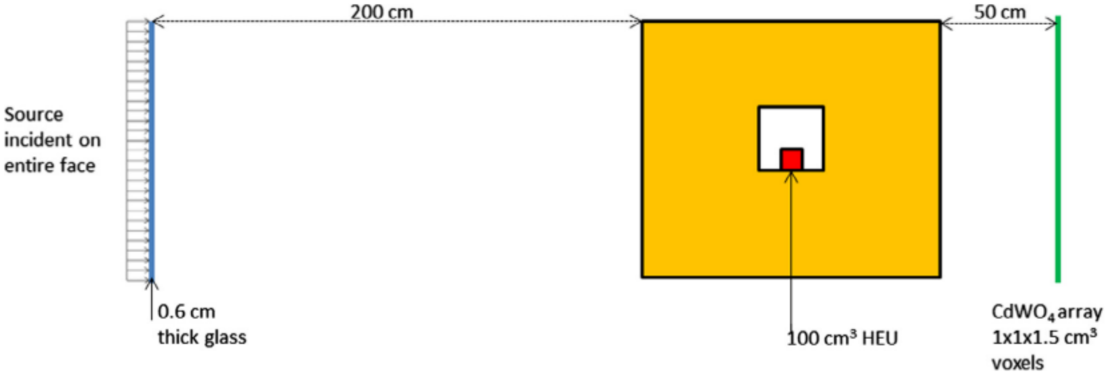

Figure 5.4: Simulation geometry for wood pallet test cases irradiated by a photon beam transmitted through a glass window, the HEU-containing pallet, and detected by a $CdWO_4$ detector 50 cm after the pallet [79].

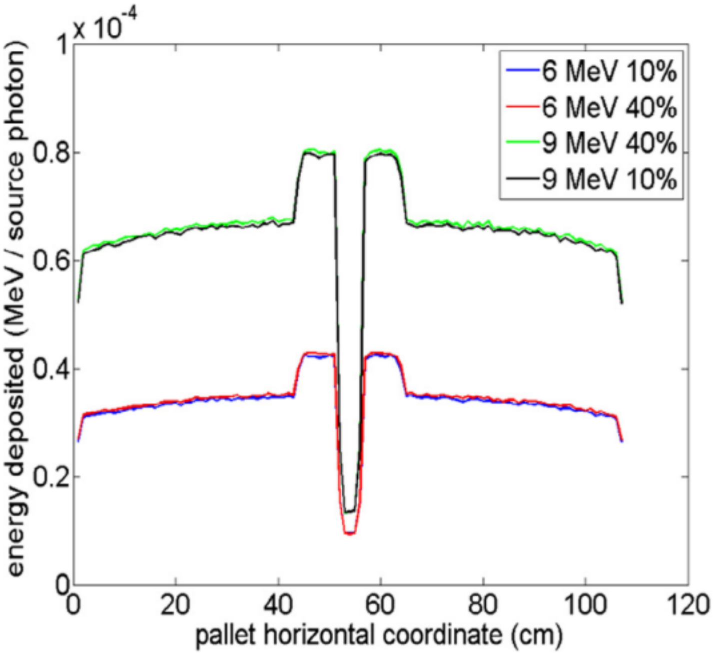

Figure 5.5: Cross sections of the energy deposited in the detector at the mid-plane of the pallet, for all source parameter combinations [79].

port to port. Materials, scan rate, detector efficiency, and distance can all affect the requirements. The wooden pallet is treated as a typical cargo composition, with a high-Z item of interest. The adopted metric was that photons must deposit 10 MeV on a detector area of 1 cm^2 to form a reliable radiograph [87]. It was found that 10^5 photon/cm^2 are required to form a radiograph with an MPS for the example wooden pallet, because the the ratio of energy deposited in the detector to the source photon energy is 10^{-4}. A typical cargo container is 2 m tall, and assuming a scan speed of 100 cm/s, a photon output of 10^9 photons per second is needed to radiograph the container in a reasonable time.

An important advantage offered by a narrow bandwidth MPS is that the photons produced are of higher value for image quality per dose imparted. Bremsstrahlung photons are much more likely to be emitted at low energies (less than about 1 MeV), and these photons impart dose but contribute little to the radiographic image of a dense or thick object. To compare imparted dose for different sources, the absolute dose to the target was measured as a function of energy deposited on the detector, an indicator of image quality.

Figure 5.6 shows that a 6 MeV, 40% FWHM MPS imparts half the dose on-target per energy deposited for the radiograph compared to a 6 MeV endpoint energy bremsstrahlung source. This reduction was also observed for a similar comparison with 9 MeV photon sources. Using the same energy deposition comparison, the dose was simulated 1 m from the pallet edge, to estimate the dose to a bystander. For this off-axis configuration, the dose reduction for using a narrowband source was found to be a factor of 10. The narrowband source is therefore more effective at screening cargo while following as low as is reasonably achievable (ALARA) principles [74].

The low spatial divergence of an MPS beam also allows for better standoff energy delivery. A bremsstrahlung source is assumed to produce 10^{14} photons/s [17] in a 60 degree half-angle cone beam. The photon flux is therefore 3.2×10^{13}/s/sr. A reasonably achievable MPS source pulsing 10^7 photons/shot at 10 Hz with a 4 mrad divergence angle could produce a photon flux of 8×10^{12}/s/sr. Accounting for the narrow energy spread as well, the MPS should have higher photon flux in the high MeV range than a bremsstrahlung source. Continuing development of MPSs will make these

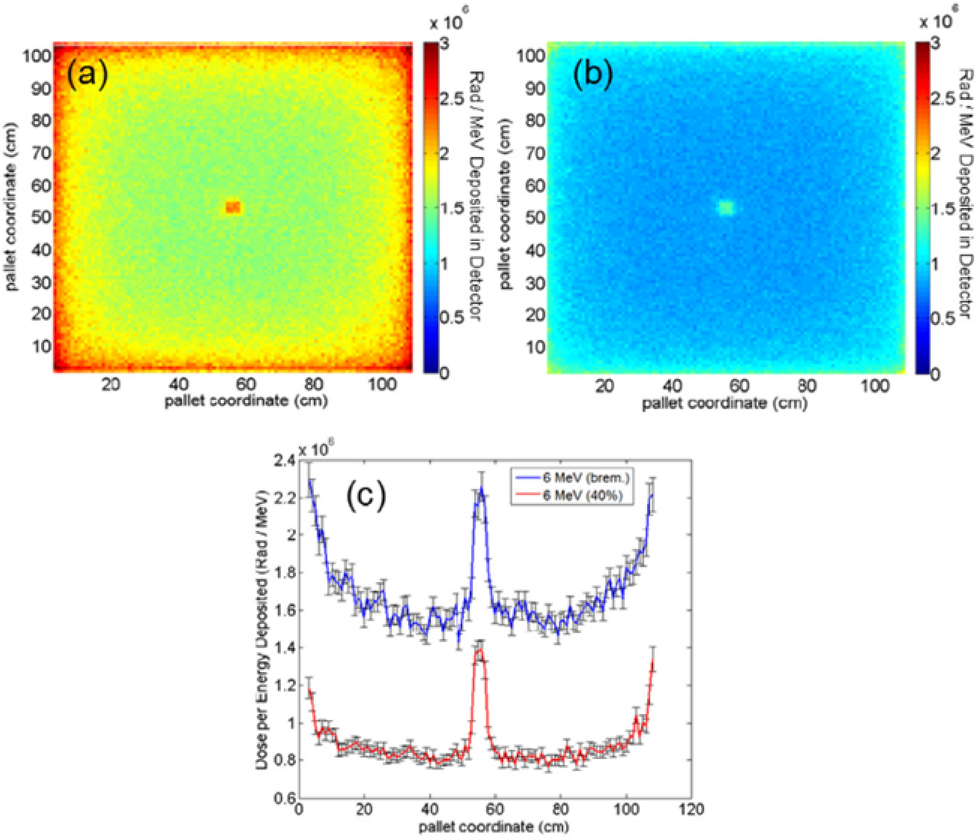

Figure 5.6: MCNPX simulation of the dose dielivered to the target as a function of energy deposited for the radiographic image. Dose delivered per energy deposited by a 6 MeV bremsstrahlung source (a) and a 6 MeV narrowband source (b). Cross sections of the dose per energy deposition maps (c). Simulation statistical uncertainty is shown by the errorbars [79].

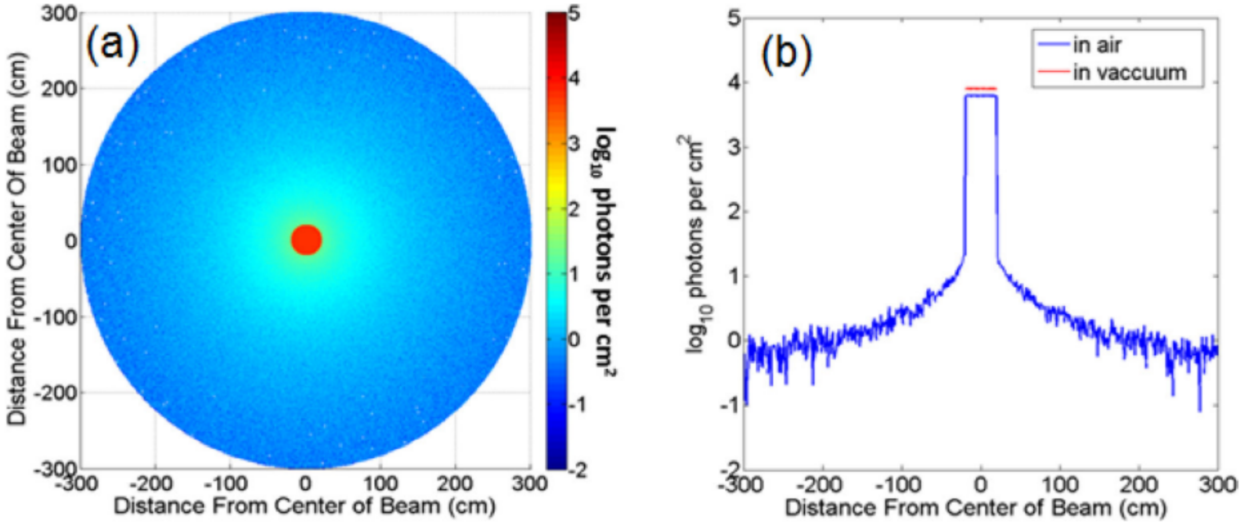

Figure 5.7: Simulated of 100 m photon propagation in air. Photon flux from one pulse of the narrowband source. The unscattered photon flux is shown by the high central concentration (a). Two-dimensional lineout of the photon flux. The beam concentration without air-scattering is shown by the red line (b) [79].

sources even more competitive with bremsstrahlung sources.

The long-standoff propagation of a 9-MeV, 10% FWHM narrowband photon beam was simulated, and scaled to 1×10^7 photons per pulse, with a 10 Hz repetition rate. The propagation of this beam was then simulated through a 100-m long by 3-m radius cylindrical column of air. The beam opening angle was onformed by measurement, and simulated as 2 mrad half-angle. Fig. 5.7 shows the flux tallied 100 m from the source. The beam is concentrated in a 20 cm diameter around the origin, as expected, 18.5% of the beam scattered out of this central diameter. Fig. 5.8 shows the softening of the simulated photon spectrum along this 100-m fight path. The high-energy portion of the spectrum is reduced, while the low-energy portion increases due to elastic scattering, annihilation photons, and molecular excitations.

The performance of an MPS source for shielded radiography was studied with these simulations validated by experiment. Simulations with MCNPX demonstrated that a narrowband photon source with 40% FWHM energy spread reduces imparted dose significantly versus a bremsstrahlung source, both to the target and to bystanders. However, the bystander dose reduction was not as significant as expected from other studies [88, 89]. Capabilities for standoff radiography and material

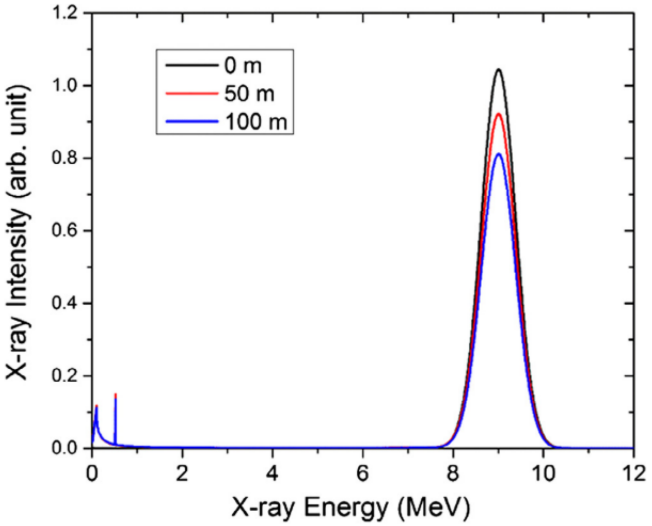

Figure 5.8: Energy spectrum of a 9-MeV, 10% FWHM narrowband beam as is propagates through air. The black line shows the emitted spectrum [79].

identification through dual-energy interrogation were also demonstrated. The combination of these advantages with current research into increasing the source strength and reducing the footprint of LPA based MPS sources offers great promise for shielded radiography applications.

5.2 Laboratory Shielding Considerations

The use of an LPA to accelerate the electrons needed for an MPS source allows these sources to be built in a compact form factor [25], meaning they can be studied in a laboratory setting. An LPA can accelerate electrons to the 200-500 MeV energies that are required to produce 1-9 MeV photons for nonproliferation applications [27, 90, 29, 91, 92]. However, after interacting with the photons these electrons must be disposed of safely.

When these 0.5-GeV electrons are bent away from the beamline and dumped into a shield, a large number of secondary particles are created [93]. Note that in the longer term, plasma deceleration is being developed to substantially reduce the dumped beam energy [94]. This technique will be important for applications but will not be available for first experiments. The secondary particles pose problems by both obscuring measured signals from the source photons and by imparting dose to the surrounding areas. Reducing the effects of secondary particle background is important for initial laboratory experiments and future nonproliferation applications.

Dose delivery is limited in initial experiments by source capability, but future nonproliferation applications will require higher flux and hence more robust shielding for dose control. An LPA based Thomson scattering MPS is under development at the Lawrence Berkeley National Laboratory that will test concepts for LPA-based MPSs at few-Hz repetition rates, including tests of electron beam deceleration. This source will also be used to establish techniques for scaling such a source to the kHz repetition rates needed to satisfy application flux requirements.

This section discusses the design of shielding scenarios optimized for the mitigation of electron-induced background for both upcoming laboratory tests and future kHz-scale application relevant sources. In the laboratory setting, a beamstop has been designed with protruding collimators to contain the resulting secondary particle flux while allowing for changes in beam direction during experimental optimization. Limiting the effect of the electron-induced background will allow for experiments demonstrating the benefits of MPSs for nonproliferation applications, including detection of signature neutrons and photons with PSD capable organic scintillators [38, 39]. For future kHz-rate sources intended to address applications, a fixed tungsten beamstop with a channel to catch the electrons was designed. In the latter case, plasma deceleration has also been considered to represent a realistic potential applications scenario. A high performance, compact combination of plasma electron deceleration and shielding will be important to allow for safe use of a mobile source for nonproliferation operations in the field. In both cases, an extra layer of low atomic number neutron shielding was used to reduce the number of photoneutrons emitted.

MCNPX 2.7.0 [72] and MCNP6 1.0 [66] were used for a simulation study of the shielding design. An 8-MeV photon beam is simulated with a 30% FWHM, which requires electrons accelerated to 500 MeV. This energy was chosen because it is close to the maximum anticipated for nonproliferation applications [82], hence representing a realistic worst-case shielding scenario. The 8 MeV photon energy also lies at a point in SNM cross sections where photonuclear reactions are somewhat likely to be induced, and there is a strong transmission contrast between SNM and possible shielding materials such as concrete and steel [95, 96, 78]. The 8-MeV spectrum is shown in Fig. 2.5, illustrating the advantage in energy concentration over broadband sources. The 500-MeV electrons are bent out of the beamline by an electromagnet at an angle of 18 degrees into a beamstop whose design was part of this study, while the photons proceed in the forward direction with an opening half-angle of 1.75 mrad. These parameters are derived from realistic photon source simulations [25]. The electron-induced background and signal resulting from the photon beam were simulated separately to limit computational requirements. A 20 cm × 10 cm × 5 cm lead brick is simulated 7 m downstream from the shielding to act as an SNM surrogate for initial possible experiments. This target is a limiting case, as the signal will increase if SNM is available for later experiments.

The high-energy electrons resulting from the accelerator source release energy in the form of photons as they are slowed down or their direction is altered [9]. The electron beam is affected by laboratory components in several different areas resulting in these energy releases.

The most significant laboratory component contributor to background is the heavy-metal beamstop, which limits the range of the electrons in the lab space. The electrons release their energy through bremsstrahlung which abruptly slows down the particles, and causes a release of photons up to the initial energy of the electrons [97]. Because the beamstop is constructed of a high atomic number material, the cross sections for this reaction are high. With electrons of this energy, the emission of bremsstrahlung photons is somewhat forward directed with respect to the electron beam direction, but photons are still emitted in all directions [97].

A second bremsstrahlung interaction that produces secondary photons occurs where the electrons pass through the vacuum window of the accelerator system. This interaction point is a less significant contributor than the secondary photon flux created in the beamstop because the window material is very thin and of lower atomic number than the beamstop. This fact reduces the probability for photon production, but it still considered in the shielding design.

Low-energy photons are also produced in the form of synchrotron radiation [5] where the electrons are accelerated, and again where an electromagnet bends the electrons out of the beam

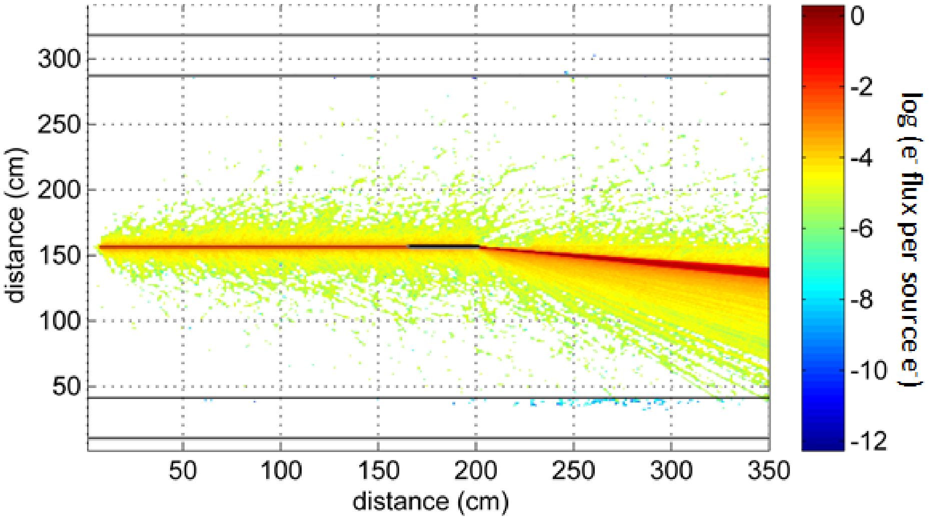

Figure 5.9: Electron flux showing electrons bent out of the beamline by the 1.25 T electromagnet.

path. The electron bend is shown in Fig. 5.9. These photons are produced due to the transverse acceleration, rather than bremsstrahlung. However, these 0.2 keV to 5 keV [98, 99] average energy photons are shielded by the vacuum enclosure and can therefore be neglected when designing shielding.

The photons in the active background also produce neutrons through photonuclear interactions. These photoneutrons are predominantly created in the beamstop and subsequent photon shielding because high-energy photons efficiently produce photoneutrons in high atomic number materials. These photoneutrons must be considered in the shielding design, which introduces the challenge that photons and neutrons must be shielded with very different materials.

All of these effects are common to both the laboratory demonstration and mobile design for nonproliferation applications. Because the mobile design will allow for source design optimization to minimize the effects of the vacuum window radiation production only the dominant effect of the main electron beam disposal was analyzed for that case.

Shielding has been designed to allow for safe operation and reliable results for both laboratory demonstration experiments and a future higher repetition-rate mobile system. The demonstration system is being implemented at Lawrence Berkeley National Laboratory, while the mobile design is dependent on further source development and the results from the demonstration system.

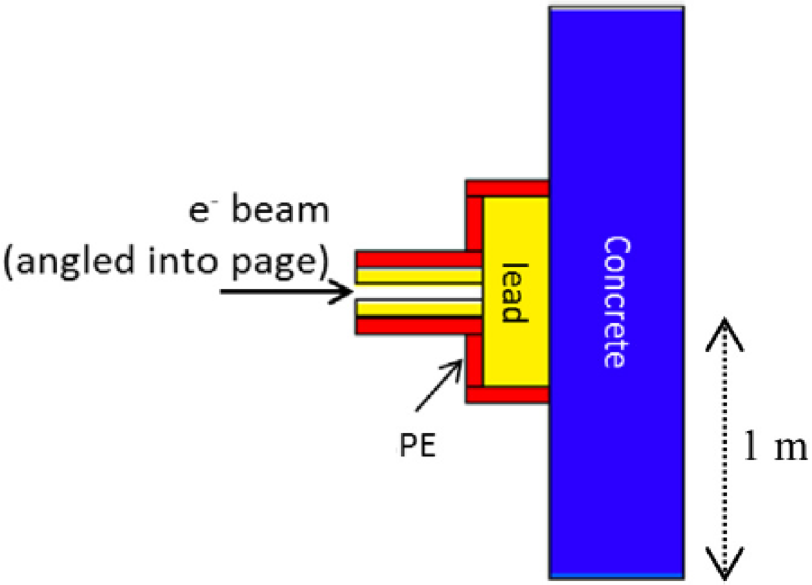

Figure 5.10: LBNL MPS beamstop design. Concrete backed lead wall with polyethylene lining.

To allow for experiments in the laboratory containing the MPS target area, shielding was developed not only for personnel protection but also to allow for efficient detection of radiation signatures induced in a target. This design is challenging, especially with respect to experimental background mitigation, due to space constraints and previously discussed sources of active background.

A concrete wall was initially designed as a beam dump to be sufficient for personnel protection. To further mitigate background for nonproliferation experiments, a 20 cm thick wall of lead bricks was added proceeding and structurally supported by the concrete. Bremsstrahlung photons up to the electron energy are produced in the lead. These high energy photons are then capable of creating neutrons through photonuclear reactions. Through simulating a flux map of the laboratory, the particles in the electron interaction location were shown to be emitted in all directions, resulting in a high scattered flux throughout the room. The 20 cm lead thickness was chosen to effectively limit through-wall flux, where particles emitted from the electron interaction point on the beamstop become dominant.

A fin collimator is used, (shown in Fig. 5.10), to address photons emitted from the electron interaction point. While a bored tube collimator would shield most effectively, it would not allow for variation of beam energy and the resulting change in bend angle. The design of the fins was iterated along with thickness of the lead wall until the limiting factor became the photons exiting back through the fin aperture, which cannot be shielded while allowing for experimental flexibility.

The fins must be about 5 cm wide to fit the full beam width, and can only be 38 cm long due to other beam components. The optimal fin configuration was determined to be 5 cm of lead, with a 5 cm thick lining of polyethylene both around the lead fins and the lead beamstop. Increasing the thickness of lead or PE had minimal effects when compared to overall scatter in the room. Using BPE reduces the neutron flux by about 12%, but it greatly increases cost. Using a coating of a lower atomic number material than lead for the beamstop was also examined, but was shown to be ineffective for electrons of such high energy. Using this design, the fins reduce flux in the laboratory to the point where background from photons leaving the fin aperture and scattering around the laboratory dominates, and any increase in fin shielding thickness has minimal effect.

With this design, the flux maps of secondary photons and neutrons resulting from the dumped electrons are shown in Fig. 5.11. There is a large flux of photons created where the electrons interact with the lead, but these photons are shielded in the forward direction by the lead and concrete and in the reverse are effectively collimated by the fins.

While the neutrons are not effectively shielded by high-Z material, and easily penetrate the lead portion of the beamstop, shielding is provided by the polyethylene layer. There are also fewer neutrons than photons initially emitted. For both particle types, the fins reduce the probability of scattering into the proposed detection area on the right side of the lab, (near 650 cm horizontally and 50 cm vertically in Fig. 5.11).

A comparison of the secondary particle flux on the plane of the target in the room with and without the additional fins is shown in Fig. 5.12. With the fins installed on the beamstop, the secondary photon flux is much more contained to the vertical plane of the electron beam. The probability of these photons scattering into the experimental area is greatly reduced compared to the case with no fins.

The photon beam was simulated incident on the lead brick target to demonstrate the relationship

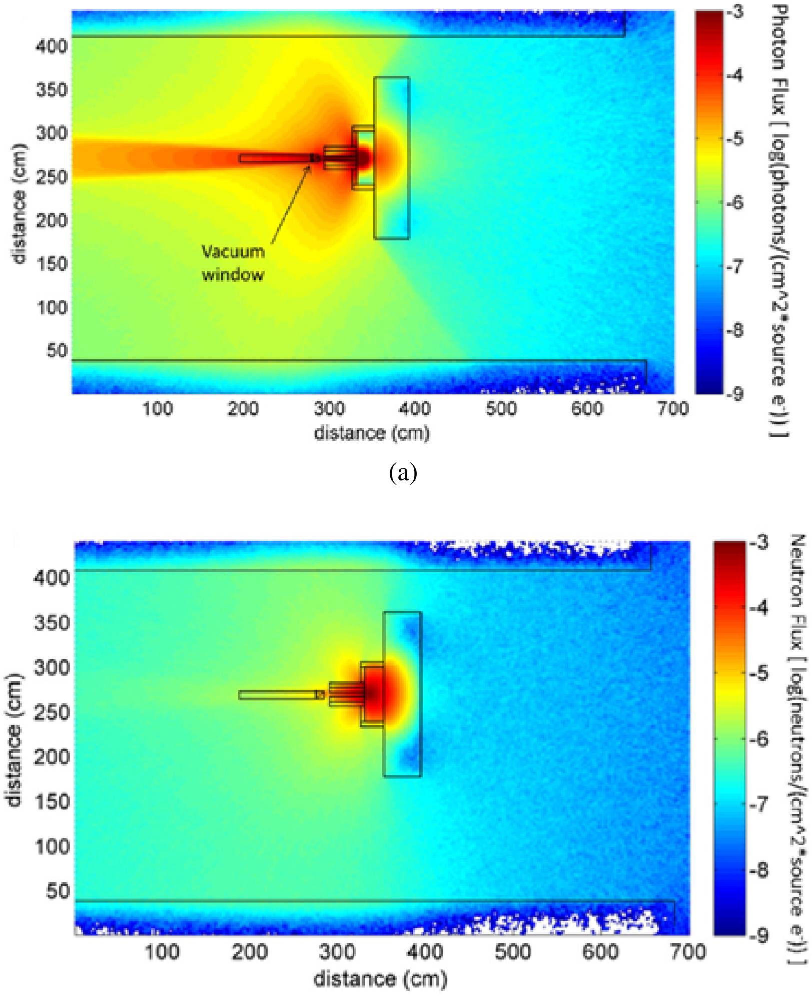

(a)

(b)

Figure 5.11: Particle flux in accelerator laboratory space at the horizontal plane where the electrons impact the lead shielding for photons (a) and neutrons (b). Effects of electron interaction with the vacuum window are included.

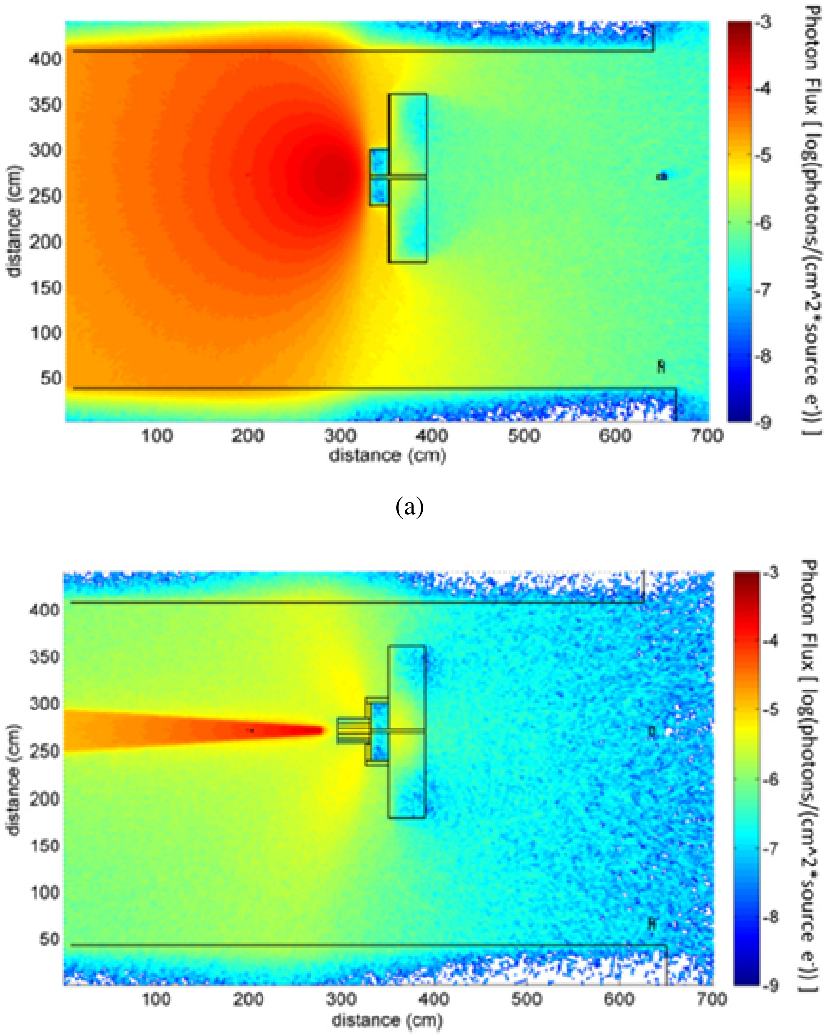

(a)

(b)

Figure 5.12: Electron-induced photon flux in accelerator laboratory space at the horizontal plane of the photon target without shielding fins (a) and with fins (b). Vacuum window effects are not included in this case.

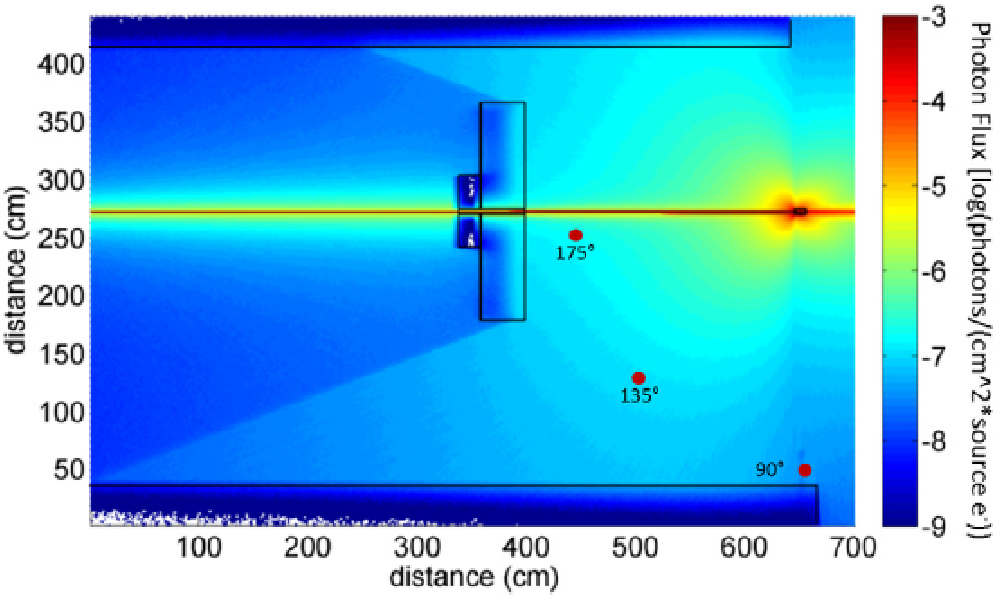

Figure 5.13: Photon flux due to the MPS photon beam incident on the SNM surrogate. The beam is very tightly focused, contributing few photons to the environment until collision with the target. Point detectors are shown as red dots, with additional detectors at 45 and 0 degrees not shown in this figure.

between the electron-induced background and the signal induced by the source. As shown in Fig. 5.13, the photon beam anticipated from upcoming experiments [25] is highly collimated, with most of the induced photons resulting from interactions in the target. In the photon beam, the photon beam flux is much higher than that from electron induced background, which will provide good signal-to-noise for detectors assessing MPS performance.

For a full picture of signal to background effects throughout the room, detectors were simulated 2.6 m from the target at various angles with respect to the beam direction on the horizontal plane of the photon beam. These detector locations are represented in Fig. 5.13. The resulting flux values, assuming 10^8 photons per MPS pulse, are shown in Table 5.1. The signal photon flux is greater than the flux of secondary photons created by dumped electrons. Due to the spatial and energy concentration of the MPS beam, even the on axis signal transmitted through the 20 cm thick lead target shown in Fig. 5.13 is more than fifty times the background level, indicating the ability to assess performance for thick targets. Note that these calculations do not include the effects of electron deceleration in the plasma structure, which is expected to further increase

Table 5.1: Particle flux at different locations through laboratory, resulting from electron induced background and photon beam.

Angle clockwise from beam direction (degrees)	**Electron induced background (particles per [cm^2 MPS pulse]**		**Photon induced signal (particles per [cm^2 MPS pulse]**	
	Neutron	**Photon**	**Neutron**	**Photon**
0	1.3	3.3	0.4	226.4
45	1.5	3.9	0.6	67.2
90	0.8	1.1	0.7	65.3
135	9.4	24.6	1.3	211.5
175	8.1	30.2	0.02	291.8

signal to background levels. The particle flux off axis is of a similar order to the electron-induced background which will be further mitigated with local detector shielding and pulse vetoing as appropriate during experiments.

5.2.1 Mobile Shield Design

A mobile beamstop has been designed for potential future in-the-field nonproliferation measurements. Such measurements will require multi-kHz operation, three or more orders of magnitude greater than the laboratory setup described above. This source strength would require a very large beam dump mass if the full electron energy were incident on the beam dump. This very large mass requirement makes clear the need to use the plasma to decelerate the electron beam after photon production [25]. Here, the beamstop required for such a source, accounting for active plasma beam dump electron deceleration, has been evaluated. The active plasma beam dump has been simulated to allow for 90% of electrons to be decelerated to $<$10% initial energy [94]. The deceleration of the electrons to be dumped allows for a large reduction in beamstop size. We have assumed that the system will have the ability to trip in the case of a plasma deceleration failure. The short pulse, high repetition rate nature of the source means that one full energy pulse contributes very little increase to the overall dose rate. Therefore, the trip-on-failure assumption eliminates the need to consider additional shielding for full energy electrons at high repetition rate in the case of a failure.

The tested mobile scenario is motivated by cargo screening, cask scanning, and other applications where previous work [82] has demonstrated the need for a source producing 10^{12} photons per second for timely operation. This requirement can be achieved with a source producing 10^{8} photons per pulse with a 10 kHz repetition rate, which is in the range of future source development. With long term development, it is expected that 10 total photons can be produced per electron [100]. The photons within a prescribed energy range are approximately proportional to that energy range, i.e., if 10 total photons are produced, but 30% energy range is required, 3 photons are produced in that energy range. For this study, it is assumed that 10% of electrons will produce a photon within the 8 MeV, 30% FWHM required spectrum. This conversion rate was adopted as a conservative value, based on personal correspondence with C.G.R. Geddes about near term expectations. For the 10^{12} photons per second requirement of this study, 10^{13} electrons per second must be dumped into the beamstop.

The beamstop was designed to be as compact as possible, while limiting dose rates to less than occupational limits of 2 mrem per hour [74]. The simulated beamstop is a 1.2 m diameter × 1.2 m tungsten cylinder with a 5.08 cm diameter × 70 cm bore for the electrons to enter. Tungsten was chosen as the beamstop material because it offers an optimal combination of density and atomic number for photon attenuation among widely available materials. The tungsten cylinder is coated with 10 cm of BPE for neutron shielding.

The mobile beamdump design has been simulated to show that 500-MeV electrons decelerated by about 90%, as in [94], yield photon dose rates less than a conservative limit of 1 mrem/h on the surface of the beamdump aside from the bore location, as shown in Fig. 5.14. The high radiation area created by the bore will either be additionally shielded by a backstop of similar thickness or access will be restricted to that area. Using current design parameters for sources under development this design provides a concept that allows for a high-flux kHz-class MPS to be operated in the field safely with compact shielding.

This compact beamdump design has been simulated to show that the electrons resulting from

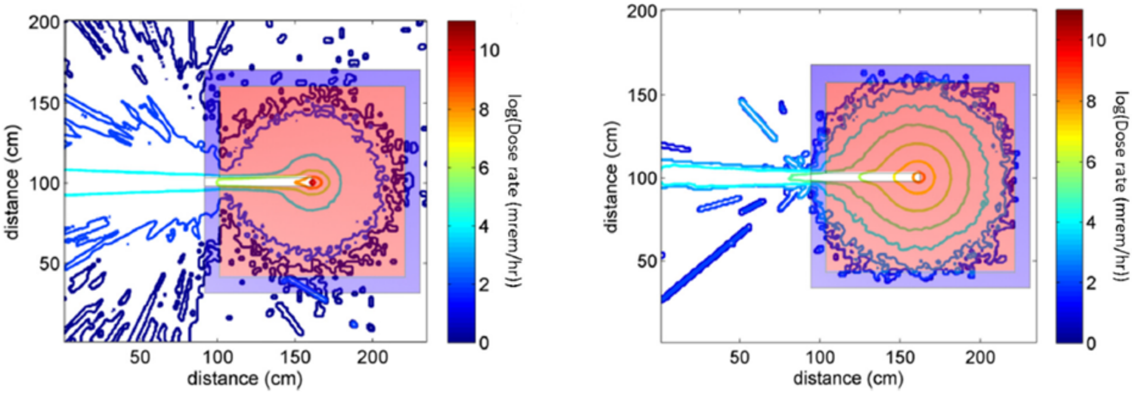

(a) (b)

Figure 5.14: Photon dose (a) and neutron dose (b) with 1.2 m diameter cylindrical mobile beamstop, 5.08 cm bore. Tungsten cylinder in red shaded area with BPE coating in blue.

a high-flux MPS can be disposed of in a manner that allows for safe field operation. The beamstop mass is still significant at 26 metric tons. Future source development to increase photon production efficiency and improve deceleration [25], along with exclusion areas during operation, may further reduce the size simulated here.

5.2.2 Shielding Conclusions

Shielding was designed to allow safe and effective use of MPSs both in laboratory based experiments for capability demonstrations, and a mobile scenario with nonproliferation applications. These designs considered the unique active background created by an MPS, and offer solutions to mitigate it. The effects of advanced plasma deceleration were also characterized in a nonproliferation context.

In the laboratory setting, a beamstop and radiation containment system was designed so that the photon flux resulting from the source signal is greater than the electron-induced background flux. The signal through a thick lead target is also many orders of magnitude greater than the active background; however, the neutron active background flux is greater than the induced signal. The laboratory shielding design has eliminated the unwanted background as much as is practical, and with minimal neutron shielding for the detectors it will therefore be possible to detect photonuclear signals from small amounts of high-Z material.

The simulated mobile design has shown a compact shielding configuration that will allow for safe operation of an MPS in the field with a photon flux suitable for many nonproliferation applications. Plasma deceleration is important for this system to achieve the necessary flux, and further advances in that technology will lead to greater reductions in beamstop mass.

This work will allow for an MPS to be used to demonstrate its advantages over traditional interrogation sources in nonproliferation. With the successful demonstration of these advantages, the mobile beamdump design described here will allow for field operation of an MPS source tailored for specific nuclear nonproliferation applications.

5.3 Dry Storage Cask Contents Verification

Nonproliferation applications that would benefit from the use of an MPS were studied through a large collaborative effort [82]. In the area of safeguards the verification of spent fuel dry-storage casks was identified as a specific application where the use of an MPS could make a large impact. In this section, sourced from [24], I discuss transmission measurements with a pulsed, narrow-divergence 'pencil' beam of monoenergetic photons as a viable approach for verifying the presence of assemblies by mapping out the transmission across the cask. A modeling study was conducted to evaluate various photon source parameters including energy spectrum, angular divergence, and pulse structure. It was found that high intensity, small divergence (several mrad), and short pulse duration are all important photon beam properties to enable practical measurement. A variety of scanning concepts were evaluated including end-on access and transverse access with several arrangements of the scanning beam.

Verification of the contents of spent fuel dry-storage casks without opening the cask is a particularly important safeguards measurement to identify and deter diversion of nuclear material, for which there is currently no solution available [82, 101]. Dry-storage casks typically have thick steel walls or large concrete overpacks and hold tens of fuel assemblies. These casks are controlled using seals and observation to maintain continuity of knowledge (CoK) to ensure that all of the fuel is in place; however, there are cases that require reestablishment of inventory after loss of CoK [101].

The International Atomic Energy Agency (IAEA) is actively pursuing methods to reduce the complexity of re-verification of light-water reactor (LWR) spent fuel stored in dry casks [102]. The goal is to periodically re-verify the contents of fuel casks to ensure that an assembly has not been removed. Previously, the Idaho National Laboratory Compton Dry-Cask Imaging Scanner (CDCIS) was developed that scans the gamma-ray emissions across the top of the cask [103]. This instrument's ability to detect empty versus full storage positions in the cask was demonstrated on a Westinghouse MC-10 cask [104]. However, the scanner was not able to distinguish empty versus full positions for casks when an additional thick steel shield was in place over the lid of a similar cask for ballistic shielding. A cosmic ray muon computed tomography imaging system is under development [105, 106]. Exposures require long dwell times on the order of tens of hours and research on the viability of this method is still in progress.

This section will cover a study on penetrating thick objects with photons, a demonstration of the capabilities of Thomson scattering MPSs for detecting shielded nuclear material in fuel casks.

5.3.1 Thick Object Photon Transmission Study

Transmission measurements through thick shielding and massive objects are very challenging due to both high attenuation that can be many orders of magnitude, and scattering, which can blur the desired signals by 'mixing' photons between adjacent detector elements. Dry storage casks are thicker than many other objects of interest, such as cargo containers or treaty items, due to the large number of spent fuel assemblies. An added challenge is posed by the intense passive 'background' from the highly radioactive spent fuel.

Attenuation is the first challenge to be addressed. The use of an MPS enables the production of the most suitable photon energies where the attenuation in steel, concrete and nuclear fuel is near the minimum. The energy selection maximizes transmission and avoids unnecessary radia-

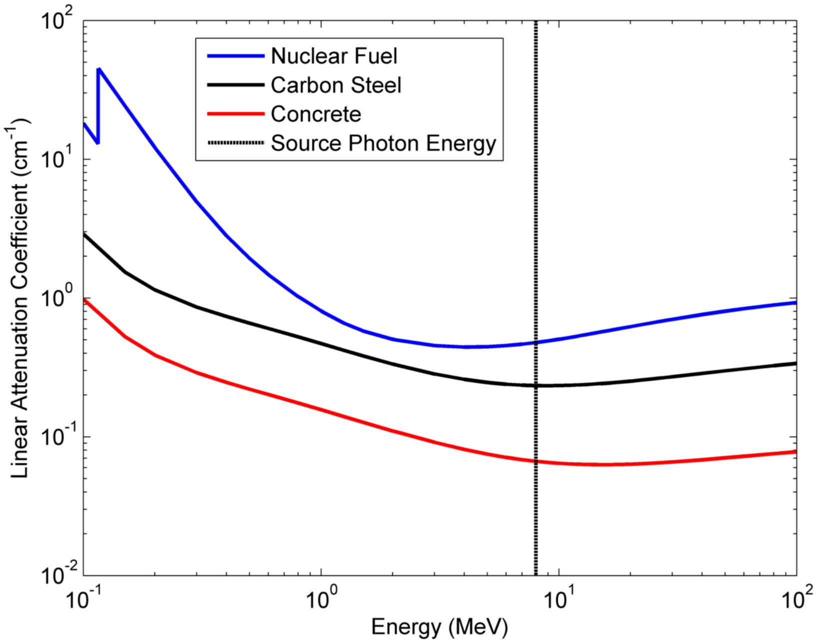

Figure 5.15: Linear attenuation coefficients for materials in cask transmission calculations [107, 108].

tion dose to the surroundings from scattered low-energy photons. Fig. 5.15 shows that the energy can be chosen to both maximize transmission and material contrast. The transmission contrast between steel and uranium has been demonstrated previously with an MPS in a laboratory setting [79], which showed agreement with MCNPX Monte Carlo [72] simulations. For a cask scanning application, 8 MeV was chosen to be near the minimum attenuation value and also to provide a strong transmission contrast between materials of interest. The materials studied here are representative [103, 104] fuel cask materials: A36 carbon steel [107], 4% enriched uranium dioxide nuclear fuel [108], and blended concrete [108] with barium and iron contents of 8.8% and 21.0%, respectively.

The transmission through typical cask shielding is on the order of 10^{-6}-10^{-8} and transmission is further reduced when fuel assemblies are penetrated. An additional ballistic shield that prohibits passive detection as in [103] would reduce transmission by less than an order of magnitude and is not expected to affect MPS transmission results. These values will be outlined later in the discussion. This study was based on the MC-10 and Holtec HI-STORM casks [104, 109], both loaded with pressurized water reactor (PWR) assemblies [110].

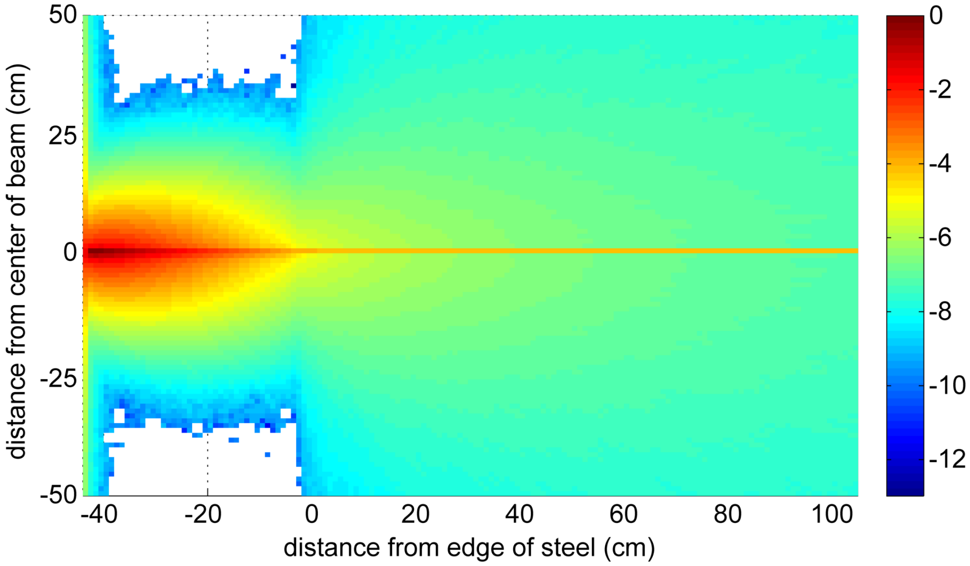

Figure 5.16: 2-D flux map in a plane through the beam axis for a 9 MeV monoenergetic photon beam penetrating 40 cm of steel.

Scattering is a significant contributor to image quality degradation in cargo radiography [111] and is even more severe for very thick objects such as fuel casks, in many cases limiting measurement. In order to investigate the energy spectrum effect of scattering on a photon beam, the propagation of pencil beams (i.e., a mono-directional beam with no spatial extent) with 9 MeV monoenergetic and 9 MeV endpoint bremsstrahlung energy spectra were modeled through steel plates. The simulated photons were transmitted through 40 cm thick steel with MCNPX, and the transmitted flux profiles are shown for the monoenergetic case in Figs. 5.16 and 5.17. The beam is heavily attenuated by the steel, and photons are scattered out of the beam into the steel. The distribution at the downstream edge of the steel (located at d = 0 cm in the fluence map) shows a significant portion of the photons in the beam are scattered out of the beamline. At a modest distance of 100 cm from the steel however, the scattered flux surrounding the unscattered core is low: approximately three orders of magnitude below the transmitted beam intensity. This low scattered flux fraction demonstrates that a transmission image can be generated by scanning with a narrow divergence beam and detecting the transmitted beam photons with an appropriately sized detector.

The narrowness of the beam divergence requirement is set by the desired scanning resolution, since beam size at the target is defined by divergence and distance from the source. For cask

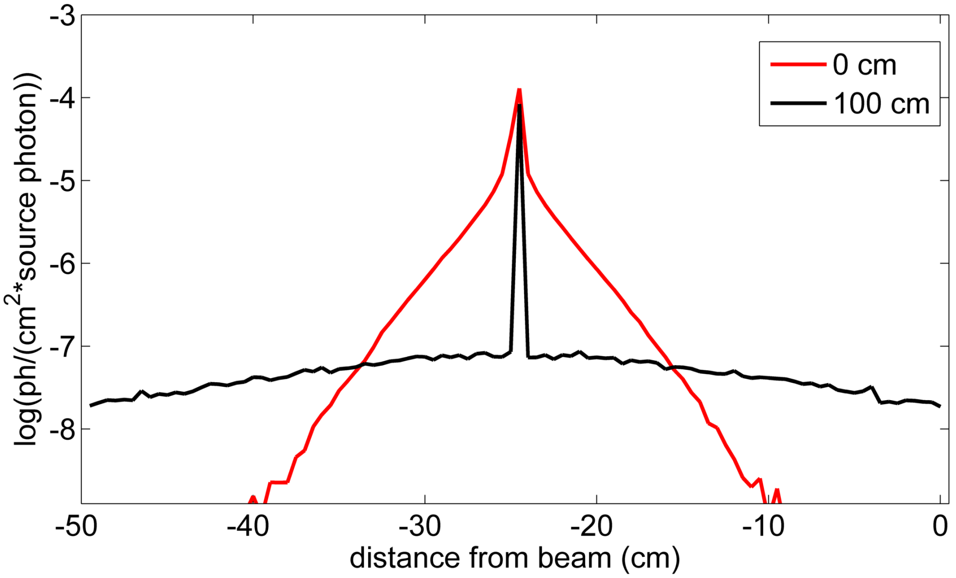

Figure 5.17: Flux measured in row of voxels shown by dashed lines in the 2-D flux map at the exit of the steel slab (0 cm) and 100 cm downstream.

re-verification applications a beam divergence of 1.75 mrad results in a spot size less than 1 cm in radius at 5.7 m on the far side of the cask. This diameter is significantly smaller than a fuel assembly cross section.

To compare the effect of source divergence on scattering contribution in a case relevant to fuel cask applications, the transmission of MPS-spectrum photons was simulated through a loaded HI-STORM cask [109] in a transverse orientation. The source was modeled with both a 1.75 mrad half-angle divergence to represent an MPS source, and in a 5 degree half-angle divergence cone to represent a collimated bremsstrahlung or nuclear reaction source. The unscattered MPS beam radius is less than one cm after emerging from the 330 cm diameter cask, which is a factor of 23,000 increase in photon concentration over a bremsstrahlung source with a 30 degree opening angle when collimated to match the Thomson scattering MPS divergence. The unscattered fraction of photons tallied with an MCNPX point detector on the opposite side of the cask is 99.3% for the MPS source and 5.7% for the 30 degree collimated bremsstrahlung source, emphasizing the need to use a narrowly collimated photon source.

It has been shown that in the case of a fuel cask the severe scattering in tens of cm of steel or concrete and in the nuclear fuel assemblies would almost entirely wash out the contrast in conventional radiography performed with a broad fan distribution bremsstrahlung source. Pencil beam scanning avoids the reduction in image contrast caused by scattering.

5.3.2 Cask Scanning Study

5.3.2.1 Photon Source Parameter Ranges for Cask Scanning

The scattering and transmission assessment motivated the types of photon beams simulated to assess scenarios of cask occupancy verification. A beam energy of 8 MeV is chosen for this study because it provides near maximum penetration (within 0.2%) through steel and a high attenuation contrast between nuclear fuel and shielding material, as seen in Fig. 5.15. In addition, 8 MeV is well above the highest gamma-ray energies in the spent fuel background, so a detection threshold can be set to only detect transmitted signal photons. Whereas increasing the beam energy to 10 MeV would improve contrast by 9% and 6% for concrete and steel respectively, the higher energy complicates operations by increasing the probability of photoneutron production and subsequent neutron reactions by a factor of 5.2. It has been shown in [79] that FWHM energy spread up to 40% has minimal effect on transmission through thick targets. For Thomson scattering sources, the use of such a broad energy spread allows for higher photon intensity. The half-angle beam divergence was chosen as 1.7 mrad to be apparent to only a single pin in a longitudinal cask scanning scenario and is consistent with Thomson source emission angles at 8 MeV. This divergence results in a spot size with radius less than 1 cm through the full length of the cask, which is less than the rod pitch of the tested fuel assemblies. A pulsed source enables rejection of the radioactive background from spent fuel with detector time gating.

These parameter ranges further motivate the consideration of a Thomson-scattering-based MPS. The properties of MPSs, discussed in Section 2.1.5, offer distinct advantages over other photon sources for this cask scanning, and these advantages will be discussed throughout this section. While current repetition rates of research systems are low (<0.1 kHz) it is anticipated that future lasers will allow 1-200 kHz operation over time [112]. Development is in progress to realize yields in the 10^8 photons/shot range at selectable energies from 1-20 MeV with energy spreads from

30% down to sub-percent [25]. Photons in this energy spread range can be delivered in beams of few mrad opening angles. The beam can be steered using magnetic systems, or for laser-plasma sources also using turret, optical scanning mirrors [113] or magnetized plasma methods [114]. Photon intensity and therefore photon dose could be controlled continuously using the scattering laser.

5.3.2.2 Cask and Scanning Setup

Two representative cask types were used for this study. The MC-10 [104] is the simpler design, with a 25 cm thick steel wall shield. The cask is 495 cm tall and 274 cm in diameter, with a 34 cm thick steel lid. The studied loading configuration was twenty-four 17 pin by 17 pin PWR assemblies [110]. The second cask, the Holtec International HI-STORM 100 [109], utilizes a thin steel shield housed in a 68 cm thick concrete overpack. The height can range from 500-570 cm, with a 330 cm overall diameter. This cask can be configured for multiple different loadings, including the tested scenarios of twenty-four 15 pin by 15 pin PWR assemblies (MPC-24), thirty-two 14 pin by 14 pin PWR assemblies (MPC-32) and sixty-eight 9 pin by 9 pin boiling water reactor (BWR) assemblies (MPC-68) [109].

Several representative scanning geometries were simulated. The simplest approach for probing the cask assembly occupancy uses longitudinal transmission measurements by rastering a beam across the face of the cask as shown in Fig. 5.18. Given the small diameter and narrow angular spread the beam will be incident on either a fuel pin or a gap. Measuring the transmission across the area of an assembly could directly reveal if an assembly is present or missing. However, this approach may not always be practical. Most casks are standing upright, making it difficult to place source and detector above or underneath the cask and moving the cask may be undesirable. In these cases, transverse scanning as shown in Fig. 5.19 would be necessary. Various methods were modeled including parallel scans in which the input beam is translated across the aperture of the cask, and angular scans in which the origin point of the beam is kept constant, but its angle changed. Furthermore, transverse scanning with a Thomson scattering MPS beam is compared to

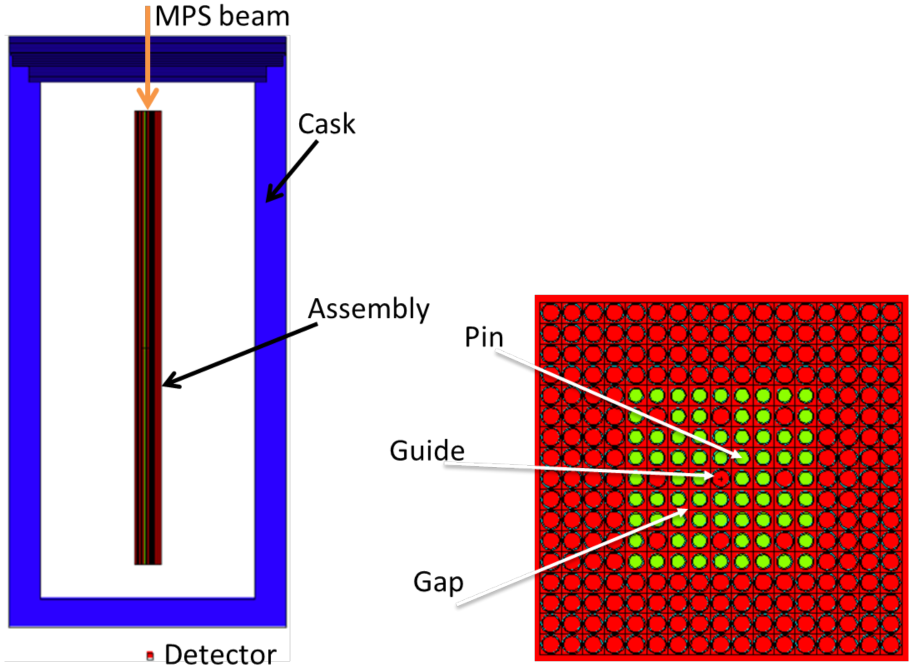

Figure 5.18: Geometry for MCNP simulation of the longitudinal photon beam transport through an MC-10 cask with steel lid and bottom (left). PWR assembly with example pins, and longitudinally scanned locations labeled (right).

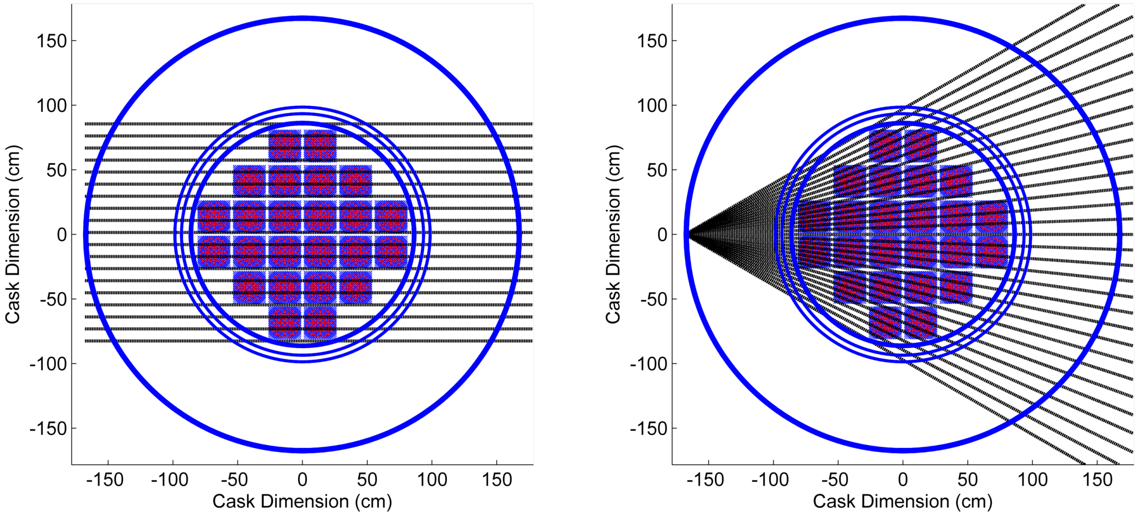

(a) (b)

Figure 5.19: Transverse MPC-24 ”Parallel” scan (a) and ”angular” scan (b); the number of illustrated beams is reduced for clarity. The beams in the ”angular” scan are illuminated in order counter-clockwise through the cask.

bremsstrahlung scanning, configured both in a fan beam and a 10 degree half-angle cone beam.

5.3.2.3 Simulation and Analytic Calculation Approaches for Cask Scanning Study

Determination of the optimal scanning configuration for multiple assembly removal scenarios necessitates determining transmission through a cask with many assembly placements and beam positions. This problem is inherently a low transmission scenario, because the storage cask is designed for shielding photons and neutrons. This high attenuation necessitates very long computation times to achieve reliable results using stochastic radiation transport codes such as MCNP that are able to accurately model scattering.

The previously discussed scattering simulations enable a different technique for this study. By using a pencil beam the scattered signal can be effectively eliminated and transmission results can be analytically calculated. By defining the cask geometry in 2-D space, the attenuation of the beam can be calculated through the various materials. Using a Python script, shown in Appendix D, the beam was transmitted through the cask from arbitrary position, at any variety of angles. Attenuation of the beam was calculated using published photon attenuation coefficients of the various materials [96] shown in Fig. 5.15. These calculations were validated with representative MCNP simulations, and then used to evaluate a larger range of geometries.

Various scanning configurations and methods were investigated for HI-STORM casks and a simplified MC-10 all-steel cask. Representative assemblies in different locations (shown in Fig. 5.20 for the HI-STORM MPC-24) in each loading pattern were removed in the calculations. Discrepancies in transmission due to the removals can then be mapped for different scanning configurations by moving the beam through different positions and angles. The attenuation through the cask for multiple beam chords was calculated to build up transmission profiles. These attenuation values are determined by calculating the source photon detection probability at a point either analytically, or with a point detector in MCNP. The beams were scanned across the cask in several different patterns. Two examples are illustrated in Fig. 5.19, corresponding to source translation or rotation. The maps produced by these scans allow for optimization of the scan pattern and

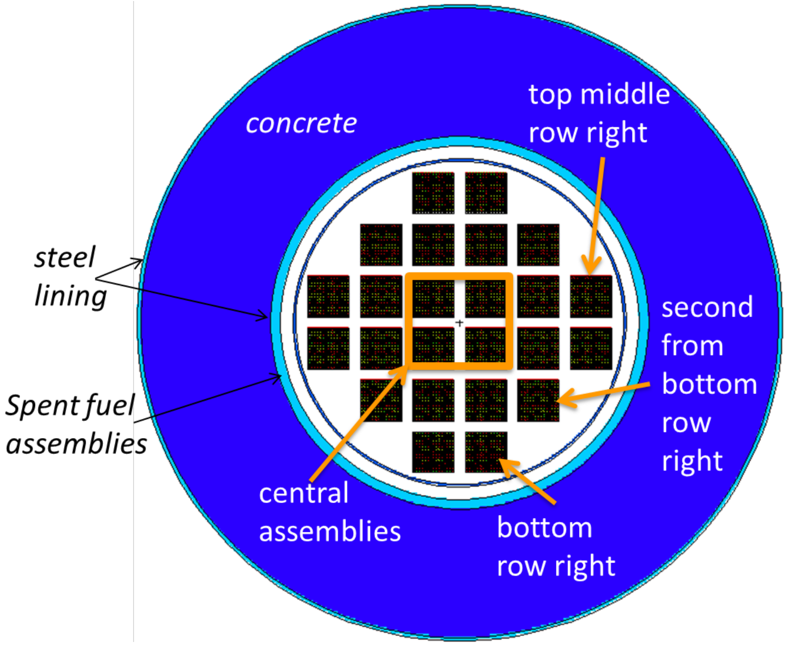

Figure 5.20: HI-STORM cask with MPC-24 loading pattern showing labeled assemblies for removal during testing.

estimation of the minimum photon intensity needed for determining assembly slot occupancy.

5.3.2.4 Spent Fuel Decay Background Estimation

Because fission products are decaying in spent fuel long after it has been placed in dry storage, the cask passively emits a significant number of photons. This background source term must be quantified to determine the signal strength necessary to detect the absence of a fuel assembly. In order to calculate a background spectrum to compare against the transmitted photon signal, ORIGEN [115] was used with the help of Brian Quiter of Lawrence Berkeley National Laboratory to calculate fuel depletion, and MCNPX was used for radiation transport.

A representative PWR fuel bundle from the Diablo Canyon Power Plant with a cooling time of 3 years was simulated [116]. Because three years is the shortest cooling time spent in the storage pool before the spent fuel can be placed in dry storage, this background spectrum can be considered a worst-case scenario. Casks would likely only need to be re-verified after many years of storage when their background intensity is greatly reduced.

For simplified radiation transport modeling, the cask was assumed to be filled with a homoge-

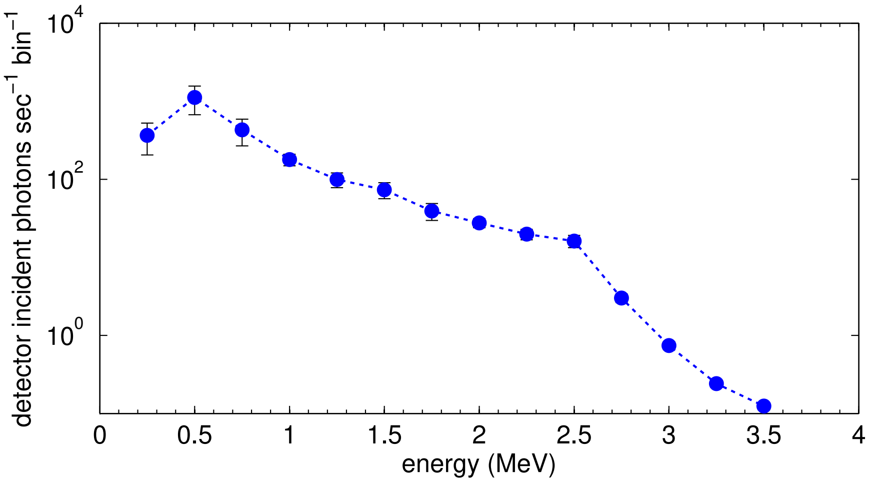

Figure 5.21: Spent fuel background spectrum outside cask simulated with MCNPX.

nized distribution of the material in the 24 assemblies. Photons resulting from the decay of spent fuel materials from the ORIGEN calculation were collected into a source energy spectrum from 0.25 MeV to 3.5 MeV (the vast majority of expected photons [117]). This spectrum was then distributed through the homogenized fuel in MCNPX and transmitted through the MC-10 cask to a 5 cm × 5 cm detector surface. Photons are tallied on the surface of the detector to neglect efficiency effects for this study. With a sufficiently thick NaI detector, on the order of 12 cm, 80% total intrinsic efficiency is expected at 8 MeV [9]. The detector thickness could also be reduced by using a higher effective-Z material, such as $CdWO_4$. For a cask scanning scenario, energy determination will not be necessary and any detected photon can be treated as a transmitted photon. The spectrum on the face of the detector cell is shown in Fig. 5.21. It gives an energy-integrated background rate of about 2,400 photons per second incident on the face of the detector. Because transmission through the HI-STORM cask is on the same order, with the same assembly loading capacity, the background rate is expected to be approximately the same.

5.3.2.5 Longitudinal Scanning Transmission

MCNPX simulations were performed to evaluate longitudinal cask measurements. In a lengthwise transmission measurement, the beam needs to penetrate the lid and bottom of the cask and the beam attenuation depends on their combined thickness. The simulated MC-10 cask has a combined

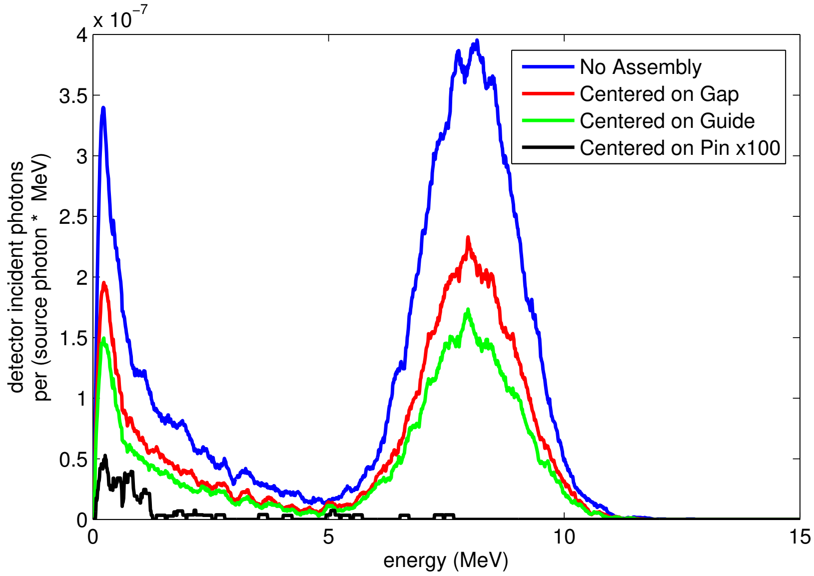

Figure 5.22: Transmitted photon spectra for the four simulated cases. The black line, which represents the photon spectra for the beam centered on a pin, has been multiplied by 100 for visual clarity because the transmission probability is three orders of magnitude less than in the other cases.

lid and base thickness of about 60 cm, leading to an unscattered photon attenuation probability of approximately 10^{-6}. Transmission values for casks with a concrete overpack in place of thick steel shielding are approximately the same. The results for an MC-10 cask can be extrapolated to casks with different lids and bottom plates by simply considering the change in attenuation.

An 8 MeV, 30% FWHM energy spread photon beam was transported through the simplified MC-10 cask [104]. The transmission was calculated for a beam through an empty slot (no assembly) and through a 17×17 PWR assembly [110] either centered on a gap between pins, a guide tube, or a fuel pin as indicated in Fig. 5.18. The half-angle divergence was chosen to be 1.7 mrad, such that the beam diameter of approximately 1.5 cm at the far end of the assembly is only apparent to a single pin. In the simulated geometry shown in Fig. 5.18, the transmitted photons were tallied across a 5 cm × 5 cm detector surface positioned in line with the beam and underneath the cask. This detector size fully captures the beam and is representative of widely available scintillators used for photon detection.

Fig. 5.22 shows the energy spectra of the photons reaching the detector for the beam positions

Table 5.2: Number of photons entering the detector per source photon for longitudinal measurements through an MC-10 cask.

No assembly	**Centered on gap**	**Centered on guide**	**Centered on pin**
1.4×10^{-6}	7.6×10^{-7}	5.7×10^{-7}	4.5×10^{-10}

mentioned above. The spectra are dominated by the broad peak around the beam energy, i.e., by the unscattered photons. The spectrum for the beam centered on a pin is not visible in this figure because the transmission probability is three orders of magnitude less than in the other cases. The probabilities for a photon being transmitted are listed in Table 5.2. The transmission value calculated in this simulated case is a factor of two greater than analytically calculated transmission due to scatter into the detector.

5.3.2.6 Transmission Signal to Radioactive Background Ratio

Transmission through a pin can be accepted as a “zero-signal” and an indication of assembly presence. Therefore, the lowest relevant transmission value for signal detection from Table 5.2 is 5.7×10^{-7} and as previously calculated the background count rate in this sample detector is 2,400 counts per second. To surpass this rate, a source strength of 4.2×10^{9} photons per second is required, with greater strength required to significantly measure signal above background. A typical Thomson scattering MPS is expected to be capable of producing 10^{12} photons per second [25]. Based on spectral and divergence comparison (order of half a steradian for bremsstrahlung with 7.2 microsteradians subtended by the detector, and 4 microsteradians for a Thomson scattering MPS) a bremsstrahlung photon is a factor of 4.9×10^{6} less likely to be transmitted through the cask and detected than a Thomson photon, therefore requiring an output of 2.1×10^{16} photons per second.

Background counts between beam pulses can be rejected by time-gating the detector on the photon pulse to further reduce passive background contribution. A gate width of 10 ns is assumed, which is conservative for a fast scintillation detector. A typical Thomson scattering MPS pulses is shorter than this gate, at less than a picosecond, and 10 kHz repetition rates are expected. A typical bremsstrahlung linac pulse is on the order of 4 microseconds, pulsed at 250 Hz [17]. Time gating applied with these operating parameters results in photon intensity requirement reduction factors of 10,000 and 1,000 for the MPS and bremsstrahlung sources, respectively. Time gating reduces the above bremsstrahlung photon intensity requirement to 2.1×10^{14}, or 34 μA average current (assuming high bremsstrahlung conversion efficiency) to induce a signal 10-times greater than expected background, which is within possible linac operation range. However, 7.8 A average current is necessary to match the MPS signal to background ratio and perform transverse scans to be discussed below, which would require an extremely powerful machine and extensive shielding. Operation at this level may also require a higher pulse repetition rate, reducing time gating effectiveness.

A high-power (9 MeV, 10 mA) Rhodotron accelerator [118] could produce a bremsstrahlung photon intensity in a few mrad divergence beam with a high enough photon intensity to surpass background. However, the typical quasi-continuous operation (100s of MHz repetition rates) of a Rhodotron [18] would preclude detector gating, necessitating a 10^3-10^4 increase in photon intensity to induce a detectable signal at the same level above background as a pulsed source. Due to this restriction, such a Rhodotron would require a factor of 6.3 increase in current to match MPS performance. Furthermore, a Rhodotron's large size and weight would make transport and positioning impractical.

As previously stated, the highest photon energy expected from spent fuel products is 3.5 MeV. Because un-scattered Thomson scattering MPS photons average 8 MeV in this investigation, a minimum energy detection threshold could be applied at 3.5 MeV so that any detected photon is a transmitted source photon. This threshold could not be applied to any broad-spectrum bremsstrahlung source as many transmitted source photons would be rejected. Energy gating introduces the challenge that single photon counting is required to determine the energy of each photon, requiring operation at very low transmission to keep the average detection rate well below 1 photon per beam pulse. Operating this way would be possible because only in situations where the transmission rates are very low would energy discrimination be helpful. However, given the high signal-to-background ratio that can be achieved with MPS time gating, additional energy discrimination is likely not necessary.

Bremsstrahlung sources with either pulsed or continuous beams have high enough photon intensity to reliably surpass spent fuel decay photon background rates. However, typical source currents would not allow for detection of missing spent fuel with a reasonable dwell time. To match the performance of an MPS for this application the current would have to be increased well beyond the current state of the art, and require a prohibitively large accelerator and shielding configuration.

5.3.2.7 Transverse Scanning Transmission

Transverse scanning methods have been examined because many cask designs do not allow for access from the bottom, prohibiting longitudinal scanning. This transverse scanning study was performed with the HI-STORM cask with the MPC-24 assembly loading pattern and then expanded to the MPC-32 and -68 loading patterns. While the distance through the cask is shorter in the transverse orientation, the geometry is more complicated than for the longitudinal scan as the beam may pass through different assembly and fuel pin configurations, air, and cask walls. Therefore, a verification of assembly occupancy must be made from transmission patterns that are dependent on the assembly configurations and beam orientation. To understand scan patterns and beam requirements for detection of a missing assembly full scans across the casks were analyzed. Each assembly that the beam passes through attenuates the beam and leaves a signature in the transmission pattern generated by all beams plotted as a function of position through the cask (e.g., Fig. 5.23). The previously discussed MCNPX-validated analytic calculations were employed to estimate beam transmission values much more quickly than a full Monte Carlo simulation.

The assumed performance goal is to accomplish a 100-beam chord scan in less than three hours. To achieve a maximum transmission statistical uncertainty of 10%, 100 counts are required per chord. In three hours the beam can dwell on each chord for 100 seconds. Assuming a source strength of 10^{12} photons per second (10^{8} photons per pulse at 10 kHz) is achievable, the transmission probability of a photon through a cask where an assembly is missing must be no less than 10^{-12} to achieve 100 counts per chord. If all assemblies are present, transmission probability of less than 10^{-12} is acceptable in this tested scenario as a no-count measurement would be a confirmation that no assemblies are missing. Note that in the simulated method scan time is determined by the lowest transmission point. Advanced scanning methods are not considered here, but could be considered to speed up the process and reduce bystander dose and therefore shielding requirements by dwelling on a given point only as long as it takes to collect the required statistics.

The orientation yielding the highest contrast between fuel and air is to transmit the photon beam parallel to the rows of assemblies, as shown in Fig. 5.19. In this orientation, a missing assembly affects the transmission of the beam in a fixed region of the scan map but a major issue with this scanning orientation is that transmission probabilities are well below 10^{-12} in the area of a missing assembly if that assembly is near the center of the cask. This setup is also challenging operationally because both the source and detector would have to be moved for each beam measurement.

An “angular” source and detector orientation shown in Fig. 5.19 improves both on operation logistics and minimum transmission probability. Because the beam only needs to be rotated, less equipment needs to be moved for each measurement. Also, by avoiding chords where the beam is attenuated by a full row of fuel pins, the transmission probability is at an acceptable level for all beams. However, with certain origin positions the difference in transmission probability between a missing and present assembly is not large. The transmission probability maps showing removal of assemblies in each scan configuration are shown in Fig. 5.23.

Although an angular scan avoids scanning full rows of pins, there are regions in these scans where a missing assembly will not register a large difference in transmission. The transmission contrast can be maximized by rotating the origin point of the angular scan around the cask. For ease of measurement, the goal for this study is a factor of 100 increase in transmission when an assembly is missing. The configuration where the origin is rotated 25 degrees around the cask from the position in Fig. 5.19 to 205°, shown in Fig. 5.24, offers optimal contrast for missing assemblies while avoiding high attenuation areas where many rows of pins block the photons. The transmission map produced with the origin at 205 degrees is shown in Fig. 5.25. Each missing assembly

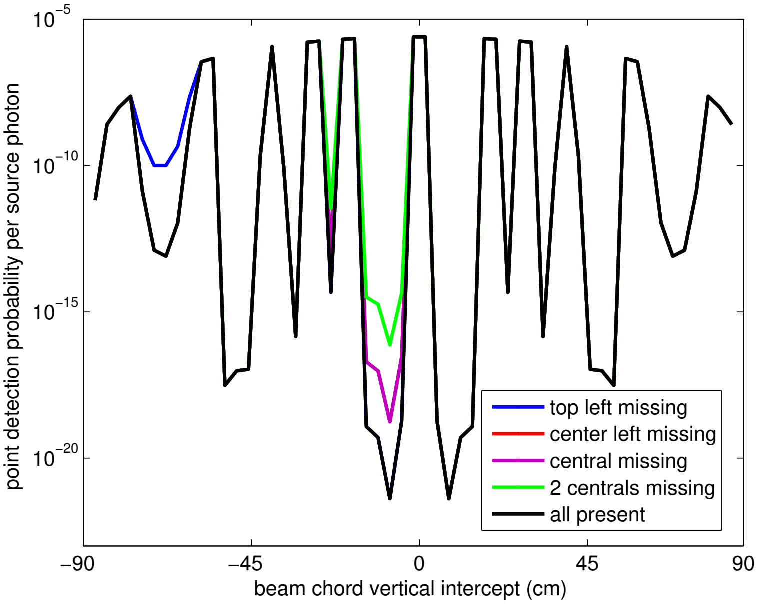

(a)

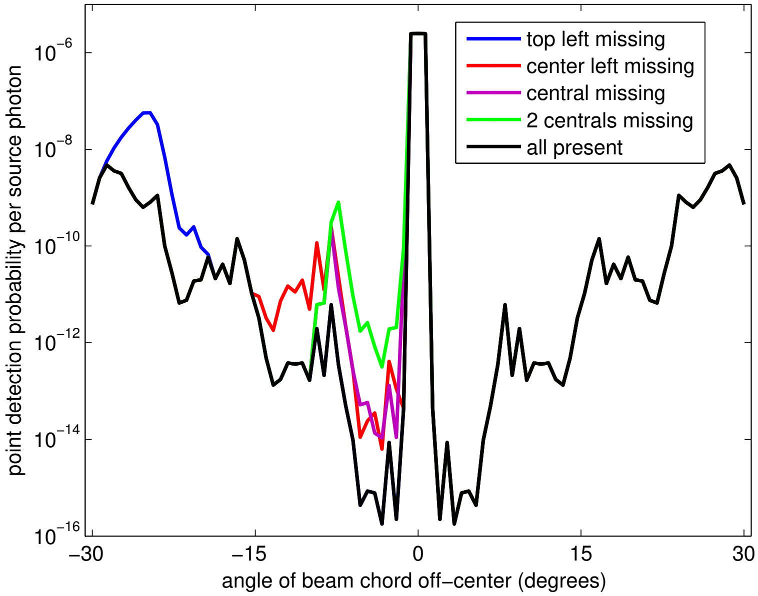

(b)

Figure 5.23: "Parallel" (a) and "angular" (b) scan MPC-24 transmission probability maps. The black lines show the transmission probabilities with all assemblies in place. The colored lines give the transmission values with specific assemblies removed as indicated in the legend. In the parallel scan, any single missing center assembly results in the same discrepancy.

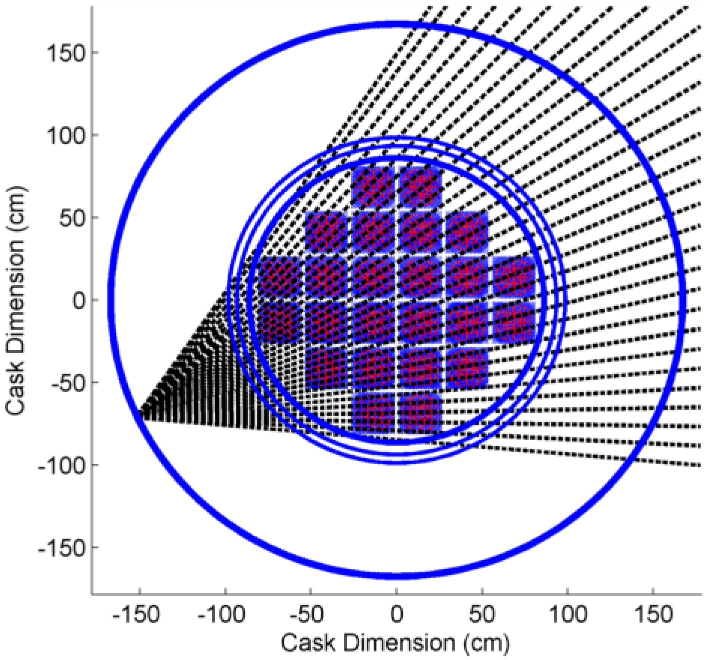

Figure 5.24: Angular scan beam chords illustrated with origin at 205 degree counterclockwise from arbitrarily defined 0 degree point at 150 cm on the x-axis and 0 cm on the y-axis of a HI-STORM cask with MPC-24 loading.

case shows at least a factor of 100 difference in attenuation from the case where all assemblies are present, and any case where an assembly is missing shows greater than 10^{-12} transmission probability. While some beam chords with all assemblies present show a transmission probability below the 10^{-12} goal, a zero-signal at this scan number confirms assembly presence. A longer measurement time could be used to establish absolute transmission along one such chord as a calibration if desired.

5.3.2.8 Validation of analytic method with MCNP

As previously discussed, analytic calculations enable optimization studies by eliminating particle transport from the transmission calculations. To confirm the assumption that secondary scattering effects do not have a significant effect on the results, full MCNPX simulations were performed for 21 demonstrative cases. The results compared to the calculated values are shown in Fig. 5.26. The MCNPX results are in close agreement with the calculated transmissions, both for cases with all assemblies present and for those with missing assemblies, confirming that calculated values can

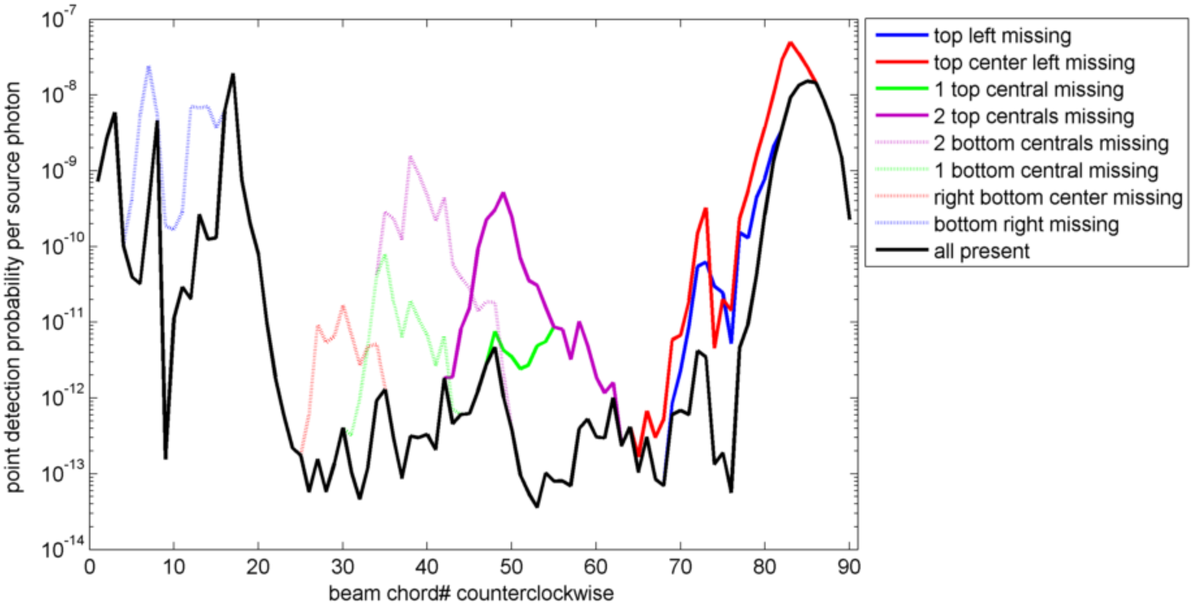

Figure 5.25: Transmission profiles for "angular" scans of a MPC-24 cask with the source at 205 degrees. The black lines show the transmission probabilities with all assemblies in place. The colored lines give the transmission values with specific assemblies removed as indicated in the legend.

adequately inform cask scanning methods.

5.3.2.9 Transmission results for other assemblies

With the analytical calculations verified by MCNP simulations, the method can be expanded to other cask loadings. The MPC-32 and MPC-68 loading configurations group smaller assemblies in the same space as the MPC-24, increasing the difficulty of detecting one missing assembly. To remain consistent with the MPC-24 scanning, the transmission profiles are calculated with the origin at 205 degrees. The scans for these casks are therefore not optimal and may be improved by testing different origin points for the specific loading patterns. Assemblies are removed in similar limiting locations to MPC-24 testing as shown in Fig. 5.27.

Fig. 5.28 shows the calculated transmission profiles for the MPC-32 and MPC-68 casks. These profiles indicate that a missing assembly will cause at least an order of magnitude increase in transmission. Similarly to the MPC-24 case, the transmission of a missing assembly case is greater than 10^{-12} leading to acceptable scan times of approximately 3 hours, as previously calculated. As in

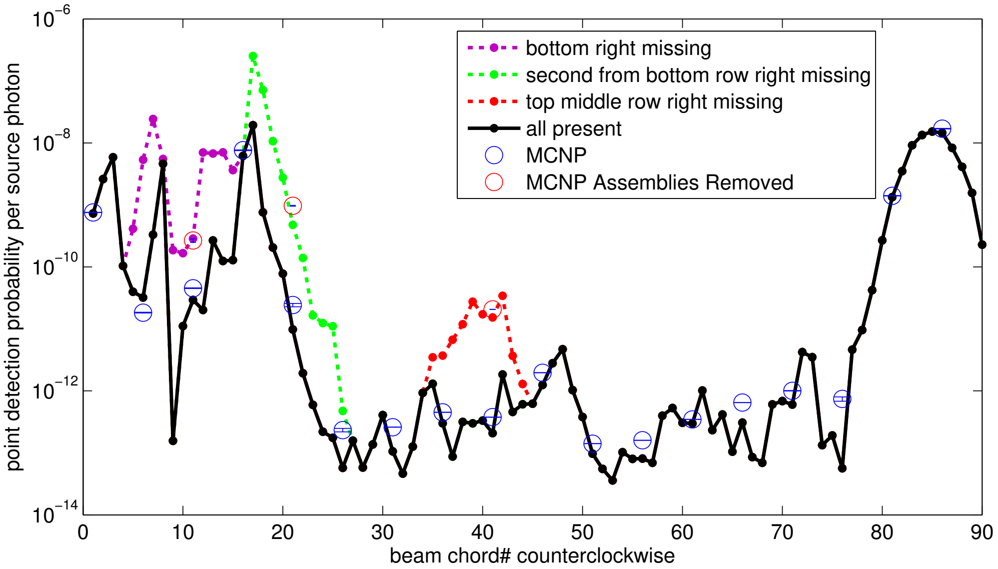

Figure 5.26: Validation of analytical calculations with MCNP simulations. Analytical calculations for transverse angular scan of a HI-STORM MPC-24 cask are shown as black (all assemblies in place) and colored data points. The MCNP results are indicated by the open blue circles (all assemblies in place) and by open red circles for beams through an unoccupied assembly location.

the case for the MPC-24 loading configuration, a missing assembly in either of these configurations will be detectable with this MPS scanning setup.

5.3.2.10 Comparison to bremsstrahlung scanning

Based on MCNPX simulations, the Thomson scattering MPS beam transmission values can be compared to fan- and cone-beam bremsstrahlung transmission and the photon intensity requirements of a bremsstrahlung source to match MPS photon delivery capabilities can be demonstrated. A 57.5 degree bremsstrahlung-spectrum fan beam was simulated to match the rastered MPS transverse scan discussed previously. Bremsstrahlung cone beams were also simulated along the same vectors as the MPS beams, collimated to 10 degrees. The simulated transmission at detector point locations identical to those in Fig. 5.26 is shown in Fig. 5.29, demonstrating the large effect collimation has on source photon transmission likelihood.

While a bremsstrahlung fan beam could scan a cask using only about two beam positions, Fig. 5.29 demonstrates that the MPS source reduces the photon intensity requirement over a bremsstrahlung source by 4 to 6 orders of magnitude. An extremely powerful, 7.8 A, bremsstrahlung

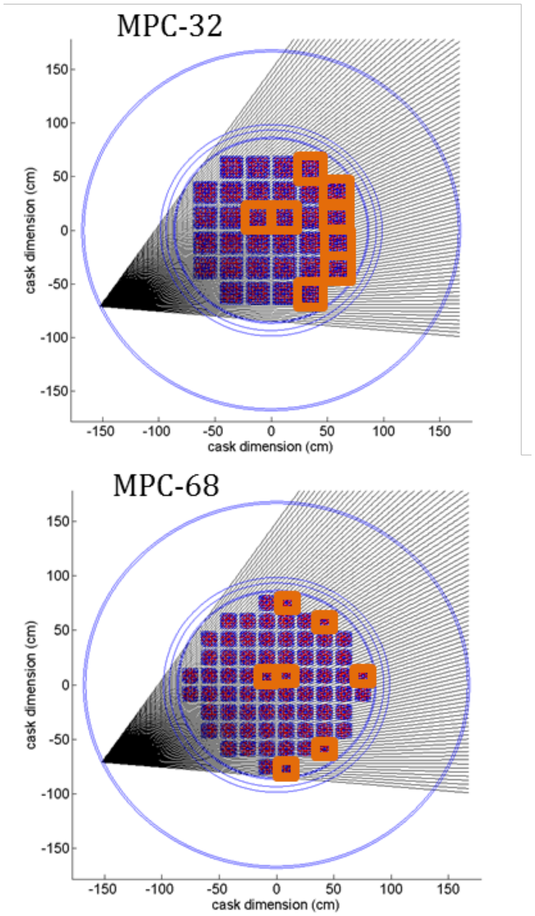

Figure 5.27: Geometry of transmission profile calculations for HI-STORM MPC-32 and HI-STORM MPC-68 cask loading configurations with the source for the angular scan at 205 degrees. Assemblies removed for testing are outlined in orange.

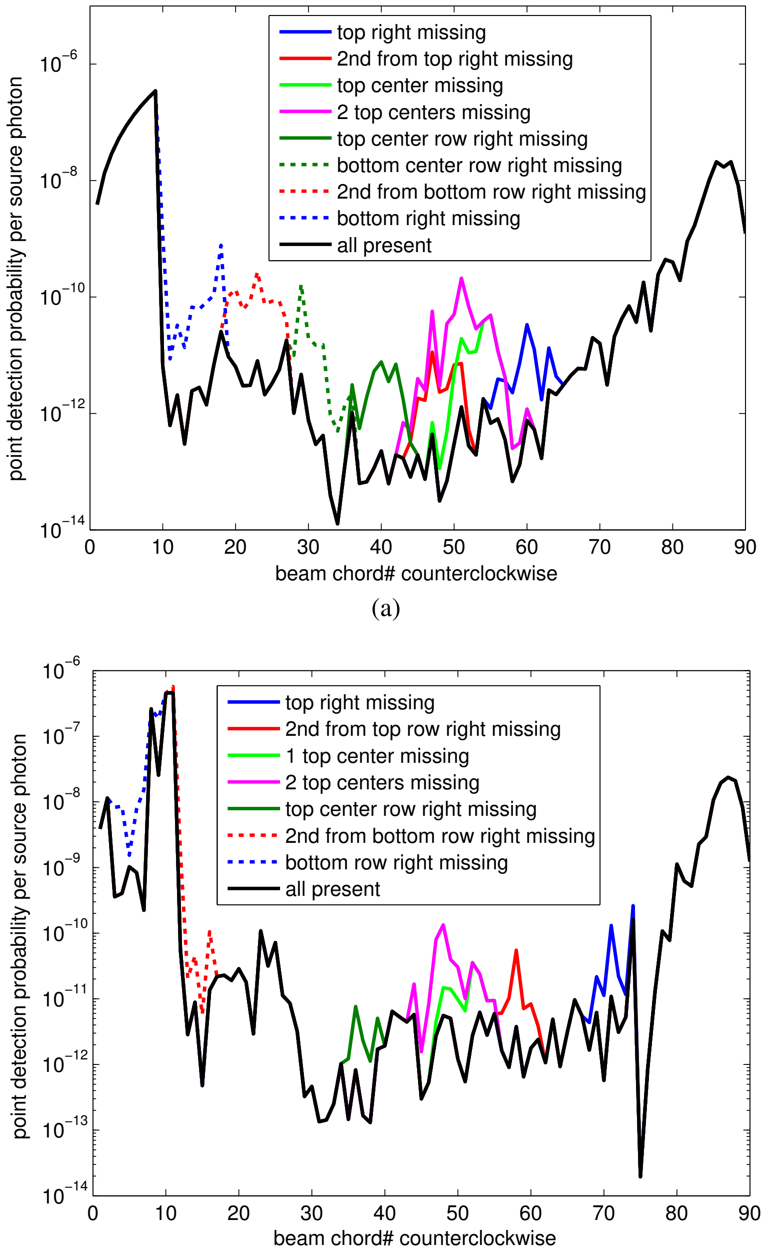

(a)

(b)

Figure 5.28: Transmission profiles for 205 degree "angular" scans of the HI-STORM MPC-32 (a) and MPC-68 (b) cask loading configurations. The black lines show the transmission probabilities with all assemblies in place. The colored lines give the transmission values with specific assemblies removed as indicated in the legend.

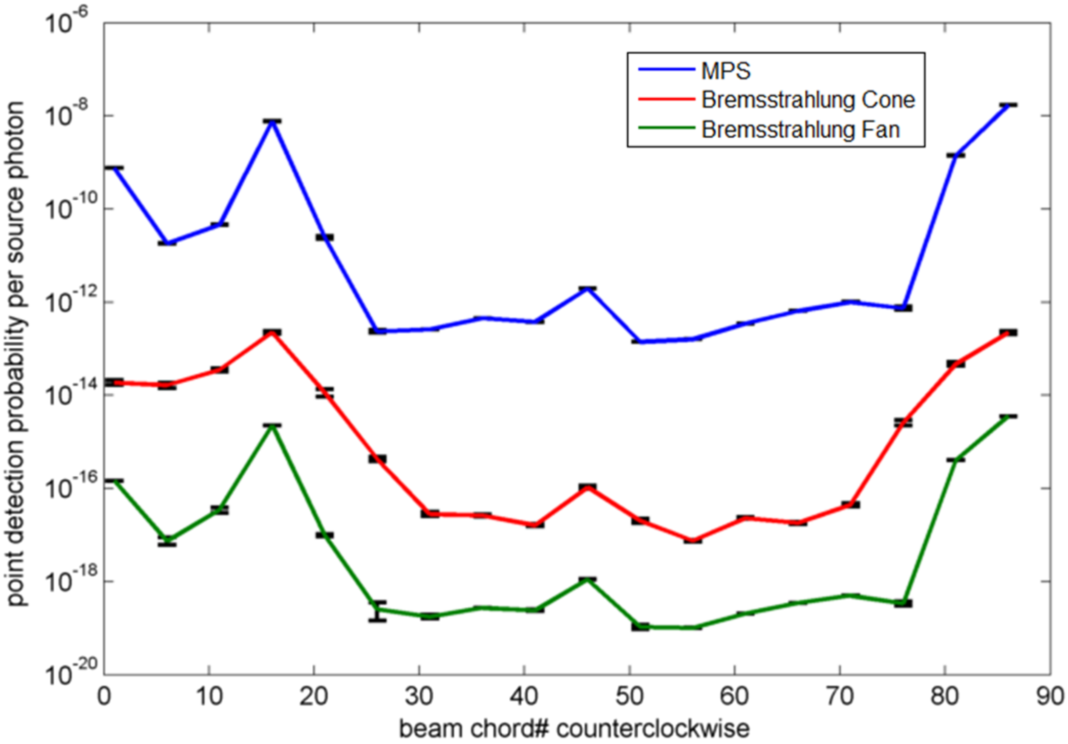

Figure 5.29: Transmission comparison of MPS, bremsstrahlung cone, and bremsstrahlung fan beams through HI-STORM cask with MPC-24 loading pattern in transverse orientation.

source would be required to match the capabilities of an anticipated Thomson scattering MPS source because most bremsstrahlung photons would be lost to collimation. The increased shielding and collimation required by such a bremsstrahlung source would therefore negate any operational advantages.

An expansion to a full-scan comparison between the analytical MPS beam and the simulated bremsstrahlung fan beam scan is shown in Fig. 5.30. Because the MPS analytical transmission profile has previously been shown to agree with the simulated transmission this comparison can be made. The six-order-of-magnitude reduction in transmission probability by using a bremsstrahlung fan source follows the predictions from Fig. 5.29. While the bremsstrahlung transmission profile generally follows the features of the MPS scanned case, some finer features are not as well resolved. Average transmission contrast for a missing assembly in the region sensitive to the removal (beam chords 6-15 in Fig. 5.30) is reduced by a factor of 3.7 for a bremsstrahlung fan beam relative to the MPS scan. The maximum contrast value for any one point in this region is reduced

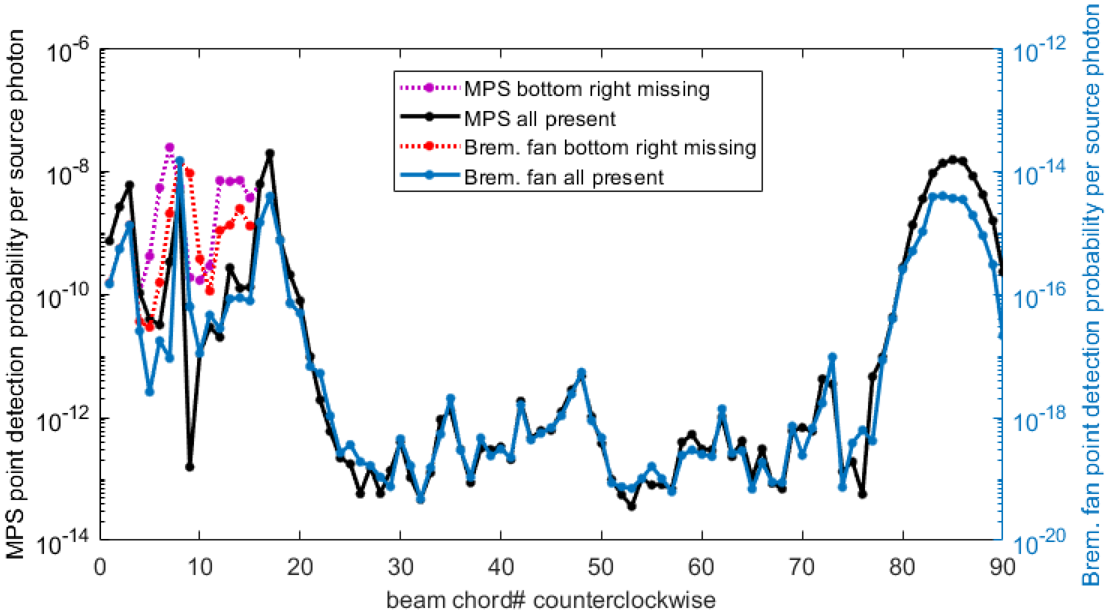

Figure 5.30: Transmission comparison between simulated bremsstrahlung fan beam scan and analytical calculation of MPS beam scan, with all assemblies present, and with the bottom right removed. MPS transmission on left axis, bremsstrahlung on right. Geometry shown in Fig. 5.20 and scan configuration shown in Fig. 5.24.

by a factor of 5.4. The use of a bremsstrahlung fan beam would therefore result in more difficulty resolving the signature from a missing assembly.

5.3.3 Dry Storage Cask Scanning Conclusions

The thick walls of dry storage casks and the additional attenuation and scatter in the stored assemblies make radiographic measurements for the verification of the canister's contents in a reasonable timeframe very challenging. Bremsstrahlung beams are not suitable for the radiographic verification of dry storage cask contents due to their broad-angle, broad-energy, and in some cases continuous operation. The photon intensity required for such a source to enable scans in a reasonable time when appropriately collimated, and produce a signal over than the radioactive background of the cask, is extremely high. Such a source is beyond the state-of-the-art and if developed would require massive shielding and collimation prohibitive of operation at a dry storage cask facility.

The results of this study demonstrate how intense, narrow-divergence beams can penetrate very thick materials and allow transmission imaging where conventional methods fail due to scatter, attenuation, and practical utility. A Thomson scattering MPS offers several advantages that could enable transmission measurements for detecting and locating empty versus full assembly storage positions in a dry storage cask. For a transverse scan of a typical dry storage cask considered in this study the source must emit 10^{12} photons per second, with an energy of 8 MeV and a spread of 20-30% with 1.7 mrad half-angle spatial divergence. A pulsed source is needed for effective suppression of the radioactive background by gating the detector with the beam pulse. The source must also be compact to allow for transport and positioning near the fuel cask. An MPS source with the required properties would be able to identify missing assemblies in either a longitudinal or transverse configuration in less than 3 hours. In the longitudinal orientation, even single missing pins may be detectable. Projected Thomson scattering MPS sources will be able to meet all of these requirements [25].

5.4 Conclusions

To demonstrate the utility of an LPA driven MPS for nonpoliferation applications a variety of considerations were tested through simulation and experiments. Radiography of shielded SNM was demonstrated through simulation validated through experiment by Chen, et. al. [79]. This simulation study was then expanded to a sensitivity study to show that the energy spread of the photons up to 40% FWHM has little effect on radiography quality. It was also shown that standoff interrogation with an MPS can be performed at long distances with little loss in beam intensity. An MPS beam also delivers less dose to the interrogated target object and bystanders for equivalent, bremsstrahlung-produced image quality.

It was also demonstrated that an MPS can be adequately shielded for personal protection for a mobile application and for sensitive measurements of induced photonuclear signatures in laboratory setting. While the laboratory shielding depends on mitigating beamdump secondary particles with traditional shielding materials, the mobile design accounts for projected advances in plasma deceleration of the LPA accelerated electrons. This work will allow for laboratory demonstration of an MPS in a nonproliferation context, and enable mobile deployment of advanced MPS technology.

Through simulation and analytical calculation studies the benefits of using an MPS for dry storage cask contents verification were demonstrated. An MPS with properties projected to be developed in the near future will be able to scan a dry storage cask in less than 3 hours if CoK has been lost. This time requirement is a significant improvement over currently proposed scanning techniques, with distinct advangtages over bremsstrahlung sources of photons. Development of a source for this application may lead towards potential areas of nonproliferation technology, including cargo screening, spent nuclear fuel tracking, pyroprocessing accountancy, materials assay in accident scenarios, and isotopic contents measurements using nuclear resonance fluorescence [82].

CHAPTER 6

Dual-Particle Dosimetry

Dosimetry is a critical issue in applying active interrogation methods in the field, because the interrogating particles cannot cause undue harm to bystanders, stowaways, or the cargo being interrogated. While a prominent signal must be produced when a contraband material is present, dose delivery should be minimized. Methods for assessing whole-body dose rates are also critical for a variety of radiation medicine, security, industrial, and research environments: accurate measurements of personal and ambient dose equivalent are required for safety and certification procedures [74, 119]. These measurements are also important in the context of this work to show that monoenergetic or quasi-monoenergetic photon sources deliver less dose per high-value interrogation photon than bremsstrahlung photon sources. Future work with MPS interrogation sources will demonstrate this dosimetric advantage.

6.1 Overview of Traditional Methods

Many of the radiation fields encountered in these applications are mixed fields, containing both neutrons and photons. Dose rates in these fields are typically measured with two separate instruments, a remcounter for neutrons[120], and an ion chamber[121] for photons. Each detector is blind to other particle types. These detectors calculate dose by using a response function to convert count rate to dose equivalent rate. The remcounter uses a response function that is dependent on the moderator size of the detector and the calibrating spectrum.

The remcounter is based on the fact that a small LiI scintillator placed in the center of a 12 inch diameter sphere of polyethylene response curve similar in shape to the dose equivalent per neutron as a function of energy [9]. This similarity is coincidental, but can yield a good estimate of neutron dose equivalent. While this is an efficient tool for measuring dose, it is difficult to trace the dose equivalent back to the energy spectrum of the field, and spectra differing from the detector's calibration spectrum can result in significant errors [122].

Ion chambers can measure dose rates accurately for a large range of photon energies, but are generally insensitive to neutrons. This insensitivity is advantageous when only the dose rate due to photons is of interest, but in many fields the neutron dose rate is the major component. This chapter discusses a methods developed to simultaneously measure both photon and neutron dose rates.

6.2 Organic Scintillator-based Method

To calculate dose equivalent from signal information obtained from organic scintillator pulses, the scintillation light must be converted to energy deposited. Since this work focuses on both neutron and photon dosimetry, it is important to reiterate that the the relationship between photon energy and light production is unity by definition, but it is nonlinear for neutron energy deposition. A minimum detection threshold is applied in light output, which when converted to energy deposition is higher in energy for neutrons than photons due to this nonlinear effect.

Charge-integration PSD is employed in this work to separate the neutron and photon components of the dose equivalent rate. For this dosimeter application, the comparison of tail to total integrations yields the lowest fraction of photons being misclassified as neutrons. Neutrons are far more biologically damaging than photons, and therefore any falsely classified neutrons have an outsized contribution to equivalent dose rate inaccuracies.

Pile-up pulses have an increased tail integral and are often falsely classified as neutrons. These pile-up pulses must be removed from the measured data to remove false neutron dose equivalent

Table 6.1: Comparison of stilbene and ICRP soft tissue properties relevant to radiation energy deposition.

	Stilbene	**ICRP Soft Tissue**
Density (g/cm^3)	1.16	1.00
Composition	$C_{14}H_{12}$	Mixture of H, C, N, O, w/ traces of Na, Mg, P, S, Cl, K, Ca, Fe and Zn
Mean Atomic Number	3.69	3.35
Hydrogen Content (wt%)	6.7	10.4

contribution. For this application, the list-mode CAEN PUR [41] feature discussed in Section 2.3.3 was implemented.

For accurate determination of dose equivalent, it must also be shown that radiation interactions in the stilbene detector medium are similar to those in human tissue [108]. Table 6.1 shows the comparable density and chemical properties, demonstrating that it is reasonable that the materials absorb radiation in a similar manner. Simulations were performed with MCNPX-PoliMi [35] to demonstrate this equivalency.

Fig. 6.1 shows a simulated ^{252}Cf spontaneous fission source used to determine the energy deposition by neutrons and photons in identical detector cells filled with either stilbene or ICRP soft tissue material. The simulated energy deposited was recorded in each cell, and then converted to light output using stilbene parameters for comparison. Through the light output range, the stilbene cell records an average neutron light output within 5% of the tissue cell, and and an average photon light output within 1.1%. The total recorded neutron and photon counts between the simulated stilbene and tissue cells are within 19.2% and 9.6% respectively. The discrepancy in neutron counts may be due to capture reactions in tissue that do not occur in stilbene, such as ^{14}N(n,p).

The calculated energy deposited is used to calculate absorbed dose, D, by normalizing to detector mass, m_{det} with

$$D = \frac{E_{\text{dep}}}{m_{\text{det}}}. \tag{6.1}$$

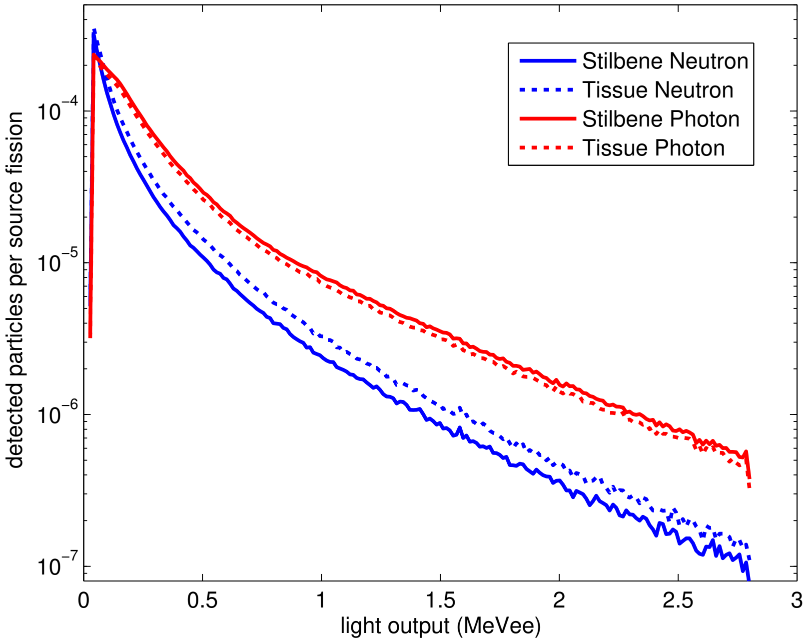

Figure 6.1: Simulated response of stilbene and human tissue to a ^{252}Cf fission source.

The absorbed dose is then used to calculate the dose equivalent, H, which captures the biological effects of the radiation. Because some types of radiation are more damaging to cells than others, energy depositions are weighted by the type and energy of the depositing particle. The weighting applied in my work presented here is the ICRP Publication 26 relationship between particle linear energy transfer (LET) and radiation "quality", or probability of biological stochastic effects[123].

The dose equivalent distribution at a coordinate r in a medium can be expressed as

$$H(r) = \int_L D(L, r)Q(L)dL, \tag{6.2}$$

where $D(L, r)$ is the absorbed dose distribution over the linear energy transfer (L) at the point r, and $Q(L)$ is the quality factor as a function of LET. In this work, neutron and photon dose rates are calculated with a Python script, shown in Appendix E.

Equations 6.1 and 6.2 allow for the calculation of neutron radiation quality based on neutron energy deposition, by way of the recoil proton energy to LET relationship [124, 125]. The relationships between proton energy (neutron energy deposition) and LET, and between LET and $Q(L)$ are shown in Fig. 6.2 from [125]. For all photons detectable in the stilbene energy range, the LET

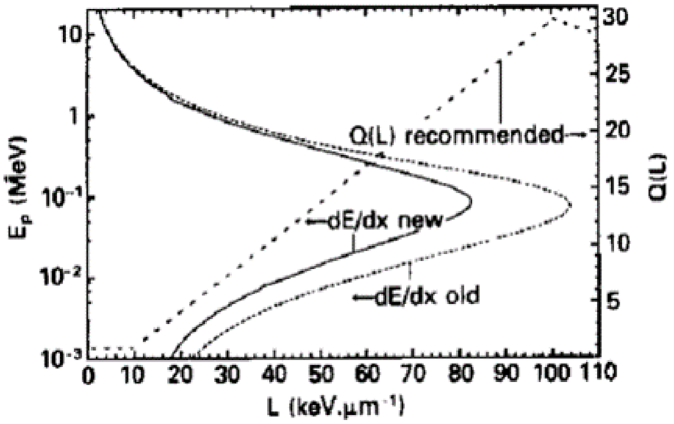

Figure 6.2: Relationships for determining $Q(L)$ from particle energy deposition [125].

is less than 10 keV/μm, resulting in a constant $Q(L)$ of 1.

Although more recent publications [126, 127] recommend a biological weighting factor based on incident radiation energy, the method described in this chapter allows for dose equivalent calculation without requiring energy spectrum unfolding. This method also retains accuracy to contemporary dose rate calculations.

6.3 Detector Size Study

Scintillators are easily manufactured in many different sizes, in theory allowing for a detector to be sized for a particular dose rate measurement application. Because absorbed dose is calculated as energy deposited normalized to the detector mass, the size of the detector used should have no effect on the calculated dose rate. However, the non-linearity of the neutron energy deposition to light output relationship, and the nature of neutron interactions in scintillators, lead to differences in calculated neutron absorbed dose. Because the photon energy deposition to light output is linear, photon absorbed dose is not a focus of this study. This study of detector size effects on dosimetry in this section is based on [128].

The effects of detector size on neutron dose were studied with three cylindrical Eljen-309 liquid scintillators [77], chosen because these detector cells were available in a variety of sizes. EJ-309

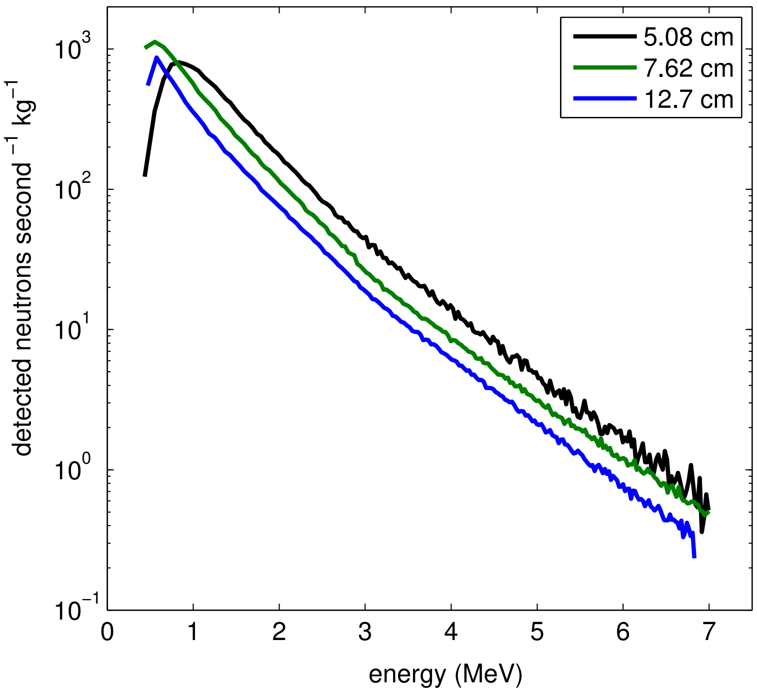

Figure 6.3: Energy deposited by ^{252}Cf neutrons in three cylindrical detectors, normalized by detector mass.

has a similar composition and density to stilbene, and therefore exhibit similar tissue equivalency. The sizes of the detectors were 5.08 cm diameter by 5.08 cm depth, 7.62 cm by 7.62 cm depth, and 12.7 cm by 12.7 cm depth. The neutron source used in this study was a 5.5 mCi ^{252}Cf and was measured one meter from the detector faces. The spectrum of energy deposited by neutrons normalized to detector mass, or absorbed dose, is shown in Fig. 6.3. The smallest detector measured the highest per mass energy deposition when no other corrections are made.

The unequal lengths of these cells alters the absorbed dose because most neutron interactions are in the front of the detector. Therefore, longer detector cells measure a lower absorbed dose because of the larger mass used for normalization. For comparison in this study, a standard 3.4 cm detector cell depth was chosen for mass normalization. MCNPX-PoliMi simulations showed that 95% of neutron interactions occurred within this depth.

As discussed in Section 2.2.2.2, it was assumed that all neutron interactions are a single scatter event on a hydrogen nucleus. While it was shown that this assumption has only a small affect when using a 5.08 cm cell, there is a larger probability that a neutron will scatter multiple times

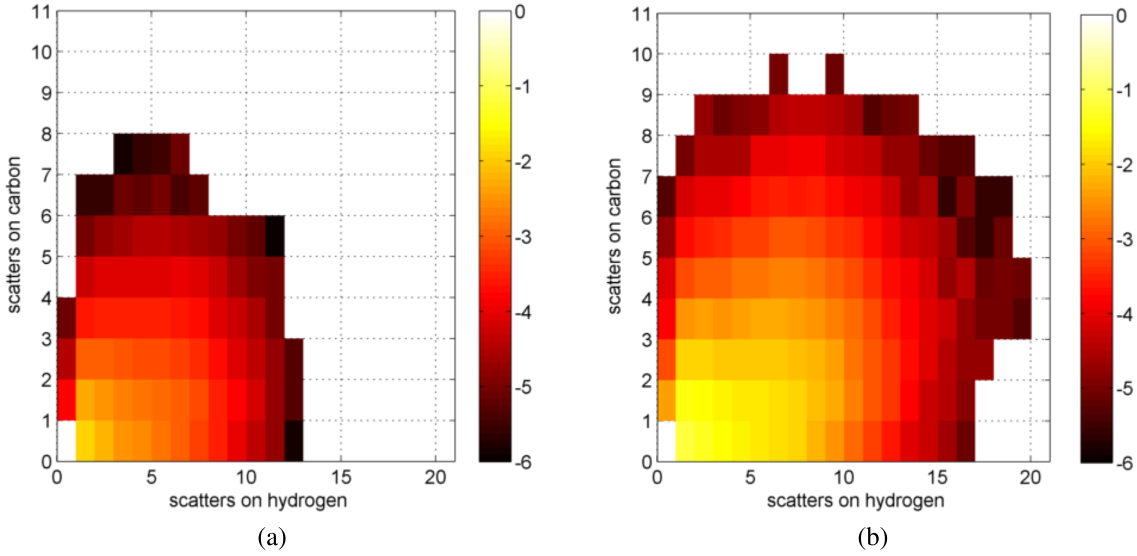

(a)

(b)

Figure 6.4: Scattering event frequencies in 7.62 cm right cylinder and 12.7 cm right cylinder EJ-309 detector cells. The colorbars represent the $\log_{10}$ of the shown combination of scatter events on either carbon or hydrogen nuclei.

in a larger cell. Fig. 6.4 shows that there is a much greater probability for multiple scatter events in the larger detector cell. In both cases, a single scatter on hydrogen is the most likely scatter interaction. However, by increasing the detector cell mass by a factor of 4.6, the chance that a pulse results from a neutron scattering a single time on hydrogen is reduced by 41%.

The effect of multiple scattering events on energy deposition calculations is illustrated in Fig. 6.5 using the semi-empirical light output function for EJ-309 [33, 44]. A neutron depositing 4 MeV in one scatter event results in 1.44 MeVee of light output, but a neutron depositing 1 and 3 MeV multiple depositions, for a total of the same 4 MeV, only results in 1.04 MeVee of light output. A multiple scatter event results in less light output, but this relationship is inverted when converting measured light output to energy deposited for dose rate calculations. Therefore, larger detectors overestimate energy deposited due to an increased multiple scattering probability, therefore overestimating absorbed dose.

By correcting for interaction depth the larger detector does measure the highest absorbed dose, shown in Fig. 6.6 and Table 6.2. While this effect is less influential than the depth of interaction, it should still be accounted for when choosing a detector for a dose measurement application, or

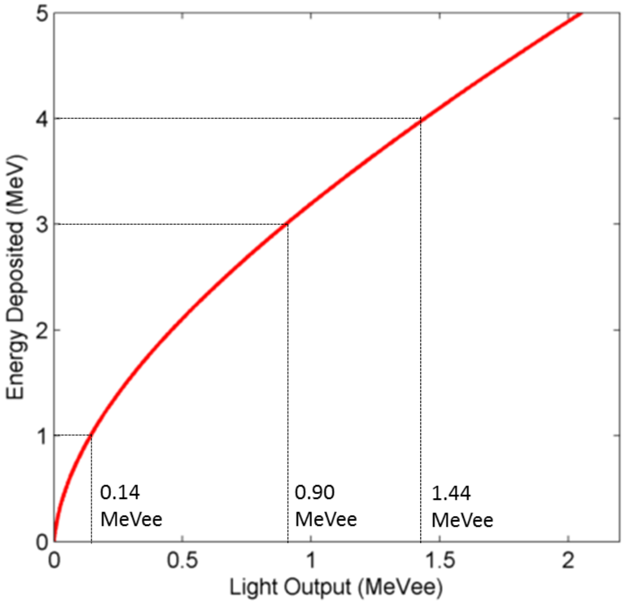

Figure 6.5: Comparison of light produced by neutrons scattering with different energy depositions in an EJ-309 detector cell.

Table 6.2: ^{252}Cf absorbed dose rates measured at 1 m with three different size detectors, depth normalized.

Detector Dimension (cm)	**Depth Normalized Absorbed Dose (μGy/hr)**
5.08	18.1 ± 0.3
7.62	18.6 ± 0.1
12.7	24.9 ± 0.1

comparing dose measured by different size detectors.

There are two competing effects that must be corrected for when using different size detectors for dose rate measurements: the depth of interaction, which decreases dose rates in relation to increased detector size, and multiple scatter probability, which increases dose rates in relation to increased detector size. For the fission spectrum measured here, 5.08 cm is a reasonable depth for a scintillator for dose rate measurements. Increasing the depth does not add appreciably to efficiency, but there is not a large amount of inactive material for mass normalization. The detector diameter should be minimized to reduce the need for corrections due to increased multiple scattering probability. While this analysis is relevant to the fission neutron spectrum, similar Monte Carlo

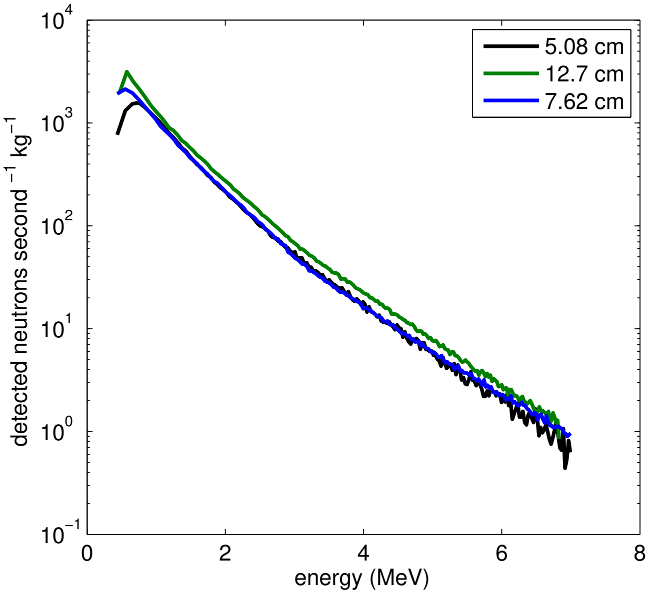

Figure 6.6: Energy deposited by ^{252}Cf neutrons in three cylindrical detectors, normalized by detector mass, corrected to 3.4 cm depth.

simulations could be used to predict the optimal detector for neutrons of different energy. Because scintillators are easily produced in a variety of shapes, the detector can be tailored to the specific application.

6.4 Isotopic Source Dose Rate Measurements

To demonstrate the organic-scintillator based dual-particle dosimeter, experiments were performed with a 5.08 cm diameter by 5.08 cm depth stilbene crystal. Data were collected using a CAEN V1730 digitizer from the x730 family discussed in Section 2.3. A light output threshold of 30.4 keVee was applied to the measurement to eliminate noise contribution to the spectrum. With the light output to energy conversions applied in this study, this threshold corressponds to 30.4 keV photon energy, and 384 keV neutron energy deposited in single scattering on hydrogen.

6.4.1 Photon Source Experiments

This detection system was used to measure a 92.4 μCi ^{137}Cs source, an 81.6 μCi ^{137}Cs source,

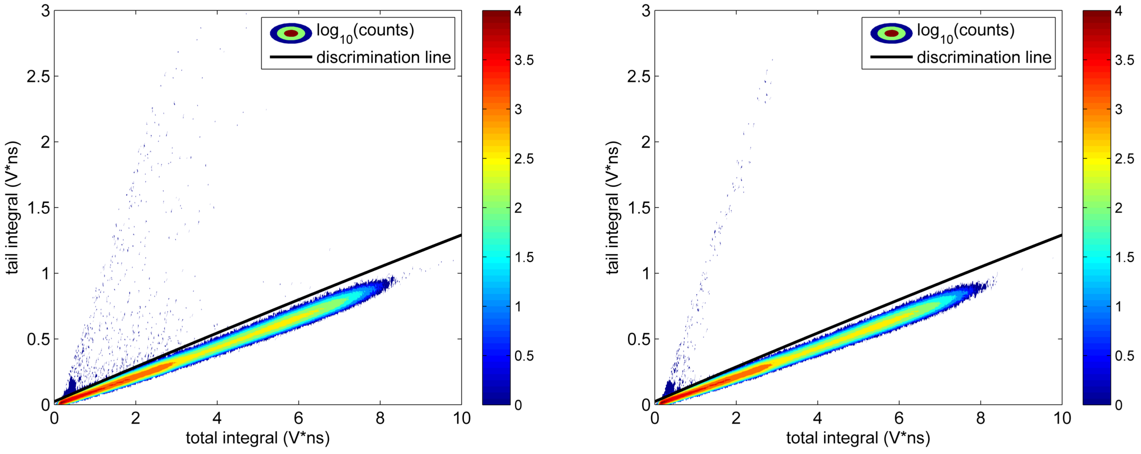

(a)

(b)

Figure 6.7: PSD tail integral vs. total integral scatter plot shown for photon source measurements, with no PUR threshold applied (a), and 65 bit PUR threshold applied (b).

a 41.6 μCi ^{22}Na source, and a 68.9 μCi ^{60}Co source, with 30 cm source-to-detector distance.

The first step of these experiments was to optimize the PSD to accurately discriminate between photons and neutrons, while preserving as many neutrons as possible. As discussed in Section 6.2, accurate PSD is especially critical in the low-energy range, where the high neutron biological effectiveness will most significantly contribute to the measured dose rate, and the on-board PUR algorithm must be employed with the list-mode acquired data.

While an aggressively low pile-up pulse threshold using the PUR routine (Section 2.3.3.2) eliminates as many pile-up pulses as possible, it also risks eliminating true counts based on noise in the pulse. This approach was balanced against preserving true counts of interest, and 65 bits was found to be the optimal value for this work. Fig. 6.7 shows the effect of applying this PUR threshold, whereby applying no threshold results in a false neutron dose equivalent rate of 6.4% of the photon dose, while the 65 bit PUR threshold reduces this rate to 2.7%, with negligible true photon dose equivalent rate losses.

The discrimination line for this study was developed using the SlicePSD algorithm[46], using a measurement of a ^{239}Pu-Be source, which has a low photon-to-neutron ratio. The discrimination line, shown in Fig. 6.8, was calculated with SlicePSD and was raised by increasing the tail-integral intercept to reduce the neutron dose observed from a photon-only source. Combined with the PUR

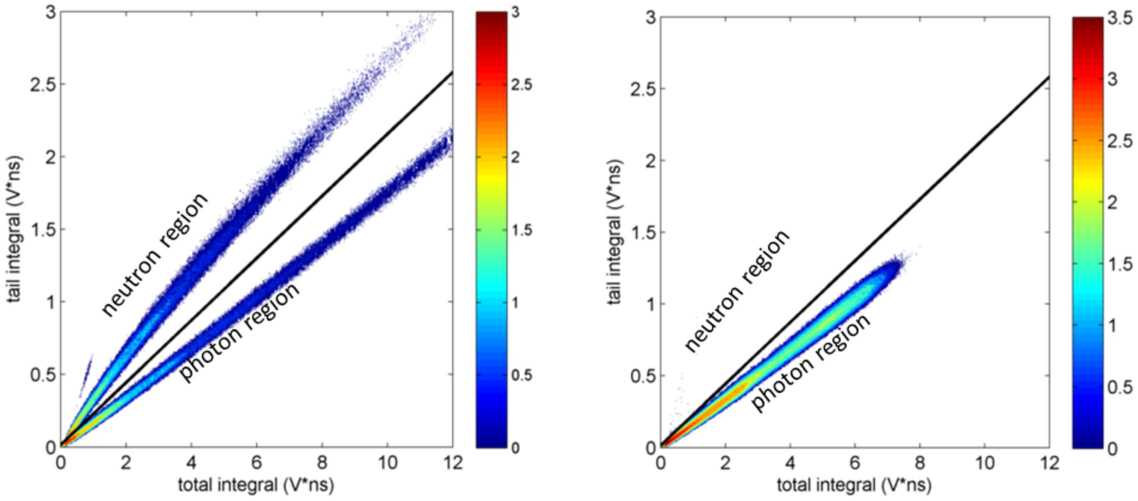

(a)

(b)

Figure 6.8: Charge integration PSD with chosen discrimination line applied to measurements of ^{239}Pu-Be (left), and ^{137}Cs, ^{22}Na, and ^{60}Co sources (right). Colorbar is $\log_{10}$ of counts per 0.01×0.01 V*ns pixel.

Table 6.3: Measured dose equivalent rates from photon-only sources.

	Background Subtracted Equivalent Dose Rate (μSv/hr)			
Isotope measured at 30 cm	**Stilbene Neutron**	**Stilbene Photon**	**RemBall Neutron**[a]	**Ion Chamber Photon**
^{137}Cs, ^{22}Na, ^{60}Co	0.20 ± 0.41	13.2 ± 0.5	0 ($large\ error$)	13.3 ± 1.5
Background	0.02 ± 0.01	0.06 ± 0.01	4 ($large\ error$)	0.12 ± 0.01

[a] Uncertainty determined visually

optimization this discrimination line minimizes dose from a photon only source, while preserving as much measured neutron dose as possible from the ^{239}Pu-Be source.

The right plot in Fig. 6.8 shows the optimal discrimination line applied to a measurement of photon-only sources. Very few neutrons are detected, whether true or misclassified; however, due to the large biological impact of neutrons in this energy range, a slight neutron dose rate above background is still registered. Table 6.3 shows the resulting neutron dose rate contribution. In the future, this effect may be further mitigated by integrating a small amount of lead shielding in front of the detector or by using a more robust pulse pile-up rejection or pulse recovery method.

Table 6.4: Measured dose equivalent rates from mixed-particle sources.

	Background Subtracted Equivalent Dose Rate (μSv/hr)			
Source measured at 50 cm	**Stilbene Neutron**	**Stilbene Photon**	**RemBall Neutron**[a]	**Ion Chamber Photon**
^{252}Cf, Bare	65.3 ± 3.0	10.5 ± 1.1	296 ± 33	13.7 ± 1.5
^{239}Pu-Be, Bare	14.5 ± 1.0	1.1 ± 0.14	76 ± 8.8	3.2 ± 0.4
Background	0.02 ± 0.01	0.06 ± 0.01	4 ($large\ error$)	0.12 ± 0.01

[a] Uncertainty determined visually

6.4.2 Mixed Source Experiments

The main focus of this study on neutron dose rates was explored using isotopic neutron sources. There are no pure neutron sources, so neutrons must be measured using a source that also produces photons. The previously described PSD method allows for efficient and accurate separation of these particles to calculate individual dose rate contributions.

The isotopic sources used for these mixed-source experiments were a ^{252}Cf spontaneous fission source with an activity of 2.27×10^6 fissions per second and a ^{239}Pu-Be source emitting 1.52×10^6 neutrons per second, both at the time of measurement. Measurements were performed with 50 cm between the source and detector face.

Table 6.4 compares equivalent dose rates from ^{252}Cf and ^{239}Pu-Be measured with the stilbene organic scintillator-based method and industry-standard dosimeters. Due to differences in dose rate calculation method, neutron dose rate measured lower with stilbene than with the RemBall. The stilbene-measured photon rate is lower than the traditional instrument as well, possibly due to differences in lower energy threshold. However, these rates show consistent discrepancies for different neutron spectra, and follow the general trend measured by the RemBall. The dose rates measured by the three instruments from these bare spectra and moderated spectra are compared to the same metric, developed through simulation, in the next section.

Table 6.5: Photon dose equivalent rates from ^{137}Cs, ^{22}Na, and ^{60}Co sources.

	Photon Equivalent Dose Rate (μSv/hr)		
Source at 30 cm	**Stilbene**	**MCNPX**	**Ion Chamber**
photon sources, bare	13.3 ± 0.6	13.8 ± 0.7	13.4 ± 1.5
photon sources, 0.64 cm lead shielded	9.1 ± 0.4	9.4 ± 0.5	8.6 ± 0.9
photon sources, 1.27 cm lead shielded	6.1 ± 0.3	6.3 ± 0.3	5.6 ± 0.6
photon sources, 2.54 cm lead shielded	2.8 ± 0.1	2.9 ± 0.1	2.8 ± 0.3

6.5 Comparisons with Simulation

The Monte Carlo transport code MCNPX 2.7.0 [72] was used to develop a benchmark equivalent dose rate value for comparison to dose rates measured both with stilbene and industry-standard survey meters. The benchmark dose rate was calculated with a track-length estimated flux tally in a simulated stilbene detector cell, modified by the ICRP 74 [129] fluence-to-dose-equivalent values to calculate the simulated equivalent dose rates. The same sources and experiments from Section 6.4 were replicated in these simulations. To compare dose rates from a variety of moderated source spectra in both measurement and simulation, the photon sources were incrementally shielded with 0.64 cm thick sheets of lead and the ^{252}Cf was shielded with 2.54 cm thick sheets of polyethylene.

6.5.1 Photon Source Experiments

Table 6.5 shows the comparison of the measured isotopic photon source dose rates with the simulated benchmark dose rates. These results show very good agreement between the measured and simulated equivalent dose rates. Fig. 6.9 shows the relative discrepancy of measured dose rates from the simulated benchmark. With a relative discrepancy of zero, the instruments would be in perfect agreement with simulation. While neither instrument is in perfect agreement, the organic scintillator dose rate detection method shows lower uncertainty and marginally better agreement to simulation than the ion chamber, with less than 5% difference from simulation.

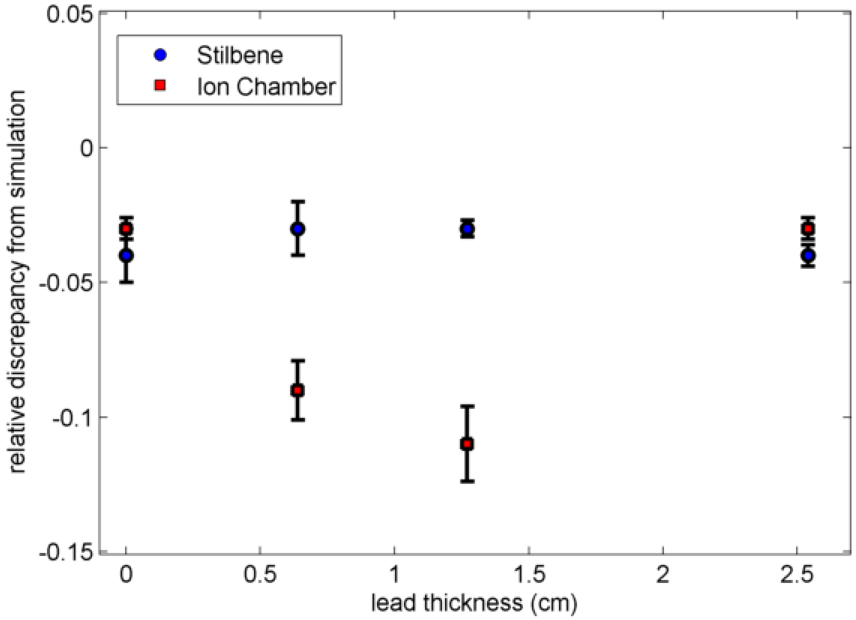

Figure 6.9: Relative discrepancy from simulated dose rate, measured with both the stilbene instrument and the traditional method.

6.5.2 Mixed Source Experiments

Neutron dose rates measured with the stilbene detector and RemBall are compared to the simulation benchmark in the same way as above. As shown in Table 6.4, the stilbene measured neutron dose rate is 65.3 μSv/hr, while the RemBall measures 296 μSv/hr, and the MCNPX dose rate is 276.8 μSv/hr, which is treated as the ”ground truth”. Of these three, the stilbene measured dose rate is the outlier due to previously discussed discrepancies in the calculation method. To correct for this discrepancy, the method was refined by using a calibration factor of 4.24, which calibrates the stilbene dosimeter to the bare ^{252}Cf spectrum. The dose rates measured with this calibration are shown in Table 6.6

Figure 6.10 shows the relative discrepancy of the ^{252}Cf neutron equivalent dose rate for the stilbene detector and the RemBall. The difference between the measured rates and the simulation for both instruments increases as the thickness of moderator increases and the spectrum is altered. This effect is expected for the RemBall because it is calibrated to a bare ^{252}Cf spectrum, and the change in neutron spectrum decreases the effectiveness of that calibration. While the stilbene has a proportional response to changes in neutron energy, an energy threshold of 340 keV is applied.

Table 6.6: Measured and simulated ^{252}Cf neutron dose equivalent rates with incremental polyethylene moderation. Both the stilbene dosimeter and RemBall have been calibrated to the ^{252}Cf neutron spectrum.

	Neutron Equivalent Dose Rate (μSv/hr)		
Source at 50 cm	**Stilbene**	**RemBall**	**MCNPX**
Unmoderated	276.8 ± 10.4	300 ± 33	276.8 ± 13.8
2.54 cm polyethylene	206.7 ± 7.9	260 ± 29	232.1 ± 11.6
5.08 cm polyethylene	140.7 ± 5.5	210 ± 23	170.4 ± 8.5
7.62 cm polyethylene	94.3 ± 3.8	130 ± 14	118.2 ± 5.9
10.16 cm polyethylene	63.6 ± 2.7	90 ± 10	80.2 ± 4.0
12.7 cm polyethylene	44.2 ± 1.9	65 ± 7	54.6 ± 2.7
15.24 cm polyethylene	31.9 ± 1.3	50 ± 6	37.9 ± 1.9

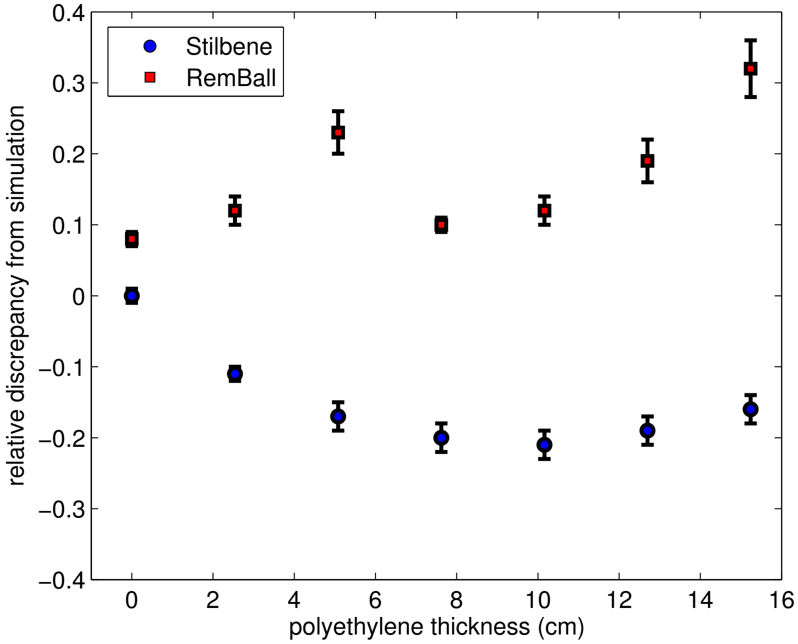

Figure 6.10: Relative discrepancy from simulated ^{252}Cf neutron dose rate, measured with both the stilbene instrument and the traditional method.

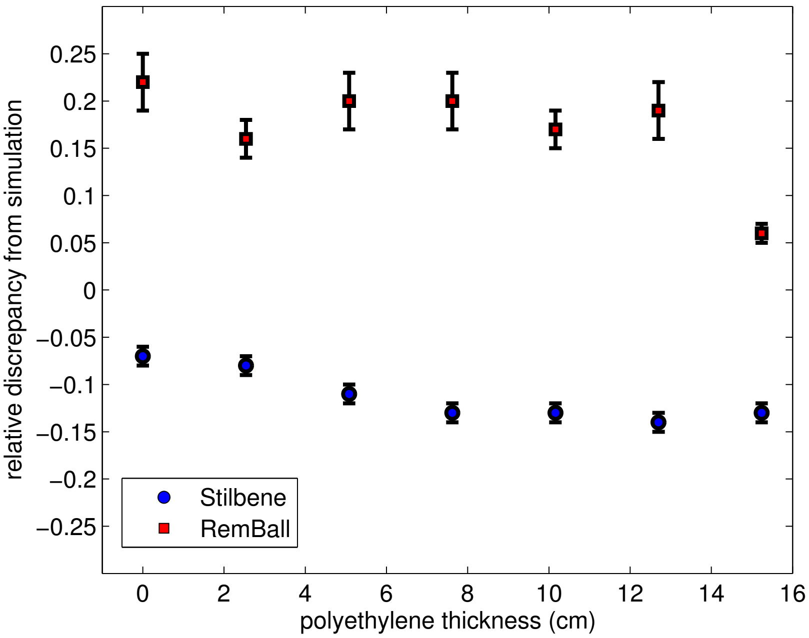

Figure 6.11: Relative discrepancy from simulated ^{239}Pu-Be neutron dose rate, measured with both the stilbene instrument and the traditional method.

Therefore, any neutron depositing less than 340 keV does not contribute to the measured dose rate, and the fraction of incoming neutrons below the threshold increases with thicker moderating material.

The instruments were also tested with a higher energy neutron spectrum, using a ^{239}Pu-Be source with the same moderator configuration as the ^{252}Cf experiments. The resulting relative discrepancies from this series of experiments are shown in Fig. 6.11. When measuring this higher energy neutron spectrum, the stilbene is much more accurate than the RemBall. The stilbene-measured dose rate again becomes less accurate with increased moderator thickness, but the effect is less pronounced than that measured in the ^{252}Cf series of experiments. MCNPX simulations of ^{239}PuBe neutrons [12] show that the fraction of the equivalent dose rate that is not detected by the stilbene ranges from 2.6% when the source is unmoderated, up to 15.6% when the source is moderated by 15.24 cm of polyethylene. In this configuration, 45% of incident neutrons fall below the detection threshold. While the threshold effect results in stilbene measured values falling below simulation, a factor of conservativism could be applied as necessary.

6.6 Conclusions

The method I present in this chapter offers a new technique for determining equivalent dose rates in mixed neutron and photon fields. This technique was enabled by employing organic scintillators , digital signal acquisition and processing, and energy-deposition to dose equivalent conversion. It was shown that this LET-based method for converting organic scintillator response to dose rate compares well with traditional survey instruments and simulated dose rates. Commonly available laboratory neutron and photon sources were examined through this work: ^{252}Cf, ^{239}Pu-Be, ^{137}Cs, ^{60}Co, and ^{22}Na. This study also demonstrated that the method responds well to changes in neutron energy spectrum when compared to traditional survey instruments with simulation as a benchmark. This method is accurate for different shielding scenarios and radiation spectra, and can be applied to many different situations and applications where dose resulting from predominately fast neutrons and photons is expected. Because stilbene cells can be produced in volumes from approximately 0.2-1500 cm^3, and this method is normalized with detector mass, it could be easily scaled to applications across a wide range of expected radiation field intensities.

To demonstrate this method in a scenario emulating a radiation therapy environment, future experiments could deploy the detector for high-energy photon measurements. These photons could be produced with a linac producing bremsstrahlung photons of energy high enough to induce photonuclear reactions, creating a mixed field. To facilitate the high photon-flux aspect of such a study, the method for PSD could be improved. A thin layer of lead could be added to the system to attenuate low-energy photons, improving PSD in the low-energy region. This reduction in photon counts could be accounted for in dose rate calculations, and would make for a simpler choice of discrimination line where the neutron and photon region overlap. A layer of lead would also reduce the probability of pulse pile-up, which was shown in Section 6.4 to require a reduction in neutron dose sensitivity through the choice of discrimination line. PSD could be further improved by using a neural network based approach for pulse identification and pile-up pulse recovery [76]. This method not only offers improved accuracy in particle discrimination, but the ability to recover the individual components of pile-up pulses, instead of discarding the entire pile-up event. In order to fully account for thermal neutron dose, future work could incorporate ^{6}Li glass [130, 131], CLYC [132], or EJ-270 [133] into the dosimeter to add sensitivity to thermal neutrons. This approach could enable the use of the dosimeter in a radiation environment containing fast neutrons, photons, and thermal neutrons.

CHAPTER 7

Summary, Conclusions, and Future Work

7.1 Summary

There are grave consequences of nuclear weapons material falling into the hands of either a state or non-state actor that intends to use it for nefarious purposes. Millions of kilograms of this material exist worldwide, and there are shortcomings currently in the technology deployed for the detection and security assurance of SNM. The use of active interrogation could close the gap for many of the necessary applications, but there are technological challenges to overcome. This dissertation demonstrates how emerging technologies can benefit the development of active interrogation methods to meet these challenges, and become more practical for widespread nuclear nonproliferation deployment.

Neutron interrogation can be used to detect not only SNM, but other contraband materials (drugs and explosives) as well. Chapter 3 discussed techniques using conventional detectors to identify the illicit materials based the detection with of unique photon-energy and neutron-time properties resulting from neutron interrogation. This study was expanded to a use of modern organic scintillators to determine fissile properties of SNM with neutron generator pulsing.

Photon interrogation is a powerful tool for SNM detection as well, and Chapter 4 outlined the installation and use of a commercial bremsstrahlung X-ray source to induce photonuclear reactions in SNM surrogate materials. Shielding was designed and implemented for personal protection and experimental optimization, and initial results were shown from experiments demonstrating photoneutron detection with an organic scintillator during the intense X-ray pulse.

The benefits of LPA Thomson scattering MPSs for photon active interrogation are discussed in Chapter 5. These sources offer very appealing photon production properties, and their use was presented as a possible solution to the challenging problem of verifying the contents of dry storage casks housing spent nuclear fuel. Shielding was also designed to enable future laboratory studies and mobile deployment of these sources. The use of Monte Carlo simulations for these studies was based on the validation by agreement with transmission experiments performed at the University of Nebraska.

Throughout this work, the dosimetric effects of the interrogating radiation has been a concern. The lower dose delivery of MPSs as a function of SNM detection capability was demonstrated in Chapter 5, and shielding designed through simulation for various accelerators depend on the relevance of the simulated results to actual dose delivered. It is difficult to directly compare traditional dosimeters to simulation, and therefore a method was developed to use organic scintillators for equivalent dose measurement. This method, presented in Chapter 6, can measure both neutron and photon dose rates simultaneously, and all conversions to dose are based on physical relationships.

7.2 Conclusions

Active interrogation can be an extremely powerful tool for the detection of SNM, even for the very difficult case of shielded HEU; however, technical and economical challenges have to this point in time prohibited its full scale deployment. The research presented in this dissertation offers possible avenues towards increasing the prevalence of this technology in the global security network.

By interrogating materials with neutrons, most shielding can be penetrated, and a variety of detectable signals can be induced in SNM or other contraband materials of interest. Neutron generators can provide a high flux of neutrons, and are readily available. However, the detectable neutrons resulting from induced reactions that signify SNM presence may be difficult to detect over source neutrons. Similarly, gamma-ray signals may be difficult to detect over source photons or neutron-induced photons from the surroundings.

Photon interrogation can be used to induce a neutron signal particles that stand out from the interrogating tool. Photofission neutrons induced by high-energy photons are a strong indicator of SNM presence. Bremsstrahlung accelerators can produce large amounts of X-rays up to the energy required, but most of the photons produced are much lower in energy. A bremmstrahlung photon source also emits in all directions. The lower-energy X-rays and X-rays not directed at the target only contribute to detection background and dose to bystanders without producing a usable signal. An LPA MPS offers a much more concentrated source of photons, both in energy and direction. An MPS can produce a higher quality signal of SNM presence faster than a bremsstrahlung source, and also delivers less dose than a bremsstrahlung source to the target and surroundings as a function of signal quality. Research is still underway to make these sources easily deployable, but they offer promising advantages over the currently available commercial bremsstrahlung sources.

Conventional radiation detectors can be used to detect illicit materials when interrogated, but the capabilites of commercially available sources for active interrogation applications can be enhanced with the use of more modern detection technology. Helium-3 capture detectors and NaI(Tl) inorganic scintillators were used to detect contraband materials interrogated by a neutron generator. The fast-timing and PSD capabilities of an organic scintillator combined with pulsed neutron irradiation of SNM also enabled quick determination of reactivity properties using prompt neutron detection. The PSD capability of organic scintillators used in this work also enables photoneutron detection in a highly photon-dominant environment, and the simultaneous measurement of neutron and photon dose rates with the same detector. The fast-timing of organic scintillator pulses also supports the detection of prompt photofission neutrons, increasing the available signal from interrogated SNM. Organic scintillators offer the advantages of affordability and mobility, because they are easily manufactured and do not require moderation.

By using a pulsed neutron generator with conventional radiation detectors, SNM was detected with DDAA and simulant drug and explosives were detected with TNA. The high flux of a the D-

T generator and signal timing isolation were essential for identifying an increase of counts in the nitrogen capture emission region for detection of the explosive compound simulant. However, in a real world situation this signal would likely be too weak, and more detector coverage with better capture gamma identification would be required for all TNA interrogations. The reactivity of a subcritical assembly was estimated by measuring the prompt neutron die-away profile after a generator pulse with an organic scintillator and inferring point-kinetics parameters with simulation. With the abundance of prompt neutrons available, the reactivity could be estimated quickly and accurately.

The detection of photoneutrons during the X-ray pulse of a commercial linac was also demonstrated with PSD-capable organic scintillators. This research provides the basis for photofission prompt neutron detection during intense photon interrogation. Methods for handling for the challenging PSD environment and pile-up pulses are currently under investigation, but the promise for this type of active SNM detection has been shown. Simulations based on advanced MPSs have also demonstrated the possibilities for these types of measurements with the additional benefits provided by a Thomson scattering source of photons.

The benefits of an MPS have been shown for a variety of metrics important to active interrogation. Radiography images of shielded SNM taken with an MPS exhibit higher contrast than those taken with a conventional bremsstrahlung source. An MPS has also been shown to be capable of taking transmission radiographs of very thick spent-fuel dry-storage casks, which contemporary bremsstrahlung photon sources cannot do. This technique would solve the problem of interest to the IAEA: verifying the contents of a spent-fuel dry-storage cask in a reasonable time while it remains sealed.

A method of measuring neutron and photon dose rates simultaneously in a single organic scintillator crystal was demonstrated, and the results compared favorably to traditional dose survey meter and simulation benchmarks. This work allows for development of a highly portable, accurate, and physically verifiable method for measuring both neutron and photon dose rates simultaneously.

7.3 Future Work

Research should continue in this important facet of nuclear security, and more mature detection techniques can serve to advance active interrogation technology towards full-scale deployment. Research into nonproliferation active interrogation capabilities offered by MPSs should continue, as development of these sources progresses in terms of energy spread, photon output, and footprint reduction. Once at a deployable stage, cost, maintenance support, and ruggedness of these sources will likely need to be improved over time, but have potential for very low energy-spread, high photon-output, and portability. Medical linacs currently available offer increased ruggedness, affordability, and streamlined maintenance over complex, custom Rhodotrons. While these medical accelerators are not currently designed to be portable, a motivated user could theoretically modify such an accelerator installation to be truck-portable. In this case, the broad-angle emission of photons by a bremsstrahlung source would create challenges for shielding, and an MPS has a distinct advantage for shielding portability.

Detecting shielded nuclear material in a short time will require large amounts of interrogating particles, and the detection system will need to efficiently detect signal particles while rejecting background and the interrogation flash. The pulsed nature of both a linac and an MPS is advantageous for rejecting background and collecting timing information of signature detection. While integrating detectors can be useful for transmission radiography, detection techniques relying on time or energy information must be fast, and efficient over a large energy range. A distributed network of small face-area detectors could serve to reduce piled-up pulse effects when compared to smaller numbers of large detectors. The detection of photofission neutrons should also be improved with advanced PSD and pile-up pulse recovery algorithms based on machine learning [76].

Further testing with reactivity analysis of neutron probed SNM should be performed, across a wide range of k_{eff} values. This testing would determine the limits of the method, and direct comparison with capture detectors would give insight into advantages offered by fast neutron detection. Low-Z contraband detection could be further studied by examining the limits of shielded material detection. Utilizing MPSs for photofission characterization could also be applied to more fundamental research. The unique energy tunability and low energy-spread of MPSs also offer opportunities for improving the quality of available photonuclear data in support of security and other applications.

Dose rate detection with organic scintillators could be improved by incorporating a thermal-neutron-sensitive material such as ^{6}Li glass, CLYC, or EJ-270 to expand the neutron energy-sensitivity range. Incorporation of one of these materials would make a detector based on this method more accurate in heavily moderated neutron environments. Such a detector should also be tested in an accelerator environment, incorporating many of the techniques discussed in the context of active interrogation signature detection with organic scintillators.

Interrogating sources, detectors, geometry, and data-processing algorithms will need to be tailored to each specific application. The improvements to current techniques discussed in this dissertation should help to overcome the difficult challenge of detecting shielded special nuclear material, without slowing down the speed of global commerce.

APPENDIX A

Real Time TNA script

```
# Real Time Photon Energy Plotting Script
# C.A. Miller, 1/17/2019
#
# Modified from He-3 Module DieawayRT_DAFCA_v1_3
# script for use in Demo
#
# Calculates pulse time in relation to accelerator pulse time,
# records energy from DAFCA long gate
#
# Read in short measurement folders
# Pull in detected pulse time, check if greater than next recorded
  accelerator pulse
# if so, increment accelerator pulse
# if not, dt is (pulse time - accelerator pulse time)
# record energy
#
# Animates, Runs DAFCA, Real-time timing optimized,
# multiprocessing for DAFCA call enabled

import math
import json
import numpy as np
import struct
import time
from matplotlib.animation import FuncAnimation
import matplotlib.pyplot as plt
import subprocess
from multiprocessing import Process
from pathlib import Path

BGfilename = 'ABG_30min_200Hz'
numBins = 400
calibrationValue = 8.5525e-04
calibrationValueBG = 8.2751e-04

channel=13
timeCut = 1 # 1 = on, 0 = off
pulseRate = 200 # Hz
```

```
duty = 0.05
# time after pulse to accept counts
minTimeBuffer = 0.00001
# Pulse on time plus time buffer
minTime = ((1/pulseRate) * duty) + minTimeBuffer
# Full period
maxTime = (1/pulseRate)

#Initializations
detTime=[]
BGdetTime=[]
detEnergy = []
BGdetEnergy=[]
figure=plt.figure()
folder = 0

def run_win_cmd(cmd):
    process = subprocess.Popen(cmd,
                               shell=False,
                               stdout=subprocess.PIPE,
                               stderr=subprocess.PIPE).pid


def update(frame):
     accTime=[]
     BGaccTime=[]
     dat=[]
     BGdat=[]
     start = time.time()

     figure.clf()
     global folder
     folder=folder+1
     print (folder)
     nextfile=Path(str(folder+1)+'/dataFile0.dat')
     #check if next file exists (proves current file is complete)
     while nextfile.exists()==False:
         time.sleep(0.1)
     with open(str(folder)+'/dataFile0.dat', mode='rb') as datFile:
         datRead = datFile.read()
     with open(BGfilename+'/'+str(folder)+'/dataFile0.dat', mode='rb') as BGdatFile:
         BGdatRead = BGdatFile.read()

     # parses binary header file, 24 bytes per pulse
     dat=struct.unpack("iihhhhii" * (len(datRead)//24), datRead)
     BGdat = struct.unpack("iihhhhii" * (len(BGdatRead)//24), BGdatRead)

     # check if any time tags are less than the first time tag
     startTime=dat[6]
     for x in range(len(dat)):
        if (x-6)%8==0 and dat[x] < startTime:
            startTime=dat[x]

```

```
    # check if any BG time tags are less than the first time tag
    BGstartTime=BGdat[6]
    for x in range(len(BGdat)):
       if (x-6)%8==0 and BGdat[x] < BGstartTime:
           BGstartTime=BGdat[x]

    # Signal files accelerator pulse time recording
    #extract accelerator pulse time from channel 0 (2nd if: condition)
    for x in range(len(dat)):
        if (x-6)%8==0 and dat[x-4]==0:
            # make sure accTime is not empty,
            #then that it's not reading both edges of pulse
            if len(accTime) > 0:
                if (dat[x]-startTime)*2e-9 - accTime[len(accTime)-1] > 5e
  -6:
                    accTime.append((dat[x]-startTime)*2e-9)
            else:
                accTime.append((dat[x]-startTime)*2e-9)
                # accelerator pulse time in sec.,
                # (original timestamp in units of 2 ns)
                # with first pulse offset subtracted

    # BG files accelerator pulse time recording
    #extract accelerator pulse time from channel 0 (2nd if: condition)
    for x in range(len(BGdat)):
        if (x-6)%8==0 and BGdat[x-4]==0:
            # make sure accTime is not empty,
            #then that it's not reading both edges of pulse
            if len(BGaccTime) > 0:
                if (BGdat[x]-BGstartTime)*2e-9 - BGaccTime[len(BGaccTime)
  -1] > 5e-6:
                    BGaccTime.append((BGdat[x]-BGstartTime)*2e-9)
            else:
                BGaccTime.append((BGdat[x]-BGstartTime)*2e-9)
                # accelerator pulse time in sec.,
                # (original timestamp in units of 2 ns)
                # with first pulse offset subtracted

    # signal files detected time calculations
    n=0
    pulseTime=0
    #Pulling detected times and recording energy
    for x in range(len(dat)):
        if (x-6)%8==0 and dat[x-4]!=0:
            # if detected time is greater than next acc pulse time,
            # break at last accelerator pulse,
            # avoids overstepping array
            while (dat[x]-startTime)*2e-9 > accTime[n]:
                 if n==len(accTime)-1:
                     break
                 n=n+1
                 # increment and go to subtract
                 # that acc pulse time off
                 pulseTime=accTime[n-1]
```

```
          detTime.append((dat[x]-startTime)*2e-9-pulseTime)
          if timeCut == 1: # Time filtering
               # check that time fits in range
               if ((dat[x]-dat[6])*2e-9-pulseTime) > minTime + minTimeBuffer and ((dat[x]-dat[6])*2e-9-pulseTime) < maxTime and dat[x-4]==channel :
                    detEnergy.append(dat[x-1]*calibrationValue)
          else:             # No time filtering, record all pulses
               detEnergy.append(dat[x-1]*calibrationValue)

  # BG files detected time calculations
  n=0
  BGpulseTime=0
  #Pulling detected times and recording energy
  for x in range(len(BGdat)):
      if (x-6)%8==0 and BGdat[x-4]!=0:
          # if detected time is greater than next acc pulse time,
          # break at last accelerator pulse,
          # avoids overstepping array
          while (BGdat[x]-BGstartTime)*2e-9 > BGaccTime[n]:
               if n==len(BGaccTime)-1:
                   break
               n=n+1
               # increment and go to subtract
               # that acc pulse time off
               BGpulseTime=BGaccTime[n-1]
          BGdetTime.append((BGdat[x]-BGstartTime)*2e-9-BGpulseTime)
          if timeCut == 1: # Time filtering
               # check that time fits in range
               if ((BGdat[x]-BGdat[6])*2e-9-BGpulseTime) > minTime + minTimeBuffer and ((BGdat[x]-BGdat[6])*2e-9-BGpulseTime) < maxTime and BGdat[x-4]==channel :
                    BGdetEnergy.append(BGdat[x-1]*calibrationValueBG)
          else:             # No time filtering, record all pulses
               BGdetEnergy.append(BGdat[x-1]*calibrationValueBG)

  signalHist = np.histogram(detEnergy,bins=numBins, range=(0,16383*calibrationValue))
  signalHist0 = np.array(signalHist[0])
  signalHist1 = np.array(signalHist[1])

  BGHist = np.histogram(BGdetEnergy,bins=numBins, range=(0,16383*calibrationValue))
  BGHist0 = np.array(BGHist[0])
  BGHist1 = np.array(BGHist[1])


  line=plt.plot(signalHist1[1:],signalHist0,label='simulant')
  line=plt.plot(BGHist1[1:],BGHist0,label='active background')
  figure.gca().relim()
  plt.xlim(-1*calibrationValue,16383*calibrationValue)
  plt.xlabel('Energy (MeV)')
  plt.ylabel('Photon Counts')
  plt.yscale('log',nonposy='clip')
```

```
    plt.legend()
    plt.title('simulant vs. background')
    figure.gca().autoscale_view(tight=None, scalex=False, scaley=True)
    print ('Update took', time.time()-start, 'seconds.')
    return line, folder

if __name__ == '__main__':
    p = Process(target=run_win_cmd,args=('DAFCA8.exe',))
    p.start()
    p.join()

    animation = FuncAnimation(figure, update, interval=1000, repeat=False, save_count=0)

    plt.show()
```

APPENDIX B

Real Time Neutron Die-Away Script

```
# Real Time Dieaway Script
# C.A. Miller, 7/10/2018
# updated 1/2019
#
# Developed for He-3 Module use in Demo
#
# Read in short measurement folders
# Pull in detected pulse time, check if greater than next recorded
#     accelerator pulse
# if so, increment accelerator pulse
# if not, dt is pulse time - accelerator pulse time
#
# Animates, Runs DAFCA, Real-time timing optimized,
#    multiprocessing for DAFCA call enabled

import math
import json
import numpy as np
import struct
import time
from matplotlib.animation import FuncAnimation
import matplotlib.pyplot as plt
import subprocess
from multiprocessing import Process
from pathlib import Path

BGfilename = 'ABG_5min'
numBins = 250 #@0.005 sec range,10 us bins
period = 0.005
detTime = []
BGdetTime = []

figure=plt.figure()
folder = 0

def run_win_cmd(cmd):
    process = subprocess.Popen(cmd,
                               shell=False,
```

```
                               stdout=subprocess.PIPE,
                               stderr=subprocess.PIPE).pid


def update(frame):
     accTime=[]
     BGaccTime=[]
     dat=[]
     BGdat=[]
     start = time.time()

     figure.clf()
     global folder
     folder=folder+1
     print (folder)
     nextfile=Path(str(folder+1)+'/dataFile0.dat')
     #check if next file exists (proves current file is complete)
     while nextfile.exists()==False:
         time.sleep(0.1)

     with open(str(folder)+'/dataFile0.dat', mode='rb') as datFile:
         datRead = datFile.read()
     with open(BGfilename+'/'+str(folder)+'/dataFile0.dat', mode='rb') as
   BGdatFile:
         BGdatRead = BGdatFile.read()

     # parses binary header file, 24 bytes per pulse
     dat=struct.unpack("iihhhhii" * (len(datRead)//24), datRead)
     BGdat=struct.unpack("iihhhhii" * (len(BGdatRead)//24), BGdatRead)

     # check if any time tags are less than the first time tag
     startTime=dat[6]
     for x in range(len(dat)):
        if (x-6)%8==0 and dat[x] < startTime:
            startTime=dat[x]

     # check if any BG time tags are less than the first time tag
     BGstartTime=BGdat[6]
     for x in range(len(BGdat)):
        if (x-6)%8==0 and BGdat[x] < BGstartTime:
            BGstartTime=BGdat[x]

     # Signal files accelerator pulse time recording
     #extract accelerator pulse time from channel 0 (2nd if: condition)
     for x in range(len(dat)):
         if (x-6)%8==0 and dat[x-4]==0:
         # make sure accTime is not empty,
         #then that it's not reading both edges of pulse
             if len(accTime) > 0:
                 if (dat[x]-startTime)*2e-9 - accTime[len(accTime)-1] > 5e
   -6:
                     accTime.append((dat[x]-startTime)*2e-9)
             else:
                 accTime.append((dat[x]-startTime)*2e-9)
```

```
                #accelerator pulse time in sec.,
                #(original timestamp in units of 2 ns)
                # with first pulse offset subtracted

    # BG files accelerator pulse time recording
    #extract accelerator pulse time from channel 0 (2nd if: condition)
    for x in range(len(BGdat)):
        if (x-6)%8==0 and BGdat[x-4]==0:
        # make sure accTime is not empty,
        # then that it's not reading both edges of pulse
            if len(BGaccTime) > 0:
                if (BGdat[x]-BGstartTime)*2e-9 - BGaccTime[len(BGaccTime)
  -1] > 5e-6:
                    BGaccTime.append((BGdat[x]-BGstartTime)*2e-9)
            else:
                BGaccTime.append((BGdat[x]-BGstartTime)*2e-9)
                # accelerator pulse time in sec.,
                # (original timestamp in units of 2 ns)
                # with first pulse offset subtracted


    # signal files detected time calculations
    n=0
    pulseTime=0
    #Pulling detected times and subtracting off acc pulse time
    for x in range(len(dat)):
        if (x-6)%8==0 and dat[x-4]!=0:
            # if detected time is greater than next acc pulse time,
            # break at last accelerator pulse,
            # avoids overstepping array
            while (dat[x]-startTime)*2e-9 > accTime[n]:
                 if n==len(accTime)-1:
                     break
                 n=n+1
                 # increment and go to subtract
                 # that acc pulse time off
                 pulseTime=accTime[n-1]
            detTime.append((dat[x]-startTime)*2e-9-pulseTime)

    # BG files detected time calculations
    n=0
    BGpulseTime=0
    #Pulling detected times and subtracting off acc pulse time
    for x in range(len(BGdat)):
        if (x-6)%8==0 and BGdat[x-4]!=0:
            # if detected time is greater than next acc pulse time,
            # break at last accelerator pulse,
            # avoids overstepping array
            while (BGdat[x]-BGstartTime)*2e-9 > BGaccTime[n]:

                 if n==len(BGaccTime)-1:
                     break
                 n=n+1
                 # increment and go to subtract
```

```
                # that acc pulse time off
                BGpulseTime=BGaccTime[n-1]
            BGdetTime.append((BGdat[x]-BGstartTime)*2e-9-BGpulseTime)

    signalHist = np.histogram(detTime,bins=numBins, range=(0,period))
    signalHist0 = np.array(signalHist[0])
    signalHist1 = np.array(signalHist[1])

    BGHist = np.histogram(BGdetTime,bins=numBins, range=(0,period))
    BGHist0 = np.array(BGHist[0])
    BGHist1 = np.array(BGHist[1])

    line=plt.plot(signalHist1[1:],signalHist0,label='SNM')
    line=plt.plot(BGHist1[1:],BGHist0,label='active background')
    figure.gca().relim()
    plt.xlim(-0.0001,period+0.0001)
    plt.xlabel('time (seconds)')
    plt.ylabel('neutron counts')
    plt.yscale('log',nonposy='clip')
    plt.legend()
    figure.gca().autoscale_view(tight=None, scalex=False, scaley=True)
    print ('Update took', time.time()-start, 'seconds.')
    return line, folder

if __name__ == '__main__':
    p = Process(target=run_win_cmd,args=('DAFCA8.exe',))
    p.start()
    p.join()

    animation = FuncAnimation(figure, update, interval=1000, repeat=False, save_count=0)

    plt.show()
```

APPENDIX C

Linac MCNP Input

```
c NEL building 1040 Lab
c Linac Input Model, Shielding Testing
c Cameron Miller, cmillera@umich.edu
c 5/22/2018
c
c
c CELL CARDS
40 0 99  $ graveyard
41 0 -99 702 707 708 709 715 #7180 #7190 74 75 $ outside outer wall
42 6 -2.3 84 -702 703 715 718 719 94 96 $ walls, floor, ceiling concrete
740 6 -2.3 -74                    $ East Wall Extension
43 20 -0.001205 -704 715 706 70 #870 91 92 30 112 116 117 118 119 120
      $ air inside shield, outside cyclotron
700 20 -0.001205 -70 03 60 61 62 71
     64 65 66 67 68 69 $ Air inside Linac enclosure
44 20 -0.001205 -703 705 715 716 718 719 712 10 802 804 805 706 111
     #790 #800 #810 #820 #830 #55 801 803 806 91 92 93 #850 #860
     #880 112 17 110 115 711 90 120 $ air inside room, outside shield
750 2 -7.92 -75                          $ Steel Wall in Source Room
840 20 -0.001205 -84 $ south gate air
8021 20 -0.001205 -802 $ source door air
8041 20 -0.001205 -804 $ storage door air
8051 20 -0.001205 -805 $ electrical door air
45 6 -2.3 -705 706 704 715 7040 91 92 112 120 $ concrete shield
1200 20 -0.001205 -120 $ Void for Vent
53 6 -2.3 -716              $ Source Room Wall
46 20 -0.001205 -706  $ air in beam port
7041 20 -0.001205 -7040  $ air in beam port
51 6 -2.3 -715  $ large beam
7180 6 -2.3 -718 $ crossed beam
7190 6 -2.3 -719 $ crossed beam
55 6 -1.15 -717 $ East Wall
47 7 -1.5 -707  $
48 7 -1.5 -708  $
49 7 -1.5 -709  $
790 6 -2.3 -79         $ Storage Room West Wall
800 8 -0.69 -80         $ Storage Room East Wall
810 6 -2.3 -81         $ Pillar 1
```

```
820 6 -2.3 -82         $ Pillar 2
830 6 -2.3 -83         $ Pillar 3
850 6 -2.3 -85         $ south wall half pillar
860 8 -0.69 -86        $ west wall drywall
870 6 -2.3 -87         $ concrete protrusion (adjusted for shielding)
880 6 -2.3 -88         $ large pillar
8010 6 -2.3 -801 802   $ source storage door
8020 8 -0.69 -803 804 805 #7190 $ drywall door wall
8030 8 -2.3  -806        $ hollow brick wall
c
52 23 -1.08 -711 715  $ BPE layer
54 23 -1.08 -712 715  $ BPE Backstop
c
010 9 -19.4 -01 $ Tungsten Converter
020 10 -8.96 -02 $ Copper Backing
030 0 -03 02 01 $ Source Writing Sphere
c
c Collimator
600 20 -0.001205  -60 03 113 114        $ Collimator Bore
610 9  -19.4 -61 60 72  $ Tungsten
620 1  -11.34 -62 61 72 73 $ Lead
c 630 1  -11.34 -63 706 $ Extra Lead
c 760 1 -11.34 -76 $ West Extra Lead
c 770 1 -11.34 -77 $ East Extra Lead
640 2  -7.92 -64 71  $ Steel Square
650 23 -1.08 -65 62 60 -70 71 $ BPE cylinder
660 2  -7.92 -66 62 60  $ Steel Square
670 23 -1.08 -67 61 -70 $ BPE cylinder
680 23 -1.08 -68 69   $ BPE smaller cylinder
690 20 -0.001205 -69  $ smaller cylinder bore
710 23 -1.08 -71 72   $ Plastic Front Plate
720 20 -0.001205 -72 706  113 114      $ Front Collimator Bore
730 9 -19.4 -73 72    $ Front Tungsten
c
c Extra Beams
900 6 -2.3 -90 $ Beam Above BPE
910 6 -2.3 -91 $ West N/S Beam
920 6 -2.3 -92 $ East N/S Beam
930 6 -2.3 -93 $ South E/W Beam
940 20 -0.001205 -94 $ Cavity for Steel Pan
960 20 -0.001205 -96 719 718 79 801 803 804 86 83 717 80 806 716
      $ Cavity for Steel Pan
c
c
c Target
100 1 -11.34 -10 $ Lead Block Target
c
c RF BOX
300 2 -1.082 -30 $ RF Box
c
c LEAD PLUG
1120 1 -11.34 -112 706    $ Lead Collimator plug
1130 1 -11.34 -113 114    $ Lead Interior Plug
1140 20 -0.001205 -114 03 $ Lead Interior Plug bore
```

```
1150 23 -1.08 -115  706   $ BPE Collimator Covering
c
c Extra Shielding
1160 6 -2.3   -116      $ Concrete West
1170 6 -2.3   -117      $ Concrete East
1180 1 -11.34 -118      $ Lead Covering
1190 1 -11.34 -119      $ More Lead
c
c Beamstop
c
1100 23 -1.08 -110 111 $ BPE Beamstop
1110 1 -11.34 -111   $ Lead Beamstop
c
c
c DETECTOR
170 99 -1.16   -17             $ Stilbene Cell #1
c
c END CELL CARDS *****************************************************

c SURFACE CARDS
99 S 1000 1000 250 2000 $ bounding sphere
c
01 1 RCC 260.25 250 121.92 0.2286 0 0 1.27      $ Tungsten Converter
02 1 RCC 260.4876001 250 121.92 0.1490 0 0 1.27 $ Copper Backing
03 1 S 260.25 250 121.92 3                      $ Source Writing Sphere
c
c ROOM 20 m x 20 m x 5 m, wall/floor/ceiling
702 RPP -15.24 2063.96 -15.24 2015.24 -15.24 439.42 $ outer
703 RPP 0 2000 0 2000 0 375.92 $ inner
715 RPP 0 2000 448.4 538.2 282.8 436.1 $ Large Beam
718 RPP 947 1008.3  538.2 1566.6  268.3 445.5     $ crossed beam
719 RPP 0 947  915.6 991.2   284.9 445.5            $ short beam
717 RPP 0 2000 1566.6 1577.9 0 403.86 $ East Wall
74  RPP 2063.96 2094.44 876.74 2014 -15.24 439.42 $ East Wall extension
75  RPP 2094.441 2338.281 998.66 1018.98 -15.24 439.42 $ Steel Door
c
81 RPP  946.025 1000  932.0 985.34   0 268.3 $ Pillar 1
82 RPP  774.06 827.4  932.0 985.34   0 284.9 $ Pillar 2
83 RPP  774.06 827.4  1350.6 1404.1  0 403.86 $ Pillar 3
84 RPP 2000   2063.96  602.6  876.7  0 243.7 $ South wall gate
85 RPP 1979.6 2000     448.4  538.2  0 282.8 $ South wall half-pillar
86 RPP 490.64 1989.84  0 11.3   0 375.91 $ west wall drywall
87 RPP 357.34  450     0  9.525 0 164   $ west wall concrete protrusion
88 RPP 930.8  1021.9  448.4  538.2 0 282.8 $ large pillar
c
79  RPP   0    483.2  833.38  853.7  0 403.86 $ Storage Room West Wall
801 RPP 462.88 483.2  669.92  833.38 0 403.86 $ Source Storage Room door Wall
802 RPP 462.88 483.2  721.5   823.7  0 219.5 $ Source Storage Room door hole
80  RPP   0    471.9 1106.16 1117.46 0 403.86 $ Storage Room East Wall
803 RPP 471.9  483.2  853.7  1419.1  0 403.86 $ Room door dryWall
804 RPP 471.9  483.2  986.1  1088.3  0 219.5 $ Storage Room door hole
805 RPP 471.9  483.2  1293.6 1395.8  0 219.5 $ electrical Room door hole
```

```
806 RPP 462.88 483.2  1419.1 1566.6  0 403.86 $ hollow brick wall
c
c Drywall is 11.3 cm thick
c
c SHIELD
704 RPP 0 450 0 487.64 0 284.48 $ open space, inner shield wall
7040 RPP 0  102.2 487.64 528.28 0 219.5 $ Storage Room door hole
705 RPP 0 490.64 0 528.28 0 284.48$ outer shield wall (704+x), change w 706
120 RPP 449.99 490.65 164.91 286.83 248.92 284.48 $ Void for Vent
716 RPP 0 483.2 649.6 669.92 0 403.86 $ Source Storage Room Wall
c BEAM PORT
706 RCC 392.5 250 71.12 110 0 0 2.54 $ 1 inch radius, change w 705
c DIRT
707 RPP -100 -15.24 -100 2015.24 -100 515.24 $ north dirt
708 RPP -15.24 2015.24 -100 -15.24 -100 515.24 $ south dirt
709 RPP -15.24 2015.24 -15.24 2015.24 -100 -15.24
c
c
c BPE LAYER
711 RPP 0 440.64 0 538.2 294.64 304.8 $ BPE layer
712 RPP 1989.84 2000 0 448.4 0 375.9199 $ BPE Backstop
c
c Collimator
60 1 RCC 254.42 250 121.92 25.4 0 0 12.065 $ collimator bore
61 1 RCC 254.42 250 121.92 22.86 0 0 24.13 $ tungsten
62 1 RCC 279.82 250 121.92 29.21 0 0 41.275 $ lead
71 1 RCC 309.03 250 121.92 2.54 0 0 41.275 $ plastic front plate
72 1 RCC 279.82 250 121.92 31.75 0 0 14.4526 $ front collimator bore
73 1 RCC 279.82 250 121.92 11.43 0 0 24.13 $ front tungsten
c 5" behind the target, 17" in front of target, based on count of square poly slabs
c 20 cm diameter tungsten
c 40 cm diameter lead
c
c 1" steel, 12" large BPE, 1" steel, 8" large BPE, 60" BPE
c 2.54 cm steel, 30.48 cm large BPE, 2.54 cm steel, 20.32 cm large BPE, 152.4 cm BPE
c 121.92 cm square, 72.39 cm radius, 121.92 cm square, 72.39 cm radius, 50.8 cm radius
64 1 RPP 309.03 311.57 189.04 310.96 60.96 182.88  $ Large steel square
65 1 RCC 279.82 250 121.92 29.21 0 0 72.39        $ Large BPE cylinder
66 1 RPP 277.28 279.82 189.04 310.96 60.96 182.88 $ Large steel square
67 1 RCC 254.42 250 121.92 22.86 0 0 72.39        $ Large BPE cylinder
68 1 RCC 102.02 250 121.92 152.4 0 0 50.8         $ Smaller BPE cylinder
69 1 RCC 102.02 250 121.92 152.4 0 0 10           $ Smaller BPE Bore
70 1 RPP 102.02 311.57 189.04 310.96 60.96 182.88  $ Linac Enclosure Surface
c
c 63 RPP 398.9 429.38 189.04 310.96 0 132.15 $ Extra Lead
c 76 RPP 335 422.9 158.56 189.04 0 132.15 $ West Extra Lead
c 77 RPP 335 422.9 310.96 341.44 0 132.15 $ East Extra Lead
c
c Extra Beams
90 RPP 359.36 400 0 448.4 322.58 375.9199 $ Beam Above BPE
```

```
91 RPP 400 1050.24 104.14 144.78 322.58 375.9199 $ West N/S Beam
92 RPP 400 1050.24 327.75 368.39 322.58 375.9199 $ East N/S Beam
93 RPP 1050.24 1090.88 11.3 448.4 322.58 375.9199 $ South E/W Beam
94 RPP 400 1050.24 144.78 327.75 375.92 403.86 $ Cavity for steel pan area
96 RPP 0 2000 538.2 2000 375.92 403.86 $ Cavity for steel pan area
c
c Target
10 RPP 1729.68 1750 247.46 252.54 66.04 76.2 $ Lead block target
c
c RF BOX
30 1 RPP 113.13 235.05 189.04 310.96 183.3 305.22 $ RF Box
c
c LEAD PLUG
112 RPP 450 490.64 213.17 286.83 34.29 107.95   $ Lead Collimator Plug
113 1 RCC 260.77 250  121.92  19.05  0 0 12.065 $ Lead Interior Plug
114 1 RCC 260.77 250  121.92  19.05  0 0  6.985 $ Lead Interior Plug Bore
115 RPP 491 501.16 210 290 0 134                $ BPE Collimator Covering
c
c Extra Shielding
116 RPP 392.52 450 203.645 244.285 0 91.44      $ Concrete West
117 RPP 392.52 450 255.715 296.355 0 91.44      $ Concrete East
118 RPP 392.52 450 213.81  286.20  91.44 93.98  $ Lead Covering
119 RPP 392.52 450 229.68  270.32  93.98 121.87 $ More Lead
c
c BeamStop
110 RPP 1959.36 1989.84 204.84 295.16 0 120.16 $ BPE Beamstop
111 RPP 1969.52 1989.84 215 285 0 110         $ Lead Beamstop
c
c DETECTOR
17  RCC 1739.84 300 71.12 0 5.08 0 2.54
c 2x2 in. stilbene #1, 50 cm from target
c END SURFACE CARDS **************************************************

c DATA CARDS
MODE   N P E
imp:n 0 1 70r
imp:p 0 1 70r
imp:e 0 1 70r
phys:p 20 0 0 1
phys:n J 20
phys:e 20
cut:n 2J 0 0
cut:p 2J 0 0
cut:e J 0.01 0 0
c
TR1 80.95 0 -50.8
c
c MATERIAL SPECIFICATION
c Lead rho = 11.34
m1 nlib=60c plib=04p pnlib=70u
     82206  -0.255
     82207  -0.221
     82208  -0.524
c steel appr. as iron, rho = 7.92
```

```
m2 nlib=60c plib=04p pnlib=70u
     26054 -0.0585
     26056 -0.9175
     26057 -0.0212
     26058 -0.0028
c Concrete, Ordinary, rho = 2.300
m6  nlib=60c plib=04p pnlib=70u $ Neutron
     1001 -0.022100
     6000 -0.002484
     8016 -0.574930
     11023 -0.015208
     12000 -0.001127
     13027 -0.019953
     14000 -0.304626
     19000 -0.010045
     20000 -0.042951
     26054 -0.000376
     26056 -0.005904
     26057 -0.000136
     26058 -0.000018
MX6:p 0 6012 8016 11023 12024 13027 14028 0 20040
      26054 26056 26057 26058
c Soil, sand and 10% water, rho= 1.5, estimate from 1-2 g/cc
m7   nlib=60c plib=04p pnlib=70u
     14000 0.3
     8016 .633
     1001 .067
MX7:p 14000 8016 0
c
c
c gypsum (main component of drywall), density = 0.69 g/cm3
m8 nlib=60c plib=04p pnlib=70u elib=03e
     001001  0.333321
     008016  0.500014
     016000  0.083324
     020000  0.083341
c
c
c Tungsten, density = 19.3 g/cm3
m9 nlib=60c plib=04p pnlib=70u elib=03e
      74182 -0.2650
      74183 -0.1431
      74184 -0.3076
      74186 -0.2843
c
c Copper, density = 8.96
m10 nlib=60c plib=04p pnlib=70u elib=03e
      29063 -0.6915
      29065 -0.3085
c
c
c AIR Dry (near sea level), rho = 0.001205
m20 nlib=60c plib=04p pnlib=70u
c $ Neutron
```

```
     6000 -0.000124 $ C
     7014 -0.755268 $ N
     8016 -0.244608 $ O
MX20:p 6012 7014 8016
c
m23 nlib=60c plib=04p pnlib=70u $ borated PE rho ~1.08
     1001 -0.136530
     6000 -0.813470
     5010 -0.0098
     5011 -0.0402
MX23:p 0 6012 0 0
c Heavy Water, rho=1.105340
M25 nlib=60c plib=04p pnlib=70u
     1002 -0.201133
     8016 -0.798867
c
c    Material 99: Stilbene, rho=1.16
c   -----------------------------------------------------------------
m99    NLIB=60c PLIB=04p
       1001.60c  .4615
       6000.60c  .5385
MX99:p 0 6012
c
c
c MESH TALLIES 50cm x 50cm x 50cm
c
TMESH
c
c
RMESH11:P DOSE 10 1 1 1
CORA11 -100 129i 550
CORB11 -100 129i 550
CORC11 68.62 73.62
c
c
RMESH31:P DOSE 10 1 1 1
CORA31 -100 129i 550
CORB31 247.5 252.5
CORC31 0 139i 700
c
c
c FLUX MESHES
c
c
RMESH71:P FLUX
CORA71 -100 129i 550
CORB71 -100 129i 550
CORC71 68.62 73.62
c
RMESH91:P FLUX
CORA91 -100 129i 550
CORB91 247.5 252.5
CORC91 0 139i 700
c
```

```
RMESH131:P DOSE 10 1 1 1
CORA131 462.74 467.74
CORB131 -100 129i 550
CORC131 0 139i 700
c
RMESH141:P FLUX
CORA141 462.74 467.74
CORB141 -100 129i 550
CORC141 0 139i 700
c
ENDMD
c
c
SDEF PAR = e  ERG = 9   POS= 340.2 250 71.12  RAD=d1 VEC = 1 0 0
     DIR = 1 AXS=1 0 0 EXT=0
SI1 0 0.25 $ radial sampling range: 0 to Rmax (=0.25cm)
SP1 -21 1  $ first order power law sampling
c
PRINT    10 40 50 100 110 126 128 140 160
NPS 1e7
PRDMP    2J  1                         $ write MCTAL file
FILES 21 dumn1
DBCN
LCA 8J 1
c IPOL 0 0 0 0 J J 1 54
c RPOL 1e-3 1e-3
c END DATA CARDS **************************************************
c END FILE
```

APPENDIX D

Analytic Transverse Attenuation Script

```
# Script for calculating attenuation of
# transverse shots through Fuel Cask
#
# C.A. Miller, cmillera@umich.edu
# 3/3/2016
# Updated 9/2016


import math
import json

PINS=15 # number of pins on a side of assembly
GUIDES=17 # number of guide tubes
FUEL_RAD=0.475234 # Fuel Pellet Diameter (cm)
CLADDING_THICKNESS=0.05842 # Cladding thickness of zircaloy (cm)
GAP=0.009906 # Gap between fuel and cladding (cm)
PITCH = 1.44272 # Center to center distance between fuel rods (cm)
assemSpace =  5.715 # spacing between assemblies, edge-to-edge pitch (cm)
outerCoreR = 168.275 #outer core radius in cm
innerCoreR =  85.5734 #inner core radius in cm
fuelAttCo = 4.569E-02 # cm^2/g
cladAttCo = 3.441E-02 # cm^2/g
concreteAttCo=2.664E-2 # cm^2/g
stainlessAttCo=2.982E-02 # cm^2/g
carbonSteelAttCo= 2.986E-02 # cm^2/g
fuelDensity = 10.4538 #g/cm^3
cladDensity = 5.8736 #g/cm^3
carbonSteelDensity = 7.83 #g/cm^3
stainlessDensity = 7.92 #g/cm^3
concreteDensity = 2.5 #g/cm^3
#
# HI_STORM SPECIFIC
innerStainlessR = innerCoreR
outerStainlessR = innerCoreR + 1.25
innerCarbonR1 = innerCoreR + 1.25 + 6.65
outerCarbonR1 = innerCarbonR1 + 5.10
innerConcreteR = outerCarbonR1
outerConcreteR = innerConcreteR + 67.9
```

```
innerCarbonR2 = outerConcreteR
outerCarbonR2 = innerCarbonR2 + 1.9

## ASSEMBLY MAP #################################################################
# map of assembly placement in cask, assumes centered, 1 for assembly
coreMap = [[0,0,1,1,0,0],[0,1,1,1,1,0],[1,1,1,1,1,1],[1,1,1,1,1,1],[0,1,1,1,1,0],[0,0,1,1,0,0] #MPC-24

print (coreMap)
sizeCoreMap=len(coreMap)*len(coreMap[1])

CASK_ID=innerCoreR*2 # inner cask diameter (cm)
CASK_OD=outerCoreR*2 # outer cask diameter (cm)
######################################################################


## ASSEMBLY DEFINITION################################################
# in pin_Centers, 1 for fuel, 2 for guide
assemPinCenters= []
g=0 # test count for guide tubes
assemDiagram=[['x' for i in range(PINS)] for j in range(PINS)]
for i in range(PINS):
    for j in range(PINS):
        assemPinCenters.append([(i*PITCH)+(PITCH/2),(j*PITCH)+(PITCH/2),1])
        #************************************************************
        #MUST BE CHANGED FOR DIFFERENT ASSEMBLIES OR GUIDE PLACEMENTS
        #starting at 0
        #************************************************************
        if (i==2 or i==12) and (j==5 or j==9):
            assemPinCenters[int((i*PINS)+j)][2]=2
            assemDiagram[i][j]='O'
            g=g+1
        if (i==3 or i==11) and (j==3 or j==11):
            assemPinCenters[int((i*PINS)+j)][2]=2
            assemDiagram[i][j]='O'
            g=g+1
        if (i==5 or i==9) and (j==2 or j==5 or j==9 or j==12):
            assemPinCenters[int((i*PINS)+j)][2]=2
            assemDiagram[i][j]='O'
            g=g+1
        if i==7 and j==7:
            assemPinCenters[int((i*PINS)+j)][2]=2
            assemDiagram[i][j]='O'
            g=g+1
#print (g)
#print len(assemblyPinCenters)
print (assemDiagram)
######################################################################

## CASK MAPPING#######################################################
vMiddle= float((len(coreMap)+1))/2 -1 # vertical middle of coreMap, 0 start
hMiddle= float((len(coreMap[1])+1))/2 -1 # horizontal middle of coreMap, 0
```

```
start
#print vMiddle
#print hMiddle
#print len(coreMap[1])%2

# for full core buliding, i is vertical, increasing values top->down
#                          is horizontal, icreasing values left->right

fullCore=[]
for i in range(len(coreMap)):
    for j in range(len(coreMap[1])):
        if coreMap[i][j] == 1:
            # finds if assembly is in middle middle of core map
            if i == vMiddle and j == hMiddle:
                for k in range(len(assemPinCenters)):
                        pinCenterX=assemPinCenters[k][0]-(PINS*PITCH/2)
                        pinCenterY=assemPinCenters[k][1]-(PINS*PITCH/2)
                        fullCore.append([pinCenterX,pinCenterY,assemPinCenters[k][2]])
            # finds if assembly is in top middle of core map
            if i != vMiddle and j == hMiddle:
                for k in range(len(assemPinCenters)):
                        pinCenterX=assemPinCenters[k][0]-(PINS*PITCH/2)
                            #centers assembly horizontally
                        if len(coreMap)% 2 == 1:
                            pinCenterY=assemPinCenters[k][1]+(PITCH*PINS*(vMiddle-i-0.5))+(assemSpace*math.ceil(vMiddle-i))
                        else:
                            pinCenterY=assemPinCenters[k][1]+(PITCH*PINS*(vMiddle-i-0.5))+(assemSpace*math.ceil(vMiddle-i))-assemSpace/2
#shifts assembly to proper place veritcally, up or down
#rounds down i to apply correct number of assembly spacings
#uses difference between i and the middle (sign flipped to preserve coordinate space)
#     to apply shift by #assemblies away from center
                        fullCore.append([pinCenterX,pinCenterY,assemPinCenters[k][2]])

            # finds if assembly is in middle left of core map
            if i == vMiddle and j != hMiddle:
                for k in range(len(assemPinCenters)):
                        if len(coreMap[1])% 2 == 1:
                            pinCenterX=assemPinCenters[k][0]+(PITCH*PINS*(-hMiddle+j-0.5))+(assemSpace*math.ceil(j-hMiddle))
                        else:
                            pinCenterX=assemPinCenters[k][0]+(PITCH*PINS*(-hMiddle+j-0.5))+(assemSpace*math.ceil(j-hMiddle))-assemSpace/2
#shifts assembly to proper place horizontally, left or right
#rounds down i to apply correct number of assembly spacings
#uses difference between i and the middle (sign flipped to preserve coordinate space)
#     to apply shift by #assemblies away from center
                        pinCenterY=assemPinCenters[k][1]-(PINS*PITCH/2)
                            #centers assembly to proper place vertically
```

```
                        fullCore.append([pinCenterX,pinCenterY, assemPinCenters[k][2]])
            # finds if assembly is in top left of core map
            if i != vMiddle and j != hMiddle:
                for k in range(len(assemPinCenters)):
                        if len(coreMap[1])% 2 == 1:
                            pinCenterX=assemPinCenters[k][0]+(PITCH*PINS*(-hMiddle+j-0.5))+(assemSpace*math.ceil(j-hMiddle))
                        else:
                            pinCenterX=assemPinCenters[k][0]+(PITCH*PINS*(-hMiddle+j-0.5))+(assemSpace*math.ceil(j-hMiddle))-assemSpace/2
#shifts assembly to proper place horizontally, left or right
#rounds down i to apply correct number of assembly spacings
#uses difference between i and the middle (sign flipped to preserve coordinate space)
#     to apply shift by #assemblies away from center
                        if len(coreMap)% 2 == 1:
                            pinCenterY=assemPinCenters[k][1]+(PITCH*PINS*(vMiddle-i-0.5))+(assemSpace*math.ceil(vMiddle-i))
                        else:
                            pinCenterY=assemPinCenters[k][1]+(PITCH*PINS*(vMiddle-i-0.5))+(assemSpace*math.ceil(vMiddle-i))-assemSpace/2
#shifts assembly to proper place veritcally, up or down
#rounds down i to apply correct number of assembly spacings
#uses difference between i and the middle (sign flipped to preserve coordinate space)
#     to apply shift by #assemblies away from center
                        fullCore.append([pinCenterX,pinCenterY, assemPinCenters[k][2]])

#write out file of all pin locations
f=open('fullCore.txt','w')
for item in fullCore:
    json.dump(item[0],f)
    f.write(' ')
    json.dump(item[1],f)
    f.write(' ')
    json.dump(item[2],f)
    f.write('\n')
f.close()
#######################################################################


## BEAM DEFINITION####################################################
scans = 90
FAN_START=205 #origin of fan Beam
ANGLE = float(61)
SHIFT = 5; # Clockwise Shift (in degrees) of first shot
ANGLE_OPTION = 0
totalAtt=[]
f=open('beamLine.txt','w') #opens file for beamline mapping
json.dump(innerCoreR,f)
f.write('\n')
json.dump(outerCoreR,f)
```

```
f.write('\n')
# Writing more cask info
json.dump(outerStainlessR,f)
f.write('\n')
json.dump(innerCarbonR1,f)
f.write('\n')
json.dump(innerConcreteR,f)
f.write('\n')
json.dump(innerCarbonR2,f)
f.write('\n')
angle_step=float(ANGLE)/(scans)
for scan_number in range(scans) :

    x1=math.cos(math.radians(FAN_START))*outerCoreR
    x2=outerCoreR
    y1=math.sin(math.radians(FAN_START))*outerCoreR
    y2=y1+(math.tan(math.radians((angle_step*scan_number)-SHIFT))*(
   outerCoreR-x1))

    if ANGLE_OPTION == 1:
         x1=outerCoreR*math.cos(math.radians(angle1))
         y1=outerCoreR*math.sin(math.radians(angle1))
         x2=outerCoreR*math.cos(math.radians(angle2))
         y2=outerCoreR*math.sin(math.radians(angle2))


    #print x1
    #print y1
    #print x2
    #print y2


    m=(y2-y1)/(x2-x1)
    y_int=y1-(m*x1)
    A=x2-x1
    B=y1-y2
    C=(x1-x2)*y1+(y2-y1)*x1

    # Writing Beamline information
    json.dump(x1,f)
    f.write('\n')
    json.dump(x2,f)
    f.write('\n')
    json.dump(m,f)
    f.write('\n')
    json.dump(y_int,f)
    f.write('\n')

    #print (x1)
    #print (y1)
    #print ((angle_step*scan_number)-SHIFT)
    ##################################################################

    ## PIN INTERSECTION TESTING ######################################
```

```
    count = 0
    fuel_count = 0
    fuel_att_length = 0
    clad_att_length = 0
    for i in range(len(fullCore)):
        distance= abs(A*fullCore[i][1]+B*fullCore[i][0]+C)/math.sqrt(A**2+B**2)
        #print distance
        if distance<(FUEL_RAD + CLADDING_THICKNESS + GAP):
            count = count +1
            Cx = fullCore[i][0]
            Cy = fullCore[i][1]

            # FUEL THICKNESS
            if fullCore[i][2] == 1:
                a = 1 + m**2
                b = 2*m*y_int - 2*Cy*m - 2*Cx
                c = Cx**2 + Cy**2 + y_int**2 - 2*Cy*y_int - FUEL_RAD**2

                x_fuel_1 = (-b + math.sqrt(abs(b**2 - 4*a*c)))/(2*a)
                x_fuel_2 = (-b - math.sqrt(abs(b**2 - 4*a*c)))/(2*a)

                y_fuel_1 = m*x_fuel_1 + y_int
                y_fuel_2 = m*x_fuel_2 + y_int

                d_fuel = math.sqrt((x_fuel_2-x_fuel_1)**2 + (y_fuel_2-y_fuel_1)**2)

                fuel_att_length = fuel_att_length + d_fuel

                fuel_count = fuel_count + 1

            # GAP + FUEL TOTAL DISTANCE
            a = 1 + m**2
            b = 2*m*y_int - 2*Cy*m - 2*Cx
            c = Cx**2 + Cy**2 + y_int**2 - 2*Cy*y_int - (FUEL_RAD + GAP)**2

            x_gap_1 = (-b + math.sqrt(abs(b**2 - 4*a*c)))/(2*a)
            x_gap_2 = (-b - math.sqrt(abs(b**2 - 4*a*c)))/(2*a)

            y_gap_1 = m*x_gap_1 + y_int
            y_gap_2 = m*x_gap_2 + y_int

            d_gap = math.sqrt((x_gap_2-x_gap_1)**2 + (y_gap_2-y_gap_1)**2)

            # CLAD TOTAL DISTANCE
            a = 1 + m**2
            b = 2*m*y_int - 2*Cy*m - 2*Cx
            c = Cx**2 + Cy**2 + y_int**2 - 2*Cy*y_int - (FUEL_RAD + GAP + CLADDING_THICKNESS)**2

            x_clad_1 = (-b + math.sqrt(abs(b**2 - 4*a*c)))/(2*a)
            x_clad_2 = (-b - math.sqrt(abs(b**2 - 4*a*c)))/(2*a)

```

```python
        y_clad_1 = m*x_clad_1 + y_int
        y_clad_2 = m*x_clad_2 + y_int

        d_clad = math.sqrt((x_clad_2-x_clad_1)**2 + (y_clad_2-y_clad_1)**2)

        clad_att_length = clad_att_length + (d_clad - d_gap)
        #Outer Distance (clad edge to edge) - gap outer distance

    Cy_cask = float(0) # Cask Center
    Cx_cask = float(0) # Cask Center


    #OUTER Stainless Steel Distance
    a = 1 + m**2
    b = 2*m*y_int - 2*Cy_cask*m - 2*Cx_cask
    c = Cx_cask**2 + Cy_cask**2 + y_int**2 - 2*Cy_cask*y_int - (outerStainlessR)**2

    x_outer_1 = (-b + math.sqrt(abs(b**2 - 4*a*c)))/(2*a)
    x_outer_2 = (-b - math.sqrt(abs(b**2 - 4*a*c)))/(2*a)
    y_outer_1 = m*x_outer_1 + y_int
    y_outer_2 = m*x_outer_2 + y_int

    d_outer_stainless = math.sqrt((x_outer_2-x_outer_1)**2 + (y_outer_2-y_outer_1)**2)


    #INNER Stainless Steel Distance
    a = 1 + m**2
    b = 2*m*y_int - 2*Cy_cask*m - 2*Cx_cask
    c = Cx_cask**2 + Cy_cask**2 + y_int**2 - 2*Cy_cask*y_int - (innerStainlessR)**2

    x_inner_1 = (-b + math.sqrt(abs(b**2 - 4*a*c)))/(2*a)
    x_inner_2 = (-b - math.sqrt(abs(b**2 - 4*a*c)))/(2*a)

    y_inner_1 = m*x_inner_1 + y_int
    y_inner_2 = m*x_inner_2 + y_int

    d_inner_stainless = math.sqrt((x_inner_2-x_inner_1)**2 + (y_inner_2-y_inner_1)**2)

    stainless_att_length = d_outer_stainless - d_inner_stainless




    #OUTER Carbon1 distance
    a = 1 + m**2
    b = 2*m*y_int - 2*Cy_cask*m - 2*Cx_cask
    c = Cx_cask**2 + Cy_cask**2 + y_int**2 - 2*Cy_cask*y_int - (outerCarbonR1)**2

```

```
    x_outer_1 = (-b + math.sqrt(abs(b**2 - 4*a*c)))/(2*a)
    x_outer_2 = (-b - math.sqrt(abs(b**2 - 4*a*c)))/(2*a)
    y_outer_1 = m*x_outer_1 + y_int
    y_outer_2 = m*x_outer_2 + y_int

    d_outer_carbon1 = math.sqrt((x_outer_2-x_outer_1)**2 + (y_outer_2-y_outer_1)**2)


    #INNER Carbon1 Distance
    a = 1 + m**2
    b = 2*m*y_int - 2*Cy_cask*m - 2*Cx_cask
    c = Cx_cask**2 + Cy_cask**2 + y_int**2 - 2*Cy_cask*y_int - (innerCarbonR1)**2

    x_inner_1 = (-b + math.sqrt(abs(b**2 - 4*a*c)))/(2*a)
    x_inner_2 = (-b - math.sqrt(abs(b**2 - 4*a*c)))/(2*a)

    y_inner_1 = m*x_inner_1 + y_int
    y_inner_2 = m*x_inner_2 + y_int

    d_inner_carbon1 = math.sqrt((x_inner_2-x_inner_1)**2 + (y_inner_2-y_inner_1)**2)

    carbon1_att_length = d_outer_carbon1 - d_inner_carbon1



    #OUTER Concrete distance
    a = 1 + m**2
    b = 2*m*y_int - 2*Cy_cask*m - 2*Cx_cask
    c = Cx_cask**2 + Cy_cask**2 + y_int**2 - 2*Cy_cask*y_int - (outerConcreteR)**2

    x_outer_1 = (-b + math.sqrt(abs(b**2 - 4*a*c)))/(2*a)
    x_outer_2 = (-b - math.sqrt(abs(b**2 - 4*a*c)))/(2*a)
    y_outer_1 = m*x_outer_1 + y_int
    y_outer_2 = m*x_outer_2 + y_int

    d_outer_concrete = math.sqrt((x_outer_2-x_outer_1)**2 + (y_outer_2-y_outer_1)**2)


    #INNER Concrete Distance
    a = 1 + m**2
    b = 2*m*y_int - 2*Cy_cask*m - 2*Cx_cask
    c = Cx_cask**2 + Cy_cask**2 + y_int**2 - 2*Cy_cask*y_int - (innerConcreteR)**2

    x_inner_1 = (-b + math.sqrt(abs(b**2 - 4*a*c)))/(2*a)
    x_inner_2 = (-b - math.sqrt(abs(b**2 - 4*a*c)))/(2*a)

    y_inner_1 = m*x_inner_1 + y_int
    y_inner_2 = m*x_inner_2 + y_int
```

```

    d_inner_concrete = math.sqrt((x_inner_2-x_inner_1)**2 + (y_inner_2-y_inner_1)**2)

    concrete_att_length = d_outer_concrete - d_inner_concrete



    #OUTER Carbon2 distance
    a = 1 + m**2
    b = 2*m*y_int - 2*Cy_cask*m - 2*Cx_cask
    c = Cx_cask**2 + Cy_cask**2 + y_int**2 - 2*Cy_cask*y_int - (outerCarbonR2)**2

    x_outer_1 = (-b + math.sqrt(abs(b**2 - 4*a*c)))/(2*a)
    x_outer_2 = (-b - math.sqrt(abs(b**2 - 4*a*c)))/(2*a)
    y_outer_1 = m*x_outer_1 + y_int
    y_outer_2 = m*x_outer_2 + y_int

    d_outer_carbon2 = math.sqrt((x_outer_2-x_outer_1)**2 + (y_outer_2-y_outer_1)**2)

    f.write('F5_X: ')
    json.dump(x_outer_1,f)
    f.write('\n')
    f.write('F5_Y: ')
    json.dump(y_outer_1,f)
    f.write('\n')

    #INNER Carbon2 Distance
    a = 1 + m**2
    b = 2*m*y_int - 2*Cy_cask*m - 2*Cx_cask
    c = Cx_cask**2 + Cy_cask**2 + y_int**2 - 2*Cy_cask*y_int - (innerCarbonR2)**2

    x_inner_1 = (-b + math.sqrt(abs(b**2 - 4*a*c)))/(2*a)
    x_inner_2 = (-b - math.sqrt(abs(b**2 - 4*a*c)))/(2*a)

    y_inner_1 = m*x_inner_1 + y_int
    y_inner_2 = m*x_inner_2 + y_int

    d_inner_carbon2 = math.sqrt((x_inner_2-x_inner_1)**2 + (y_inner_2-y_inner_1)**2)

    carbon2_att_length = d_outer_carbon2 - d_inner_carbon2

    #ATTENUATION CALCULATION

    stainlessExp=stainless_att_length*stainlessDensity*stainlessAttCo
    fuelExp=fuel_att_length*fuelDensity*fuelAttCo
    cladExp=clad_att_length*cladDensity*cladAttCo
    carbon1Exp=carbon1_att_length*carbonSteelDensity*carbonSteelAttCo
    carbon2Exp=carbon2_att_length*carbonSteelDensity*carbonSteelAttCo
    concreteExp=concrete_att_length*concreteDensity*concreteAttCo
```

```

    totalAtt.append(math.exp(-(stainlessExp)-(fuelExp)-(cladExp)-(
   carbon1Exp)-(concreteExp)-(carbon2Exp)))

f.close() #closes file for beamline mapping

f=open('scanMap.txt','w')
for item in totalAtt:
    json.dump(item,f)
    f.write('\n')
f.close()
```

APPENDIX E

Dose Rate Calculation Script

```
# LET based Dose Calculation
# C.A. Miller
# cmillera@umich.edu
# 2/12/2019
# Updated 5/2019
#
# Calculate energy using Birks Light output to Energy conversion
# Divide by mass for absorbed dose
#
# Determine stopping power
# Calculate Q-value from stopping power
# Multiply absorbed dose by Q-value

import math
import json
import numpy as np
import matplotlib.pyplot as plt
from pathlib import Path

#Inputs
Measurement='../CfBare_50cm/'
MeasurementTime=600 #seconds
folders=10
channel=0
nScalingFactor=1

psdA=-0.00007679
psdB=0.2149
psdC=0.0148502

C_EDGE=2.52 #detemined from DualRead integrals

DetMass=0.1194
DetDensity=1.16

ErgConvert=np.linspace(0,10,1001)
Lconvert=[]
nIntegral=[]
```

```
pIntegral=[]
VnsDep=[]
pVnsDep=[]
LDepCounts=[]
pLDepCounts=[]
nEdep=[]
pEdep=[]
LETenergy=[]
LET=[]
LETbinned=[]
Q_LETread=[]
Qread=[]
Qbinned=[]
Dose=[]
pDose=[]
DoseError=[]
pDoseError=[]
PHDtoDoseE_bins=[]
PHDtoDoseE_vals=[]
DosePHDtoDoseE=[]
figure=plt.figure()


####OPENING AND READING

#stilbene LET, Edep ,Ep
LETdata = open('stilbene_dedx_data.txt','r')
# stilbene light matrix from 0:0.01:10 MeV
LfromE = open('Stilbene2inchBirks_2027_2783_L_E0to10_Pintegral.txt','r')
#load in QvL Siebert Data
QvLRead=open('ICRUflesh_QvLET.txt','r')

LfromElines=LfromE.readlines()
for x in LfromElines: # reading in Light from E values
    Lconvert.append(x.split()[0])
LfromE.close()

LETlines=LETdata.readlines()
for x in LETlines: # reading in LET data
    LETenergy.append(x.split()[0])
    LET.append(x.split()[2]) #proton Data
LETdata.close()

QvLReadLines=QvLRead.readlines()
for x in QvLReadLines: # reading in Q v. LET data
    Q_LETread.append(x.split()[0])
    Qread.append(x.split()[1])
QvLRead.close()

for i in range(folders):
    #load in neutron Int distribution
    psdRead=open( Measurement +str(i+1)+ '/psd'+str(channel),'r')
    psdReadLines=psdRead.readlines()
    for x in psdReadLines:
```

```
        total=np.array(x.split()[1], dtype='f')
        tail=np.array(x.split()[0], dtype='f')
        if tail > psdA*total**2 + psdB*total +psdC:
            nIntegral.append(total)
        else:
            pIntegral.append(total)
    print('folder: '+str(i+1))

LDepCounts,VnsDep=np.histogram(nIntegral,bins=200)
pLDepCounts,pVnsDep=np.histogram(pIntegral,bins=200)

VnsDep=np.array(VnsDep, dtype='f')
pVnsDep=np.array(pVnsDep, dtype='f')
LDepCounts=np.array(LDepCounts, dtype='f')
pLDepCounts=np.array(pLDepCounts, dtype='f')


LETenergy=np.array(LETenergy, dtype='f')
LET=np.array(LET, dtype='f')
Q_LETread=np.array(Q_LETread, dtype='f')
Qread=np.array(Qread, dtype='f')

####INTERPOLATING AND CONVERTING

for i in range(len(VnsDep[1:])):
    #convert L to pEdep
    nEdep.append(np.interp(VnsDep[i]*0.478/C_EDGE,Lconvert,ErgConvert))

for i in range(len(pVnsDep[1:])):
    #convert L to pEdep
    pEdep.append(pVnsDep[i]*0.478/C_EDGE)

for i in range(len(nEdep)):
    #interpolate and convert Edep to LET
    LETbinned.append(np.interp(nEdep[i],LETenergy,LET))
LETbinned=np.array(LETbinned, dtype='f')
# converting (MeV/(mg/cm^2)) to (keV/um)
LETbinned = LETbinned*DetDensity*100

for i in range(len(LETbinned)):
    #build Q from LET values
    Qbinned.append(np.interp(LETbinned[i],Q_LETread,Qread))

for i in range(len(nEdep)):
    #Converting MeV to J, dividing by mass for Gray to Sievert
    Dose.append(nEdep[i]*Qbinned[i]*nScalingFactor*LDepCounts[i]*1.602E-13/
   DetMass)
for i in range(len(pEdep)):
    #Converting MeV to J, dividing by mass for Gray, Q=1 for photons
    pDose.append(pEdep[i]*pLDepCounts[i]*1.602E-13/DetMass)

for i in range(len(nEdep)):
    #Converting MeV to J, dividing by mass for Gray to Sievert
    DoseError.append(nEdep[i]*Qbinned[i]*math.sqrt(LDepCounts[i])*1.602E
```

```
    -13/DetMass)
for i in range(len(pEdep)):
    #Converting MeV to J, dividing by mass for Gray, Q=1 for photons
    pDoseError.append(pEdep[i]*math.sqrt(pLDepCounts[i])*1.602E-13/DetMass)


Dose=np.array(Dose, dtype='f')
pDose=np.array(pDose, dtype='f')
MeasurementTime=np.array(MeasurementTime, dtype='f')

# Converting from total to per hour,
# then Sievert -> Rem, then Rem -> mrem
Dose = Dose*3600/MeasurementTime*100*1000
# Converting from total to per hour,
# then Sievert -> Rem, then Rem -> mrem
pDose = pDose*3600/MeasurementTime*100*1000


DoseError = DoseError*3600/MeasurementTime*100*1000
pDoseError = pDoseError*3600/MeasurementTime*100*1000

print('Neutron Dose = '+repr(sum(Dose))+ ' +/- '+  repr(sum(DoseError)))
print('Photon Dose = '+repr(sum(pDose))+ ' +/- '+repr(sum(pDoseError)))
```

BIBLIOGRAPHY

[1] Patricia Rife. *Lise Meitner and the Dawn of the Nuclear Age*. Birkhauser, Boston, MA, 1999.

[2] Treaty on the Non-Proliferation of Nuclear Weapons, 1970.

[3] 10 CFR part 74.4: Definitions, 2017.

[4] James E. Doyle. *Nuclear Safeguards, Security, and Nonproliferation*. Elsevier Inc., Burlington, MA, 2008.

[5] D.A. Edwards and M.J. Syphers. *An Introduction to the Physics of High Energy Accelerators*. John Wiley & Sons, 2008.

[6] 6 USC § 982 . Screening and scanning of cargo containers. Technical Report Title 6: Domestic Security, The Code of Laws of the United States of America.

[7] Bernard Kempinski and Chris Murphy. Scanning and imaging shipping containers overseas: costs and alternatives. Technical Report June, Congressional Budget Office, 2016.

[8] Robert C. Runkle, David L. Chichester, and Scott J. Thompson. Rattling nucleons: New developments in active interrogation of special nuclear material. *Nuclear Instruments and Methods in Physics Research, Section A: Accelerators, Spectrometers, Detectors and Associated Equipment*, 663(1):75–95, 2012.

[9] Glen F. Knoll. *Radiation Detection and Measurement*. John Wiley & Sons, Hoboken, 4 edition, 2010.

[10] A.I. Blokhin, M.B. Chadwick, T. Fukahori, Y. Han, Y.-O. Lee, M.N. Martins, S.F. Mughabghab, P. Obložinský, V.V. Varlamov, B. Yu, and J. Zhang. Handbook on Photonuclear Data for Applications: Cross-sections and Spectra. Technical report, International Atomic Energy Agency, Vienna, Austria, 2000.

[11] M. B. Chadwick, M. Herman, P. Obložinský, M. E. Dunn, Y. Danon, a. C. Kahler, D. L. Smith, B. Pritychenko, G. Arbanas, R. Arcilla, R. Brewer, D. a. Brown, R. Capote, a. D. Carlson, Y. S. Cho, H. Derrien, K. Guber, G. M. Hale, S. Hoblit, S. Holloway, T. D. Johnson, T. Kawano, B. C. Kiedrowski, H. Kim, S. Kunieda, N. M. Larson, L. Leal, J. P. Lestone, R. C. Little, E. a. McCutchan, R. E. MacFarlane, M. MacInnes, C. M. Mattoon, R. D. McKnight, S. F. Mughabghab, G. P a Nobre, G. Palmiotti, A. Palumbo, M. T. Pigni, V. G. Pronyaev, R. O. Sayer, a. a. Sonzogni, N. C. Summers, P. Talou, I. J. Thompson, A. Trkov,

R. L. Vogt, S. C. van der Marck, A. Wallner, M. C. White, D. Wiarda, and P. G. Young. ENDF/B-VII.1 nuclear data for science and technology: Cross sections, covariances, fission product yields and decay data. *Nuclear Data Sheets*, 112(12):2887–2996, 2011.

[12] K.W. Geiger and L. Van Der Zwan. Radioactive neutron source spectra from 9Be(α, n) cross section data. *Nuclear Instruments and Methods*, 131(2):315–321, 1975.

[13] Cory Scott Waltz. *Characterization of Deuteron-Deuteron Neutron Generators*. PhD thesis, University of California, Berkeley, 2016.

[14] Jani Reijonen, Tak P. Lou, Bryan Tolmachoff, and Ka-Ngo Leung. Compact neutron source development at LBNL. In *Charged Particle Detection, Diagnostics, and Imaging*, volume 4510, pages 80–87. SPIE, 12 2001.

[15] nGen-400 Protable Neutron Interrogation, Rev 01-19. Technical report, Starfire Industries, Champaign, IL, 2019.

[16] Phil Kerr, Mark Rowland, Dan Dietrich, Wolfgang Stoeffl, Boyd Wheeler, Les Nakae, Doug Howard, Chris Hagmann, Jason Newby, and Robert Porter. Active detection of small quantities of shielded highly-enriched uranium using low-dose 60-kev neutron interrogation. *Nuclear Instruments and Methods in Physics Research, Section B: Beam Interactions with Materials and Atoms*, 261(1-2 SPEC. ISS.):347–350, 2007.

[17] Varian Medical Systems. Linatron-M9 & M9A: Modular high-energy X-ray Source. Technical report.

[18] Areg Danagoulian, William Bertozzi, Curtis L. Hicks, Alexei V. Klimenko, Stephen E. Korbly, Robert J. Ledoux, and Cody M. Wilson. Prompt neutrons from photofission and its use in homeland security applications. *2010 IEEE International Conference on Technologies for Homeland Security, HST 2010*, pages 379–384, 2010.

[19] Thomas J.T. Kwan, Richard E. Morgado, Tai Sen F. Wang, B. Vodolaga, V. Terekhin, L. M. Onischenko, S. B. Vorozhtsov, E. V. Samsonov, A. S. Vorozhtsov, Yu G. Alenitsky, E. E. Perpelkin, A. A. Glazov, D. L. Novikov, V. Parkhomchuk, V. Reva, V. Vostrikov, V. A. Mashinin, S. N. Fedotov, and S. A. Minayev. The development of enabling technologies for producing active interrogation beams. *Review of Scientific Instruments*, 81(10), 2010.

[20] A. Antolak, B. Doyle, K.-N. Leung, D. Morse, and P. Provencio. Active interrogation using low-energy nuclear reactions. *Proceedings of SPIE - The International Society for Optical Engineering*, 5923(September 2005), 2005.

[21] R W Garnett, S S Kurennoy, L J Rybarcyk, T N Taddeucci, and Los Alamos. A Monochromatic Gamma Source Without Neutrons. *6th International Particla Accelerator Conference*, pages 2292–2294, 2015.

[22] Buckley E. O'Day, Zachary S. Hartwig, Richard C. Lanza, and Areg Danagoulian. Initial results from a multiple monoenergetic gamma radiography system for nuclear security. *Nuclear Instruments and Methods in Physics Research, Section A: Accelerators, Spectrometers, Detectors and Associated Equipment*, 832:68–76, 2016.

[23] P. B. Rose, A. S. Erickson, M. Mayer, J. Nattress, and I. Jovanovic. Uncovering Special Nuclear Materials by Low-energy Nuclear Reaction Imaging. *Scientific Reports*, 6(April):24388, 2016.

[24] C. A. Miller, C.G.R Geddes, B.A. Ludewigt, S.D. Clarke, and S.A. Pozzi. Verification of Dry Storage Cask Loading using Monoenergetic Photon Sources. *Annals of Nuclear Energy*, 2019.

[25] Cameron G R Geddes, Sergey Rykovanov, Nicholas H. Matlis, Sven Steinke, Jean Luc Vay, Eric H. Esarey, Bernhard Ludewigt, Kei Nakamura, Brian J. Quiter, Carl B. Schroeder, Csaba Toth, and Wim P. Leemans. Compact quasi-monoenergetic photon sources from laser-plasma accelerators for nuclear detection and characterization. *Nuclear Instruments and Methods in Physics Research, Section B: Beam Interactions with Materials and Atoms*, 350:116–121, 2015.

[26] Sudeep Banerjee, Shouyuan Chen, Nathan Powers, Daniel Haden, Cheng Liu, G. Golovin, Jun Zhang, Baozhen Zhao, S. Clarke, S. Pozzi, J. Silano, H. Karwowski, and Donald Umstadter. Compact source of narrowband and tunable X-rays for radiography. *Nuclear Instruments and Methods in Physics Research, Section B: Beam Interactions with Materials and Atoms*, 350, 2015.

[27] H. Schwoerer, B. Liesfeld, H. P. Schlenvoigt, K. U. Amthor, and R. Sauerbrey. Thomson-backscattered X rays from laser-accelerated electrons. *Physical Review Letters*, 96(1):1–4, 2006.

[28] T. Scott Carman, Vladimir Litveninko, John Madey, Charles Neuman, Blaine Norum, Patrick G. O'Shea, N. Russell Roberson, Carol Y. Scarlett, Eric Schreiber, and Henry R. Weller. The TUNL-FELL inverse Compton γ-ray source as a nuclear physics facility. *Nuclear Instruments and Methods in Physics Research, Section A: Accelerators, Spectrometers, Detectors and Associated Equipment*, 378(1-2):1–20, 1996.

[29] S. Chen, N. D. Powers, I. Ghebregziabher, C. M. Maharjan, C. Liu, G. Golovin, S. Banerjee, J. Zhang, N. Cunningham, A. Moorti, S. Clarke, S. Pozzi, and D. P. Umstadter. MeV-energy X rays from inverse compton scattering with laser-wakefield accelerated electrons. *Physical Review Letters*, 110(15):1–5, 2013.

[30] W. Schumaker, G. Sarri, M. Vargas, Z. Zhao, K. Behm, V. Chvykov, B. Dromey, B. Hou, A. Maksimchuk, J. Nees, V. Yanovsky, M. Zepf, A. G R Thomas, and K. Krushelnick. Measurements of high-energy radiation generation from laser-wakefield accelerated electron beams. *Physics of Plasmas*, 21(5), 2014.

[31] John M. Dawson and T Tajima. Laser Electron Accelerator. *Physical Review Letters*, 43(4):267–270, 1979.

[32] Los Alamos National Laboratory. ENDF Data.

[33] J.B. Birks. *The Theory and Practice of Scintillation Counting*. Pergamon Press, Oxford, U.K., 1964.

[34] T.H. Shin, P.L. Feng, J. Carlson, S.D. Clarke, and S.A. Pozzi. Measured neutron light output response for trans-stilbene and small-molecule organic glass scintillators. *Nuclear Inst. and Methods in Physics Research, A*, Under Revi, 2019.

[35] Sara a. Pozzi, Enrico Padovani, and Marzio Marseguerra. MCNP-PoliMi: A Monte-Carlo code for correlation measurements. *Nuclear Instruments and Methods in Physics Research, Section A: Accelerators, Spectrometers, Detectors and Associated Equipment*, 513(3):550–558, 2003.

[36] L. M. Bollinger and G. E. Thomas. Measurement of the time dependence of scintillation intensity by a delayed-coincidence method. *Review of Scientific Instruments*, 32(9):1044–1050, 1961.

[37] Roland Lee Bowles. *Analysis of scintillation pulse shapes for stilbene using neutron and gamma-ray excitation*. PhD thesis, University of Richmond, 1961.

[38] M. M. Bourne, S. D. Clarke, N. Adamowicz, S. A. Pozzi, N. Zaitseva, and L. Carman. Neutron detection in a high-gamma field using solution-grown stilbene. *Nuclear Instruments and Methods in Physics Research, Section A: Accelerators, Spectrometers, Detectors and Associated Equipment*, 806:348–355, 2016.

[39] Natalia Zaitseva, Andrew Glenn, Leslie Carman, H. Paul Martinez, Robert Hatarik, Helmut Klapper, and Stephen Payne. Scintillation properties of solution-grown trans-stilbene single crystals. *Nuclear Instruments and Methods in Physics Research, Section A: Accelerators, Spectrometers, Detectors and Associated Equipment*, 789:8–15, 2015.

[40] User Manual UM2792: V1730/Vx1730 & V1725/Vx1725 Rev. 2. Technical report, CAEN S.p.A., Viareggio, IT, 2016.

[41] User Manual UM2580: DPP-PSD Digital Pulse Processing for Pulse Shape Discrimination Rev. 8. Technical report, CAEN S.p.A., Viareggio, IT, 2016.

[42] Marc L Ruch. *Silicon Photomultipliers for Compact Neutron Scatter Cameras*. PhD thesis, University of Michigan, 2017.

[43] User Manual UM5960: CoMPASS Rev. 3. Technical report, CAEN S.p.A., Viareggio, IT, 2018.

[44] Mark A. Norsworthy, Alexis Poitrasson-Rivière, Marc L. Ruch, Shaun D. Clarke, and Sara A. Pozzi. Evaluation of neutron light output response functions in EJ-309 organic scintillators. *Nuclear Instruments and Methods in Physics Research, Section A: Accelerators, Spectrometers, Detectors and Associated Equipment*, 842(June 2016):20–27, 2017.

[45] F.D. Brooks. A scintillation counter with neutron and gamma-ray discriminators. *Nuclear Instruments and Methods*, 4(3):151–163, 1959.

[46] J.K. Polack, M. Flaska, A. Enqvist, C.S. Sosa, C.C. Lawrence, and S.A. Pozzi. An algorithm for charge-integration, pulse-shape discrimination and estimation of neutron/photon misclassification in organic scintillators. *Nuclear Instruments and Methods in Physics Research*

Section A: Accelerators, Spectrometers, Detectors and Associated Equipment, 795:253–267, 9 2015.

[47] J.T. Caldwell, W.E. Kunz, and J.D. Atencio. APPARATUS AND METHOD FOR QUANTITATIVE ASSAY OF GENERIC TRANSURANC WASTES FROM NUCLEAR REACTORS, 1984.

[48] Kelly A. Jordan and Tsahi Gozani. Pulsed neutron differential die away analysis for detection of nuclear materials. *Nuclear Instruments and Methods in Physics Research, Section B: Beam Interactions with Materials and Atoms*, 261(1-2 SPEC. ISS.):365–368, 2007.

[49] Michael C. Hamel, J. Kyle Polack, Marc L. Ruch, Matthew J. Marcath, Shaun D. Clarke, and Sara A. Pozzi. Active neutron and gamma-ray imaging of highly enriched uranium for treaty verification. *Submitted to Scientific Reports*, 2017.

[50] Tsahi Gozani. Neutron based non-intrusive inspection techniques. In *Proceedings of The International Society for Optical Engineering, Volume 2867*, pages 174–181, 1997.

[51] Andy Buffler. Contraband detection with fast neutrons. *Radiation Physics and Chemistry*, 71(3-4):853–861, 2004.

[52] Xinjie Qiu. Neutron Interaction with Germanium Detector Germanium Detector in the simulation. Technical report, University of Minnesota, 2005.

[53] Idaho National Laboratory. Gamma-ray Spectrometry Catalog.

[54] A. F. M. Ishaq and T. J. Kennett. A Study of Thermal Neutron Capture in Chlorine. *Canadian Journal of Physics*, 50(24):3090–3099, 1972.

[55] G.A. Bartholomew and P.J. Campion. Neutron Capture Gamma Rays from Lithium, Boron, and Nitrogen. *Canadian Journal of Physics*, (504), 1957.

[56] S. Raman, E. T. Jurney, J. W. Starner, and J. E. Lynn. Thermal-neutron capture by silicon isotopes. *Physical Review C*, 46(3):972–983, 1992.

[57] Kelly A. Jordan and Tsahi Gozani. Detection of 235U in hydrogenous cargo with Differential Die-Away Analysis and optimized neutron detectors. *Nuclear Instruments and Methods in Physics Research, Section A: Accelerators, Spectrometers, Detectors and Associated Equipment*, 579(1):388–390, 2007.

[58] Hiroshi Taninaka, Kengo Hashimoto, Cheol Ho Pyeon, Tadafumi Sano, Tsuyoshi Misawa, and Takaaki Ohsawa. Determination of lambda-mode eigenvalue separation of a thermal accelerator-driven system from pulsed neutron experiment. *Journal of Nuclear Science and Technology*, 47(4):376–383, 2010.

[59] T. Gozani. *Active Nondestructive Assay of Nuclear Materials*. U.S. Nuclear Regulatory Commission, Washington, D.C., 1981.

[60] I. Pázsit and Y. Yamane. Backward theory of Feynman- and Rossi-alpha methods with multiple emission sources. *Nuclear Science and Engineering*, 133(3):269–281, 1999.

[61] Michael Y. Hua, Jesson D. Hutchinson, George E. McKenzie, Tony H. Shin, Shaun D. Clarke, and Sara A. Pozzi. Derivation of the Two-Exponential Probability Density Function for Rossi-Alpha Measurements of Reflected Assemblies and Validation for the Special Case of Shielded Measurements. *Nuclear Science and Engineering*, pages 1–13, 9 2019.

[62] Alexis C. Kaplan, Vladimir Henzl, Howard O. Menlove, Martyn T. Swinhoe, Anthony P. Belian, Marek Flaska, and Sara A. Pozzi. Determination of total plutonium content in spent nuclear fuel assemblies with the differential die-away self-interrogation instrument. *Nuclear Instruments and Methods in Physics Research, Section A: Accelerators, Spectrometers, Detectors and Associated Equipment*, 764:347–351, 11 2014.

[63] Tony H. Shin, Jesson Hutchinson, Rian Bahran, and Sara A. Pozzi. A Note on the Nomenclature in Neutron Multiplicity Mathematics. *Nuclear Science and Engineering*, 193(6):663–679, 2019.

[64] Y. S. Rana and S. B. Degweker. Feynman-alpha and rossi-alpha formulas with delayed neutrons for subcritical reactors driven by pulsed non-poisson sources. *Nuclear Science and Engineering*, 162(2):117–133, 2009.

[65] nGen-300 for Sharp Pulsed Neutrons. Technical report, Starfire Industries, 2018.

[66] J T Goorley, M R James, T E Booth, F B Brown, J S Bull, L J Cox, J W Durkee, J S Elson, M L Fensin, R A Forster, J S Hendricks, H G Hughes, R C Johns, B C Kiedrowski, and S G Mashnik. MCNP6 User's Manual, Version 1.0, LA-CP-13-00634. *Los Alamos National Laboratory*, (LA-CP-13-00634):765, 2013.

[67] Inc. MathWorks. MATLAB Curve Fitting Toolbox.

[68] Natalia Zaitseva, Leslie Carman, Andrew Glenn, Jason Newby, Michelle Faust, Sebastien Hamel, Nerine Cherepy, and Stephen Payne. Application of solution techniques for rapid growth of organic crystals. *Journal of Crystal Growth*, 314(1):163–170, 2011.

[69] C. A. Miller, C. A. Meert, A. K. Harvis, S. D. Clarke, and S. A. Pozzi. Accelerator Shielding Design for Active Interrogation Methods Development Cameron. In *Transactions of the American Nuclear Society*, volume 118, pages 787–790, Philadelphia, Pennsylvania, 2018.

[70] Cameron A Miller, Christopher A Meert, Shaun D Clarke, and Sara A Pozzi. Mitigation of Photon Active Interrogation Background for Fast Neutron Detection. *American Institute of Physics*, Accepted J, 2019.

[71] Kim Roth. Nuclear Engineering Laboratory dedication: Connecting the past and future, 2017.

[72] Denise B Pelowitz. MCNPX User's Manual: Version 2.7.0. *LA-CP-11-00438*, 2011.

[73] The International Commission on Radiological Protection. ICRP PUBLICATION 21: Data for Protection against Ionizing Radiation from External Sources: Supplement to ICRP Publication 15. Technical report, 1971.

[74] 10 C.F.R § 20. Standards for Protection Against Radiation, 2017.

[75] Caen. User Manual UM2792: V1730/Vx1730 & V1725/Vx1725. Technical Report Rev. 2-10, CAEN S.p.A, Viareggio, IT, 2016.

[76] C. Fu, A. Di Fulvio, S. D. Clarke, D. Wentzloff, S. A. Pozzi, and H. S. Kim. Artificial neural network algorithms for pulse shape discrimination and recovery of piled-up pulses in organic scintillators. *Annals of Nuclear Energy*, 120:410–421, 2018.

[77] A. C. Kaplan, M. Flaska, A. Enqvist, J. L. Dolan, and S. A. Pozzi. EJ-309 pulse shape discrimination performance with a high gamma-ray-to-neutron ratio and low threshold. *Nuclear Instruments and Methods in Physics Research, Section A: Accelerators, Spectrometers, Detectors and Associated Equipment*, 729:463–468, 2013.

[78] M. B. Chadwick, M. Herman, P. Obložinský, M. E. Dunn, Y. Danon, a. C. Kahler, D. L. Smith, B. Pritychenko, G. Arbanas, R. Arcilla, R. Brewer, D. a. Brown, R. Capote, a. D. Carlson, Y. S. Cho, H. Derrien, K. Guber, G. M. Hale, S. Hoblit, S. Holloway, T. D. Johnson, T. Kawano, B. C. Kiedrowski, H. Kim, S. Kunieda, N. M. Larson, L. Leal, J. P. Lestone, R. C. Little, E. a. McCutchan, R. E. MacFarlane, M. MacInnes, C. M. Mattoon, R. D. McKnight, S. F. Mughabghab, G. P a Nobre, G. Palmiotti, A. Palumbo, M. T. Pigni, V. G. Pronyaev, R. O. Sayer, a. a. Sonzogni, N. C. Summers, P. Talou, I. J. Thompson, A. Trkov, R. L. Vogt, S. C. van der Marck, A. Wallner, M. C. White, D. Wiarda, and P. G. Young. ENDF/B-VII.1 nuclear data for science and technology: Cross sections, covariances, fission product yields and decay data. *Nuclear Data Sheets*, 112(12):2887–2996, 2011.

[79] Shouyuan Chen, Grigory Golovin, Cameron Miller, Daniel Haden, Sudeep Banerjee, Ping Zhang, Cheng Liu, Jun Zhang, Baozhen Zhao, Shaun Clarke, Sara Pozzi, and Donald Umstadter. Shielded radiography with a laser-driven MeV-energy X-ray source. *Nuclear Instruments and Methods in Physics Research, Section B: Beam Interactions with Materials and Atoms*, 366(October):217–223, 2016.

[80] C.A. Miller, C.G.R. Geddes, S.D. Clarke, and S.A. Pozzi. Shielding a monoenergetic photon source for nonproliferation applications analysis. *Nuclear Instruments and Methods in Physics Research Section A: Accelerators, Spectrometers, Detectors and Associated Equipment*, (January), 2019.

[81] J.L. Jones, J W Sterbentz, W Y Yoon, and D R Norman. Bremsstrahlung Versus Monoenergetic Photon Dose and Photonuclear Stimulation Comparisons at Long Standoff Distances. *AIP Conference Proceedings*, 43, 2009.

[82] C.G.R Geddes, B. Ludewigt, J. Valentine, B.J. Quiter, M.-A. Descalle, G. Warren, M. Kinlaw, S. Thompson, D. Chichester, C. Miller, and S. Pozzi. Impact of Monoenergetic Photon Sources on Nonproliferation Applications. Technical report, 2017.

[83] I Jovanovic and A. S. Erickson, editors. *Active Interrogation in Nuclear Security: Science, Technology and Systems*. Springer, 1 edition, 2018.

[84] A. A. Zavadtsev, D. A. Zavadtsev, A. A. Krasnov, N. P. Sobenin, S. V. Kutsaev, D. V. Churanov, and M. O. Urbant. A dual-energy linac cargo inspection system. *Instruments and Experimental Techniques*, 54(2):241–248, 2011.

[85] Harry E. Martz, Steven M. Glenn, Jerel A. Smith, Charles J. Divin, and Stephen G. Azevedo. Poly- Versus Mono-Energetic Dual-Spectrum Non-Intrusive Inspection of Cargo Containers. *IEEE Transactions on Nuclear Science*, 64(7):1709–1718, 2017.

[86] Research at the University of Nebraska-Lincoln: 2013-2014 Report. Technical report, University of Nebraska-Lincoln, Lincoln, NE, 2014.

[87] J. I. Katz. X-radiography of Cargo Containers.

[88] Victor Orphan and Ernie Muenchau. Advanced Cargo Container Scanning Technology Development. Technical report, Science Applications International Corporation, 2009.

[89] Siraj M. Khan, Paul E. Nicholas, and Michael S. Terpilak. Radiation dose equivalent to stowaways in vehicles. *Health Physics*, 86(5):483–492, 2004.

[90] K. Ta Phuoc, S. Corde, C. Thaury, V. Malka, A. Tafzi, J. P. Goddet, R. C. Shah, S. Sebban, and A. Rousse. All-optical Compton gamma-ray source. *Nature Photonics*, 6(5):308–311, 2012.

[91] G. Sarri, D. J. Corvan, W. Schumaker, J. M. Cole, A. Di Piazza, H. Ahmed, C. Harvey, C. H. Keitel, K. Krushelnick, S. P.D. Mangles, Z. Najmudin, D. Symes, A. G.R. Thomas, M. Yeung, Z. Zhao, and M. Zepf. Ultrahigh brilliance multi-MeV γ-ray beams from nonlinear relativistic thomson scattering. *Physical Review Letters*, 113(22):1–5, 2014.

[92] Hai En Tsai, Xiaoming Wang, Joseph Shaw, Alexey V. Arefiev, Zhengyan Li, Xi Zhang, Rafal Zgadzaj, Watson Henderson, V. Khudik, G. Shvets, and M. C. Downer. Compact tunable Compton x-ray source from laser wakefield accelerator and plasma mirror. *AIP Conference Proceedings*, 1777(2015), 2016.

[93] G.R. Blumenthal and R.J. Gould. Bremsstrahlung, Synchotron Radiation, and Compton Scattering of High-Energy Electrons Traversing Dilute Gases. *Reviews of Modern Physics*, 42(2):237–270, 1973.

[94] A. Bonatto, C. B. Schroeder, J. L. Vay, C. G.R. Geddes, C. Benedetti, E. Esarey, and W. P. Leemans. Passive and active plasma deceleration for the compact disposal of electron beams. *Physics of Plasmas*, 22(8), 2015.

[95] Matthias Frankl and Rafael Macián-juan. Photonuclear Benchmarks of C , Al , Cu , Ta , Pb , and U from the ENDF / B-VII Cross-Section Library ENDF7U Using MCNPX. 183, 2016.

[96] M.J. Berger, J.H. Hubbell, S.M. Seltzer, J. Chang, J.S. Coursey, R. Sukumar, D.S. Zucker, and K. Olsen. XCOM: Photon Cross Sections Database, 2010.

[97] Anthony L. Meadowcroft and Ray D. Edwards. High-energy bremsstrahlung diagnostics to characterize hot-electron production in short-pulse laser-plasma experiments. *IEEE Transactions on Plasma Science*, 40(8):1992–2001, 2012.

[98] S. Mobilio, F. Boscherini, and C. Meneghini. *Synchotron Radiation: Basics, Methods and Applications*. Springer, 2015.

[99] G. R. Plateau, C. G.R. Geddes, D. B. Thorn, M. Chen, C. Benedetti, E. Esarey, A. J. Gonsalves, N. H. Matlis, K. Nakamura, S. Rykovanov, C. B. Schroeder, S. Shiraishi, T. Sokollik, J. Van Tilborg, Cs Toth, S. Trotsenko, T. S. Kim, M. Battaglia, Th Stöhlker, and W. P. Leemans. Low-emittance electron bunches from a laser-plasma accelerator measured using single-shot X-ray spectroscopy. *AIP Conference Proceedings*, 1507(August):278–283, 2012.

[100] S. G. Rykovanov, C. G.R. Geddes, J. L. Vay, C. B. Schroeder, E. Esarey, and W. P. Leemans. Quasi-monoenergetic femtosecond photon sources from Thomson Scattering using laser plasma accelerators and plasma channels. *Journal of Physics B: Atomic, Molecular and Optical Physics*, 47(23), 2014.

[101] Safeguards Techniques and Equipment. Technical report, IAEA, Vienna, Austria, 2011.

[102] International Atomic Energy Agency. International Safeguards in the Design of Facilities for Long Term Spent Fuel Management. Technical report, Vienna, Austria, 2018.

[103] C. J. Wharton, E. H. Seabury, A. J. Caffrey, and P. L. Winston. Summary Report: INL CDCIS Cask Scanner Testing at Doel, Belgium. Technical report, 2013.

[104] E.R. Johnson and K.J. Notz. Shipping and Storage Cask Data for Spent Nuclear Fuel. Technical report, Oak Ridge National Laboratory, Oak Ridge, TN, 1988.

[105] D. Poulson, J. M. Durham, E. Guardincerri, C. L. Morris, J. D. Bacon, K. Plaud-Ramos, D. Morley, and A. A. Hecht. Cosmic ray muon computed tomography of spent nuclear fuel in dry storage casks. *Nuclear Instruments and Methods in Physics Research, Section A: Accelerators, Spectrometers, Detectors and Associated Equipment*, 842(June 2016):48–53, 2017.

[106] Zhengzhi Liu, Jason Hayward, Can Liao, and Haori Yang. Detection of Missing Assemblies and Estimation of the Scattering Densities in a VSC-24 Dry Storage Cask with Cosmic-Ray-Muon- Based Computed Tomography. *Journal of Nuclear Materials Management*, 45(12), 2017.

[107] ASTM A36 Steel, bar, 2019.

[108] RJ McConn Jr, CJ Gesh, RT Pagh, RA Rucker, and RG Williams III. Compendium of Material Composition Data for Radiation Transport Modeling. Technical report, 2011.

[109] HI-STORM Final Safety Analysis Report. Technical report, Holtec International, 2016.

[110] John A. McClure, Sedat Goluoglu, and Peter Gottlieb. Estimation of the Westinghouse 17x17 MOX SNF Assembly Weight. Technical report, CRWMS/M&O, 1998.

[111] Erin A. Miller, Joseph A. Caggiano, Robert C. Runkle, Timothy A. White, and Aaron M. Bevill. Scatter in cargo radiography. *Applied Radiation and Isotopes*, 69(3):594–603, 2011.

[112] Laser Technology for k-BELLA and Beyond. Technical report, Lawrence Berkeley National Laboratory, 2017.

[113] Piezo Positioning Systems with Parallel Kinematics, 2019.

[114] Nobuhiko Nakanii, Tomonao Hosokai, Kenta Iwasa, Shinichi Masuda, Alexei Zhidkov, Naveen Pathak, Hiroki Nakahara, Yoshio Mizuta, Naoki Takeguchi, and Ryosuke Kodama. Transient magnetized plasma as an optical element for high power laser pulses. *Physical Review Special Topics - Accelerators and Beams*, 18(2):2–7, 2015.

[115] O W Hermann and R M Westfall. ORIGEN-S: SCALE system module to calculate fuel depletion, actinide transmutation, fission product buildup and decay, and associated radiation source terms. *Vol. II, Sect. F7 of SCALE: A Modular Code System for Performing Standardized Computer Analyses for Licensing Evaluation, NUREG/CR-0200, Rev*, 6:1–2, 1995.

[116] Jacopo Buongiorno. PWR Description Pressurized Water Reactor (PWR), 2010.

[117] S. Vaccaro, S. J. Tobin, A. Favalli, B. Grogan, P. Jansson, H. Liljenfeldt, V. Mozin, J. Hu, P. Schwalbach, A. Sjöland, H. Trellue, and D. Vo. PWR and BWR spent fuel assembly gamma spectra measurements. *Nuclear Instruments and Methods in Physics Research, Section A: Accelerators, Spectrometers, Detectors and Associated Equipment*, 833:208–225, 2016.

[118] Rhodotron TT300-HE: High Energy Electron Generator. Technical report, IBA Ind., Louvain-La-Neuve, Belgium, 0.

[119] J K Shultis and R E Faw. *Radiation Shielding*. Prentice-Hall, Inc., Upper Saddle River, New Jersey, 1996.

[120] Thermo Fisher Scientific. ASP-2e/NRD: Portable Neutron REM Meter. Technical report.

[121] 451B Ion Chamber Survey Meter: Operators Manual. Technical report, Fluke Biomedical, Everett, WA, 2013.

[122] D. W. Rogers. Why not to trust a neutron remmeter. *Health Physics*, 37(6):37–735, 1979.

[123] The International Commission on Radiological Protection. *ICRP Publication 26: Recommendations of the International Commission on Radiological Protection*. Pergamon Press, Oxford, U.K., 1977.

[124] Coursey J.S. Zucker M.A. Berger, M.J. and J. Chang. ESTAR, PSTAR, and ASTAR: Computer Programs for Calculating Stopping-Power and Range Tables for Electrons, Protons, and Helium Ions (version 1.2.3), 2005.

[125] B.R.L Siebert and H. Schumacher. Quality factors , ambient dose and personal dose equivalent for neutrons, based on the new icru sttoping power data for protons and apha particles. *Radiation Protection Dosimetry*, 1995.

[126] The International Commission on Radiological Protection. *ICRP Publication 103: The 2007 Recommendations of the International Commission on Radiological Protection*. Elsevier, 2007.

[127] The International Commission on Radiological Protection. *ICRP Publication 60: 1990 Recommendation of the International Commission on Radiological Protection*. Pergamon Press, Oxfor, U.K., 1991.

[128] C. A. Miller, S. D. Clarke, and S. A. Pozzi. Effects of Detector Cell Size on Dose Rate Measurements using Organic Scintillators. *2017 IEEE Nuclear Science Symposium and Medical Imaging Conference, NSS/MIC 2017 - Conference Proceedings*, pages 2–4, 2018.

[129] ICRP Pub 74. *Annals of the ICRP*, 1990.

[130] H Y Lee, T N Taddeucci, R C Haight, T a Bredeweg, A Chyzh, M Devlin, N Fotiades, J M Gostic, R a Henderson, M Jandel, E Kwan, A Laptev, R O Nelson, J M O'Donnell, B a Perdue, S a Wender, M C White, and C Y Wu. Li-glass detector response study with a 252Cf source for low-energy prompt fission neutrons. *Nuclear Instruments and Methods in Physics Research Section A: Accelerators, Spectrometers, Detectors and Associated Equipment*, 703(0):213–219, 2013.

[131] Matthew J I Balmer, Kelum A A Gamage, and Graeme C Taylor. A novel approach to neutron dosimetry.

[132] M. M. Bourne, C. Mussi, E. C. Miller, S. D. Clarke, S. a. Pozzi, and a. Gueorguiev. Characterization of the CLYC detector for neutron and photon detection. *Nuclear Instruments and Methods in Physics Research, Section A: Accelerators, Spectrometers, Detectors and Associated Equipment*, 736:124–127, 2014.

[133] Mark E Ellis, Charles Hurlbut, Chris Allwork, and Brooke Morris. Neutron and Gamma Ray Pulse Shape Discrimination with EJ-270 Lithium-Loaded Plastic Scintillator. pages 2–6, 2017.